Atomic Force Microscopy at Mineral–Water Interfaces: Hydration, Chemical Identification and Point Defects

Dissertation zur Erlangung des Grades
“Doktor der Naturwissenschaften” im Promotionsfach Chemie
am Fachbereich Chemie, Pharmazie und Geowissenschaften der

Johannes Gutenberg-Universität in Mainz

Hagen Söngen
geb. in Rüdesheim am Rhein

Mainz, den 4. Mai 2017

D77 (Dissertation Johannes Gutenberg-Universität Mainz)

Dean of faculty	[redacted]
First report	[redacted]
Second report	[redacted]
Third report	[redacted]
Submitted	May 4, 2017
Oral examination	June 19, 2017

Contents

1 Introduction

What makes mineral–water interfaces important?

Minerals and liquid water are abundant constituents of the earth. Interactions taking place at the *mineral–water interface* have tremendous environmental, biological and industrial impact.[1,2] For example, the dissolution and growth of minerals governs the composition of sea waters,[3] impacts the global carbon dioxide cycle[4] and plays a crucial role in biomineralization.[5] For understanding these processes, knowledge concerning the properties of interfacial water is critical.[6,7] The aim of the present thesis is therefore to gain insights into mineral–water interfaces at the atomic scale.

I focus on a particularly interesting group of minerals: The carbonate minerals calcite, dolomite and magnesite. Calcite, the most stable polymorph of $CaCO_3$, is a major constituent of sedimentary rock.[8] Moreover, calcite occurs as biomineral in the shells of marine animals[9] and even in the human brain.[10] The minerals dolomite ($CaMg(CO_3)_2$) and magnesite ($MgCO_3$) are obtained by substituting either half or all of the calcium ions in calcite with magnesium. This exchange of ions opens up the possibility for systematic studies on the interfacial behavior of calcium (the "cation of choice for most organisms")[11] and magnesium ions.

Investigating mineral–water interfaces with AFM

Atomic force microscopy (AFM) is the ideal tool for investigating surfaces in real space.[12] Numerous technical improvements have made it possible to atomically resolve surfaces in water using dynamic AFM modes.[13–16] AFM is based on scanning the sample surface with a sharp tip – consequently, for probing the interfacial *volume*, three-dimensional (3D) scanning of the tip is necessary.[17] This technique is very recent and typically not implemented in commercially-available microscopes. Therefore, I implemented a highly-flexible 3D scanning routine that can be used to extend existing dynamic atomic force microscopes.

The central quantity in AFM is the tip-sample force. In this thesis, I provide a unifying theory for quantitative AFM, that makes use of only one approximation, the *harmonic approximation.* This theory reveals the three and only pieces of information about the tip-sample force that are accessible with dynamic AFM. Using the quantitative analysis, I present the hydration structure at the most stable surfaces of calcite, dolomite and magnesite. Subtle differences in the 3D hydration structure of calcium and magnesium ions at the dolomite surface allow for the identification of the ions. This *chemical* *identification* is a major advance for the study of mineral–water interfaces with AFM. Moreover, I take advantage of the real-space imaging capabilities of AFM to resolve the hydration structure around point defects at the calcite–water interface. The data demonstrate that point defects cause a minute, yet detectable change in the hydration structure with a lateral extent of few atoms.

As stimulus for future studies, I additionally provide in this thesis a comprehensive theory for Kelvin probe force microscopy (KPFM), a technique closely related to AFM. In KPFM, a voltage is applied between tip and sample. As a result detailed in this thesis, the charge distribution at the sample can be specifically probed. In future studies, this technique could provide an even more detailed insight into solid–liquid interfaces.

Thesis structure

I present the *three AFM equations* – a unifying theoretical approach for describing AFM in section 2.1. Contrary to previous works, the theoretical approach presented in this section does not rely on mode-specific assumptions, making the three AFM equations applicable for a wide community of AFM users.

In section 2.2, the implementation of an *interactive* virtual AFM (VAFM) is described. The simulation allows users to interactively explore the parameter space available in real AFM experiments, since the interactive VAFM takes measurement electronics into account. The interactive VAFM does not only provide a useful learning and testing platform: As demonstrated in this section, the interactive VAFM also allows for checking the validity of the *harmonic approximation*, the only approximation used to derive the three AFM equations in section 2.1.

In section 3.1, I address the question whether *order* at solid–liquid interface can be induced purely by the confinement of the surface, regardless of attractive interactions between solid and liquid. For this purpose, a Monte Carlo (MC) simulation of a most simple solid–liquid interface is conducted. The simulation demonstrates that an ordered arrangement of liquid molecules at the solid–liquid interface does not necessarily mean that there are attractive interactions between the liquid molecules and the surface.

I introduce the dynamic AFM setup employed in this thesis in section 3.2, where I particularly focus on my implementation of the 3D scanning and data acquisition. A most flexible data acquisition system has proven to be necessary to record all quantities that are relevant for quantitative dynamic AFM.

The hydration structure above the three minerals *calcite*, *dolomite* and *magnesite* is presented in section 3.3. In this section, I also present the chemical identification of calcium and magnesium ions at the dolomite–water interface. The next three sections are devoted to the calcite–water interface at conditions that resemble naturally occurring mineral–water interfaces: In section 3.4, I investigate the hydration structure near point defects. The dependency of the hydration structure on the concentrations of ions is discussed in section 3.5. Finally, I provide an outlook towards more comprehensive studies on the adsorption of molecules at the calcite–water interface. For this, I present 3D AFM results at the ethanol–water interface in section 3.6.

Finally, I explore the signal obtained in KPFM measurements. I present a detailed derivation of the KPFM signal obtained in different KPFM modes in section 4.1. In a similar spirit as the section on quantitative AFM, this discussion eliminates most mode-specific aspects and shows that the KPFM signal generally contains a weighted sum over charges in the tip-sample system. The *weight function for charges* is explored in detail in section 4.2 and a summary of preliminary KPFM experiments at the mineral–water interface is presented in section 4.3.

2 Quantitative AFM

2.1 The three AFM equations

Section 2.1 is based on the article “Quantitative Dynamic Atomic Force Microscopy” by H. Söngen, R. Bechstein and A. Kühnle, which has been accepted for publication in *Journal of Physics: Condensed Matter* (reference 18). I have written the manuscript with contributions by R. Bechstein and comments by A. Kühnle. I measured and analyzed the shown experimental data and prepared the figures. Parts of the article are reproduced verbatim, changes have been made to make the section consistent with the other sections in this thesis.

A variety of atomic force microscopy (AFM) modes is employed in the field of surface science. The most prominent AFM modes include the amplitude modulation (AM) and the frequency modulation (FM) mode. Over the years, different ways for analyzing data acquired with different AFM modes have been developed, where each analysis is usually based on mode-specific assumptions and approximations. Checking the validity of the seemingly different approximations employed in the various analysis methods can be a tedious task. Moreover, a straightforward comparison of data analyzed with different methods can, therefore, be challenging. Here, we combine the existing evaluation methods which have been separately developed for the different AFM modes and present a unifying set of three equations. These three AFM equations *allow for a straightforward analysis of AFM data within the* harmonic approximation*, regardless of the AFM mode. The three AFM equations provide the three and only pieces of information about the tip-sample force available within the harmonic approximation. We demonstrate the generality of our approach by quantitatively analyzing three-dimensional AFM data obtained in both the AM and FM mode.*

2.1.1 Introduction

Three decades have passed since atomic force microscopy (AFM) has been invented.[12] During this time a number of experimental strategies for obtaining AFM data have been developed, namely static AFM as well as the dynamic AFM modes using “amplitude modulation”[19] (AM), “phase modulation”[20] (PM) and “frequency modulation”[21] (FM). Numerous theoretical studies have been devoted to a quantitative understanding of the recorded AFM data in the respective modes. Each of these studies focuses on a specific operation mode, giving the impression that different approximations and specific theoretical treatment of AFM data is required for each AFM mode and different amounts of information about the tip-sample interaction are available in the different modes.

Here, based on existing theories that have been discussed in the view of specific modes only, we establish a comprehensive and generalized set of three equations that unifies the quantitative analysis of AFM data for the various AFM modes. We employ one approximation only, namely the *harmonic approximation*, which is equivalent to the perturbation approach by Giessibl[22,23] and Dürig,[24–27] the "Krylov–Bogoliubov averaging method" by Sasaki and Tsukada *et al.*,[28–31] the Fourier expansion up to the first harmonic by Hölscher *et al.*[32–34] and Ebeling and Hölscher[35] as well as the "method of slowly varying parameters"[36] and others.[37]

With AFM, the force between tip and sample is investigated. Observing the full movement of the AFM tip allows to determine the tip-sample force. Within the harmonic approximation, the movement of the tip is approximated using three observables: the static deflection, the amplitude and the phase shift for a given excitation force amplitude and excitation frequency. Consequently, three pieces of information about the tip-sample force can be obtained, namely the average even contribution to the tip-sample force, the average tip-sample force gradient and the average tip-sample damping constant. Here, we provide the three *AFM equations* which allow to obtain these three pieces of information. They are valid for analyzing AFM data irrespective of the specific AFM mode.

In the next section, we will derive the three AFM equations: First, we will split the tip-sample force into an even and an odd part. Second, we will introduce the path of the tip in the harmonic approximation. Third, we will analyze the average force acting on the tip, as well as the average kinetic energy and power. Finally, the three AFM equations will be obtained. They connect the quantities measured in AFM with the three and only pieces of information about the tip-sample force available in AFM within the harmonic approximation. We will discuss the physical meaning of the three obtained results in section 2.1.3. To demonstrate the applicability of the AFM equations, we have conducted three-dimensional (3D) AFM measurements above calcite(10.4) in pure water using both the AM and the FM mode. In section 2.1.4, we present the results of the quantitative analysis of both data sets.

2.1.2 Derivation of the three AFM equations

In atomic force microscopy, a sample is probed with a tip. The obtained AFM data provide a depiction of the sample based on the force acting on the tip caused by the sample, *i.e.*, the tip-sample force $\mathbf{F}_{\mathrm{ts}}$. In general, the tip-sample force has a component normal to the surface and components in the lateral directions. In this section (and the remainder of the thesis), we will only discuss the normal component of the tip-sample

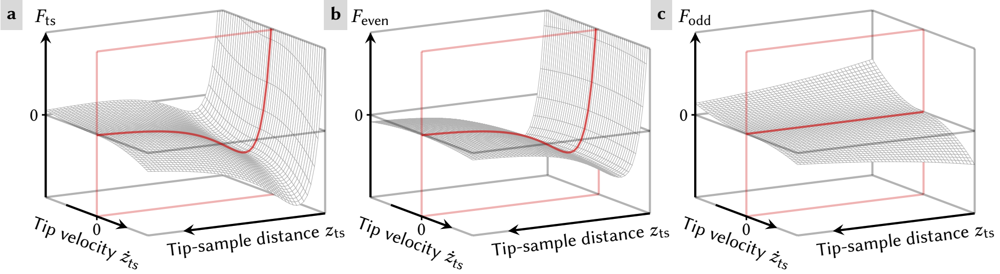

Figure 2.1: A tip-sample force F_{ts} and its components F_{even} and F_{odd} plotted as functions of the tip-sample distance and the tip velocity. Red curves indicate the static AFM case $\dot{z}_{ts} = 0$.

force F_{ts} and the resulting effect on the tip.

It appears plausible that the tip-sample force may in general depend on the tip-sample displacement $\mathbf{r}_{ts} = (x_{ts}, y_{ts}, z_{ts})$ and on the tip velocity $\dot{\mathbf{r}}_{ts}$. If the lateral tip displacement is constant (x_{ts} = const. and y_{ts} = const.), it is interesting to study the normal component of the tip-sample force F_{ts} as function of both the tip-sample distance z_{ts} and the normal component of tip velocity $\dot{z}_{ts}$. A typical tip-sample force $F_{ts}(z_{ts}, \dot{z}_{ts})$ is drawn in figure 2.1 a. At zero velocity, *i.e.*, in static AFM, a force-distance curve is obtained as indicated by the solid red line. This curve shows two prominent features which are typically observed: at large tip-sample distance, the tip-sample force approaches zero while the force increases sharply at small distance. In dynamic AFM, the tip velocity is not zero at all times and, therefore, both the distance and velocity dependence of the tip-sample force is probed by the tip. A frictional force decelerates the tip. Accordingly, friction decreases the tip-sample force when the tip-sample distance is increasing, *i.e*, at positive tip velocity and *vice versa*.

It is always possible to split the tip-sample force into two terms F_{even} and F_{odd}:[27,34,38]

$$F_{ts}(z_{ts}, \dot{z}_{ts}) = F_{even}(z_{ts}, \dot{z}_{ts}) + F_{odd}(z_{ts}, \dot{z}_{ts}) \tag{2.1}$$

The term F_{even} describes the contribution to the tip-sample force that is *even* with respect to the tip velocity

$$F_{even}(z_{ts}, \dot{z}_{ts}) = F_{even}(z_{ts}, -\dot{z}_{ts}) \tag{2.2}$$

and the term F_{odd} describes the contribution to the tip-sample force that is *odd* with respect to the tip velocity

$$F_{odd}(z_{ts}, \dot{z}_{ts}) = -F_{odd}(z_{ts}, -\dot{z}_{ts})\,. \tag{2.3}$$

It is necessary to consider the even and odd components separately,[27,34,38] since AFM can only extract these components of the tip-sample force, as already claimed in the introduction. We will later see that this is correct when we discuss the three AFM equations.

The even and odd contributions to the tip-sample force shown in figure 2.1 a are depicted in figure 2.1 b and c, respectively. Since F_{ts}, F_{even} and F_{odd} can depend on the tip velocity, none of these quantities is in general a *unique* function of the tip-sample distance: At a given tip-sample distance, F_{ts}, F_{even} and F_{odd} can have different values depending on the tip velocity, as can be seen in figure 2.1.

For conducting an AFM experiment, the tip is mounted on the free end of a mechanical resonator which can be, *e.g.*, a cantilever, a tuning fork or a length-extension sensor. This resonator is treated as a harmonic oscillator (see section 2.1.6 for the mathematical treatment), characterized by three properties: effective mass m, spring constant k and damping constant γ. Alternatively, the resonator can be characterized by its spring constant k, eigenfrequency $\nu_{\mathrm{e}} = (2\pi)^{-1}\sqrt{k/m}$ and quality factor[39] $Q = \sqrt{km}/\gamma$. The other end of the resonator is fixed and the position of this fixed end with respect to the sample can be adjusted by a positioning system. Lateral positioning allows for obtaining AFM images and normal positioning allows for distance-dependent measurements. The tip-sample distance is derived from measuring the *deflection* q of the free end of the resonator. This is detailed in section 2.1.5.

In a dynamic AFM experiment, the mechanical resonator is externally excited, *e.g.*, by using a shake piezo or an excitation laser with an external excitation force according to $F_{\mathrm{exc}} = F_0 \cos(2\pi\nu_{\mathrm{exc}}t)$. The two excitation parameters excitation force amplitude F_0 and excitation frequency ν_{exc} are free to be picked by the experimentalist. Feedback loops can be optionally employed to adjust the excitation parameters during the experiment.

As a consequence of the excitation, the tip is moving. Observing the *full* movement of the tip allows to determine the tip-sample force (as detailed in section 2.1.7). Typically, however, the deflection q and the tip-sample distance z_{ts} are approximated by

$$\begin{aligned} q &= q_{\mathrm{s}} + A\cos(2\pi\nu_{\mathrm{exc}}t + \varphi) \\ z_{\mathrm{ts}} &= z_{\mathrm{c}} + A\cos(2\pi\nu_{\mathrm{exc}}t + \varphi)\,. \end{aligned} \tag{2.4}$$

In this case, the three observables static deflection q_{s}, amplitude A and phase shift φ are sufficient to describe the tip movement. Equation 2.4 is the *harmonic approximation* – the only approximation needed to derive the AFM equations. Its validity can be checked at any time during the experiment by analyzing the deflection, *e.g.*, with an oscilloscope or a spectrum analyzer. The harmonic approximation (equation 2.4) implies that the resonator is in steady state, *i.e.*, F_0, ν_{exc}, q_{s}, A, φ and the center position z_{c} are constant and the tip velocity is $\dot{z}_{\mathrm{ts}} = \dot{q}$.

Several modes of conducting AFM experiments have been established. They differ in the number of employed feedback loops and their respective tasks. Figure 2.2 provides an overview starting in (a) with a static AFM experiment, in which no external excitation is applied and only the static deflection is observed. In dynamic AFM experiments

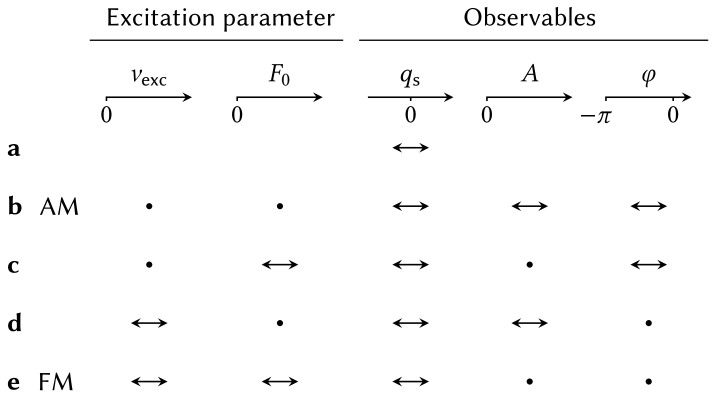

Figure 2.2: Overview of the static AFM mode (a) and the dynamic AFM modes (b–e). Points mark excitation parameters (F_0, ν_{exc}) and observables (q_s, A, φ) that are held constant, double arrows indicate quantities that can change. The mode in (b) is usually referred to as amplitude-modulation AFM (AM-AFM) while (e) is known as frequency-modulation AFM (FM-AFM).

both excitation parameters can be chosen to be constant (figure 2.2 b). Alternatively, a feedback loop can be used to keep the amplitude constant by adjusting the excitation force amplitude (figure 2.2 c and e). Another feedback loop can be used to keep the phase shift constant (usually at $-\pi/2$) by adjusting the excitation frequency (figure 2.2 d and e). In all cases, another additional feedback loop can be employed to adjust the normal position of the fixed end of the resonator in order to keep one of the varying quantities at a predefined value. In all dynamic AFM experiments, the two excitation parameters F_0 and ν_{exc} as well as the three observables q_s, A and φ are necessary for a quantitative analysis. The three observables allow to extract in total three pieces of information about the tip-sample force. The connection between these three aspects of the tip-sample force and the three observables are stated in the three *AFM equations* as will be introduced in the following.

As a physically insightful way to derive the three AFM equations, we analyze the time-averaged force acting on the tip $\langle F\rangle_t$ as well as the average kinetic energy $\langle T\rangle_t$ of the resonator and the average power $\langle P\rangle_t$. The force $F = m\ddot{q}$ acting on the tip consists of four contributions: (1) the tip-sample force, (2) the external excitation force, (3) the restoring force $-kq$ caused by the mechanical support keeping one end of the resonator in a fixed position and (4) the decelerating force $-\gamma\dot{q}$ caused by both internal friction in the moving resonator and friction of the resonator and tip moving through the surrounding medium:

$$F = m\ddot{q} = F_{\text{ts}}(z_{\text{ts}}, \dot{z}_{\text{ts}}) + F_0\cos(2\pi\nu_{\text{exc}}t) - kq - \gamma\dot{q}. \tag{2.5}$$

The time average of the force acting on the tip is

$$\langle F \rangle_t = m \langle \ddot{q} \rangle_t \overset{(2.4)}{=} 0 \tag{2.6}$$

when the deflection is given by equation 2.4, as is indicated above the equal sign. Inserting the tip-sample force (equation 2.1) and the deflection (equation 2.4) into equation 2.5 and averaging over time yields

$$\langle F \rangle_t = \langle F_{\text{even}}(z_{\text{ts}}, \dot{z}_{\text{ts}}) \rangle_t - kq_{\text{s}} \tag{2.7}$$

since $\langle F_{\text{odd}}(z_{\text{ts}}, \dot{z}_{\text{ts}}) \rangle_t = 0$. Combining the two equations 2.6 and 2.7 yields

$$\langle F_{\text{even}}(z_{\text{ts}}, \dot{z}_{\text{ts}}) \rangle_t = kq_{\text{s}}\,. \tag{2.8}$$

Knowing the spring constant of the resonator and measuring the static deflection allows to obtain the time average of the even contribution to the tip-sample force.[40] The time-averaged kinetic energy of the resonator is given by:

$$\langle T \rangle_t = \frac{m}{2} \left\langle \dot{z}_{\text{ts}}^2 \right\rangle_t \overset{(2.4)}{=} \frac{m}{4}(2\pi\nu_{\text{exc}})^2 A^2 \tag{2.9}$$

Another way to calculate the time-average of the kinetic energy is given by the virial theorem (VT):

$$\begin{aligned} \langle T \rangle_t &\overset{(\text{VT})}{=} -\frac{1}{2} \langle F \cdot z_{\text{ts}} \rangle_t \\ &\overset{(2.4)}{=} -\frac{1}{2} \langle F \cdot (z_{\text{ts}} - z_{\text{c}}) \rangle_t \\ &\overset{(2.5)}{=} -\frac{1}{2} \langle F_{\text{even}}(z_{\text{ts}}, \dot{z}_{\text{ts}}) \cdot (z_{\text{ts}} - z_{\text{c}}) \rangle_t - \frac{F_0 A}{4} \cos\varphi + \frac{kA^2}{4} \end{aligned} \tag{2.10}$$

From equations 2.9 and 2.10 it follows that:

$$\langle F_{\text{even}}(z_{\text{ts}}, \dot{z}_{\text{ts}}) \cdot (z_{\text{ts}} - z_{\text{c}}) \rangle_t = \frac{kA^2}{2} - \frac{m}{2}(2\pi\nu_{\text{exc}})^2 A^2 - \frac{F_0 A}{2} \cos\varphi\,. \tag{2.11}$$

The time-averaged power[41–43] is:

$$\langle P \rangle_t = \langle F \cdot \dot{z}_{\text{ts}} \rangle_t \overset{(2.4)}{=} 0 \tag{2.12}$$

when the deflection is given by equation 2.4. Using equation 2.5, the tip-sample force (equation 2.1) and averaging over time yields

$$\begin{aligned} \langle P \rangle_t &= \langle F \cdot \dot{z}_{\text{ts}} \rangle_t \\ &\overset{(2.5)}{=} \langle F_{\text{odd}}(z_{\text{ts}}, \dot{z}_{\text{ts}}) \cdot \dot{z}_{\text{ts}} \rangle_t - \frac{F_0}{2}(2\pi\nu_{\text{exc}}) A \sin\varphi - \frac{\gamma}{2}(2\pi\nu_{\text{exc}})^2 A^2 \end{aligned} \tag{2.13}$$

Inserting equation 2.12 in equation 2.13 results in

$$\langle F_{\text{odd}}(z_{\text{ts}}, \dot{z}_{\text{ts}}) \cdot \dot{z}_{\text{ts}} \rangle_t = \frac{F_0}{2}(2\pi\nu_{\text{exc}})A \sin\varphi + \frac{\gamma}{2}(2\pi\nu_{\text{exc}})^2 A^2. \tag{2.14}$$

The time-averaged force (equation 2.6) and power (equation 2.12) are both zero, which is in agreement with equation 2.4 describing the steady state. Only the even part of the tip-sample force contributes to the average kinetic energy (equation 2.10), while only the odd part contributes to the average power (equation 2.13).[27,34,38] It will be discussed in section 2.1.3 that conservative tip-sample forces contribute to the even part, but non-conservative forces can, in general, contribute to both the even and the odd part.

In static AFM, a single piece of information about F_{ts} is gained from the measured static deflection according to the special case of equation 2.8: $F_{\text{even}}(z_{\text{ts}} = z_{\text{c}},\ \dot{z}_{\text{ts}} = 0) = kq_{\text{s}}$. Since the velocity of the tip is zero, nothing can be learned about F_{odd} with static AFM.

In dynamic AFM the tip oscillates. In this case, the static deflection allows to asses the time-average of the even part of the tip-sample force according to equation 2.8. Moreover, dynamic AFM provides two more pieces of information about F_{ts}, namely the distance dependence of F_{even} and the velocity dependence of F_{odd}. To see that, we rearrange equations 2.11 and 2.14 in two steps. In the first step, the derivative of F_{even} is introduced as the tip-sample force gradient

$$k_{\text{ts}}(z_{\text{ts}}, \dot{z}_{\text{ts}}) = \frac{\partial F_{\text{even}}(z_{\text{ts}}, \dot{z}_{\text{ts}})}{\partial z_{\text{ts}}} \tag{2.15}$$

and F_{odd} is rewritten as the product of an even and an odd function[27,36]

$$F_{\text{odd}}(z_{\text{ts}}, \dot{z}_{\text{ts}}) = -\gamma_{\text{ts}}(z_{\text{ts}}, \dot{z}_{\text{ts}}) \cdot \dot{z}_{\text{ts}} . \tag{2.16}$$

The obvious choice for the odd function is the tip velocity, the even function $\gamma_{\text{ts}}(z_{\text{ts}}, \dot{z}_{\text{ts}})$ is introduced as the tip-sample damping constant.[34,38] In the second step, the time-averages in equation 2.8, 2.11 and 2.14 are expressed as weighted averages over the tip-sample distance (see section 2.1.8 for details):

$$\langle F_{\text{even}}(z_{\text{ts}}, \dot{z}_{\text{ts}}) \rangle_t = \langle F_{\text{even}}(z_{\text{ts}}, \dot{z}_{\text{ts}}) \rangle_{\cup} \tag{2.17}$$

$$\frac{2}{A^2} \langle F_{\text{even}}(z_{\text{ts}}, \dot{z}_{\text{ts}}) \cdot (z_{\text{ts}} - z_{\text{c}}) \rangle_t = \langle k_{\text{ts}}(z_{\text{ts}}, \dot{z}_{\text{ts}}) \rangle_{\cap} \tag{2.18}$$

$$-\frac{2}{(2\pi\nu_{\text{exc}})^2 A^2} \langle F_{\text{odd}}(z_{\text{ts}}, \dot{z}_{\text{ts}}) \cdot \dot{z}_{\text{ts}} \rangle_t = \langle \gamma_{\text{ts}}(z_{\text{ts}}, \dot{z}_{\text{ts}}) \rangle_{\cap} \tag{2.19}$$

Here, we use the weighted averages “cup” (∪) and “cap” (∩) according to

$$\langle f\rangle_\cup = \int_{-A}^{A} \mathrm{d}z f(z_\mathrm{c}+z)\, w_\cup(z), \quad w_\cup(z) = \frac{1}{\pi\sqrt{A^2-z^2}} \tag{2.20}$$

$$\langle f\rangle_\cap = \int_{-A}^{A} \mathrm{d}z f(z_\mathrm{c}+z)\, w_\cap(z), \qquad w_\cap(z) = \frac{2}{\pi A^2}\sqrt{A^2-z^2} \tag{2.21}$$

with the positive and normalized weight functions $w_\cup$ and $w_\cap$ which average in the tip-sample distance interval $[z_\mathrm{c} - A, z_\mathrm{c} + A]$ around the center position of the tip z_c (see figure 2.6 in section 2.1.8).

Finally, the three AFM equations are obtained from combining equations 2.8, 2.11 and 2.14 with equations 2.17, 2.18 and 2.19

$$\langle F_\mathrm{even}(z_\mathrm{ts}, \dot{z}_\mathrm{ts})\rangle_\cup = kq_\mathrm{s} \tag{2.22}$$

$$\langle k_\mathrm{ts}(z_\mathrm{ts}, \dot{z}_\mathrm{ts})\rangle_\cap = k\left(1-\left(\frac{\nu_\mathrm{exc}}{\nu_\mathrm{e}}\right)^2\right) - \frac{F_0}{A}\cos\varphi \tag{2.23}$$

$$\langle \gamma_\mathrm{ts}(z_\mathrm{ts}, \dot{z}_\mathrm{ts})\rangle_\cap = -\frac{k}{2\pi\nu_\mathrm{e}Q} - \frac{F_0}{2\pi\nu_\mathrm{exc}A}\sin\varphi \tag{2.24}$$

using the eigenfrequency ν_e and the quality factor Q of the resonator. These are the three AFM equations, which allow to obtain the three pieces of information about the tip-sample force that are available within the harmonic approximation. The right-hand sides of the three AFM equations 2.22–2.24 are fully determined by the resonator properties k, ν_e and Q, the excitation parameters F_0 and ν_exc, and the observables q_s, A and φ. The three obtained quantities on the left-hand side are the average even part of the tip-sample force $\langle F_\mathrm{even}\rangle_\cup$, the average tip-sample force gradient $\langle k_\mathrm{ts}\rangle_\cap$ and the average tip-sample damping constant $\langle \gamma_\mathrm{ts}\rangle_\cap$. Thus, in contrast to static AFM, where only the even tip-sample force contribution F_even can be obtained, dynamic AFM allows to additionally probe the distance dependence of F_even using $\langle k_\mathrm{ts}\rangle_\cap$ as well as the velocity dependence of F_odd using $\langle \gamma_\mathrm{ts}\rangle_\cap$. The three averages $\langle F_\mathrm{even}\rangle_\cup$, $\langle k_\mathrm{ts}\rangle_\cap$ and $\langle \gamma_\mathrm{ts}\rangle_\cap$ are discussed in more detail in section 2.1.3.

The major advantage of the three AFM equations is that they hold true without restrictions to the experimental mode, as long as the harmonic approximation is valid. They can be applied, independent on how many feedback loops are used and irrespective of which of the five quantities discussed in figure 2.2 are held constant. Even in the case of poorly adjusted feedback loops, *i.e.*, when all five quantities are varying to some extent, both excitation parameters (F_0 and ν_exc) and all three observables (q_s, A, and φ) are always experimentally accessible. Therefore, in all of these cases, AFM data can be analyzed quantitatively using the AFM equations, if the excitation parameters and all three observables are recorded. In the next section, we will discuss the three pieces of information that can be obtained with the three AFM equations 2.22–2.24.

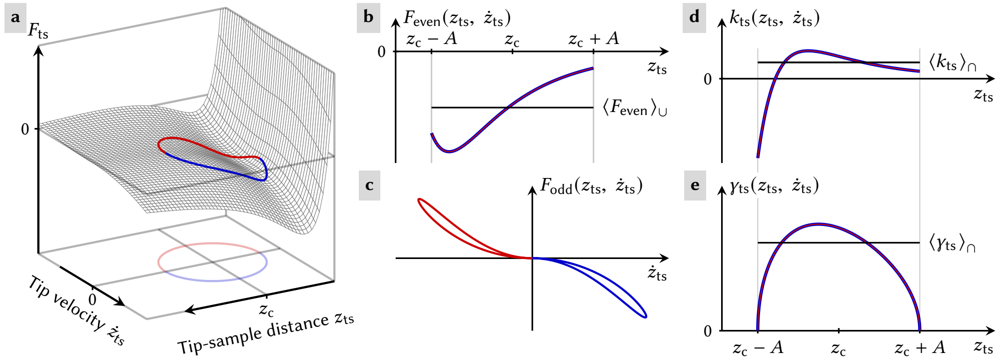

Figure 2.3: Panel a shows the tip-sample force as introduced in figure 2.1. The harmonic approximation (equation 2.4) corresponds to a tip trajectory as indicated by the solid line (red–approach, blue–retract). In dynamic AFM, the tip-sample force is probed by the oscillating tip along this path. In static AFM, the tip-sample force at $z_{ts} = z_c$ and $\dot{z}_{ts} = 0$ is measured. The even and odd contribution to F_{ts} along the path of the tip are shown in panel b and c. In panel d and e, k_{ts} and γ_{ts} along the path of the tip are shown. The black horizontal lines in (b, d and e) indicate the averages that can be obtained with the three AFM equations.

2.1.3 The three pieces of information about the tip sample force

In this section, we discuss the physical meaning of the three quantities that can be obtained using the three AFM equations: The average even contribution of the tip sample force, the average tip-sample force gradient and the average tip-sample damping constant. Within the harmonic approximation, the tip probes the tip-sample force along the path described by equation 2.4 and indicated by the solid line in figure 2.3 a. The red line depicts the path of the approaching tip (negative tip velocity), the blue line the path of the retracting tip (positive tip velocity). Within one oscillation cycle, the tip probes the tip-sample force twice at each tip-sample distance – with a velocity that differs in its sign, but not in its absolute value.

In figure 2.3 b, F_{even} is plotted as a function of z_{ts} for the approaching (red) and retracting (blue) tip. According to equation 2.2, F_{even} is equal for the approaching and retracting tip along this path.[33] Consequently, the blue and red curve overlap. Within the harmonic approximation, F_{even} is a unique function of z_{ts} along a given path.

The other contribution to the tip-sample force is F_{odd}, which has an opposite sign for the approaching and retracting tip. This follows from equation 2.3 and can be recognized in figure 2.3 c, which shows F_{odd} as a function of the tip velocity. Even within the harmonic approximation, F_{odd} is not a unique function of z_{ts}.

The tip-sample force gradient k_{ts} and the tip-sample damping constant γ_{ts} are plotted in figure 2.3 d and e as function of the tip-sample distance. Since both functions are even with respect to the tip velocity, they are unique functions of z_{ts} along a given path within the harmonic approximation.

The three AFM equations allow to obtain the average values for F_{even}, k_{ts} and γ_{ts} from the experimentally obtained observables q_{s}, A and φ and the excitation parameters F_0 and ν_{exc}. The first AFM equation 2.22 allows to determine the cup-average of the even force $\langle F_{\mathrm{even}}\rangle_{\cup}$, which is indicated by the horizontal black line in figure 2.3 b. The time-average of the odd force is always zero as can be seen in figure 2.3 c. The cap-average of the tip-sample force gradient $\langle k_{\mathrm{ts}}\rangle_{\cap}$ is the second piece of information about the tip-sample force that is available in dynamic AFM. It is obtained with the second AFM equation 2.23 and it is indicated by the horizontal black line in figure 2.3 d. The weighted cap-average of the tip-sample damping constant $\langle \gamma_{\mathrm{ts}}\rangle_{\cap}$ is the third piece of information about the tip-sample force that can be obtained from dynamic AFM data. The quantity is obtained with the third AFM equation 2.24 and is shown as a horizontal black line in figure 2.3 e.

It is straightforward to quantify the tip-sample interaction in terms of $\langle F_{\mathrm{even}}\rangle_{\cup}$, $\langle k_{\mathrm{ts}}\rangle_{\cap}$ and $\langle \gamma_{\mathrm{ts}}\rangle_{\cap}$ using the AFM equations. Importantly, these three pieces of information about $F_{\mathrm{ts}}(z_{\mathrm{ts}}, \dot{z}_{\mathrm{ts}})$ represent a complete description of the tip-sample force within the harmonic approximation (see section 2.1.7). However, the average values might be a poor local description of F_{even}, k_{ts} and γ_{ts}, especially when large amplitudes are used in the experiment, *i.e.*, when the average is performed over a large tip-sample distance range. In those cases it might be interesting to deconvolve $\langle F_{\mathrm{even}}\rangle_{\cup}$, $\langle k_{\mathrm{ts}}\rangle_{\cap}$ and $\langle \gamma_{\mathrm{ts}}\rangle_{\cap}$, *e.g.*, as suggested by Dürig,[26] Giessibl[44] as well as Sader et al.[45,46] (see section 2.1.8 for a detailed description).

Obviously, it is possible to distinguish between *even* and *odd* contributions to the tip-sample force. Is it also possible to distinguish between the *conservative* and the *non-conservative* part of the tip-sample force? Any conservative force is necessarily independent of the tip velocity and, therefore, contributes solely to F_{even}. Any odd force has to be velocity-dependent and is, therefore, not conservative. In general, however, the even contribution is not necessarily purely conservative and the odd contribution does not necessarily contain all non-conservative contributions.[38] A simple example is a force contribution that we used in our plots of F_{ts} in figure 2.1 and 2.3: a force contribution that is proportional to $(\dot{z}_{\mathrm{ts}})^2$ is not conservative, yet it contributes only to F_{even} and not to F_{odd}.

How can the experimentalist find out whether F_{even} is purely conservative? To answer this important question, it is certainly not enough to measure only the normal component of the tip-sample force. One feasible strategy might be to first exclude that F_{even} depends on the tip velocity. This can be done, for example, by comparing the even force measured with static and dynamic AFM.[47] If F_{even} is independent of $\dot{z}_{\mathrm{ts}}$ it is *possible* that it is purely conservative. Second, the lateral components of the tip-sample force need to be calculated from analyzing the lateral movement of the tip. Only if the even part of the resulting tip-sample force field $\mathbf{F}_{\mathrm{ts}}(\mathbf{r}_{\mathrm{ts}})$ can be written as the negative gradient of a potential energy, the measured even force is purely conservative. In all other cases, it is dangerous to interpret the *even* part of F_{ts} as purely *conservative*, as pointed out in detail by Sader *et al.*[38]

In the next section, we will demonstrate the applicability of the three AFM equations 2.22–2.24 by quantitatively analyzing AM-AFM and FM-AFM data.

2.1.4 Experimental demonstration

For demonstrating the applicability of the three AFM equations, we performed 3D AFM measurements at the calcite (10.4)–water interface.[48–52] We employed a setup[15,16,53] that allows to switch between the AM and FM mode (see figure 2.2) during the experiment to minimize changes at the tip and the sample. The used setup and all experimental details are described in section 3.2, where we also show the corresponding raw data. In both modes, we simultaneously recorded all five channels of data: the two excitation parameters F_0 and ν_{exc} as well as the three observables q_{s}, A and φ. Using the three AFM equations, we computed the three quantities available from dynamic AFM data: the cup-averaged even contribution to the tip-sample force $\langle F_{\mathrm{even}} \rangle_{\cup}$, the cap-averaged tip-sample force gradient $\langle k_{\mathrm{ts}} \rangle_{\cap}$ and the cap-averaged tip-sample damping constant $\langle \gamma_{\mathrm{ts}} \rangle_{\cap}$.

Figure 2.4 shows these three pieces of information about the tip-sample force in a vertical slice through the 3D volume along the $[48\bar{1}]$ direction. The left and right column of figure 2.4 show the result of the quantitative analysis of AFM data obtained in AM- and FM-AFM measurements, respectively. Both sets of slices show the same features. A detailed interpretation of the data is presented in section 3.3. The measured values for even force, force gradient and damping constant obtained from the AM and FM data sets are very similar. Of course they are not exactly the same, since the paths along which the averaging was done (equation 2.4) were not exactly the same, as discussed in the previous sections. In section 2.1.8 we describe which further assumptions are necessary to deconvolve the averages using the approach by Sader *et al.*[45,46] The description of their deconvolution method as well as the deconvolution of the data shown in figure 2.4 c and d can be found in section 2.1.8 as well.

2.1.5 Tip-sample distance and coordinate system

In this section, we present an overview over the various distances and the coordinate system used in the previous sections. In general, the tip-sample force has a component normal to the surface and components in the lateral directions. As a consequence, the deflection of the resonator is affected in normal and lateral directions by the tip-sample force. We employ a coordinate system where the z-direction is oriented normal to the sample surface, pointing away from the sample. We discuss only the normal component of the force acting on the tip and the resulting normal component of the

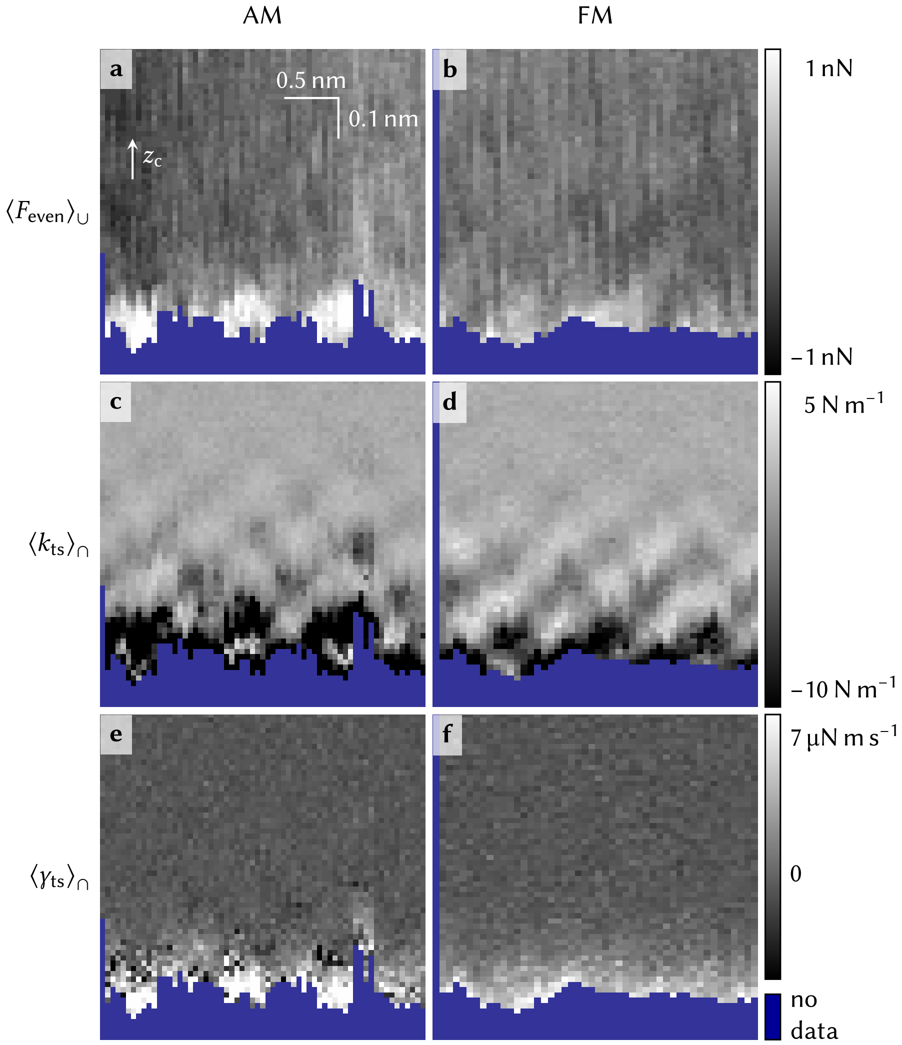

Figure 2.4: The three pieces of information about the tip-sample force, obtained with the three AFM equations 2.22–2.24. The 3D AFM data was obtained using the AM (a, c, e) and the FM (b, d, f) mode, respectively. The first row shows the cup-averaged even force $\langle F_{\mathrm{even}} \rangle_{\cup}$, the second row shows the cap-averaged tip-sample force gradient $\langle k_{\mathrm{ts}} \rangle_{\cap}$ and the third row shows the cap-averaged tip-sample damping constant $\langle \gamma_{\mathrm{ts}} \rangle_{\cap}$. Each frame is plotted in a way that the vertical axis corresponds to the center position of the tip oscillation z_c and the horizontal axis corresponds to a lateral tip-sample displacement along the $[48\bar{1}]$ direction on the calcite (10.4) surface. The color scales apply to both data within a row.

deflection. The three-dimensional case reduces to a one-dimensional case with the normal components of the tip-sample force $F_{\mathrm{ts}} = \mathbf{F}_{\mathrm{ts}} \cdot \mathbf{e}_z$, the deflection $q = \mathbf{q} \cdot \mathbf{e}_z$ and the tip-sample distance $z_{\mathrm{ts}} = \mathbf{r}_{\mathrm{ts}} \cdot \mathbf{e}_z$, where $\mathbf{e}_z$ is the unit vector in z.

It is desirable to obtain F_{ts} as a function of tip-sample distance z_{ts}. However, the tip-sample distance is experimentally not accessible. Instead, the deflection q is detected, and the *relative* displacement of the fixed end of the resonator with respect to the sample $\mathbf{r}_{\mathrm{p}} = \left(x_{\mathrm{p}}, y_{\mathrm{p}}, z_{\mathrm{p}}\right)$ can be adjusted with a positioning system, usually consisting of piezo elements. Obtaining the *absolute* tip-sample distance z_{ts} requires to know the distance z_{o} between tip and sample when resonator and positioning system are in their respective rest positions ($q = 0$ and $z_{\mathrm{p}} = 0$). The tip-sample distance is then given as $z_{\mathrm{ts}} = z_{\mathrm{o}} + z_{\mathrm{p}} + q$ and the center position of the tip is given as $z_{\mathrm{c}} = z_{\mathrm{o}} + z_{\mathrm{p}} + q_{\mathrm{s}}$.

2.1.6 Transfer function of the harmonic oscillator

The aim of this section is to relate the resonator's deflection q to any excitation force. Any external excitation F_{exc} employed to drive the resonator and any tip-sample force $F_{\mathrm{ts}}(z_{\mathrm{ts}}, \dot{z}_{\mathrm{ts}})$ excite the resonator and are, therefore, considered as excitation force. Applying the Fourier transform[1] ($\mathcal{F}$) to equation 2.5 and using

$$\mathcal{F}[\dot{q}] = (2\pi\nu\mathrm{i})\ \mathcal{F}[q] \tag{2.25}$$

$$\mathcal{F}[\ddot{q}] = (2\pi\nu\mathrm{i})^2\ \mathcal{F}[q] \tag{2.26}$$

leads to a linear relationship between the spectrum of the deflection $\mathcal{F}[q]$ and the spectrum of the excitation force

$$\mathcal{F}[q] = G_{\mathrm{ho}}(\nu) \cdot \mathcal{F}[F_{\mathrm{ts}}(z_{\mathrm{ts}}, \dot{z}_{\mathrm{ts}}) + F_{\mathrm{exc}}] \tag{2.27}$$

with the transfer function of the harmonic oscillator

$$G_{\mathrm{ho}}(\nu) = \frac{1}{k - (2\pi\nu)^2\, m + 2\pi\nu\mathrm{i}\,\gamma} \tag{2.28}$$

$$= \frac{1/k}{1 - \left(\frac{\nu}{\nu_{\mathrm{e}}}\right)^2 + \mathrm{i}\frac{\nu}{Q\nu_{\mathrm{e}}}} \tag{2.29}$$

$$= |G_{\mathrm{ho}}(\nu)| \exp\left(\mathrm{i}\,\varphi_{\mathrm{ho}}(\nu)\right)\ . \tag{2.30}$$

The magnitude $|G_{\mathrm{ho}}(\nu)|$ of the transfer function relates the magnitude of a spectral component of the excitation force with the magnitude of a spectral component of the deflection. Therefore, the function

$$|G_{\mathrm{ho}}(\nu)| = \frac{1/k}{\sqrt{\left(1 - \left(\frac{\nu}{\nu_{\mathrm{e}}}\right)^2\right)^2 + \left(\frac{\nu}{Q\nu_{\mathrm{e}}}\right)^2}} \tag{2.31}$$

---

[1] The Fourier transform $\mathcal{F}$ of a function f is defined as $\mathcal{F}[f] = \int_{-\infty}^{\infty} \mathrm{d}t\, f(t) \exp(-2\pi\nu\mathrm{i}t)$, the inverse Fourier transform of a function s as $\mathcal{F}^{-1}[s] = \int_{-\infty}^{\infty} \mathrm{d}\nu\, s(\nu) \exp(+2\pi\nu\mathrm{i}t)$.

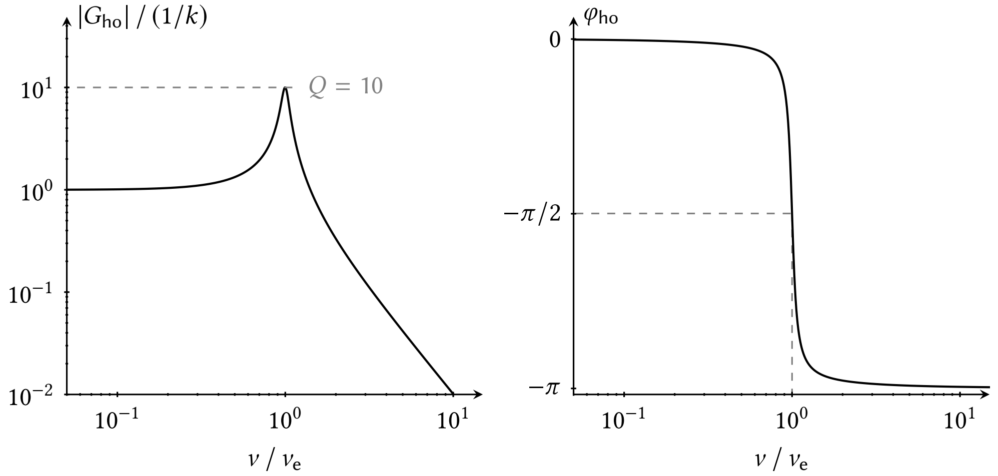

Figure 2.5: Plot of the gain function $|G_{\mathrm{ho}}|$ (left) and the phase shift function φ_{ho} (right) as function of the frequency for a quality factor $Q = 10$.

is called *gain function.* The argument $\varphi_{\mathrm{ho}}(\nu)$ of the transfer function of the harmonic oscillator relates the argument of a spectral component of the excitation force with the argument of a spectral component of the deflection. Therefore, the function $\varphi_{\mathrm{ho}}(\nu)$ is called *phase shift function.*

As the imaginary part of $G_{\mathrm{ho}}(\nu)$ is equal to or less than zero, the phase shift function has values in the range of $-\pi \leq \varphi_{\mathrm{ho}}(\nu) \leq 0$. The inversion of

$$\tan \varphi_{\mathrm{ho}}(\nu) = -\frac{\nu}{Q\nu_\mathrm{e}} \Bigg/ \left(1 - \left(\frac{\nu}{\nu_\mathrm{e}}\right)^2\right) \tag{2.32}$$

is therefore given by

$$\varphi_{\mathrm{ho}}(\nu) = \begin{cases} \arctan\left(-\frac{\nu}{Q\nu_\mathrm{e}} \Big/ \left(1 - \left(\frac{\nu}{\nu_\mathrm{e}}\right)^2\right)\right) & 0 \leq \nu < \nu_\mathrm{e} \\ -\pi/2 & \nu = \nu_\mathrm{e} \\ -\pi + \arctan\left(-\frac{\nu}{Q\nu_\mathrm{e}} \Big/ \left(1 - \left(\frac{\nu}{\nu_\mathrm{e}}\right)^2\right)\right) & \nu > \nu_\mathrm{e} \end{cases} \tag{2.33}$$

or, alternatively, by using the *atan2* function, which takes the imaginary and real part of $G_{\mathrm{ho}}(\nu)$ as two separate arguments:

$$\varphi_{\mathrm{ho}}(\nu) = \operatorname{atan2}\left(-\frac{\nu}{Q\nu_\mathrm{e}},\ 1 - \left(\frac{\nu}{\nu_\mathrm{e}}\right)^2\right) \tag{2.34}$$

Since $G_{\mathrm{ho}}(\nu = 0) = 1/k$, any static excitation force F_{s} leads to a static deflection $q_{\mathrm{s}} = F_{\mathrm{s}}/k$. For $F_{\mathrm{ts}} = 0$ and $F_{\mathrm{exc}} = F_0 \cos(2\pi\nu_{\mathrm{exc}} t)$, the deflection of the resonator is derived using equation 2.27 as

$$
\begin{aligned}
q &= A\cos(2\pi\nu_{\mathrm{exc}} t + \varphi) && (2.35)\\
\text{with} \quad A &= |G_{\mathrm{ho}}(\nu_{\mathrm{exc}})| \cdot F_0 && (2.36)\\
\text{and} \quad \varphi &= \varphi_{\mathrm{ho}}(\nu_{\mathrm{exc}}) && (2.37)
\end{aligned}
$$

Note that $|G_{\mathrm{ho}}(\nu = \nu_{\mathrm{e}})| = Q/k = Q\ |G_{\mathrm{ho}}(\nu = 0)|$. A plot of $|G_{\mathrm{ho}}|$ and φ_{ho} as function of frequency ν is shown in figure 2.5.

2.1.7 Fourier series

We rely on the harmonic approximation to derive the three AFM equations. In this section, we show the connection between the harmonic approximation and the expansion of the tip-sample force and the deflection as a Fourier series. The tip-sample force F_{ts} can be any function of the tip-sample distance z_{ts} and of the tip velocity $\dot{z}_{\mathrm{ts}}$ as illustrated in figure 2.1 a. The tip is moving and, therefore, senses the tip-sample force along a certain path through the tip-sample force landscape. Consequently, F_{ts} becomes a function of time. The tip-sample force which is sensed by the tip changes the way the tip is moving. The path and the force which is sensed along that path are connected according to equation 2.27.

Assuming $F_{\mathrm{ts}}(t)$ and $q(t)$ are periodic functions in time with a period of $1/\nu_{\mathrm{exc}}$, they can be expressed using the following Fourier series:

$$
F_{\mathrm{ts}}(t) = F_{\mathrm{even}}^{(0)} + \sum_{n=1}^{\infty}\left(F_{\mathrm{even}}^{(n)} \cos(2\pi n\nu_{\mathrm{exc}} t + \varphi) + F_{\mathrm{odd}}^{(n)} \sin(2\pi n\nu_{\mathrm{exc}} t + \varphi)\right) \tag{2.38}
$$

$$
q(t) = q_{\mathrm{s}} + A\cos(2\pi\nu_{\mathrm{exc}} t + \varphi) + \sum_{n=2}^{\infty} A^{(n)} \cos\left(2\pi n\nu_{\mathrm{exc}} t + \varphi^{(n)}\right). \tag{2.39}
$$

The Fourier coefficients of F_{ts} are obtained according to

$$
\begin{aligned}
F_{\mathrm{even}}^{(0)} &= \langle F_{\mathrm{ts}}\rangle_t = \langle F_{\mathrm{even}}\rangle_t && (2.40)\\
F_{\mathrm{even}}^{(n)} &= 2\,\langle F_{\mathrm{ts}} \cos(2\pi n\nu_{\mathrm{exc}} t + \varphi)\rangle_t = 2\,\langle F_{\mathrm{even}} \cos(2\pi n\nu_{\mathrm{exc}} t + \varphi)\rangle_t && (2.41)\\
F_{\mathrm{odd}}^{(n)} &= 2\,\langle F_{\mathrm{ts}} \sin(2\pi n\nu_{\mathrm{exc}} t + \varphi)\rangle_t = 2\,\langle F_{\mathrm{odd}} \sin(2\pi n\nu_{\mathrm{exc}} t + \varphi)\rangle_t\ . && (2.42)
\end{aligned}
$$

Employing equation 2.5, the Fourier coefficients describing the constant force and the first harmonic ($n = 1$) are

$$F^{(0)}_{\text{even}} = \langle F_{\text{even}} \rangle_t = kq_{\text{s}} \tag{2.43}$$

$$F^{(1)}_{\text{even}} = \frac{2}{A} \langle F_{\text{even}} \cdot (z_{\text{ts}} - z_{\text{c}}) \rangle_t = kA \left(1 - \left(\frac{\nu_{\text{exc}}}{\nu_{\text{e}}} \right)^2 \right) - F_0 \cos \varphi \tag{2.44}$$

$$F^{(1)}_{\text{odd}} = \frac{2 \langle F_{\text{odd}} \cdot \dot{z}_{\text{ts}} \rangle_t}{-(2\pi \nu_{\text{exc}})A} = -kA \left(\frac{\nu_{\text{exc}}}{Q\nu_{\text{e}}} \right) - F_0 \sin \varphi \, . \tag{2.45}$$

The higher harmonics ($n > 1$) are described by

$$F^{(n)}_{\text{even}} = kA^{(n)} \left(\left(1 - \left(\frac{n\nu_{\text{exc}}}{\nu_{\text{e}}} \right)^2 \right) \cos \left(\varphi - \varphi^{(n)} \right) + \left(\frac{n\nu_{\text{exc}}}{Q\nu_{\text{e}}} \right) \sin \left(\varphi - \varphi^{(n)} \right) \right) \tag{2.46}$$

$$F^{(n)}_{\text{odd}} = kA^{(n)} \left(\left(1 - \left(\frac{n\nu_{\text{exc}}}{\nu_{\text{e}}} \right)^2 \right) \sin \left(\varphi - \varphi^{(n)} \right) - \left(\frac{n\nu_{\text{exc}}}{Q\nu_{\text{e}}} \right) \cos \left(\varphi - \varphi^{(n)} \right) \right) . \tag{2.47}$$

In case the amplitude $A^{(n)}$ and the phase shift $\varphi^{(n)}$ of a harmonic of the deflection are available from the experiment, the corresponding Fourier coefficient of F_{ts} can be obtained using equations 2.43–2.47. However, it is not particularly interesting to calculate these Fourier coefficients, since the most straightforward way to obtain F_{ts} is to measure directly $q(t)$ or its spectrum and employ equation 2.27. No further approximations are necessary in this case and F_{ts} can be fully reconstructed along the sampled path.

In the *harmonic approximation*, the deflection is approximated by equation 2.4 and the tip-sample force is accordingly approximated as

$$F_{\text{ts}}(t) = F^{(0)}_{\text{even}} + F^{(1)}_{\text{even}} \cos(2\pi \nu_{\text{exc}} t + \varphi) + F^{(1)}_{\text{odd}} \sin(2\pi \nu_{\text{exc}} t + \varphi) \tag{2.48}$$

while equations 2.43–2.45 remain valid. In this case, the physical meaning of the Fourier coefficients becomes obvious

$$F^{(0)}_{\text{even}} = \langle F_{\text{even}} \rangle_{\cup} \tag{2.49}$$

$$F^{(1)}_{\text{even}} = A \langle k_{\text{ts}} \rangle_{\cap} \tag{2.50}$$

$$F^{(1)}_{\text{odd}} = (2\pi \nu_{\text{exc}})A \langle \gamma_{\text{ts}} \rangle_{\cap} \, , \tag{2.51}$$

since $\langle k_{\text{ts}} \rangle_{\cap}$ is the cap-averaged tip-sample force gradient and $\langle \gamma_{\text{ts}} \rangle_{\cap}$ is the cap-averaged tip-sample damping constant. Within the harmonic approximation, it is a feasible approach to obtain F_{even} from a deconvolution of $\langle k_{\text{ts}} \rangle_{\cap}$ and F_{odd} from a deconvolution of $\langle \gamma_{\text{ts}} \rangle_{\cap}$ if both quantities are velocity-independent.

2.1.8 Convolution and Deconvolution

In this section, we discuss the convolution of F_{even}, k_{ts} and γ_{ts} into $\langle F_{\text{even}}\rangle_{\cup}$, $\langle k_{ts}\rangle_{\cap}$ and $\langle \gamma_{\text{ts}}\rangle_{\cap}$ as well as the inverse operation, the deconvolution. We employ the harmonic approximation, which means the path of the tip is given by the deflection and velocity as expressed in equation 2.4.

First, we convert each time-average introduced in equations 2.8, 2.11 and 2.14 into a convolution, *i.e.*, a weighted average over the tip-sample distance. Using equation 2.20, the time-average of F_{even} can be written as

$$\begin{aligned}
\langle F_{\text{even}}(z_{\text{ts}}, \dot{z}_{\text{ts}})\rangle_t &= \lim_{T\to\infty} \frac{1}{2T} \int\limits_{-T}^{T} \mathrm{d}t\, F_{\text{even}}(z_{\text{c}} + A\cos\left(2\pi\nu_{\text{exc}}t + \varphi\right),\, \dot{z}_{\text{ts}}) \\
&= \frac{1}{\pi} \int\limits_{0}^{\pi} \mathrm{d}\theta\, F_{\text{even}}(z_{\text{c}} + A\cos\theta,\, \dot{z}_{\text{ts}}) \\
&= \int\limits_{-A}^{A} \mathrm{d}z\, F_{\text{even}}(z_{\text{c}} + z,\, \dot{z}_{\text{ts}})\, \frac{1}{\pi\sqrt{A^2 - z^2}} \\
&= \langle F_{\text{even}}(z_{\text{ts}}, \dot{z}_{\text{ts}})\rangle_{\cup}
\end{aligned} \tag{2.52}$$

From the time-average of $F_{\text{even}} \cdot (z_{\text{ts}} - z_{\text{c}})$ we obtain the following convolution of the tip-sample force gradient k_{ts}:

$$\begin{aligned}
&\langle F_{\text{even}}(z_{\text{ts}}, \dot{z}_{\text{ts}}) \cdot (z_{\text{ts}} - z_{\text{c}})\rangle_t \\
&\quad= A \lim_{T\to\infty} \frac{1}{2T} \int\limits_{-T}^{T} \mathrm{d}t\, F_{\text{even}}(z_{\text{c}} + A\cos(2\pi\nu_{\text{exc}}t + \varphi),\, \dot{z}_{\text{ts}})\, \cos(2\pi\nu_{\text{exc}}t + \varphi) \\
&\quad= \frac{A}{\pi} \int\limits_{0}^{\pi} \mathrm{d}\theta\, F_{\text{even}}(z_{\text{c}} + A\cos\theta,\, \dot{z}_{\text{ts}})\, \cos\theta \\
&\quad= \frac{1}{\pi} \int\limits_{-A}^{A} \mathrm{d}z\, F_{\text{even}}(z_{\text{c}} + z,\, \dot{z}_{\text{ts}})\, \frac{z}{\sqrt{A^2 - z^2}} \\
&\quad= \frac{A^2}{2} \int\limits_{-A}^{A} \mathrm{d}z\, \frac{\partial F_{\text{even}}(z_{\text{c}} + z,\, \dot{z}_{\text{ts}})}{\partial z}\, \frac{2}{\pi A^2}\sqrt{A^2 - z^2} \\
&\quad= \frac{A^2}{2}\, \langle k_{\text{ts}}(z_{\text{ts}}, \dot{z}_{\text{ts}})\rangle_{\cap}
\end{aligned} \tag{2.53}$$

Here, we made use of equation 2.2, the definition of the cap-average in equation 2.21 and the definition of the tip-sample force gradient according to equation 2.15. From

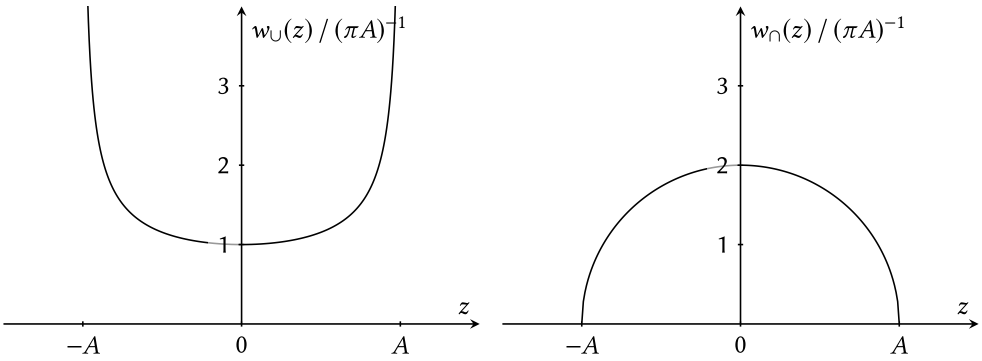

Figure 2.6: Plot of the weight functions *cup* (a) and *cap* (b) that are used to average the quantities F_{even} as well as k_{ts} and γ_{ts}, respectively. Both weight functions are normalized, meaning that an integral of the weight function from $-A$ to A equals 1.

the time-average of $F_{\text{odd}} \cdot \dot{z}_{\text{ts}}$ we obtain the following convolution of the tip-sample damping constant γ_{ts}:

$$\begin{aligned}
\langle F_{\text{odd}}(z_{\text{ts}}, \dot{z}_{\text{ts}}) \cdot \dot{z}_{\text{ts}} \rangle_t &= -\lim_{T\to\infty} \frac{1}{2T} \int\limits_{-T}^{T} \mathrm{d}t\, \gamma_{\text{ts}}(z_{\text{c}} + A\cos(2\pi\nu_{\text{exc}}t + \varphi),\, \dot{z}_{\text{ts}}) \cdot (\dot{z}_{\text{ts}})^2 \\
&= -\frac{(2\pi\nu_{\text{exc}}A)^2}{\pi} \int\limits_{0}^{\pi} \mathrm{d}\theta\, \gamma_{\text{ts}}(z_{\text{c}} + A\cos\theta,\, \dot{z}_{\text{ts}})\, \sin^2\theta \\
&= -\frac{(2\pi\nu_{\text{exc}}A)^2}{2} \int\limits_{-A}^{A} \mathrm{d}z\, \gamma_{\text{ts}}(z_{\text{c}} + z,\, \dot{z}_{\text{ts}})\, \frac{2}{\pi A^2} \sqrt{A^2 - z^2} \\
&= -\frac{(2\pi\nu_{\text{exc}}A)^2}{2} \langle \gamma_{\text{ts}}(z_{\text{ts}}, \dot{z}_{\text{ts}}) \rangle_{\cap} \qquad (2.54)
\end{aligned}$$

In the above equation, we used equations 2.3 and 2.21 as well as the definition of the tip-sample damping constant according to equation 2.16.

The weighted average in equation 2.52 is a convolution of F_{even} with $w_{\cup}$ (equation 2.20, figure 2.6 a). The weighted averages obtained in equations 2.53 and 2.54 are convolutions of k_{ts} and γ_{ts} with $w_{\cap}$ (equation 2.21, figure 2.6 b). The inverse operation needed for extracting k_{ts}, γ_{ts} and F_{even} from the weighted averages is the *deconvolution.* Different numerical recipes have been proposed for the deconvolution of the cup-average and the cap-average.[26,44–46] Here, we have chosen to reproduce the result originally obtained by Sader *et al.*,[45,46] which has been described in numerous works.[36–38,43] The procedure is described in the following. We first start by motivating the general idea: When the tip is not interacting with the sample (at a center position z_{∞}), F_{ts} is zero over the entire path probed by the tip. Consequently, all three averages are zero as well. This is usually the case if the tip is far away from the sample. When the tip is gradually approached to the sample, at some point it will start to probe along a path where the tip-sample force is not always zero. The non-zero F_{ts} gives rise to a change in the three averages that arises from the part of the path that has not been sampled before. Obtaining averages for various, yet partly overlapping paths is the basis for deconvolution. There are several possibilities for finding sufficiently overlapping paths: Typically, the z-piezo displacement z_{p} is varied in the experiment to change the tip-sample distance range. In this approach, the excitation parameters (F_0, ν_{exc}) and the observables (q_{s}, A, φ) are recorded as function of z_{p}. Using the AFM equations 2.22–2.24 allows to extract the average of k_{ts}, γ_{ts} and F_{even} as a function of the center position of the tip $z_{\mathrm{c}} = z_{\mathrm{o}} + z_{\mathrm{p}} + q_{\mathrm{s}}$. The dependence of the average on the center position of the tip is in the following indicated with the notation $\langle f \rangle_{\cup}^{(z_{\mathrm{c}})}$ and $\langle f \rangle_{\cap}^{(z_{\mathrm{c}})}$, respectively.

While convolution is always possible, deconvolution requires to impose further conditions. The convolution equations 2.52–2.54 represent weighted averages along the tip-sample distance interval probed by the tip, although F_{even}, k_{ts} and γ_{ts} are in general velocity-dependent. The convolutions are possible, because all three quantities are even with respect to velocity and, therefore, unique functions of the tip-sample distance as discussed in section 2.1.2. The latter is only true on the specific path described by equation 2.4. For a deconvolution along the tip-sample distance, we additionally require the quantities F_{even}, k_{ts} and γ_{ts} to be *unique* functions of the tip-sample distance *in the entire z_{ts} interval* probed by the tip during the measurement. Otherwise there would be no sufficient overlap of the paths. This criterion is only fulfilled if F_{even}, k_{ts} and γ_{ts} do not depend on the tip velocity.

The following two equations for the deconvolution have been derived:[45,46]

$$f(z_{\mathrm{c}} - A) = \langle f \rangle_{\cup}^{(z_{\mathrm{c}})} - \int_{z_{\mathrm{c}}-A}^{z_\infty} \left[\sqrt{\frac{2A}{z - (z_{\mathrm{c}} - A)}} \left(\frac{d \langle f \rangle_{\cup}^{(z-A)}}{\mathrm{d}z} - \sqrt{\frac{2}{\pi}} \frac{d \langle f \rangle_{\cup}^{(z)}}{\mathrm{d}z} \right) \right] \mathrm{d}z \tag{2.55}$$

$$\begin{aligned} f(z_{\mathrm{c}} - A) = -\frac{\partial}{\partial z_{\mathrm{c}}} \int_{z_{\mathrm{c}}-A}^{z_\infty} \Bigg[& \left(1 + \sqrt{\frac{A}{64\pi (z - (z_{\mathrm{c}} - A))}} \right) \langle f \rangle_{\cap}^{(z-A)} \\ & - \sqrt{\frac{A^3}{2(z - (z_{\mathrm{c}} - A))}} \frac{\partial \langle f \rangle_{\cap}^{(z)}}{\partial z} \Bigg] \mathrm{d}z \end{aligned} \tag{2.56}$$

Note that the even contribution to the tip-sample force F_{even} can either be obtained by deconvolving the cup average $\langle F_{\mathrm{even}} \rangle_{\cup}$ according to equation 2.55 or by deconvolving the cap-averaged tip-sample force gradient $\langle k_{\mathrm{ts}} \rangle_{\cap}$ according to equation 2.56 and subsequent integration along z_{c}.

As demonstration, we obtained the even contribution F_{even} by deconvolution and subsequent integration of the averaged tip-sample force gradient shown in figure 2.4 c and d with the following equation[54] that can be used for N discrete data points with spacing Δz.

$$\begin{aligned} F_{\mathrm{even}}(z_{\mathrm{k}}) = &+ \langle k_{\mathrm{ts}} \rangle_{\cap}^{(z_k)} \Delta z + \sqrt{\frac{A}{16\pi}} \langle k_{\mathrm{ts}} \rangle_{\cap}^{(z_k)} \sqrt{\Delta z} \\ &+ \sqrt{\frac{4A^3}{2}} \frac{\langle k_{\mathrm{ts}} \rangle_{\cap}^{(z_{k+1})} - \langle k_{\mathrm{ts}} \rangle_{\cap}^{(z_k)}}{\sqrt{\Delta z}} \\ &\sum_{i=k+1}^{N-1} \left[1 + \sqrt{\frac{A}{64\pi(z_i - z_k)}} \langle k_{\mathrm{ts}} \rangle_{\cap}^{(z_i)} - \right. \\ &\left. \sqrt{\frac{A^3}{2(z_i - z_k)}} \frac{\langle k_{\mathrm{ts}} \rangle_{\cap}^{(z_{i+1})} - \langle k_{\mathrm{ts}} \rangle_{\cap}^{(z_i)}}{\Delta z} \right] \Delta z \end{aligned} \tag{2.57}$$

The first three terms in the above equation (without the summation bracket) are correction terms first introduced in the by now unavailable Mathematica notebook by Sader and Jarvis[45] and reproduced in reference 54. The resulting even contribution to the tip-sample force F_{even} is shown in figure 2.7. Both datasets show similar features, however, F_{even} is not quantitatively equal. A possible explanation for the discrepancy could be that F_{even} depends on the tip-velocity. Accordingly, the requirement for the deconvolution of F_{even} being a unique function of z_{ts} along the full tip-sample distance interval probed by the tip would not be fulfilled.

2.1.9 Prevalent, yet restrictive approximations in FM-AFM

In the literature reporting FM-AFM data analysis,[22,23] the following approximations of the AFM equations are often found:

$$\langle F_{\mathrm{even}}(z_{\mathrm{ts}}, \dot{z}_{\mathrm{ts}}) \rangle_t = k q_{\mathrm{s}} \approx 0 \tag{2.58}$$

$$\langle k_{\mathrm{ts}}(z_{\mathrm{ts}}, \dot{z}_{\mathrm{ts}}) \rangle_{\cap} = k \left(1 - \left(\frac{\nu_{\mathrm{exc}}}{\nu_{\mathrm{e}}} \right)^2 \right) - \frac{F_0}{A} \cos\varphi \approx -2k \, \frac{\nu_{\mathrm{exc}} - \nu_{\mathrm{e}}}{\nu_{\mathrm{e}}} \tag{2.59}$$

$$\langle \gamma_{\mathrm{ts}}(z_{\mathrm{ts}}, \dot{z}_{\mathrm{ts}}) \rangle_{\cap} = -\frac{k}{2\pi \nu_{\mathrm{e}} Q} - \frac{F_0}{2\pi \nu_{\mathrm{exc}} A} \sin\varphi \approx \frac{k}{2\pi \nu_{\mathrm{e}} Q} \left(\frac{F_0}{F_0\,(F_{\mathrm{ts}} = 0)} - 1 \right) . \tag{2.60}$$

Here, several restrictions and approximations have been employed:

- The static deflection q_{s} is negligible.
- Both FM-AFM feedback loops are working ideally and, thus, the amplitude is assumed to be exactly the amplitude setpoint and the phase shift is assumed to be exactly $-\pi/2$.

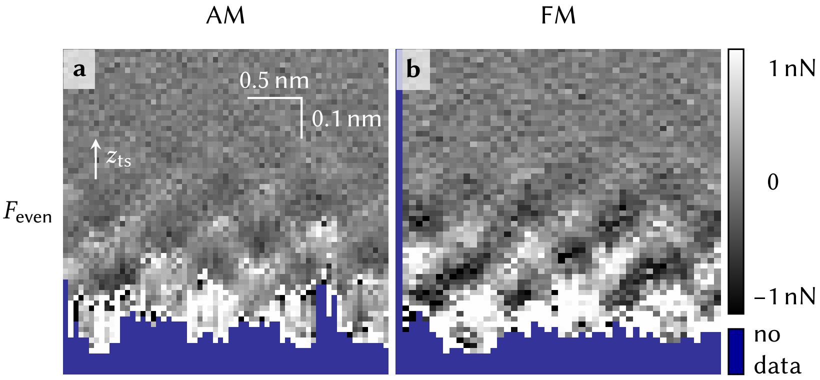

Figure 2.7: The even contribution of the tip-sample force obtained by deconvolution of the averaged tip-sample force gradient and subsequent integration. Data in panel a results from AM-AFM data (figure 2.4 c), data in b from FM-AFM data (figure 2.4 d). The vertical axis corresponds to the tip-sample distance z_{ts}. As in figure 2.4, the horizontal axis corresponds to the lateral $[48\bar{1}]$ direction of the calcite(10.4) surface. The color bar applies to both data sets.

- The difference between excitation frequency and eigenfrequency $\nu_{exc} - \nu_e$ (referred to as "frequency shift" or "detuning") is small compared to ν_e (for equation 2.59) or negligible (for equation 2.60).

These approximations are not always justified. The magnitude of the static deflection q_s can be significant in both ultra-high vacuum[40] as well as in liquid environment.[49] Relying on ideally working feedback loops is an unnecessary limitation since the AFM equations can handle any AFM data irrespective of how well the employed feedback loops (if any) work. The excitation frequency can differ significantly from the eigenfrequency. In the data presented in figure 2.4 a for example, the excitation frequency reaches values of up to 1.2 ν_e. Therefore, we recommend using the three AFM equations 2.22–2.24 instead of the approximated equations 2.58–2.60, even when using FM-AFM.

2.1.10 Conclusion

In this section, we derived three AFM equations that can be universally applied to analyze AFM data. These three equations fully describe the tip-sample force regardless of the specific measurement mode (*e.g.* AM or FM-AFM) and even at poor feedback-loop performance – as long as the harmonic approximation is valid. As a result, raw data from any dynamic AFM experiment can always be related to three pieces of information about the tip-sample force: the average even force, the average tip-sample force gradient and the average tip-sample damping constant. We demonstrate the generality of the three AFM equations by analyzing 3D AFM data measured at the calcite(10.4)-water interface with AM- and FM-AFM.

2.2 The interactive virtual AFM

2.2.1 Introduction

A virtual AFM (VAFM) determines the motion of the tip and emulates the function of all electronic components necessary to perform AFM experiments numerically. There are a number of use cases for a VAFM:

- A VAFM can be used to simulate AFM data resulting from a specific model for the tip-sample force which has been obtained from, *e.g.*, theoretical simulations. Thereby, simulation data can be directly compared with experimental data.
- A real atomic force microscope can be a delicate device—Even if all electronic components are working correctly and tip and sample have been properly prepared, the experimentalist still has to decide on imaging parameters, feedback loop gains, scan speeds and detection bandwidths. Optimizing these parameters to achieve the desired signal-to-noise ratio within a given measurement time is a crucial task. A VAFM can provide a safe and reliable way for experimentalists to optimize and explore these parameters without risking to crash the tip or to damage the sample.
- A VAFM can be used to check the validity of the AFM equations, which have been derived using the harmonic approximation (which also implied that the resonator is in steady state). In contrast, a VAFM does not rely on the harmonic approximation. Comparing data generated by a VAFM with data calculated using the AFM equations provides means to assess the validity of the harmonic approximation. Moreover, the VAFM is not limited to investigating the steady-state resonator oscillation, but allows to also study the transient oscillation of the resonator.

VAFMs have been developed[55–57] and used previously, *e.g.*, for investigating dissipation at the nanoscale[58,59] or for identifying contrast patterns obtained when imaging the (10.4) surface of calcite in water.[60] The usual procedure of running these VAFMs consists of three steps: First, the user defines the settings of the VAFM beforehand in an input script. Secondly, the VAFM is run. In a third and final step, the resulting raw data is analyzed. This means that the user cannot straightforwardly monitor and change quantities of the VAFM during the run. An interactive VAFM eliminates this problem by providing a convenient and intuitive way to monitor and change parameters on the fly, just like in a real experiment.

In this section, I describe the implementation of an interactive VAFM. This interactive VAFM allows to monitor the excitation parameters (F_0, ν_{exc}) and the observables (q_{s}, A, φ) as function of time and tip-sample position. During the run, quantities such as the distance between tip and sample or feedback-loop gains can be changed interactively.

The implementation I describe here is based on modeling all components of the VAFM (resonator, low-pass filters, lock-in amplifier and feedback loops) using first-order

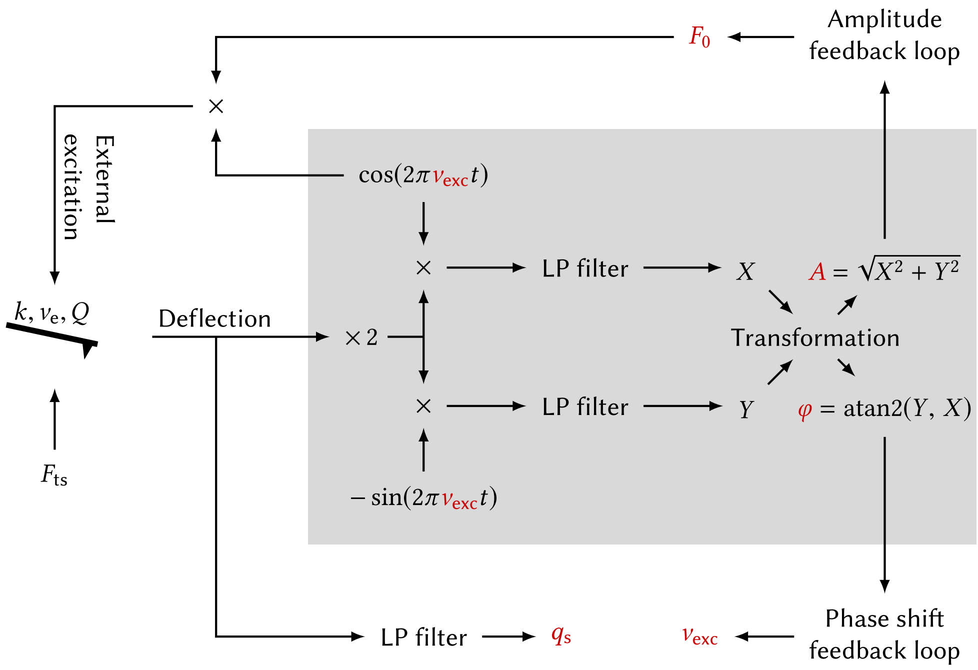

Figure 2.8: The setup simulated in the interactive VAFM. The gray box indicates the lock-in amplifier.

differential equations. Thereby, the interactive VAFM can easily be implemented, since solvers for first-order differential equations are readily available in most scientific computation packages (such as MATLAB, scipy[2] for use with Python or Igor Pro by Wavemetrics[3]).

2.2.2 The system of equations

A schematic overview of the setup that is simulated in the interactive VAFM is depicted in figure 2.8. The system includes a tip mounted on a mechanical resonator. The resonator is modeled as a harmonic oscillator described by its spring constant k, its eigen frequency ν_e and its quality factor Q. The sample beneath the tip gives rise to the normal component of the tip-sample force F_{ts} as function of the tip displacement $\mathbf{r}_{\mathrm{ts}}$.

The deflection of the tip q is fed into two devices: A low-pass (LP) filter (at the bottom of figure 2.8) and a lock-in amplifier (gray box in figure 2.8). The low-pass filter extracts the static deflection q_s and the lock-in amplifier determines amplitude A and phase shift φ of the deflection. Both amplitude and phase shift are fed into feedback loops.

---

[2] In scipy (www.scipy.org), the function `scipy.integrate.odeint` can be used.

[3] In Igor Pro (www.igorpro.net), the function `IntegrateODE` can be used.

If desired by the user, the amplitude feedback loop attempts to fix the amplitude at a setpoint A^{sp} by adjusting the excitation force amplitude F_0. Similarly, a phase shift feedback loop can optionally be used to fix the phase shift at a phase shift setpoint φ^{sp} by adjusting the excitation frequency ν_{exc}. The two excitation parameters F_0 and ν_{exc} fully describe the external excitation force acting on the tip, which is $F_0 \cos(2\pi\nu_{\mathrm{exc}} t)$.

The complete set of equations describing the interactive VAFM is shown below (equations 2.61a–2.61p). In the following, I will discuss the individual components separately.

$$
\begin{aligned}
&\text{Resonator} && \dot{q} = v \tag{2.61a}\\
& && \dot{v} = \left(-kq - \gamma\dot{q} + F_0\cos\phi + F_{\mathrm{ts}}\left(z_{\mathrm{p}} + q,\, v\right)\right)/m \tag{2.61b}\\
&\text{Excitation phase } \phi && \dot{\phi} = 2\pi\nu_{\mathrm{exc}} \tag{2.61c}\\
&\text{Static deflection } q_{\mathrm{s}} && \dot{q}_{\mathrm{s}}^{(1)} = (2\pi\tau_{\mathrm{s}})^{-1}\left(q_{\mathrm{s}} - q_{\mathrm{s}}^{(1)}\right) \tag{2.61d}\\
&\text{(low-pass filter} && \dot{q}_{\mathrm{s}}^{(i)} = (2\pi\tau_{\mathrm{s}})^{-1}\left(q_{\mathrm{s}}^{(i-1)} - q_{\mathrm{s}}^{(i)}\right) \tag{2.61e}\\
&\text{of order } n\text{)} && \dot{q}_{\mathrm{s}} = (2\pi\tau_{\mathrm{s}})^{-1}\left(q^{(n-1)} - q^{(n)}\right) \tag{2.61f}\\
&\text{Lock-in } X && \dot{X}^{(1)} = (2\pi\tau_{\mathrm{LIA}})^{-1}\left(2q\cos\phi - X^{(1)}\right) \tag{2.61g}\\
&\text{(low-pass filter} && \dot{X}^{(j)} = (2\pi\tau_{\mathrm{LIA}})^{-1}\left(X^{(j-1)} - X^{(j)}\right) \tag{2.61h}\\
&\text{of order } m\text{)} && \dot{X} = (2\pi\tau_{\mathrm{LIA}})^{-1}\left(X^{(m-1)} - X^{(m)}\right) \tag{2.61i}\\
&\text{Lock-in } Y && \dot{Y}^{(1)} = (2\pi\tau_{\mathrm{LIA}})^{-1}\left(-2q\sin\phi - Y^{(1)}\right) \tag{2.61j}\\
&\text{(low-pass filter} && \dot{Y}^{(i)} = (2\pi\tau_{\mathrm{LIA}})^{-1}\left(Y^{(j-1)} - Y^{(j)}\right) \tag{2.61k}\\
&\text{of order } m\text{)} && \dot{Y} = (2\pi\tau_{\mathrm{LIA}})^{-1}\left(Y^{(m-1)} - Y^{(m)}\right) \tag{2.61l}\\
&\text{Amplitude } A && \dot{A} = \left(\dot{X}X + \dot{Y}Y\right)/\sqrt{X^2 + Y^2} \tag{2.61m}\\
&\text{Phase shift } \varphi && \dot{\varphi} = \left(X\dot{Y} - \dot{X}Y\right)/\left(X^2 + Y^2\right) \tag{2.61n}\\
&A\text{-feedback adjusts } F_0 && \dot{F}_0 = K_{\mathrm{I}}^{(A)}\left(A^{\mathrm{sp}} - A\right) - K_{\mathrm{P}}^{(A)}\dot{A} \tag{2.61o}\\
&\varphi\text{-feedback adjusts } \nu_{\mathrm{exc}} && \dot{\nu}_{\mathrm{exc}} = K_{\mathrm{I}}^{(\varphi)}\left(\varphi^{\mathrm{sp}} - \varphi\right) - K_{\mathrm{P}}^{(\varphi)}\dot{\varphi} \tag{2.61p}
\end{aligned}
$$

Resonator deflection and velocity

Equation 2.5 (on page 13) describes the deflection q of the resonator as a second-order differential equation. Introducing the tip velocity as $v = \dot{z}_{\mathrm{ts}} = \dot{q}$ (for a fixed z-piezo displacement) and the acceleration as $\ddot{q} = \dot{v}$ allows to rewrite this *second-order* differential equation as the two *first-order* differential equations 2.61a and 2.61b. In these two equations, the eigen frequency $\nu_{\mathrm{e}} = (2\pi)^{-1}\sqrt{k/m}$ and the quality factor $Q = \sqrt{km}/\gamma$ have been expressed using the effective mass m of the resonator and its damping constant γ. In equation 2.61a, the argument in the cosine term is the excitation phase $\phi = 2\pi\nu_{\mathrm{exc}}t$. The time-derivative of the excitation phase is proportional to the excitation frequency (equation 2.61c).

When initializing the interactive VAFM (at $t = 0$), the tip is assumed to oscillate with amplitude A, phase shift $\varphi = -\pi/2$ and frequency ν_{e}. This is expressed in the initial values of $q(t = 0) = 0$, $v(t = 0) = 2\pi\nu_{\mathrm{e}}A$ and $\phi(t = 0) = 0$.

Static deflection: The low-pass filter

The static deflection q_{s} of the tip is the spectral component of the deflection at zero frequency. Therefore, q_{s} can be obtained by low-pass filtering the deflection signal. Here, I model a cascaded resistor-capacitor (RC) low-pass filter.

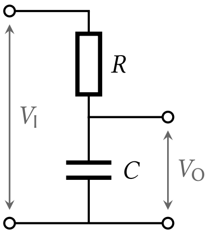

A single RC low-pass filter stage with input voltage V_{I} and output voltage V_{O} is depicted on the right. The voltage $V_{\mathrm{I}} - V_{\mathrm{O}}$ across the resistor with resistance R is given according to Ohms law

$$V_{\mathrm{I}} - V_{\mathrm{O}} = RI = R\dot{Q} = RC\dot{V}_{\mathrm{O}}, \tag{2.62}$$

where the current I was expressed as the time-derivative of the charge Q stored in the capacitor, which is given as the product of capacitance C and V_{O}. Therefore, the time-propagation of a single RC low-pass filter stage is given by the first-order differential equation

$$\dot{V}_{\mathrm{O}} = (2\pi\tau)^{-1}(V_{\mathrm{I}} - V_{\mathrm{O}}), \tag{2.63}$$

where $\tau = RC/(2\pi)$ is the *time constant* of the filter stage.[4] In the interactive VAFM, the time constant is the parameter of the low-pass filter that can be adjusted by the user.

Multiple low-pass filter stages can be cascaded, *i.e.*, the output of the first filter stage is the input to the second filter stage, and so forth. The number of stages is called the *order* of the low-pass filter. For determining the static deflection q_{s} in the interactive VAFM, the deflection q is used as the input signal for the first filter stage. The static deflection low-pass filter of order n is therefore described by equations 2.61d to 2.61f, with $i = 2 \ldots n - 1$ in equation 2.61e. The time constant for the static deflection low-pass filter is denoted as τ_{s}. The initial value (at $t = 0$) of all filter stages of the static deflection low-pass filter are set to zero.

---

[4] Practical considerations for choosing the time constant and an elaborate description of its relation to the bandwidth are given in the white paper *Principles of lock-in detection and the state of the art* by Zurich Instruments (https://www.zhinst.com/sites/default/files/li_primer/zi_whitepaper_principles_of_lock-in_detection.pdf)

Amplitude and phase shift: The lock-in amplifier

In the interactive VAFM, I model a lock-in amplifier that detects the spectral component (*i.e.*, the Fourier transform) of the deflection (multiplied by a factor of two[5]) at the frequency ν_exc. The Fourier transform of $2q$ at frequency ν_exc is given as

$$\begin{aligned}\mathcal{F}[2q](\nu_\mathrm{exc}) &= \int_{-\infty}^{\infty} \mathrm{d}t\, 2q(t) \exp(-2\pi \mathrm{i} \nu_\mathrm{exc} t) \\ &= + \int_{-\infty}^{\infty} \mathrm{d}t\, 2q(t) \cos(2\pi \nu_\mathrm{exc} t) \\ &\quad - \mathrm{i} \int_{-\infty}^{\infty} \mathrm{d}t\, 2q(t) \sin(2\pi \nu_\mathrm{exc} t) = X + \mathrm{i}Y.\end{aligned} \tag{2.64}$$

The workings of a lock-in amplifier can be readily deduced from the above equation (and are also shown schematically in the gray box in figure 2.8). First, the input signal $2q$ is multiplied with $\cos\phi$. Next, according to equation 2.64, this product needs to be integrated. Obviously, choosing a time interval ranging from $-\infty$ to ∞ is impractical. Instead, a shorter time-interval is considered by filtering the product $2q\cos\phi$ with a low-pass of order m and time constant τ_LIA. By doing so, the Fourier transform of $2q$ is obtained within a spectral range centered around ν_exc.[6] The quantity resulting from the low-pass filter is the real part $X = \Re\{\mathcal{F}[2q]\}$ of the spectral component around ν_exc (equations 2.61g to 2.61i, with $j = 2 \ldots m-1$ in equation 2.61h).

For determining the imaginary part $Y = \Im\{\mathcal{F}[2q]\}$ of the spectral component around ν_exc, the deflection is multiplied with $(-\sin\phi)$. Again, the product is further low-pass filtered to obtain Y (equations 2.61j to 2.61l, with $k = 2 \ldots m-1$ in equation 2.61k). The low-pass filter used for detecting Y is described by the same order m and the same integration time τ_LIA as for the low-pass filter that was used for detecting X.

Amplitude A and phase-shift φ of the tip oscillation are readily obtained by the relations

$$A = \sqrt{X^2 + Y^2}, \tag{2.65}$$

$$\varphi = \mathrm{atan2}(Y, X). \tag{2.66}$$

---

[5] The factor of two makes it easier to relate the output of the lock-in amplifier to the input signal: The spectrum of an input signal described by $A\cos(2\pi\nu_\mathrm{exc}t)$ is $\mathcal{F}[A\cos(2\pi\nu_\mathrm{exc}t)] = \frac{A}{2}\delta(\nu - \nu_\mathrm{exc}) + \frac{A}{2}\delta(\nu + \nu_\mathrm{exc})$. Therefore, the absolute value of the spectral component integrated within a small frequency range around ν_exc would be $A/2$. For convenience, the lock-in amplifier measures $\mathcal{F}[2q]$, which results in obtaining A directly.

[6] Again I would like to refer the reader to the white paper by Zurich Instruments for a detailed analysis of the spectral range, *i.e.*, the bandwidth of the lock-in amplifier.

The time-derivatives of amplitude and phase shift are needed for the feedback-loops described in the next section. They follow from equations 2.65 and 2.66 and are stated in equations 2.61m and 2.61n.

The initial values at $t = 0$ are zero for all filter stages of the X low-pass filter and $(-A)$ for all filter stages of the Y low-pass filter. For the amplitude and phase shift, the initial values are A and $-\pi/2$, respectively.

Excitation force amplitude and excitation frequency: The feedback loops

A integral-proportional feedback loop calculates the output signal $V_\mathrm{O}(t)$ at time t for an input signal V_I and a setpoint of V^sp according to

$$V_\mathrm{O}(t) = \int_0^t \mathrm{d}t' K_\mathrm{I} V_\mathrm{E}(t') + K_\mathrm{P} V_\mathrm{E}(t) + V_\mathrm{O}(t=0) \qquad \text{with} \quad V_\mathrm{E} = V^\mathrm{sp} - V_\mathrm{I}. \tag{2.67}$$

The parameter K_I is called *integral gain*, K_P is the *proportional gain*, $V_\mathrm{O}(t = 0)$ is the initial output of the feedback loop. Setting both gains to zero effectively disables the feedback loop.

For simulating the interactive VAFM, the above equation needs to be written as a first-order differential equation. This can be achieved by taking the time-derivative of the output signal:

$$\dot{V}_\mathrm{O} = K_\mathrm{I} V_\mathrm{E} + K_\mathrm{P} \dot{V}_\mathrm{E} = K_\mathrm{I} V_\mathrm{E} - K_\mathrm{P} \dot{V}_\mathrm{I}. \tag{2.68}$$

In the interactive VAFM, two feedback loops are used:

- The amplitude feedback loop keeps the amplitude constant, *i.e.*, the amplitude A is the input and the excitation force amplitude F_0 is the output of the feedback loop. This is written in equation 2.61o using $K_\mathrm{I}^{(A)}$ as integral gain and $K_\mathrm{P}^{(A)}$ as proportional gain. The initial value for the output follows from the gain function of the resonator and is $F_0(t = 0) = kA/Q$.
- The phase shift feedback loop keeps the phase shift φ (input) constant by adjusting the excitation frequency ν_exc (output). The feedback loop is described by equation 2.61p using $K_\mathrm{I}^{(\varphi)}$ as integral gain and $K_\mathrm{P}^{(\varphi)}$ as proportional gain. The initial value for the excitation frequency is $\nu_\mathrm{exc}(t = 0) = \nu_\mathrm{e}$.

Positioning system and distance feedback

A real AFM allows to record distance-dependent curves, two-dimensional images, and three-dimensional volumes by controlling the piezo displacement $\mathbf{r}_\mathrm{p}$, *i.e.*, the relative displacement between the sample and the fixed end of the resonator. The resonator of the interactive VAFM can be scanned in a similar fashion. In the most simple case, the changes in the piezo displacement $\dot{\mathbf{r}}_{\mathrm{ts}}$ are approximated to be significantly slower compared to the velocity of the tip v. Scanning is therefore approximated by stepwise changes in $\mathbf{r}_{\mathrm{p}}$. Distance-dependent curves can be obtained by stepwise changes of z_{p}. The z-piezo displacement quantity is listed as an explicit argument of the tip-sample force in equation 2.61a. Similarly, scanning in the lateral positions is simulated by stepwise changes in x_{p} and y_{p}. This requires to consider a tip-sample force that depends also on the lateral tip-sample distance, which is related to the lateral piezo displacement according to $x_{\mathrm{ts}} = x_{\mathrm{p}}$ and $y_{\mathrm{ts}} = y_{\mathrm{p}}$. The scan speed is determined by both the step size and the time between two step-wise changes of $\mathbf{r}_{\mathrm{p}}$.

Moreover, an additional feedback loop can be used to fix one of the the quantities F_0, q_{s}, A, φ and ν_{exc} by adjusting the z-piezo displacement z_{p}. Considering an additional feedback loop requires to add one equation to the system of differential equations. For example, when using FM-AFM, the z-piezo displacement can be adjusted to fix the excitation frequency at a setpoint $\nu_{\mathrm{exc}}^{\mathrm{sp}}$. This is modeled by the equation

$$\dot{z}_{\mathrm{p}} = K_{\mathrm{I}}^{(z_{\mathrm{p}})} \left(\nu_{\mathrm{exc}}^{\mathrm{sp}} - \nu_{\mathrm{exc}}\right) - K_{\mathrm{P}}^{(z_{\mathrm{p}})} \dot{\nu}_{\mathrm{exc}}, \tag{2.69}$$

where $K_{\mathrm{I}}^{(z_{\mathrm{p}})}$ and $K_{\mathrm{P}}^{(z_{\mathrm{p}})}$ are the feedback loop gains.

2.2.3 Implementation

I have implemented the interactive VAFM in Igor Pro using the `IntegrateODE` function to solve the system of differential equations. Less than 200 lines of code are sufficient for the core functionality, which makes the implementation easy to comprehend. This also lowers the barrier for implementing future extensions (such as virtual KPFM). By employing a background task in Igor Pro, the numerical solver can be run in parallel to the user interface, allowing the interactive usage of the VAFM.

A screenshot of the interface is shown in figure 2.9. In this particular example, the user is currently adjusting the feedback loop parameters by comparing data obtained from approaching and retracting the tip. A clear hysteresis can be recognized when comparing approach and retract curves shown in the plot to the right in figure 2.9 – indicating to the user that the feedback loops have not yet been properly adjusted.

2.2.4 Demonstration

In this section, I demonstrate a possible use case of the interactive VAFM: Checking the validity of the harmonic approximation used to derive the three AFM equations (section 2.1). This check can be performed for a specific tip-sample force model and specific resonator properties.

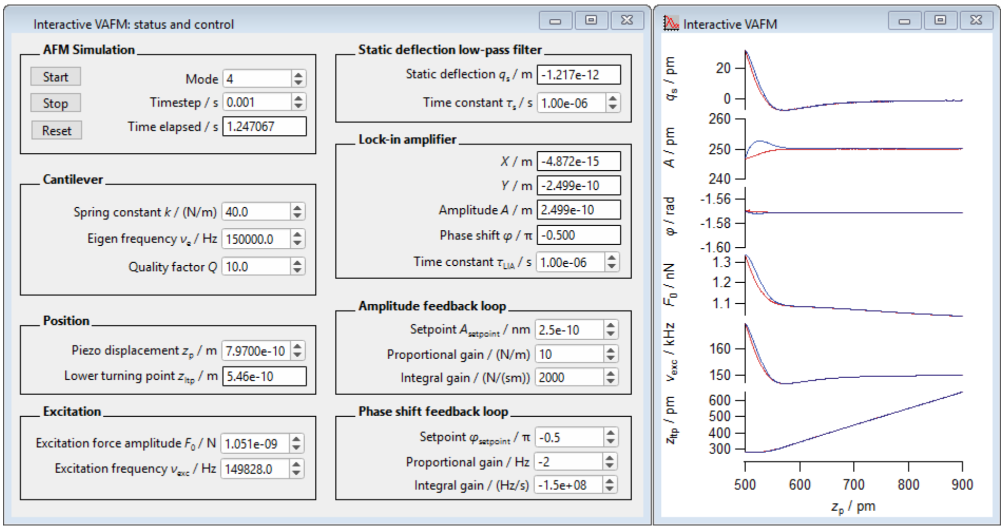

AFM Simulation

Mode 4
Timestep / s 0.001
Time elapsed / s 1.247067

Cantilever

Spring constant k / (N/m) 40.0
Eigen frequency ν_e / Hz 150000.0
Quality factor Q 10.0

Position

Piezo displacement z_p / m 7.9700e-10
Lower turning point z_{ltp} / m 5.46e-10

Excitation

Excitation force amplitude F_0 / N 1.051e-09
Excitation frequency ν_{exc} / Hz 149828.0

Static deflection low-pass filter

Static deflection q_s / m -1.217e-12
Time constant τ_s / s 1.00e-06

Lock-in amplifier

X / m -4.872e-15
Y / m -2.499e-10
Amplitude A / m 2.499e-10
Phase shift φ / π -0.500
Time constant τ_{LIA} / s 1.00e-06

Amplitude feedback loop

Setpoint $A_{setpoint}$ / nm 2.5e-10
Proportional gain / (N/m) 10
Integral gain / (N/(sm)) 2000

Phase shift feedback loop

Setpoint $\varphi_{setpoint}$ / π -0.5
Proportional gain / Hz -2
Integral gain / (Hz/s) -1.5e+08

Figure 2.9: Screenshot of the interactive VAFM implemented in Igor Pro. The panel on the left allows to monitor and change parameters of the interactive VAFM. On the right, the resulting quantities are directly plotted as function of the z-piezo displacement (red–approach, blue–retract). The software is available from `www.self-assembly.uni-mainz.de/software/ivafm`.

Here, I will assume that the tip-sample force is given by

$$F_{ts}(z_{ts}, \dot{z}_{ts}) = \frac{12E_{eq}}{z_{eq}} \left[\left(\frac{z_{eq}}{z_{ts}} \right)^{13} - \left(\frac{z_{eq}}{z_{ts}} \right)^{7} \right] - \alpha \exp\left(-\frac{z_{ts}}{z_{eq}} \right) \dot{z}_{ts} |\dot{z}_{ts}| - \beta \dot{z}_{ts}^2, \tag{2.70}$$

where $E_{eq} = 10^{-19}$ J, $z_{eq} = 0.3$ nm, $\alpha = 0.015\,\mathrm{N\,s^2\,m^{-2}}$, $\beta = 0.001\,\mathrm{N\,s^2\,m^{-2}}$. This model for F_{ts} (which is the same model used for the schematic figures in section 2.1) contains a Lennard-Jones contribution (first term), a non-conservative odd contribution that depends non-linearly on the tip velocity (second term) and a non-conservative even contribution that depends on the tip velocity (third term). For the resonator, I select a spring constant of $k = 40\,\mathrm{N\,m^{-1}}$, an eigen frequency of $\nu_e = 150$ kHz and a quality factor of $Q = 10$. The time constant of the static deflection low-pass filter was set to $\tau_s = 10\,\mu$s, the lock-in amplifier time constant was set to $\tau_{LIA} = 1\,\mu$s. Moreover, feedback loop parameters of $K_I^{(A)} = 200\,\mathrm{kN\,s^{-1}\,m^{-1}}$, $K_P^{(A)} = 10\,\mathrm{N\,m^{-1}}$, $K_I^{(\varphi)} = -150$ MHz and $K_P^{(\varphi)} = -2\,\mathrm{Hz\,s^{-1}}$ were used.

First, I used the interactive VAFM to calculate the three observables q_s, A and φ for fixed excitation parameters of $F_0 = 1$ nN and $\nu_{exc} = \nu_e$. The resulting data is shown as function of the z-piezo displacement z_p in the first column of figure 2.10. Blue curves apply for the left axes and red curves to the right axes. Additionally, I show the lower-turning point $z_{ltp} = z_c + q_s - A$ of the oscillation (third row, right axis).

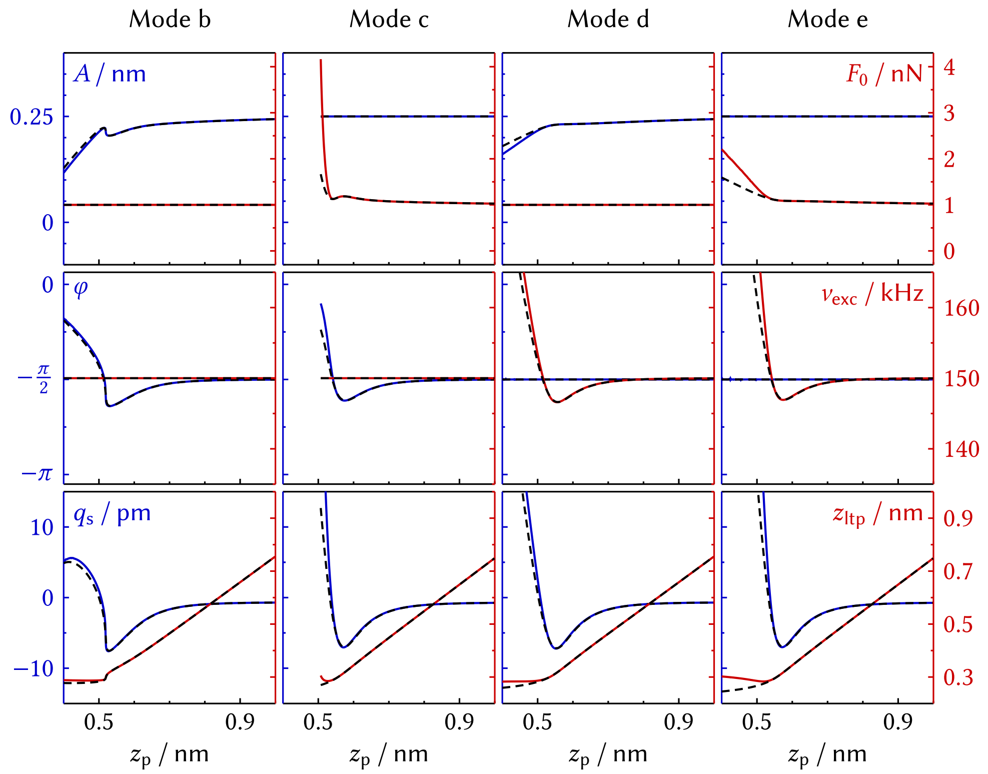

Figure 2.10: Comparison of AFM data that has been obtained with the interactive VAFM (solid lines) and the three AFM equations (dashed black lines). Blue curves apply for the left axes and red curves to the right axes.

The simulation data corresponding to the other AFM modes (where the amplitude or the phase shift or both observables are held constant at $A^{\mathrm{sp}} = 0.25\,\mathrm{nm}$ and $\varphi^{\mathrm{sp}} = -\pi/2$ by their respective feedback loop) are shown in the second, third and forth column. I confirmed for each case that there is no significant hysteresis between the data obtained for the approaching and retracting tip.

Next, I used the three AFM equations 2.22–2.24 to calculate the same quantities that have been obtained with the interactive VAFM, using the same expression for the tip-sample force (equation 2.70) and the same resonator properties. The obtained data is shown as black dashed lines in figure 2.10.

The VAFM data and the data obtained with the three AFM equations agrees well for the specific model of the tip-sample force and the resonator properties considered here. A slight deviation between the curves can be recognized at very small z-piezo displacement z_{p}, where the lower-turning point z_{ltp} of the tip is nearly constant. The constant z_{ltp} indicates that the tip is repelled from the surface and does not, even upon further decrease of z_p, significantly approach the surface further. Therefore, this demonstration shows that (for the specific system considered here) the harmonic approximation is a reasonable approximation in the entire range of z_ts that is accessible by the tip.

2.2.5 Conclusion

In this section, I presented the implementation of an interactive VAFM. The resonator and all electronic components necessary to perform AFM experiments in *any* AFM mode all have been described by a set of first-order differential equations. This system of equations can easily be solved numerically with little effort – an exemplary implementation in Igor Pro was achieved using less than 200 lines of code. A potential use case of the VAFM has been demonstrated by assessing the validity of the harmonic approximation.

3 Three-dimensional AFM at mineral–water interfaces

3.1 Order at the solid–liquid interface

3.1.1 Introduction

At solid–liquid interfaces, the presence of the solid surface influences the structure of the adjacent liquid.[61–63] I refer to *order* at the interface if the density of the interfacial liquid exhibits a regular pattern of local minima and maxima. A most simple example of order at the solid–liquid interface is the formation of layered structures, *i.e.*, vertically alternating layers of increased and decreased liquid density.

Experimentally, order has been observed for a large variety of solid–liquid interfaces, including mineral–water interfaces,[17,52,64] graphite–water and metal–water interfaces,[65–67] the interface of organic crystals and various solvents,[68,69] and even at the interface between solids and liquid metal.[70–72] Moreover, the observation of order at the solid–liquid interface is not limited to specific techniques, since order has been observed using X-ray reflectivity measurements,[73–75] the surface force apparatus[62,76–78] and, as also detailed in the remainder of this thesis, using high-resolution 3D AFM.[17]

A possible origin for the order are attractive interactions between the liquid molecules and the surface – giving rise to preferred positions for the liquid molecules to be located, and, consequently, to local maxima in the liquid density. Another reason for the ordering of the liquid is the confinement due to the surface of the solid: Since the liquid molecules cannot penetrate the solid surface, their positions are confined. A flat surface confines the liquid vertically, a corrugated surface additionally confines the liquid laterally.

It would be desirable to differentiate between order through attraction and order through confinement—While the attraction *specifically* results from the interaction between the liquid molecules and the surface, liquid confinement would be *generally* expected from any solid surface. As a first step, I address two questions:

- Why does confinement induce order?
- Can confinement alone (without any attraction between the liquid molecules and the surface) be responsible for ordering the liquid at the interface?

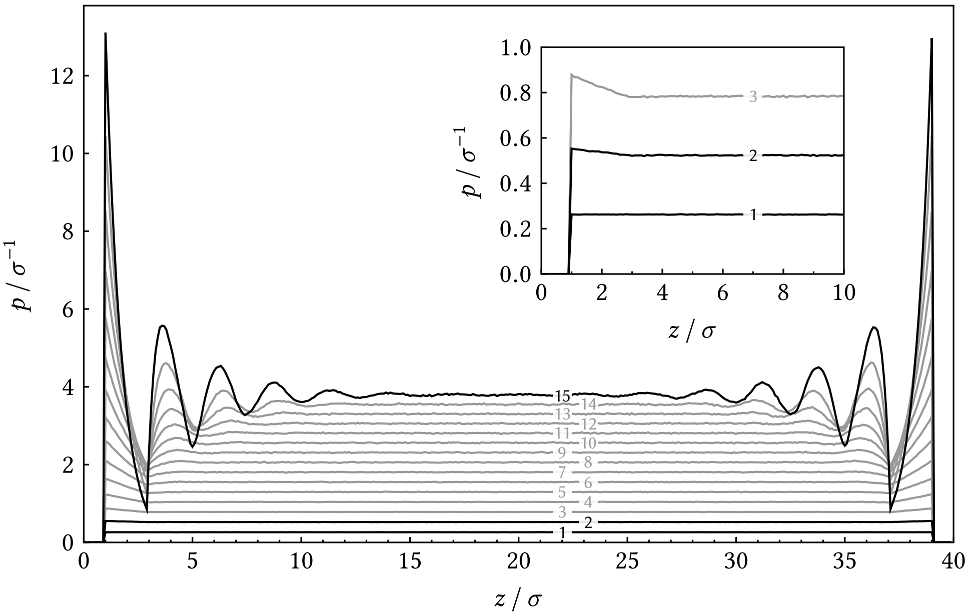

Figure 3.1: MC simulation of a one-dimensional system of hard spheres with radius σ between two hard walls. The probability density p of finding a sphere is plotted as function of the position z between the two walls. Different curves correspond to different numbers of spheres placed between the walls, ranging from one sphere (bottom) to 15 spheres (top). The maximum number of spheres that can be placed between the two walls that are spaced 40σ apart is 20. The inset magnifies the curves corresponding to placing one, two and three spheres.

3.1.2 Monte Carlo simulation

For this, I performed a Monte Carlo (MC) simulation of a most simple solid–liquid interface: A one-dimensional system of hard spheres as liquid molecules, confined between two hard walls representing two solid surfaces. This model assumes zero force between the hard spheres and between the spheres and the walls, *i.e.*, there is no attraction between the liquid molecules and the surface. The only constraint is that the spheres and the walls are rigid, meaning they cannot be penetrated by other spheres.

I denote the sphere radius (*i.e.*, half of the sphere width) as σ and choose a wall-to-wall distance of $L = 40\sigma$. Therefore, a maximum number of 20 spheres can be placed between the two walls. More details on the MC simulation can be found at the end of this section on page 45. In figure 3.1, I plot the simulated probability density p of finding a sphere at a certain position z between the two walls. The different curves show the probability densities corresponding to placing one sphere between the two walls (black bottom curve, magnified in inset) to placing 15 spheres between the two walls (black top curve).

If only one sphere is placed between the two walls, the probability of finding a sphere is constant in the range where the sphere can be placed (bottom curve indicated with "1", also shown in the inset). For $z < \sigma$ and $z > L - \sigma$ the probability is zero, since wall and spheres are impenetrable. This is indicated by the red area in the sketch below, in which the walls are depicted by the two blocks to the left and the right:

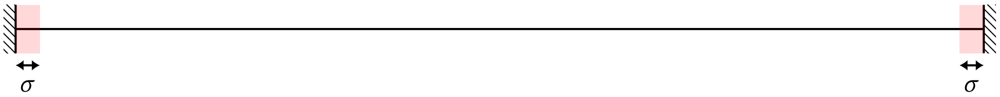

Thus, in this case, no ordering is obtained within the liquid.

However, already when placing *two* spheres between the two walls, a deviation from the uniform distribution can be recognized (curve indicated with "2" in figure 3.1, also shown in the inset). For a two-sphere-system, the probability of placing the second sphere at position z is equal to the probability of the first sphere not blocking position z. Therefore, finding the second sphere at any given position depends on the position of the first sphere. If the first sphere is placed far away from the wall, the sphere blocks a space of 4σ for the position of the second sphere:

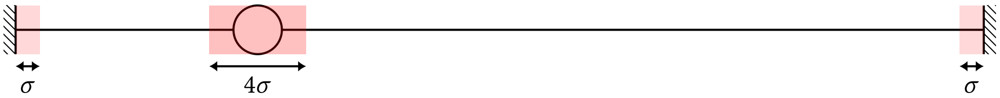

However, if the first sphere is placed directly at the wall, it only blocks an additional space of 2σ for the position of the second sphere:

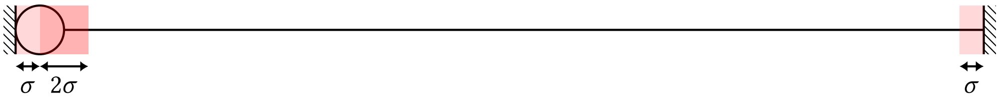

Thus, any sphere placed close to a wall excludes a smaller space compared to placing it away from the wall. Consequently, the space away from the walls is, on average, more often blocked. Therefore, the probability of finding the second sphere close to the wall is increased.

When considering more spheres between the walls, the accumulation of spheres directly at the interface becomes even more pronounced (peaks at $z = \sigma$ and $z = L - \sigma$ in figure 3.1). I will refer to these peaks as the *first layer*. The first layer can be considered as an additional *effective wall*. Therefore, the first layer confines the liquid further away from the wall and causes the formation of a second layer. Consequently, a pronounced layered structure emerges when increasing the number of spheres. In the extreme case of placing the maximum number of spheres between the walls, the liquid is perfectly structured. This discussion concludes that order in the form of layering can be obtained in the simplified case of a one-dimensional hard sphere liquid with hard walls – even without attractive interactions.

This finding is supported by numerous more sophisticated theoretical approaches that consider three-dimensional systems and use different models for the interaction between the liquid molecules and their interaction with the surface:

- Henderson, Abraham and Barker[79] as well as Snook and van Megen[80] have found a vertical ordering for the hard sphere model in three dimensions. They have used approximative analytical calculations and MC simulations.
- MC simulations using different combinations of purely repulsive wall interactions with different liquid-liquid interactions (such as hard spheres and Lennard-Jones interactions) all result in layering.[81]
- Recently, molecular dynamics (MD) simulations by different authors confirm that layering is obtained for water between purely repulsive walls.[82,83]

There are other research papers that argue the opposite: without attraction, there is no ordering, even if the liquid is confined. This is claimed in a later publication by Abraham[84] when using a Lennard-Jones liquid in contact with a hard wall in three dimensions. Only if he additionally considers attractive interactions between the liquid molecules and the wall (again using a Lennard-Jones model), he obtains layering. The author argues that the discrepancy to the publication by Snook,[81] in which layering has been observed for a similar system with a hard wall, emerges from a smaller average bulk density. Moreover, recent MD simulations by Choudhury[85] show that the layering scales with the degree of the attraction, which appears reasonable. However, it is left open whether the layering completely vanishes when considering no attraction. Mozaffari claims that for vanishing attraction, no layering can be observed,[86] although some of the vertical density profiles shown in reference 86 exhibit a slight layering.

A possible explanation for these somewhat contradictory reports could result from considering different "degrees of repulsion": While the hard wall and hard sphere potential is infinitely steep at the boundary, Lennard-Jones models result in more "smooth" interactions–effectively smearing out the wall and therefore the confinement. The liquid–gas interface could be considered as an example of such a smooth repulsive confinement. Indeed, at the liquid–gas interface, no layering is obtained.[62,87–89] Importantly for solid–liquid interfaces, both the overwhelming number of research papers and the most simple one-dimensional hard sphere liquid support the statement: Confinement alone can induce order at solid–liquid interfaces, without attractive interactions between the liquid molecules and the surface.

3.1.3 Conclusion

The purpose of this chapter was to discuss general mechanisms that lead to the formation of ordered structures at solid–liquid interfaces. Attractive interactions between the liquid molecules and the surface straightforwardly explain local deviations in the liquid density in the proximity of the surface. However, a simple MC simulation revealed that even in the absence of any attractive interactions, an ordered structure with pronounced layers can be obtained purely due to confinement. This layering is explained by the smaller volume that is excluded by the liquid molecules that are placed close to a confining wall, compared to liquid molecules placed away from the confining wall. As a consequence, the observation of order at solid–liquid interfaces does not allow to conclude that there are attractive interactions between the liquid molecules and the solid surface. This is a noteworthy thought to keep in mind for the data presented in the following sections.

Details of the MC simulation. In the MC simulation, the positions of the spheres were discretized on a grid with spacing of $\sigma/10$. For the starting configuration I placed all spheres directly adjacent to each other, starting at the left wall. A simulation step is as follows: First, a random sphere is selected. This sphere is then placed at a random position chosen within the accessible range between the neighboring sphere to the left and the neighboring sphere to the right. The first 10^4 steps of the simulation are discarded to eliminate any influence due to the choice of the starting configuration. The next 10^8 steps are used as production run. After each step, a histogram of the sphere positions was recorded. After the simulation, the histograms were averaged to obtain the probability density $p(z)$ of finding a sphere at position z. The integral of the probability density p ranging from $z = 0$ to $z = 40\sigma$ equals the number of spheres between the two walls.

3.2 Implementation of a 3D AFM setup

The following section 3.2 is based on the article "Three-dimensional atomic force microscopy mapping at the solid–liquid interface with fast and flexible data acquisition" by H. Söngen, M. Nalbach, H. Adam and A. Kühnle which has been published in *Review of Scientific Instruments* (reference 53). For this project, I developed and implemented all modifications except for the trigger detection functionality (the counter), which was implemented by H. Adam. I have written the code for both the microcontroller and the data acquisition system. I measured and analyzed the data and prepared the figures and the manuscript with comments from all authors. Parts of the article are reproduced verbatim. Modifications were made to make this section consistent with the other sections in this thesis. As a major modification, I have chosen a different representation of the data, made the description more general to include the AM-AFM mode and present additional data.

We present the implementation of a three-dimensional mapping routine for probing solid–liquid interfaces using dynamic atomic force microscopy. Our implementation enables fast and flexible data acquisition of up to 20 channels simultaneously. The acquired data can be directly synchronized with commercial atomic force microscope controllers, making our routine easily extendable for related techniques that require additional data channels, e.g., Kelvin probe force microscopy. Moreover, the closest approach of the tip to the sample is limited by a user-defined threshold, providing the possibility to prevent potential damage to the tip. The performance of our setup is demonstrated by visualizing the hydration structure above the calcite (10.4) surface in water.

3.2.1 Introduction

Dynamic AFM is a most valuable tool for studying solid–liquid interfaces in real space. Numerous technical improvements have made it possible to resolve mineral surfaces,[13,90,91] molecular crystals[68] and molecular adsorbates[92–95] with atomic-scale resolution. In addition, the introduction of 3D AFM by Fukuma *et al.*[17] has enabled the visualization of the interfacial hydration structure.[48,49,96,97]

In 3D AFM, the volume above the surface is scanned by the tip. This can be performed by acquiring multiple images at different tip-sample distances.[98,99] Since measurements in liquids are often subject to large drift, a more robust method is to approach and retract the tip to and from the sample periodically while laterally scanning across its surface. However, in contrast to conventional imaging, where a feedback loop is used to adjust the distance between tip and sample, a different method for regulating the tip-sample distance needs to be employed in 3D AFM. One possibility is to use the distance feedback loop with low gain to adjust the *average* tip-sample distance.

This concept has been successfully applied in frequency modulation (FM-)AFM,[17] bimodal AFM[100] and amplitude modulation (AM-)AFM.[49] Another option, which is more suited to non-planar samples, is to stop the cantilever approach whenever a used-defined threshold is reached. This opens up the possibility to investigate, *e.g.*, step edges, other non-planar structures[101,102] and, additionally, allows to minimize potential damage to the tip. Kobayashi *et al.*[103] employed a field-programmable gate array in combination with a home-built AFM[104] to perform threshold-based 3D mapping.

Here, similar to the above mentioned approach by Kobayashi *et al.*, we present an easy-to-realize microcontroller-based implementation of 3D mapping at solid–liquid interfaces. While being highly robust due to tip retraction upon reaching a threshold, the main advantage of the present implementation is given by the large number of simultaneously recordable data channels that are directly synchronized with the scan movement. This provides means to employ more elaborate AFM-based measurement modes, *e.g.*, related to the rapidly-growing field of probing voltage-modulated electrostatic effects at solid–liquid interfaces.[105–108]

3.2.2 Technical realization

The setup is based on a commercially-available Multimode AFM with a Nanoscope V controller (Bruker Nano Surfaces Division, USA) optimized for low-noise operation in liquids using the FM operation mode.[15] This instrument has been further extended to perform photothermal cantilever excitation.[16] However, the number of channels that can be recorded with the originally used controller is limited to four (z-piezo displacement and three additional data channels), making the controller insufficient for some applications (*e.g.*, quantitative 3D dynamic AFM with all five data channels described in section 2.1). By combining custom electronics with a HF2LI lock-in amplifier (Zurich Instruments, Switzerland), which also includes a phase-locked loop (PLL) and four feedback controllers, we are able to record an increased number of up to 20 channels. The setup is schematically depicted in figure 3.2 while its individual components are described in the following.

AM-AFM operation

For AM-AFM operation, the tip is excited at a constant excitation force amplitude F_0 and a constant excitation frequency ν_{exc} – both of which can be selected by the user. Both the PLL and the amplitude feedback loop are switched off. The *feedback signal* (figure 3.2) for the z-piezo displacement can be, *e.g.*, the amplitude A subtracted by an amplitude setpoint A^{sp}. This feedback signal is fed into the Nanoscope V controller using its external signal access module (SAM III, Bruker Nano Surfaces Division, USA). The controller nullifies the difference between amplitude and its setpoint by employing a feedback loop that adjusts the z-piezo displacement. While for conventional imaging,

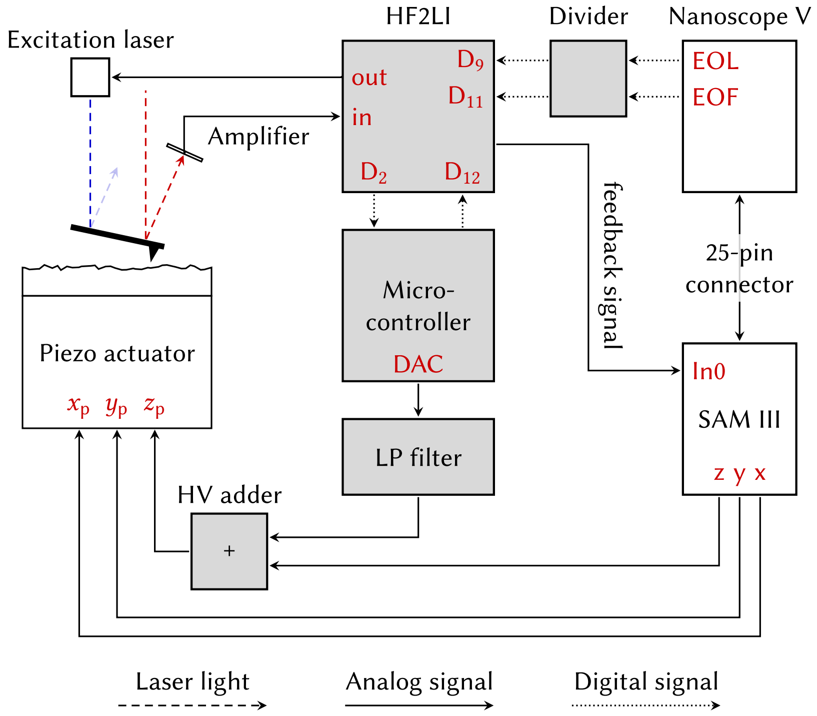

Figure 3.2: Wiring diagram of the setup. The components added for 3D mapping are shaded gray. The laser used for photothermal excitation is described in reference 16, the amplifier of the deflection signal in reference 15. The Nanoscope V controller and the HF2LI are described in section 3.2.2, the signal access module (SAM III) in section 3.2.2, the microcontroller and the low-pass (LP) filter in section 3.2.2 and the divider in section 3.2.2.

the tip is scanned, *e.g.*, at constant amplitude, we decrease the gain of the z-piezo feedback loop when performing 3D mapping. This ensures a compensation for sample tilt and vertical drift, but does not interfere with the mapping routine described below.

FM-AFM operation

For FM-AFM operation, the PLL of the HF2LI is used to excite the cantilever at a fixed phase shift φ of $-\pi/2$ by adjusting the excitation frequency ν_{exc}. The amplitude A of the oscillating cantilever is kept constant by adjusting the excitation force amplitude F_0 using a feedback loop of the HF2LI. In this case, the feedback signal is obtained by subtracting the excitation frequency shift $\Delta\nu_{\mathrm{exc}} = \nu_{\mathrm{exc}} - \nu_{\mathrm{e}}$ provided by the PLL by a user-adjustable setpoint $\Delta\nu_{\mathrm{exc}}^{\mathrm{sp}}$.

Three-dimensional mapping in liquids

We implement 3D mapping by modulating the *z*-piezo displacement with a microcontroller (Atmel SAM3X8E as provided with the Arduino Due platform) while the AFM controller ensures the lateral scanning of the tip over the surface. The modulation is performed by applying a voltage with a triangular waveform using the digital-to-analog (DAC) converter of the microcontroller. The triangular waveform ensures a uniform sampling of the entire range as well as a constant velocity for both the approaching and retracting tip. The vertical velocity, which can be set from a computer using a serial connection emulated over USB, is chosen to be larger (typically by a factor of 100) than the scan velocity in the fast scan direction. For noise reduction the bandwidth of the analog output of the microcontroller is limited to 10 kHz by a second-order low-pass (LP) filter based on the LT1363 operational amplifier (Linear Technology, USA). The filtered signal is added to the *z*-voltage provided by the AFM controller by using a high-voltage (HV) adder.

To prevent approaching the tip too close to the sample during the 3D mapping, a retraction criterion is provided by exploiting a feedback loop of the HF2LI. The feedback loop is adjusted as a pure proportional controller which considers the excitation frequency shift (FM-AFM) or the negative amplitude (AM-AFM) as its error value. If the error value exceeds a user-defined threshold, the feedback loop outputs a digital signal, which triggers an interrupt at the microcontroller. Subsequently, if the tip is approaching the sample when the interrupt is triggered, the direction of the vertical tip movement is reversed.

Data acquisition and synchronization

Data are acquired, processed and displayed with a self-written software based on IGOR Pro (Wavemetrics, USA). A self-written IGOR Pro extension (written in C due to performance considerations) utilizes the HF2LI software interface to digitally capture data (*i.e.*, excitation force amplitude, excitation frequency, static deflection, amplitude and phase shift) at a user-adjustable sampling rate of up to 28 kHz per channel for up to 20 channels. The IGOR Pro extension runs as a separate thread in which the data is continuously polled from the HF2LI in an asynchronous fashion. Subsequently, the data is stored in cyclic buffers. To allow for an assignment of the recorded data with the position of the tip, a synchronization with both the scan engine of the AFM controller as well as the microcontroller that adjusts the *z*-piezo displacement is necessary. The synchronization with the scan engine is achieved by digital end-of-line (EOL) and end-of-frame (EOF) triggers provided by the AFM controller. Most commercial AFM controllers provide similar signals that can be used for synchronization. Thereby, our implementation can easily be modified for other controllers. After each line, the AFM controller outputs a trigger pulse at its EOL output. Since the pulses are too short for a reliable detection, they are used as a clock signal for a binary counter (74HC4040,

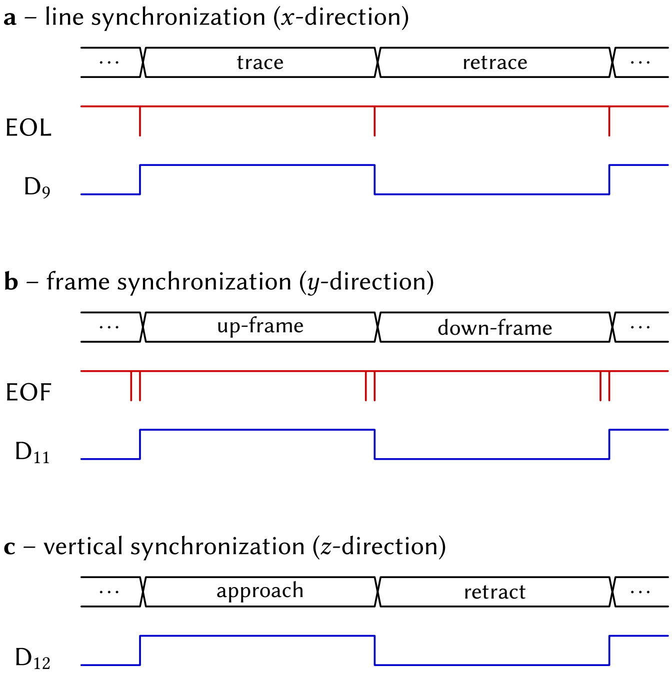

Figure 3.3: Timing diagram of the line (a) and frame (b) synchronization of the scan controller as well as the vertical synchronization with the microcontroller (c). The naming of the digital inputs to the HF2LI (D_x) is consistent with figure 3.2.

.

Fairchild Semiconductor, USA). The output Q_0 of the counter (division by 2) represents each trace and retrace scan as a HIGH and LOW signal, respectively (x-direction, figure 3.3 a). Thus, the fast lateral scan direction is directly available for further data assignment. Similarly, the AFM controller outputs two short digital LOW pulse after each frame. We use a second binary counter (which performs a division by 4, output Q_1) to obtain a HIGH and LOW signal for each up and down frame, respectively (y-direction, figure 3.3 b). Therefore, we directly obtain the slow lateral scan direction for further data assignment. The microcontroller indicates the direction of the vertical cantilever movement by an additional digital signal (z-direction, figure 3.3 c). The processed triggers from the EOL and EOF outputs of the AFM controller as well as the trigger of the microcontroller are fed into the digital inputs of the HF2LI. The HF2LI records the trigger channels as well as its other data channels which are used for further data processing within the self-written software.

Using the recorded triggers, we can assign the data to individual frames and lines. For each lateral scan line, the digitally encoded vertical direction (z-direction, figure 3.3 c)

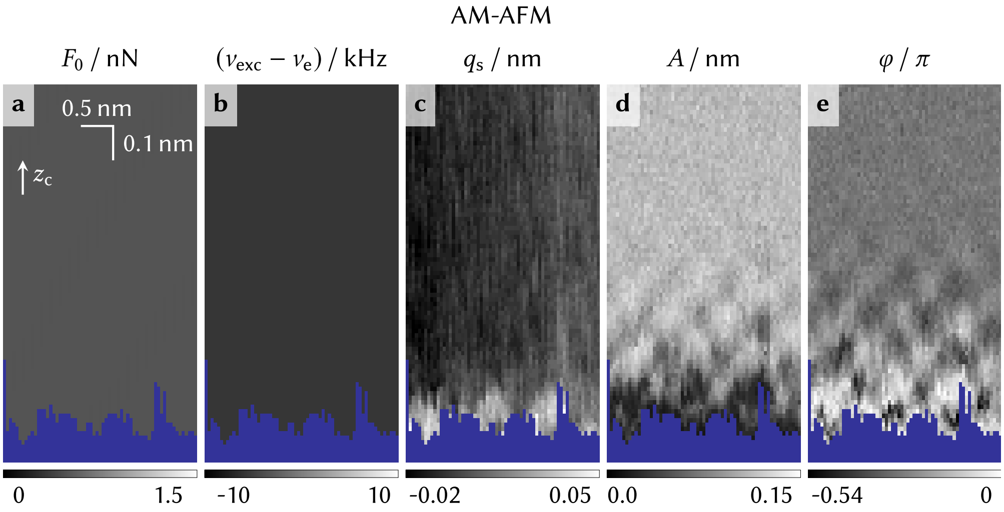

Figure 3.4: Vertical slices of the excitation parameters (F_0, ν_{exc}) and observables (q_s, A, φ) obtained in a AM-AFM experiment. The slice is aligned along the $[48\bar{1}]$ direction of calcite. Data is shown for the approaching tip. Blue color is assigned to regions of no data, *i.e.* to positions that have not been accessed by the tip.

is used to reconstruct the vertical position of the tip. We perform this line-by-line data processing online during the measurement, allowing the AFM user to quickly evaluate the data and react to potential changes during the recording of a 3D map.

3.2.3 Proof of concept

We demonstrate the 3D mapping capability of our setup by resolving the hydration structure of the calcite (10.4) surface in water. After cleaving the calcite crystal (Korth Kristalle GmbH, Germany), pure water (Millipore GmbH, Germany) was injected in a closed liquid cell (Bruker Nano Surface Division, USA) that was sealed with an O-ring. In water, the used silicon cantilever (PPP-NCHAuD, Nanosensors, Switzerland with a gold-coated backside) exhibited an eigen frequency of 129.6 kHz and a quality factor of 9. We determined the deflection sensitivity by a distance-dependent static deflection measurement and obtained a spring constant of 32 N m^{-1} by evaluating the thermal noise.[109] For operation in the AM mode, we set $F_0 = 0.6$ nN and $\nu_{exc} \approx 0.95\nu_e$. The closest approach to the sample was limited to the position where the amplitude A decreased to 0.1 of the amplitude of the retracted cantilever. For FM-AFM operation, the oscillation amplitude was kept constant at 0.11 nm and the excitation frequency shift retraction threshold was set to 20 kHz.

We present exemplary vertical (xz) slices from an AM-AFM dataset in figure 3.4. The data for the full 3D AM-AFM dataset were acquired in 420 s (corresponding to 128

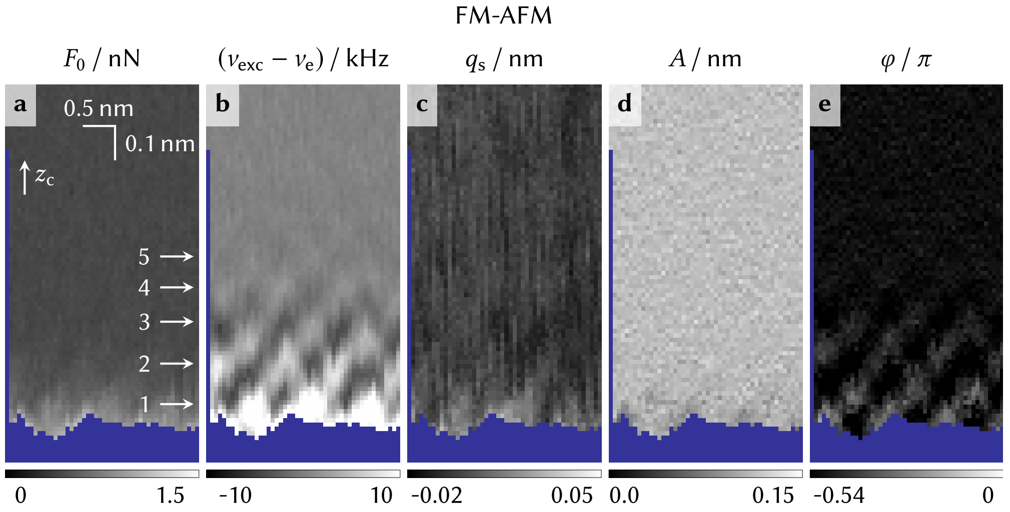

Figure 3.5: Vertical slices of the excitation parameters (F_0, ν_{exc}) and observables (q_s, A, φ) obtained in a FM-AFM experiment, aligned along the $[48\bar{1}]$ direction.

scan lines and a time of 3.3 s per trace and retrace) with a vertical cantilever velocity of $92\,\mathrm{nm\,s^{-1}}$ (yielding approximately 190 pixel in vertical direction and 63 pixel in the fast scan direction). Due to the independent vertical and lateral tip movement, not the entire data is collected for the first and last approach or retract curve within each slice, respectively. This explains the additional regions with no data available (color-coded blue) on the left and right edges in the experimental data. We use the center position of the tip oscillation z_{c} as distance coordinate, *i.e.*, we plot all data against the sum of the adjusted z-piezo displacement z_{p} and the measured static deflection q_{s}. Additionally, the data is corrected for sample tilt and vertical drift by subtracting the vertical distances by a linear fit of the position of closest approach to the sample.

The vertical slices of the AM-AFM dataset in figure 3.4 show the excitation parameters (F_0, ν_{exc}) and observables (q_s, A, φ). Both the excitation force amplitude (a) and excitation frequency (b) are constant. A checkerboard-like pattern can be recognized in both the amplitude (e) and phase shift (f) slices. These observations are qualitatively in line with both previous experimental[48–51] 3D AFM measurements and theoretical calculations[51,110,111] on calcite (10.4), where water has been found to be vertically ordered in several layers.

The setup allows to straightforwardly switch between AM-AFM and FM-AFM. In figure 3.5 we present FM-AFM data obtained within the same measurement session as the AM-AFM data, *i.e.*, with the same cantilever and sample. Vertical slices show the excitation parameters (F_0, ν_{exc}) and observables (q_s, A, φ) for the FM-AFM measurement in figure 3.5. Here, the excitation frequency exhibits again a regular checkerboard-like pattern of extrema. The vertical slices in figure 3.5 e and f also show that amplitude

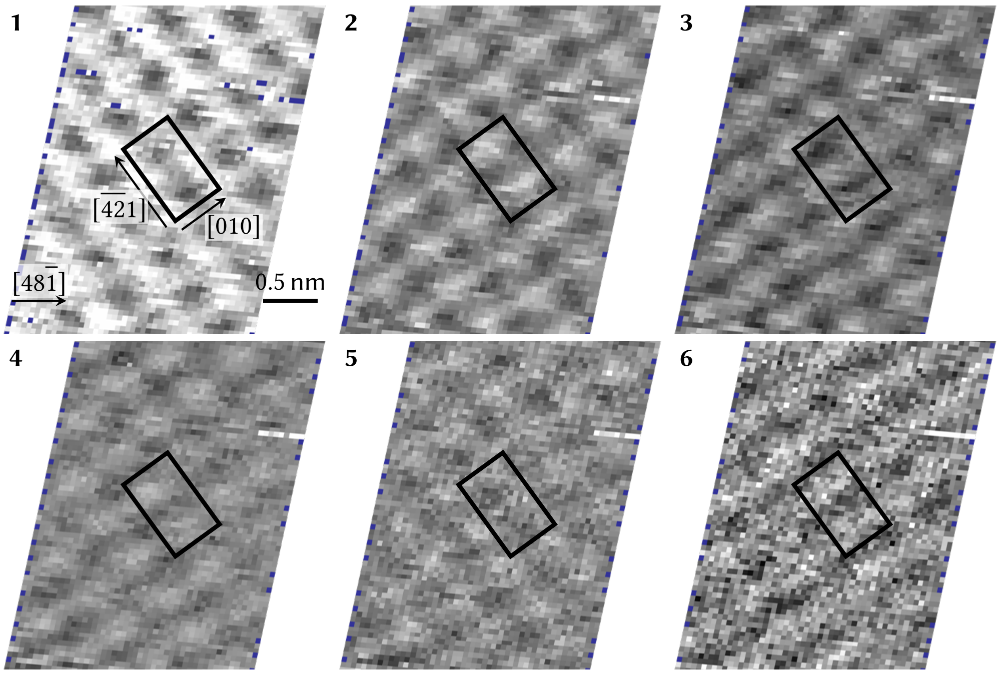

Figure 3.6: Lateral slices extracted from a three-dimensional excitation frequency shift map above the calcite (10.4) surface in water. This figure is a visual representation of the same data set used for figure 3.5. The tip center position where the data has been extracted is indicated by the arrows in figure 3.5 a. The black-to-white color scale is limited to values from (1) ±14 kHz, (2) ±10 kHz, (3) ±6 kHz, (4) ±4 kHz, (5) ±2 kHz, (6) ±1 kHz.

and phase shift are not perfectly constant. For the quantitative analysis of the data performed in the following sections (and shown in section 2.1), this is not problematic, as detailed in section 2.1.

Finally, we present lateral slices through the FM-AFM data set in figure 3.6. Through comparison with reference 51 and with the assumption that the drift velocity was small compared to the slow scan velocity, the shown data was laterally distorted to match the surface unit cell dimensions of the calcite (10.4) surface.[112] The lateral slices in figure 3.6 (extracted at various heights parallel to the sample surface as indicated by the arrows in figure3.5 a) each reveal a periodic pattern. The observed patterns are commensurate to each other. Moreover, at a fixed lateral position, minima and maxima alternate within the different layers (the surface unit cell of calcite is shown by the black rectangle and can act as a fixed point of reference).

Note that the data shown here is the raw data used for the calculation the three pieces of information about the tip-sample force shown in figure 2.4 section 2.1. An detailed interpretation and discussion of the checkerboard-pattern is given in the section 3.3.

3.2.4 Conclusion

In conclusion, we present the implementation of three-dimensional mapping at solid–liquid interfaces using a custom data acquisition system. Up to 20 channels can be recorded simultaneously in synchronization with the scan movement. The z-piezo displacement is performed by a microcontroller which is able to reverse the vertical direction of the tip movement based on a user-defined threshold. This flexible architecture makes our setup easily extendable for techniques related to AFM, such as Kelvin probe force microscopy, open-loop electric potential measurements and bimodal AFM techniques. We demonstrate the high-resolution capabilities of our 3D FM-AFM setup by successfully imaging the hydration structure of the calcite (10.4) surface in water.

3.3 Chemical identification

Section 3.3 is based on the article “Chemical Identification at the Solid–Liquid Interface” by H. Söngen, C. Marutschke, P. Spijker, E. Holmgren, I. Hermes, R. Bechstein, S. Klassen, J. Tracey, A. S. Foster and A. Kühnle, which has been published in *Langmuir* (reference 52). For this project, I performed or supervised measurements (some measurements were performed by S. Klassen and E. Holmgren). Moreover, I analyzed the experimental data, prepared the figures and wrote the manuscript (with the exception of the simulation methods section), with contributions by P. Spijker, R. Bechstein, A. S. Foster and A. Kühnle. The MD simulations shown in this section were performed in the Group of A. S. Foster by P. Spijker. Analysis of the MD simulation was done in parts by J. Tracey. Parts of the publication are reproduced verbatim. Besides modifications to make this section consistent with the other sections in this thesis, there are four major changes: I include magnesite in the discussion, I show the tip-sample force gradient as primary data for the chemical identification, added a discussion on the tip-sample damping factor and show reproduction data.

Solid-liquid interfaces are decisive for a wide range of natural and technological processes, including fields as diverse as geochemistry and environmental science as well as catalysis and corrosion protection. Dynamic atomic force microscopy nowadays provides unparalleled structural insights into solid–liquid interfaces, including the solvation structure above the surface. In contrast, identifying the chemical composition of individual interfacial atoms still remains a considerable challenge. So far, an identification of chemically alike atoms in a surface alloy has only been demonstrated under well-controlled ultra-high vacuum conditions. In liquids, the recent advent of three-dimensional force mapping has opened the potential to discriminate between anionic and cationic surface species. However, a full chemical identification will also include the far more challenging situation of alike interfacial atoms (i.e., with the same net charge). Here we demonstrate the chemical identification capabilities of dynamic atomic force microscopy at solid–liquid interfaces by identifying calcium and magnesium cations at the dolomite–water interface. Analyzing site-specific vertical positions of hydration layers and comparing them with molecular dynamics simulations unambiguously unravels the minute, but decisive difference in ion hydration and provides a clear means for telling calcium and magnesium ions apart. Our work, thus, demonstrates the chemical identification capabilities of dynamic AFM at the solid–liquid interface.

3.3.1 Introduction

Dynamic atomic force microscopy[21,23] (AFM) has developed into a most versatile tool that is capable of imaging surfaces with atomic resolution not only in a well-controlled ultra-high vacuum (UHV) environment,[113] but also at the solid–liquid interface.[13] When analyzing distance-dependent data, dynamic AFM can even provide chemical information on individual atoms at the surface, as has first been demonstrated in UHV: Force-distance curves have been collected on Si(111)-(7×7), revealing site-specific differences and, thus, demonstrating the potential to differentiate inequivalent adatoms by a careful analysis of force-distance curves.[114] Later, ionic crystal sublattices have been identified on several crystals, including, *e.g.*, CaF_2 (111),[115] NiO (001),[116,117] NaCl (001)[118] and calcite (10.4).[119] A particularly challenging system has been studied by Sugimoto *et al.*, who have been the first to demonstrate the identification of individual surface atoms in an alloy of Pb, Sn and Si, even though these atoms occupy identical surface positions and are not oppositely charged.[120] All the above studies have been carried out in UHV.

At the solid–liquid interface, however, the situation is usually significantly more complex due to the presence of the solvent molecules that can form a solvation structure not only at the surface but also at the probe tip.[121] Nevertheless, due to the omnipresence of water films on surfaces, especially the solid–water interface has attracted considerable attention in the last decades,[1,2,6,122] with the first demonstration of atomic-scale imaging with dynamic AFM on a mica (001) surface in 2005 by Fukuma *et al.*[13] Using conventional imaging on calcite (10.4), ionic sublattices have been assigned based on the different lateral structure.[90] Recently, the development of three-dimensional (3D) force mapping in liquids[17] has considerably pushed this field of research. Three-dimensional force maps have been collected on, *e.g.*, calcite (10.4),[48,51] mica,[17,64] α-Al_2O_3,[123] graphite,[65] alkanethiol films[124,125] and organic crystals.[126] Analyzing site-specific differences in the force-distance curves has allowed for the discrimination between anionic and cationic surface species.[51] So far, however, the identification of chemically alike interfacial species possessing the same net charge has not been demonstrated. Such a differentiation is, however, an essential prerequisite for chemical identification, one of the major challenges of surface science. For such a demonstration, we investigate an ideally suited model system, namely dolomite (10.4), possessing two chemically alike cation species that can be benchmarked against both the well-studied calcite (10.4) surface and the magnesite (10.4) surface. Here, by comparing high-resolution 3D AFM measurements with molecular dynamics (MD) simulations, we show that the different hydration of magnesium (Mg) ions as compared to calcium (Ca) ions leads to a shift of interfacial water above Mg ions that allows for their discrimination from Ca ions on the surface of dolomite.

3.3.2 Methods

Experimental

Experiments were performed with a custom 3D-AFM[15,16,53] operated in the frequency-modulation mode,[21] as described in the previous section 3.2. Calcite ($CaCO_3$) crystals (Korth Kristalle, Germany), dolomite ($CaMg(CO_3)_2$) crystals and magnesite ($MgCO_3$) crystals (SurfaceNet, Germany) were cleaved prior to the measurement. We used Si cantilevers exhibiting an eigenfrequency of approximately 150 kHz, a quality factor of approximately 8 and a spring constant of approximately $40\,\mathrm{N\,m^{-1}}$ in liquids (types PPP-NCHAuD, Tap300G and Tap300GB-G were used). Oscillation amplitudes in the order of 0.7 Å to 0.8 Å have been used. All AFM measurements were performed in pure water (MilliPore). The deflection sensitivity was determined from static deflection *versus* z-piezo-displacement curves, and the spring constant by evaluation of the thermal noise.[109] The crystallographic surface directions were obtained from the direction of birefringence.[54] Experimental data sets were corrected for sample tilt and vertical drift as described in the previous section 3.2.[53] Moreover, data were corrected for lateral drift by comparison of up and down images to identify the surface unit cell. Subsequently, the images were adjusted so that the surface unit cell dimensions correspond to the unit cell dimensions determined from the dimension of the bulk unit cell.[112] We obtained the averaged tip-sample force gradient $\langle k_{\mathrm{ts}} \rangle_{\cap}$ and the averaged damping factor $\langle \gamma_{\mathrm{ts}} \rangle_{\cap}$ from the measured quantities F_0, ν_{exc}, q_{s}, A and φ according to the AFM equations described in section 2.1 (equations 2.23–2.24).[18] If experimental data was averaged, a shaded area below and above each average curve indicates a 95 % confidence interval determined from the standard deviation s and the number of samples n according to $\pm 1.96 s/\sqrt{n}$.

Simulations

For all simulations, the large scale molecular dynamics code LAMMPS[127] was used. The simulations were run in parallel on a typical Linux commodity cluster, and analysis was performed visually using VMD[128] or numerically using the Python library MDAnalysis.[129] In order to model the crystal structure of the (10.4) cleavage plane, we used a crystal that is seven layers thick and where each layer consists of five unit cells along the $[42\bar{1}]$ and eight along the [010] direction. For dolomite and magnesite, the simulation box dimensions were scaled down (while keeping the internal carbonate bonds at the correct length) with respect to the dimensions for calcite, in order to match the surface unit cell size. Each simulation consists of a similar protocol. First, the seven-layer crystal is modeled as if it is a bulk crystal in order to relax our initial scaling, during which no external constraints other than a common barostat and thermostat were applied to the atoms. Subsequently, the crystal is placed in a larger box and solvated on either side of the (10.4) surface by ample water, such that far away from the surface bulk properties can be reached, adding approximately 16 nm in the direction perpendicular to the surface. The total number of atoms in each of the simulations is in the range of 25 000. In the next steps, the lateral dimensions of the simulation box were fixed, along with the carbon atoms of the center-most layer in order to ensure the proper crystal dimensions and no thermal drift of the system. First, the entire system is allowed to relax for at least 50 ps (using a 1 fs time step) at ambient conditions (310 K and 1013.25 hPa). After that, a longer run (0.5 ns) is performed to allow for the hydration layers to form. Following this, the unit cell dimension along z as well as the total and separate energy components were constant (except for thermal oscillations), confirming that equilibrium has been reached. The next 8 ns are the simulation production run, where each 2.5 ps a snapshot of the system is saved to disk and used for subsequent analysis.

An accurate force field for calcite simulations was developed by Raiteri *et al.*, and has been used successfully in simulating the growth of calcium carbonate in aqueous solutions.[130] Here, we used the same force field, except that we replace the intramolecular angle and improper terms for the carbonates by more common harmonic potentials providing equivalent interactions. Magnesium terms were taken from the extended potentials of Tomono *et al.*, which allows for the modeling of dolomite and magnesite.[131] This proved to show no significant differences in the the calculated density to more recently published potentials.[132] For water, we used the single point charge flexible model (SPC/Fw).[133]

3.3.3 Results: Hydration and chemical identification

Figure 3.7 shows an atomistic model of the (10.4) surfaces of calcite, dolomite and magnesite. In all cases, the surface unit cell (black rectangle) contains two cations and two carbonate groups. In case of calcite the cations are Ca, for magnesite both cations are Mg. For dolomite, the surface unit cell contains both a Ca and a Mg ion, which leads to alternating Ca and Mg ions oriented along the $[42\bar{1}]$ direction. Therefore, the solid–liquid interface of the dolomite (10.4) surface constitutes an ideal test system to assess the feasibility of chemical identification of the two equally charged cations.

To obtain the water density in the volume above the substrates, we performed MD simulations. In figure 3.8 we show the density of water oxygen atoms extracted along a row of alternating cations and anions (dashed lines in figure 3.7). In case of calcite (figure 3.8 a), we find that water forms a laterally as well as vertically ordered structure above the surface. The water molecules in the first layer are located above calcium ions, the ones in the second layer above carbonate groups. This alternating arrangement of interfacial water above the cations and anions continues in several layers and leads to a characteristic checkerboard pattern. Our simulations agree with previous theoretical studies on interfacial water above calcite.[51,110,111,134]

For dolomite, the simulated water density shown in figure 3.8 b shows a similar checker-

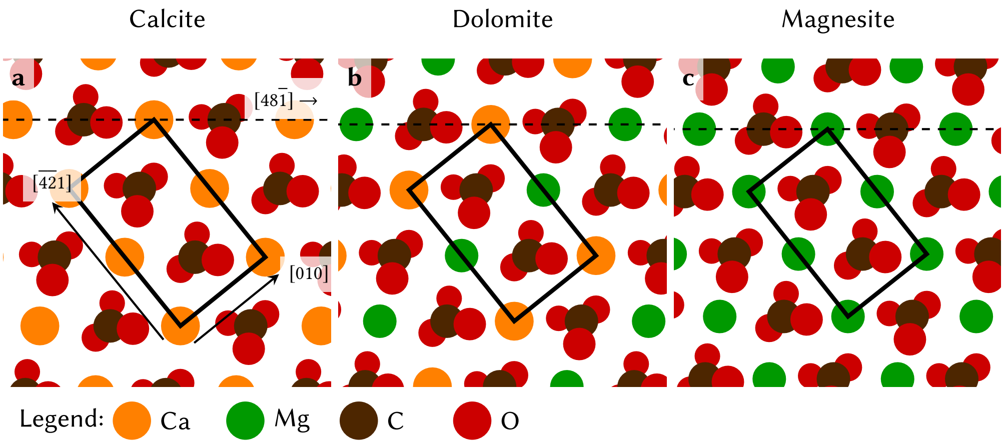

Figure 3.7: Schematic model of the (10.4) surface of calcite (a), dolomite (b) and magnesite (c). The unit cell dimensions are 0.81 nm · 0.50 nm, 0.77 nm · 0.48 nm and 0.73 nm · 0.46 nm, respectively.[112] The crystallographic directions in panel a apply to all panels. The two carbonate groups in the surface unit cell are tilted with respect to the surface. As the protruding oxygen atom of the carbonate group points in alternating directions, the carbonate groups are not equivalent.

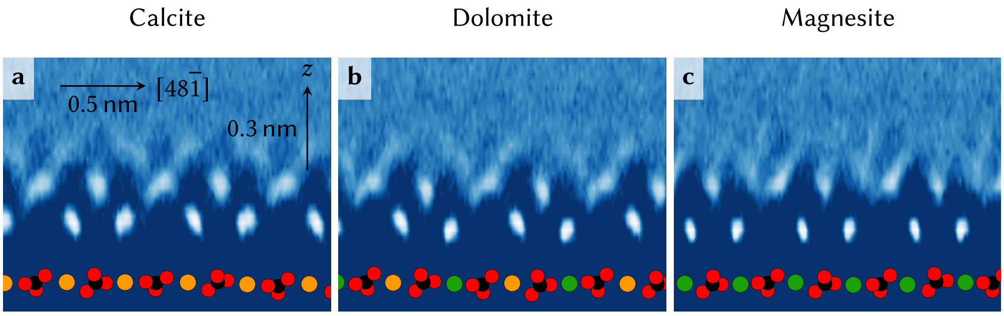

Figure 3.8: Interfacial water obtained from MD simulations. The number density of water oxygen atoms is shown for calcite (a), dolomite (b) and magnesite (c) as a vertical slice extracted along the [48$\bar{1}$] direction indicated by the dashed lines in figure 3.7. The color scale ranges from dark blue (low density) to white (high density).

board pattern of water density maxima. Similar to calcite, the first layer is placed above the cations, which are now Ca and Mg. However, although Ca and Mg cations occupy virtually identical positions in the crystal lattice, the oxygen water density maximum above Mg sites is shifted closer to the surface compared to the Ca site. This finding can be rationalized by the smaller size and, consequently, the larger charge density of Mg compared to Ca.[135]

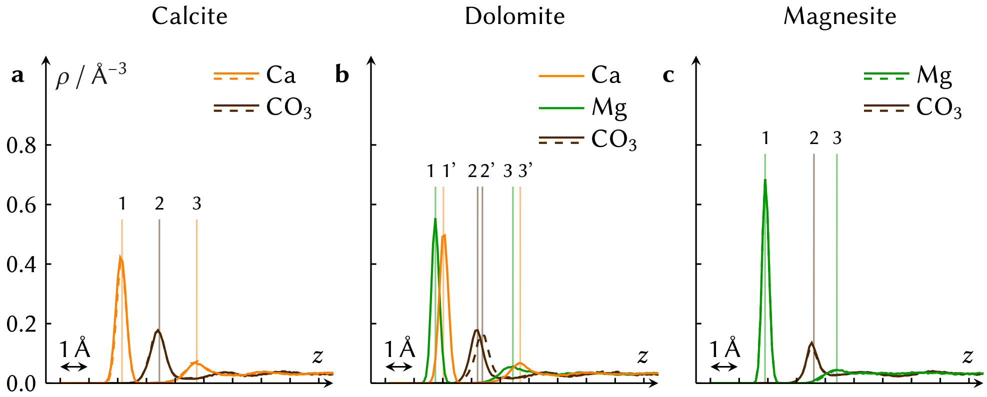

Figure 3.9: Site-specific density profiles obtained from the MD simulations. The site-specific density profiles result from averaging individual density profiles within a circle of 1.25 Å radius centered on each respective ion. Each symmetry equivalent ion within the simulation box was considered.

The water density above magnesite shows again the checkerboard-like arrangement of water. Since here all surface cations are Mg, the oxygen water density maximum is consistently shifted towards smaller distances above each cation, compared to the calcium case. However, similar to calcite and in contrast to dolomite, the oxygen water density maxima within one layer are all located at a similar distance from the surface.

Site-specific profiles of the water density above the four atoms within each surface unit cell are shown in figure 3.9. These data provide another way of showing the position of water molecules above the surfaces. For calcite (figure 3.9 a), alternating peaks are obtained above the cations (yellow) and the anions (brown). Moreover, the density profiles obtained for the two different Ca sites within the surface unit cell are very similar. The same applies for the two density profiles extracted above the carbonate sites. For dolomite (figure 3.9 b), the shift in the water oxygen density maxima is visible when comparing the profile obtained above Ca (yellow) with the Mg profile (green). A shift in the profiles obtained above the carbonate sites can also be recognized. For magnesite (figure 3.9 c), the density profiles are consistently shifted towards smaller distances for both Mg sites and both carbonate sites, respectively. As for calcite, this again results in very similar profiles above the respective cation and anion sites. A comparison between the density profiles between calcite, dolomite and magnesite shows that water is not only positioned closer above Mg ions compared to Ca ions, but that water in the first layer is also more confined above Mg ions. This corresponds to the increasingly narrower and more pronounced first-layer density peaks shown in figure 3.9 when considering first calcite (a), then dolomite (b) and finally magnesite (c). In contrast, the peak height of the other hydration peaks, in particular the second and third-layer peak, decreases for increasing the Mg content.

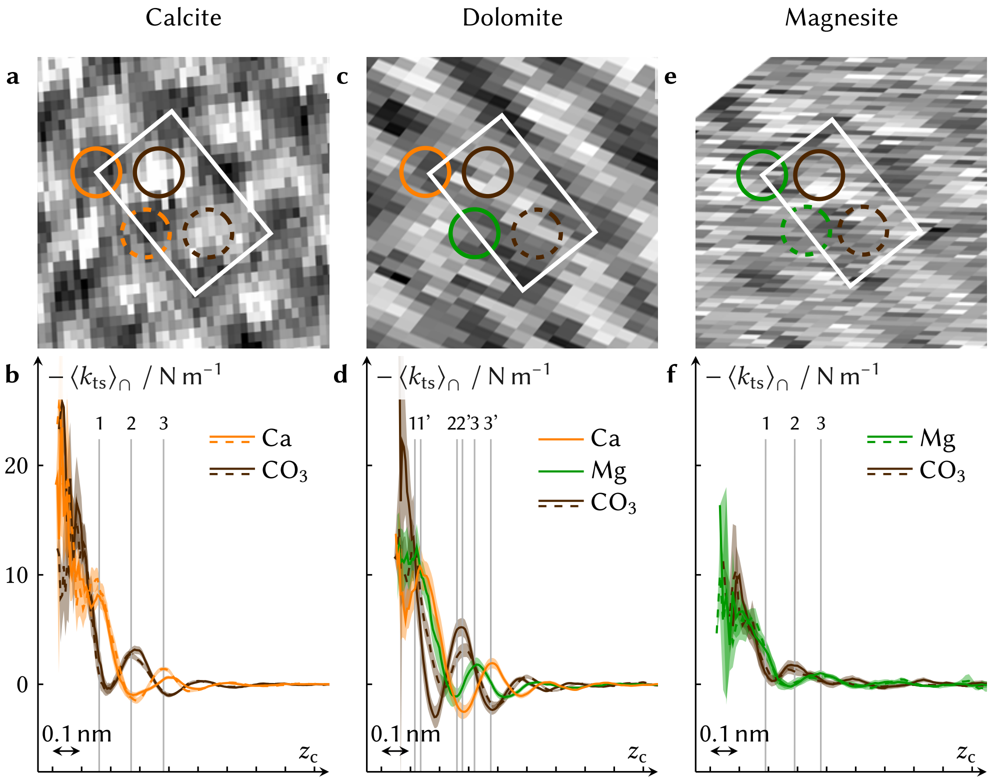

Figure 3.10: Experimental hydration data for calcite, dolomite and magnesite. Drift-corrected lateral (xy) slices of the negative cap-averaged tip-sample force gradient ($-\langle k_{ts}\rangle_\cap$) are presented in the first row (a, c, e). The surface unit cell is oriented identically as the one in figure 3.7. Profiles of $-\langle k_{ts}\rangle_\cap$ as function of the center position of the tip z_c extracted above the different sites indicated in the first row are shown in the second row (b, d, f). Yellow, green and brown color indicate Ca, Mg and CO$_3$ sites, respectively. Dashed lines in the graphs correspond to the lower site indicated in the lateral slices.

Next, we explore whether we can make use of the subtle difference between the Ca and Mg hydration to provide chemical identification of the two interfacial cations on the surface of dolomite. To address this challenging task, we have optimized a commercial AFM setup for performing high-resolution imaging at the solid–liquid interface[15,16] and added a highly flexible routine for collecting 3D AFM data.[53] This setup is also described in the previous section 3.2 of this thesis. As reference, we first analyze distance-dependent data on calcite at four sites (two above the cations, two above the anions) within the calcite surface unit cell. A lateral (xy) slice of a 3D data set showing the negative cap-averaged tip-sample force gradient ($-\langle k_{ts}\rangle_\cap$) obtained on calcite in pure water is shown in figure 3.10 a. We ensure that this lateral slice is extracted within a hydration layer (in this case the second layer), as is explained in detail in section 3.3.4. In figure 3.10 b, we show site-specific profiles of $-\langle k_{\mathrm{ts}} \rangle_{\cap}$ extracted at the two minima and the two maxima observed within each surface unit cell by averaging over the areas indicated by the circles in figure 3.10 a and several symmetry-equivalent sites. All extraction sites are shown in figure 3.13. A clear agreement between the two profiles extracted at sites that are shifted by half a unit cell length along the $[42\bar{1}]$ direction can be observed (both colored either yellow or brown, respectively). Moreover, all four extracted profiles exhibit an oscillatory shape. We interpret each maximum (minimum) in the negative cap-averaged tip-sample force gradient ($-\langle k_{\mathrm{ts}} \rangle_{\cap}$) as a maximum (minimum) in the water density, which is in line with the solvent tip approximation (STA).[136–138] Details on the STA are discussed in section 3.3.4. Note that the negative tip-sample force gradient close to the surface shows an overall increase that it interpreted by increasingly repulsive interactions originating from the presence of a rigid surface solely.

Next, we identify whether the profiles were extracted above Ca or CO_3 sites. By comparison with the simulated water density (figure 3.9 a), the profile with the minimum in $-\langle k_{\mathrm{ts}} \rangle_{\cap}$ at the smallest tip-sample distance (brown profiles) can be readily assigned to a CO_3 ion, while the other set of profiles (yellow profiles) is assigned to Ca ions. The excellent agreement between the profiles extracted above Ca and CO_3 sites, respectively, is confirmed by identical water density profiles obtained by MD simulations (figure 3.9 a). The obtained vertical distance between two water density maxima is 1.3 Å. This distance agrees remarkably well with the layer-to-layer distances for the presented data in figure 3.10 b As our description is based on the simple STA model deviations between the theoretically obtained and the experimentally determined layer-to-layer distances can be expected.

After having analyzed calcite as a reference, we applied the same analysis protocol to a 3D data set obtained on the dolomite (10.4) surface. Here, $-\langle k_{\mathrm{ts}} \rangle_{\cap}$ profiles extracted at the sites indicated in figure 3.10 c are presented in figure 3.10 d. The individual profiles exhibit a very similar shape compared to calcite as they also show alternating extrema. Two of the four profiles (extracted at sites shifted half a unit-cell along the $[42\bar{1}]$ direction) exhibit a clear minimum at the smallest tip-sample distance and are, consequently, again identified as CO_3 sites (brown). In clear contrast to calcite, however, the other two profiles – extracted above the cation sites – show a distinctive shift relative to each other. This shift is also reflected in the MD simulations (figure 3.9 b), as water molecules are located closer to Mg ions compared to Ca sites. Therefore, we assign the cation-site curve that is shifted more closely to the surface (green, without prime) to a magnesium site, while the other site (yellow, with primes) is assigned to a Ca site. This is a demonstration of chemical identification of interfacial ions possessing the same charge. Note that even the shift in the profiles obtained above carbonate sites is in excellent agreement with the MD simulations.

The magnesite data further supports our assignment, as the two $-\langle k_{\mathrm{ts}} \rangle_{\cap}$ profiles extracted above the Mg sites are very similar and do not exhibit the shift relative to each other. Moreover, the layering beyond the second layer visible in the magnesite data is not as pronounced compared to calcite and dolomite, which is in agreement to the density profiles from the MD simulation (figure 3.9).

3.3.4 Hydration layer assignment with the solvent tip approximation

A number of theoretical works have been devoted to understanding the mechanism by which the tip of an atomic force microscope interacts with samples that are immersed in a liquid.[136–139] Recently, Fukuma *et al.*[51] have provided evidence that both the hydration structure of the tip and of the sample play a key role: As the tip approaches the surface, the two hydration structures start to merge and overlap. The free energy of the system has been found to decrease if positions with increased local liquid density at the tip coincide with positions of locally increased liquid density above the sample. Consequently, the free energy of the system was found to increase when liquid molecules were not able to occupy sites favored by both tip and sample. A stable equilibrium results from placing the liquid molecules confined at the tip at positions that are energetically favored due to *both* the interaction with the tip and with the sample. The changes in free energy as a function of the tip-sample displacement result in a contribution to the tip-sample force.[51]

The simplest model for the tip hydration structure is to consider just a single molecule of the liquid that is confined at the tip. This is done in the *solvent tip approximation*[136–139] (STA). According to the STA, the attached molecule probes the density of the liquid ρ and experiences a force F_{sta} that is proportional to the vertical gradient of $\ln \hat{\rho}$. If the change of the solvent density due to the presence of the sample is small compared to the bulk density ρ_{bulk} (*i.e.*, $\hat{\rho} = \rho/\rho_{\mathrm{bulk}} \approx 1$), the force can be approximated as being directly proportional to the derivative of the solvent density:

$$F_{\mathrm{sta}} \propto \frac{\partial \ln \hat{\rho}}{\partial z} \approx \frac{\partial \hat{\rho}}{\partial z} \quad \text{for} \quad \hat{\rho} \approx 1 \tag{3.1}$$

For very simplified solvent densities (such as sinusoidal density modulations), this results in a simple relationship: A maximum (minimum) in the density corresponds to a maximum (minimum) in the negative derivative of F_{sta}. Note that the force resulting from the STA model is conservative and, therefore, even with respect to the tip velocity. As a consequence, both the force and its gradient resulting from the STA only contribute to the even contribution to the tip-sample force and the tip-sample force gradient, respectively. Experimentally, the negative *cap-average* of the tip-sample force gradient was determined (figure 3.10). The cap-average is a weighted average that results from the oscillation of the probe tip. The weight function for the cap average is positive as well as symmetric with respect to the center position of

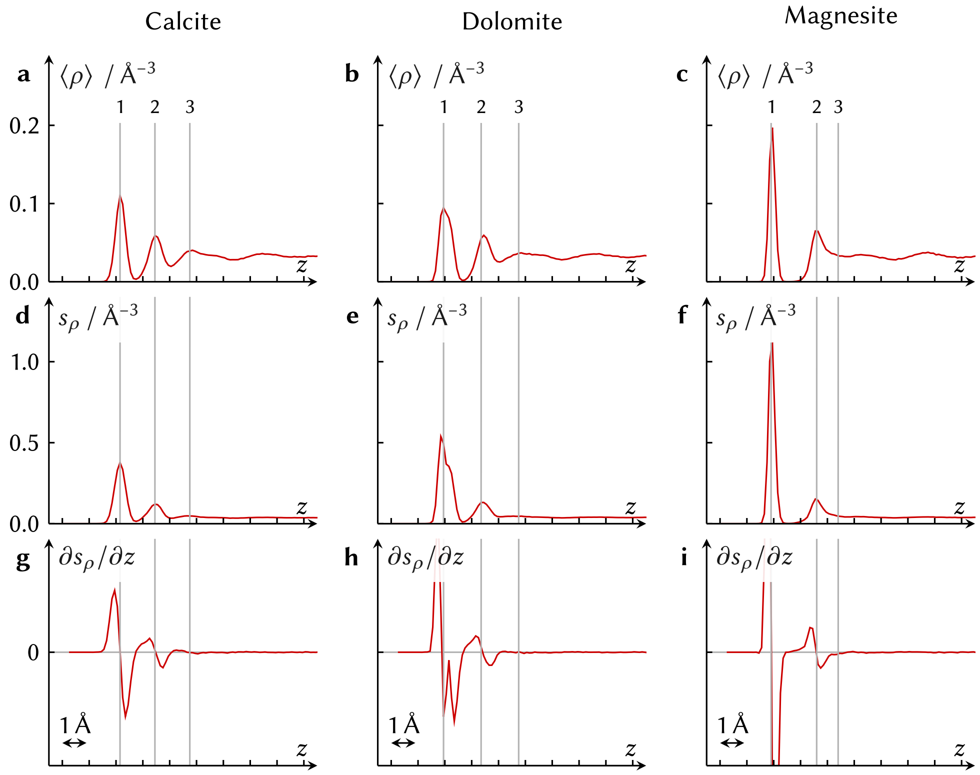

Figure 3.11: Plots in the first row show the average of all density versus distance profiles $\langle\rho\rangle$ within the simulation volume for calcite, dolomite and magnesite (a–c). The corresponding standard derivation s_ρ of the averages and its derivative with respect to z are shown in the second row (d–f) and third row (g–i), respectively. Hydration layer are identified by local maxima in the average water density, which corresponds to a maxima in the standard deviation, as indicated by vertical lines.

the tip (section 2.1, figure 2.6). Since in our case the amplitude of the oscillation is in the order of the vertical distance of two density maxima, extrema in the negative force gradient correspond to extrema in the negative cap-averaged tip-sample force gradient $-\langle k_{\mathrm{ts}}\rangle_\cap$ as well. Consequently, we interpret minima (maxima) in the negative cap-averaged tip-sample force gradient as minima (maxima) in the water density. We therefore assigned the profiles with the first minimum (closest to the surface) to carbonate sites, as the water density in the first layer above the CO_3 sites is smaller compared to the density above the cation sites. Importantly, this assignment using the STA is consistent with tip-sample force data that have been computed using molecular dynamics simulations explicitly including different probe tips.[51]

Next, we describe the procedure we used to select the distance, at which we extracted

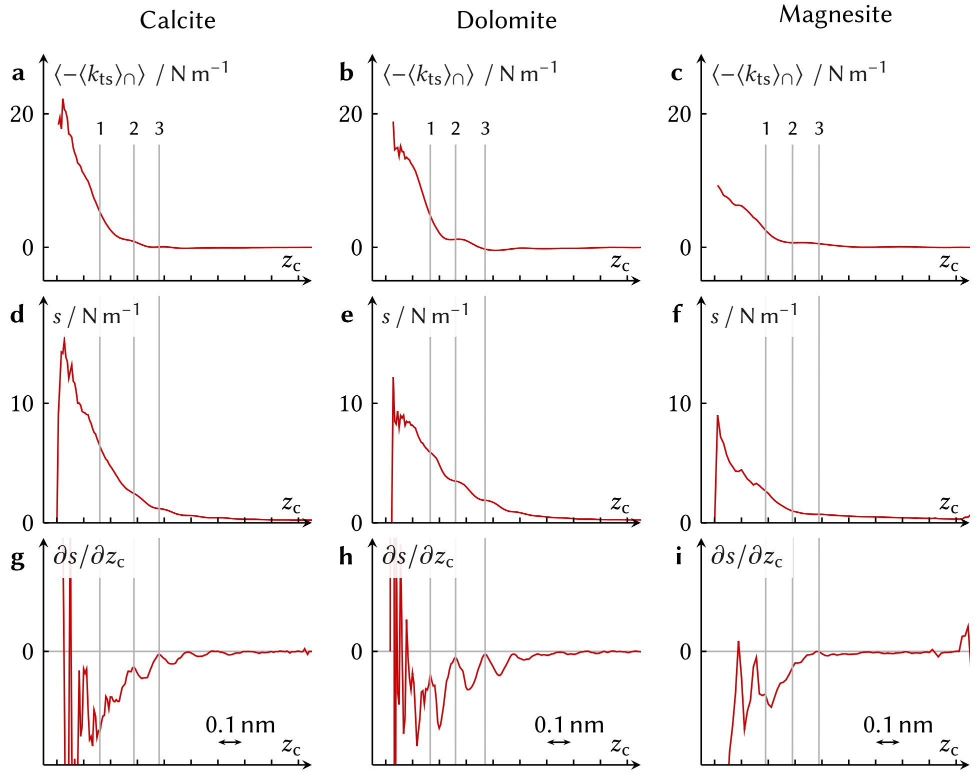

Figure 3.12: Averaged cap-averaged negative force gradient profiles (first row), their standard deviation s (second row) and its derivative (third row) for calcite, dolomite and magnesite in pure water. The numbers indicate at which position the corresponding layers shown in figure 3.13 have been extracted.

the lateral slices of the negative cap-averaged tip-sample force gradient shown in figures 3.10, 3.13 and 3.16. The aim is to select a distance, at which the probe tip is scanned within a hydration layer, as this is a prerequisite for identifying the sites within the surface unit cell used in the consecutive analysis. Since the average over all density profiles within the volume considered in the MD simulations (figure 3.11 a–c) clearly shows density maxima corresponding to the hydration layer, it appears obvious to assign maxima in the average over all cap-averaged tip-sample force gradient profiles $\langle -\langle k_{ts}\rangle_\cap\rangle$ within a 3D data set (figure 3.12 a–c) to the vertical positions of the hydration layers. However, the tip-sample force gradient profiles do not *solely* contain the contribution due to the hydration layers but also additional contributions due to the interaction of the probe tip with the sample surface. This makes it difficult to clearly identify maxima within the averaged $-\langle k_{ts}\rangle_\cap$ profiles.

Thus, we base the vertical hydration layer identification based on the fact, that within a hydration layer, lateral density variations (*i.e.*, lateral contrast) are at its maximum. This is obvious from the standard deviation s_ρ of the averaged density profiles (figure 3.11 d–f) which exhibits maxima or inflection points at distances where hydration layer are found within the simulation. Consequently, we analyzed the standard deviation s of the $-\langle k_{\mathrm{ts}} \rangle_\cap$ averages (figure 3.12 d–f). In most cases, the standard deviation shows a number of inflection points (identified using the first derivative of the standard deviation shown in the figures 3.11 and 3.12 g–i). We therefore assign the vertical position of the hydration layer in the experimental data as indicated by the gray lines shown in figure 3.12. This allows to identify most, but not always all layers: For magnesite, for example, only one layer was identified using its deflection point. In such cases, the other layers are assigned using the site-specific profiles. The lateral slices corresponding to the first three hydration layers are presented in figure 3.13. For completeness, we show the excitation frequency ν_{exc} (as part of the raw data) and the even contribution of the tip-sample force F_{even} in figure 3.14. The even contribution to the tip-sample force F_{even} was obtained by deconvolution of $\langle k_{\mathrm{ts}} \rangle_\cap$, as detailed in section 2.1.8.

3.3.5 The damping constant

In figure 3.15, we show the cap-averaged tip-sample damping constant $\langle \gamma_{\mathrm{ts}} \rangle_\cap$ as function of the center position of the tip oscillation z_{c}. The profiles were extracted above the same sites as shown in figure 3.10 a–c and figure 3.13. For all three substrates, $\langle \gamma_{\mathrm{ts}} \rangle_\cap$ is zero away from the surface and increases monotonically when approaching the surface. The profiles are very similar, despite the fact that they have been extracted at different surface sites. In some cases, there are slight variations in the curves, which are, however, not as pronounced as in the profiles of $-\langle k_{\mathrm{ts}} \rangle_\cap$ (figure 3.10).

Previous studies on the damping constant at solid–liquid interfaces report in part on similar results, in part on different results. Labuda *et al.*[140] and Kaggwa *et al.*[141] report on results that are similar to the ones observed here: No significant oscillation of γ_{ts} was observed in their measurements, which have been performed at the mica–water and the mica–octamethylcyclotetrasiloxane (OMCTS) interfaces, respectively. In contrast, de Beer *et al.*[142,143] and other authors[144] report on the experimental observation of oscillatory damping constant profiles at the graphite–OMCTS interface, which also have been obtained using molecular dynamics simulations.[142]

There are two reasons that might explain the observed discrepancy: Even slight deviations in the reference phase shift (induced, *e.g.*, by the electronics of the AFM detection) can lead to an incorrect evaluation of the three AFM equations, including equation 2.24 which is used to obtain the damping constant.[42,145] As pointed out by O'Shea,[145] the erroneously computed damping constant can reflect features (such as the oscillation) present in the tip-sample force gradient. When assuming that the calibration has been performed correctly in all the experiments, there is an additional

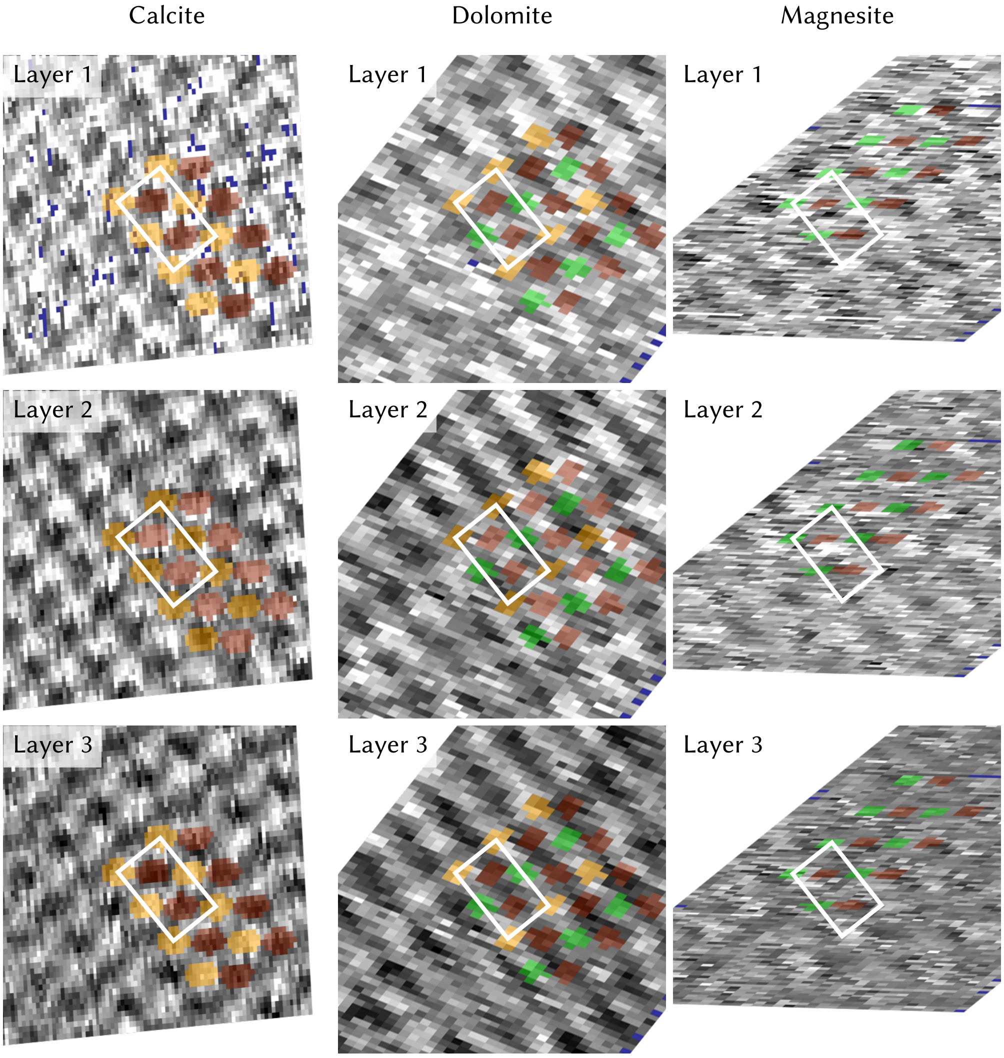

Figure 3.13: Drift-corrected lateral slices showing the negative cap-averaged tip-sample force gradient extracted from 3D data obtained on calcite, dolomite and magnesite. The distance (z_c) at which the layers have been extracted is indicated in figure 3.12. The surface unit cell is indicated by the white rectangle, which is placed at the same position and has the same orientation as the one in figures 3.7 and 3.10. The sites at which the profiles in figures 3.10, 3.14 and 3.15 have been acquired are indicated by the colored overlay.

influence of the tip size that may explain the discrepancy between the experiments: By employing MD simulations, de Beer *et al.* have described a reduction of the oscillation in the damping constant profiles when considering a spherical tip instead of a (flat)

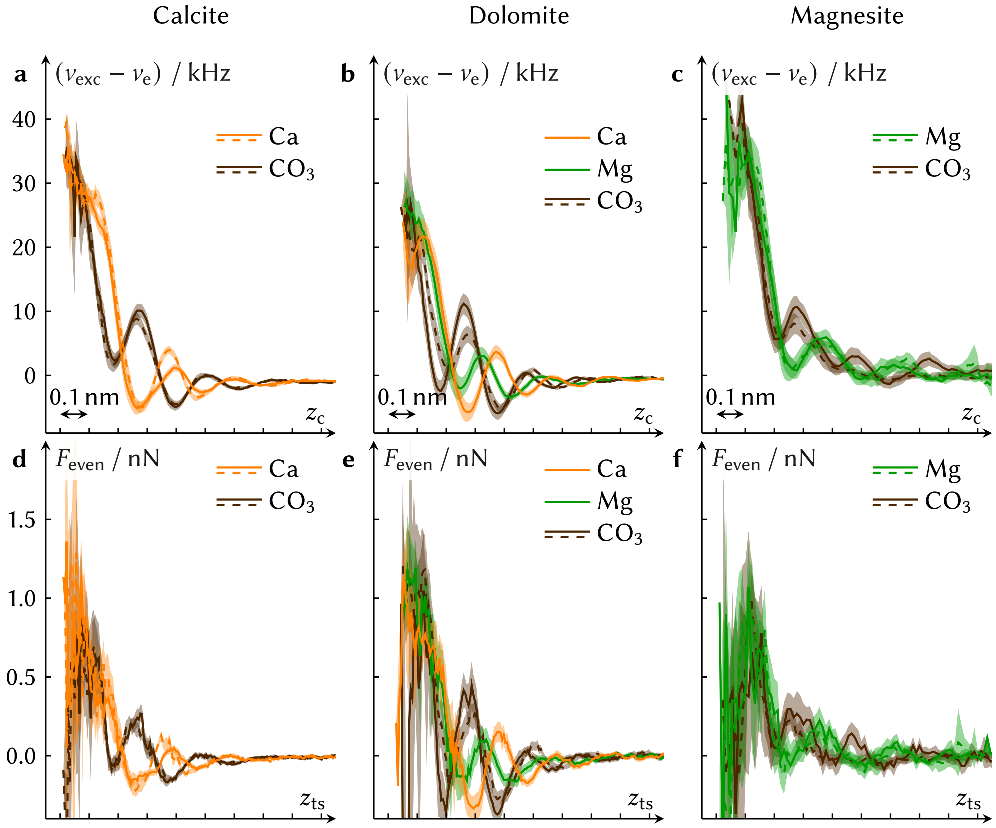

Figure 3.14: Profiles of the excitation frequency ν_{exc} subtracted by the eigen frequency ν_{e} as function of the center position of the tip oscillation z_{c} (first row) and the even contribution to the tip-sample force F_{even} as function of the tip-sample distance z_{ts} (second row).

larger blunt tip. This is similar to the argument by Labuda *et al.*,[140] who claim that the monotonic damping constant profile they obtain results from the interaction of the nanoscopic tip apex. The argument that a sufficiently large tip is necessary to observe the oscillatory damping profiles would corroborate the assumption that a sharp tip has been used in the experiments presented here.

3.3.6 Reproduction data

In this section, we present another dataset for obtained for each of the three substrates calcite, dolomite and magnesite as lateral layers in figure 3.16 and as profiles ($-\langle k_{\mathrm{ts}}\rangle_{\cap}$, $\langle \gamma_{\mathrm{ts}} \angle_{\cap}$ and F_{even}) in figure 3.17.

Note that for the calcite case (which is the same data set as the FM-AFM data shown in

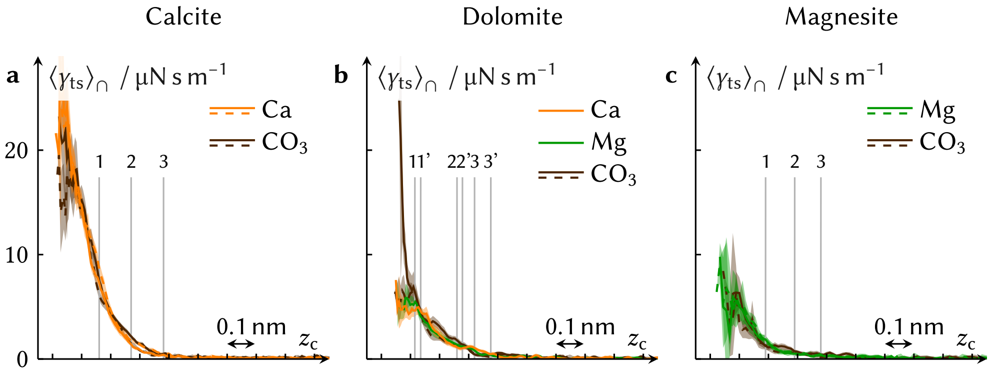

Figure 3.15: Profiles of the averaged tip-sample damping factor $\langle \gamma_{\mathrm{ts}} \rangle_\cap$ as function of the center position of the tip z_{c}. The profiles are extracted at the same sites as the profiles in figure 3.10. For reference, the same number markers as in figure 3.10 are shown.

section 3.2), the data has not been drift-correct based on a comparison of up- and down scans. Instead, the data has been distorted to match the lateral unit cell dimensions based on the assumption that the drift velocity is small, as described in section 3.2.3. Due to an experimental error during the static deflection *vs* z_{p} profile acquisition, a spring constant of 40 N m^{-1} is assumed for the dolomite data set shown in figure 3.16 and 3.17. In this case, the deflection sensitivity has been obtained from thermal noise spectra. Moreover, the tip was not scanned in the slow scan direction during this measurement, the tip was most likely scanned by drift across the sample. Thereby, no drift correction based on comparison of up and down images was performed. Instead, by comparison with the previously presented dolomite data, the data was distorted to match the surface unit cell of dolomite. The magnesite data set shows data plotted against the z-piezo displacement z_{p} instead as the center position $z_{\mathrm{c}} = z_{\mathrm{p}} + q_{\mathrm{s}}$ since the additional noise contribution resulting from considering the static deflection makes it very difficult to recognize any contrast in the data.

All data sets exhibit similar features:

- Similar cation profiles are obtained for calcite and magnesite, while for dolomite a clear shift in the profiles above Ca and Mg sites is visible.
- The cap-averaged tip-sample damping constant $\langle \gamma_{\mathrm{ts}} \rangle_\cap$ shows an overall monotonic increase when approaching the tip to the sample without showing a layering as pronounced as in $-\langle k_{\mathrm{ts}} \rangle_\cap$.

Comparing the reproduction data with the data shown in the previous figures also shows that the quantitative values of $-\langle k_{\mathrm{ts}} \rangle_\cap$, $\langle \gamma_{\mathrm{ts}} \rangle_\cap$ and F_{even} vary to a large degree. A possible explanation for the observed variation in the quantitative values is the usage of different tips.

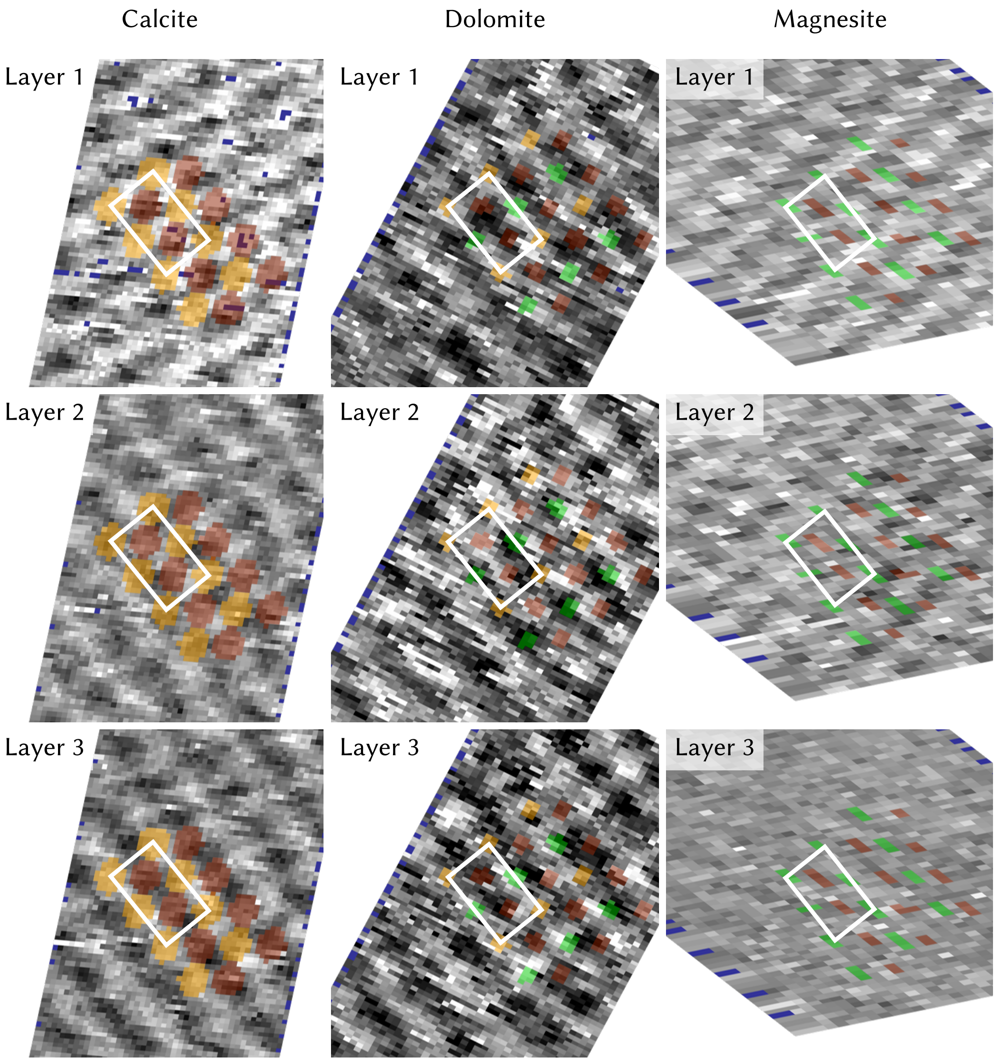

Figure 3.16: Reproduction data showing the lateral contrast in $-\langle k_{\mathrm{ts}}\rangle_{\cap}$ slices obtained from drift-corrected 3D datasets. The orientation of the slices is the same as in figure 3.7. For the dolomite measurement shown in the second column, the $[\bar{4}21]$ and $[42\bar{1}]$ directions (and, consequently, the [010] and $[0\bar{1}0]$ directions) can not be differentiated.

3.3.7 Conclusions

In conclusion, we have identified individual cations at the solid–liquid interface by the subtle difference in their 3D hydration structure. The capability of dynamic AFM to provide chemical identification of single atoms at the solid–water interface allows for

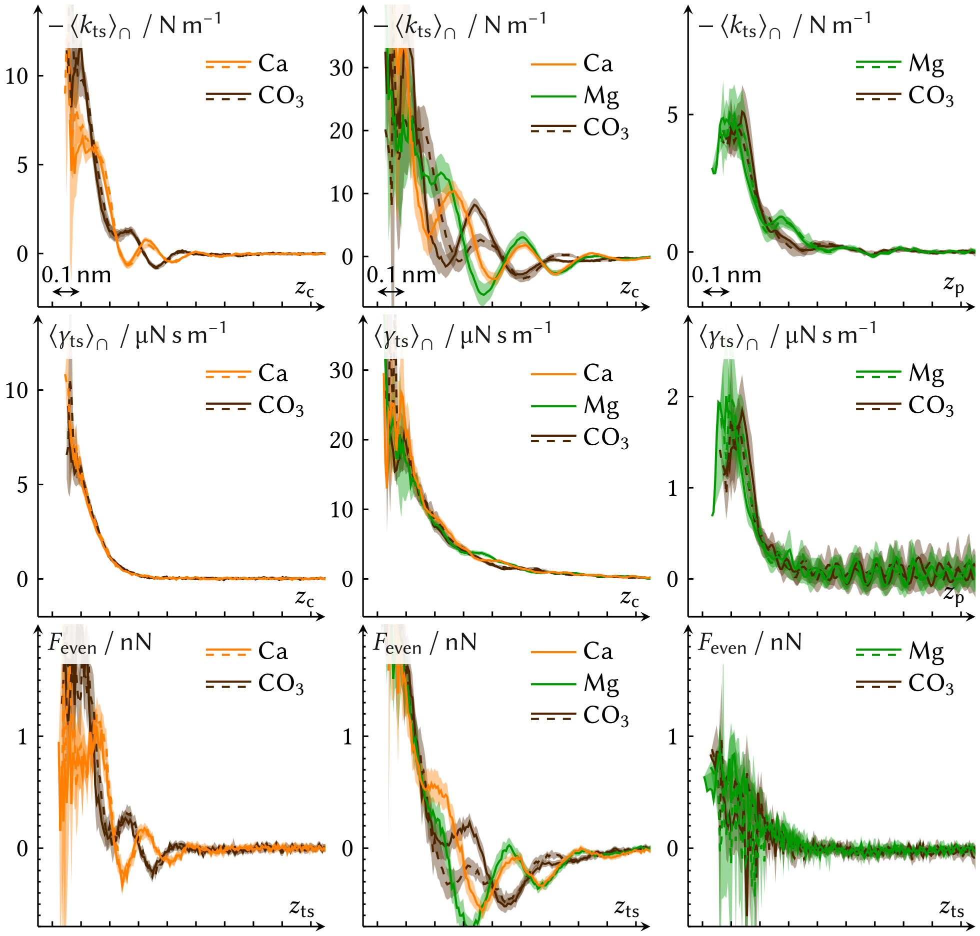

Figure 3.17: Reproduction data showing site-specific profiles of $-\langle k_{ts}\rangle_\cap$, $\langle \gamma_{ts}\rangle_\cap$ and F_{even} for calcite, dolomite and magnesite in pure water. The profiles are averages acquired at the sites indicated in figure 3.16, analogously to the previously shown data.

unraveling so far undiscovered insights into the reactivity of aqueous interfaces. As aqueous interfaces are ubiquitous both in nature and technology, we anticipate that this will have a significant impact on both research and technological development.

3.4 Hydration structure of point defects at the calcite–water interface

3.4.1 Introduction

Crystal surfaces are typically not perfectly pure and well-ordered but exhibit defects, *e.g.*, vacancies, adatoms and substitutions.[61,146,147] In many cases, the presence of defects can critically influence the reactivity of the surface, making them a crucial aspect to consider. In the specific case of the calcite (10.4) surface, defects have been suggested as the starting point for dissolution and growth processes:[148,149] Experimentally, Harstad and Stipp[149] have found that even trace amounts of impurities present in natural calcite samples (such as Mg, Fe, Sr, Mn) influence the dissolution of the calcite (10.4) surface. Moreover, in a recent theoretical study, the substitution of trace amounts of Ca ions with similar divalent ions on the calcite (10.4) surface has been found to significantly alter the affinity of water towards the surface.[150] As a consequence, trace amounts of defects can steer the competitive adsorption between water and organic molecules – a highly relevant interplay in the field of biomineralization.[150] For this reason, I here focus on the hydration structure at point defects at the calcite–water interface.

Theoretically, water at surface defects on calcite (10.4) has been studied using density functional theory (DFT).[151] The simulation system included the calcite surface with a carbonate vacancy, a calcium vacancy and a *single* water molecule. Compared to the flat (10.4) terrace, the binding energy of water at both defects has been found to increase (by 0.55 eV and 0.65 eV for the carbonate and calcium vacancy, respectively). Moreover, the water molecule was found to dissociate at carbonate vacancies, but not at calcium vacancies.

A recent molecular dynamics (MD) study by Reischl *et al.*[152] considers both bulk water instead of a single water molecule as well as the presence of a nanoscopic AFM tip. The authors have considered both calcium and carbonate vacancies as well as the substitution of a single Ca atom with a Mg atom. Two major results have been obtained:[152]

- At the calcium vacancy, the water structure has been found to be perturbed. At the carbonate vacancy the distortion of the water structure was significantly less pronounced compared to the calcium vacancy. In case of the magnesium substitution, water has been found to be shifted more closely to the surface (similar to the Mg ions on the dolomite and magnesite surfaces presented in section 3.3). Therefore, in all cases, defects influence the water structure in their vicinity. For the three different types of defects that have been considered, the lateral extent of the influence on the hydration structure has been reported to be within the order of 2 × 2 surface unit cells.
- Moreover, it was found that the defects are stable, meaning they did not change

> or move – even though the vacancy-induced local charge of $\pm 2e$ has not been compensated by other ions (which have not been included in the simulation). This behavior has been observed both in the presence and in the absence of the AFM tip. The stability reported by the authors refers to at least the time frame of the simulation (50 ns for the simulation without the tip and a total of 6.4 µs for the combined simulations with the tip).

Surface defects at the calcite–water interface have been observed before in 2D AFM experiments.[90,153] In these studies, the observation of defects has been used to characterize the AFM tip – only atomically sharp AFM tips image *single* atomic-scale features, such as point defects. However, the defect itself and its hydration structure have not been the focus of these studies. Here, I performed high-resolution 3D AFM experiments to analyze the hydration structure in the vicinity of point defects at the calcite–water interface.

Thereby, I answer the question "Can point defects in surfaces in solution be atomically resolved by atomic force microscopy?" raised by Reischl *et al.* in the title of their paper with "yes – even in 3D AFM data".

3.4.2 Experimental method

I performed the experiments described within this section in the group of T. Fukuma in Kanazawa (Japan) using a custom-built AFM.[14,154] Silicon cantilevers (AC55, Olympus) with a nominal spring constant of $85\,\mathrm{N\,m^{-1}}$ and an eigenfrequency of approximately 1.2 MHz in water were used. In most cases, the cantilevers have been coated by an additional layer of silicon (of approximately 15 nm thickness) by sputtering as described in reference 155. The excitation of the cantilever was performed with a photothermal excitation system.[156,157]

Amplitude and phase shift of the cantilever oscillation were detected by a commercial oscillation controller (OC4, Specs). The oscillation controller was operated in the frequency modulation (FM) mode, meaning that two feedback loops tried to keep amplitude and phase shift constant by adjusting the excitation force amplitude F_0 and the excitation frequency ν_{exc}. The quantities F_0 and ν_{exc} provided by the oscillation controller were fed into an AFM controller (ARC2, Asylum Research). The AFM controller performed data acquisition and adjusted the positioning of the scan piezo. The typical resolution of 3D datasets was $64 \cdot 64$ pixel laterally and 512 pixel vertically, with a data acquisition time in the order of 2 min.

Three-dimensional mapping was performed by employing a customized software for the AFM controller that has been developed in the group of T. Fukuma. Note that phase shift and static deflection have not been recorded due to a limited number of data acquisition channels. Therefore, I will not use the three AFM equations to calculate the three pieces of information about the tip-sample force ($\langle F_{\mathrm{even}}\rangle_{\cup}$, $\langle k_{\mathrm{ts}}\rangle_{\cap}$, $\langle \gamma_{\mathrm{ts}}\rangle_{\cap}$, equations 2.22–2.24 in section 2.1). Instead, I will show the excitation frequency ν_{exc}

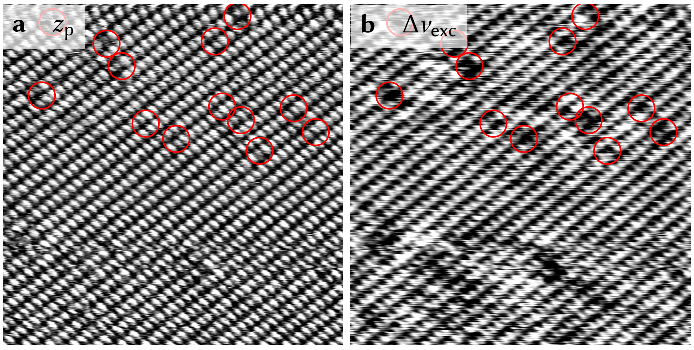

Figure 3.18: Atomically resolved image of the calcite (10.4) surface with defects. Panel a shows the z-piezo displacement (data range 10 pm) and panel b the corresponding excitation frequency shift (data range −3 kHz to 11.3 kHz). As a visual aid, the locations of the defects in the upper half of the image (either visible in panel a, b, or both) are marked by the red circles. Both images are trace-down images, the $[42\bar{1}]$ direction points to the lower right corner. A line-by-line median subtraction has been applied to the image in panel a.

as raw data. When assuming that the phase shift feedback loop keeps the phase shift at $-\pi/2$ and that the excitation frequency shift $\nu_{exc} - \nu_e$ is small compared to ν_e, the excitation frequency shift is proportional to the negative cap-averaged tip-sample force gradient (section 2.1.9). According to the solvent tip approximation and the discussion in section 3.3.4, maxima in the excitation frequency shift $\nu_{exc} - \nu_e$ are interpreted as maxima in the water density.

In all experiments shown in this section, I used calcite crystals with a brown coloration that have been available in the lab of T. Fukuma. Due to the limited amount of the samples, one of the calcite samples was cleaved once. After this initial cleaving, the sample was repeatedly immersed in pure water (MilliPore) prior to each measurement. This has not shown to yield any significant differences in both small-scale and large-scale AFM images compared to freshly cleaved calcite samples. The crystallographic directions of the crystal have been determined from the birefringence.[54] The liquid droplet of pure water, in which each measurement was performed, was exposed to air.

3.4.3 Experimental results

Figure 3.18 presents an atomically resolved image of the (10.4) surface of calcite. The z-piezo displacement z_p is shown in panel a, the corresponding excitation frequency shift $\nu_{exc} - \nu_e$ in panel b. At various positions in the image (marked in the upper half with red circles in both panels at equal positions), deviations from the periodic lattice of the calcite (10.4) surface can be observed. In previous AFM works, similar atomic-scale

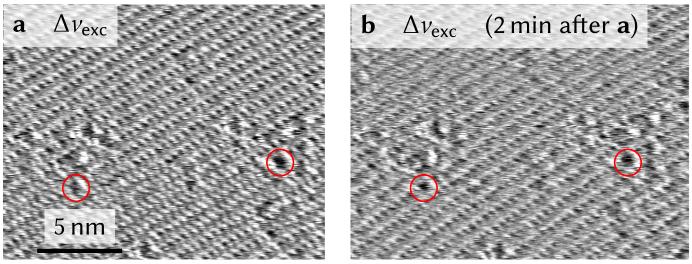

Figure 3.19: Two images repeatedly showing defects on atomically-resolved calcite (10.4) taken with a time difference of 2 min. Two red circles shown at equivalent positions in both images serve as a guide to the eye by showing the same defects, illustrating that the locations of the defects are fixed. The black-to-white color scale ranges from 1 kHz to 6 kHz. Both images are trace-down images, the $[42\bar{1}]$ direction points to the lower right corner.

inhomogeneities on the calcite surface have been assigned to point defects.[90,119,153] In the above shown image, the number density of surface unit cells exhibiting a defect is in the order of approximately 1 %. The measurements show that point defects on the surface of calcite (10.4) are present on the sample. They can be observed with the experimental setup, which also means that an atomically-sharp tip has been used in this experiment.

Stability of the observed defects on calcite

Next, I asses whether the defects are located at fixed positions or whether they are diffusing, appearing or disappearing in the course of time. To this end, consecutive 2D images at a fixed surface site were recorded. Care was taken to select a series of images that showed a stable (non-dissolving) terrace of the calcite surface without step edges. As AFM measurements are typically subject to (non-linear) drift as well as piezo creep effects, two consecutive images are not necessarily showing the exact same section of the sample surface. To align the images, the two-dimensional cross-correlation of two images was computed for each consecutive image pair. Consequently, each image was shifted by an offset given by the maximum of the cross-correlation function.

Two images from a series of 48 images (spanning a total time of approximately 25 min) are shown in figure 3.19. Several point defects are located at fixed positions within the time-scale of several minutes (*e.g.*, the two defects marked by the red circles at identical positions in both images). This observation is consistent with the MD simulations by Reischl *et al.*[152] which indicate that calcium and carbonate vacancies as well as magnesium substitutions on calcite (10.4) are stable, even in the presence of an AFM tip. Moreover, the presented data show that defects can be observed at least within a time that is similar compared to the time it takes to record a typical 3D dataset (which

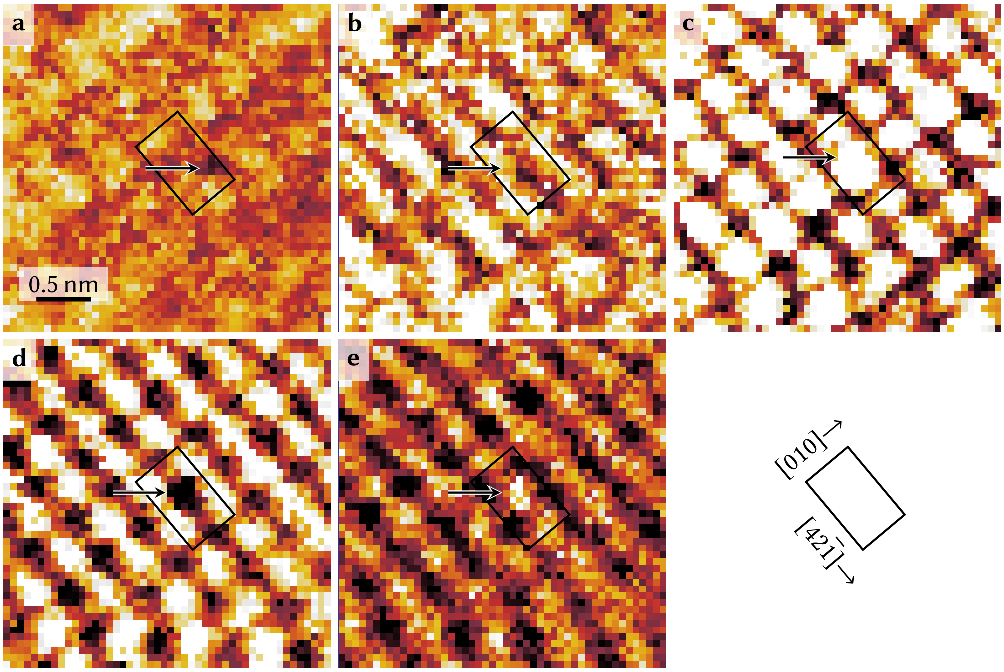

Figure 3.20: Lateral slices of a 3D excitation frequency shift dataset showing a defect (marked by an arrow). The color scale ranges from black (low) over orange to white (high).

is in the order of 2 min).

Hydration structure in the vicinity of defects

Lateral slices of an exemplary 3D excitation frequency dataset extracted at different z-piezo displacements are presented in figure 3.20 a–e. The surface unit cell of calcite (10.4) can be identified by the pattern of minima and maxima (indicated by the rectangular overlay). An inhomogeneity is visible in the center of the lateral slices (indicated by the arrow). The deviation from the otherwise periodic structure was repeatedly observed in at least 3 scan lines. In analogy to the 2D images, I interpret this inhomogeneity as a point defect. Interestingly, the defect does not cause a major disruption of the hydration structure. Only a slightly enhanced contrast (smaller or larger excitation frequency compared to equivalent sites) is visible at the defect site. In the presented data, the deviation from the otherwise periodic pattern is only visible within an area that measures one $CaCO_3$ unit, *i.e.* half a calcite (10.4) surface unit cell. Considering the different noise present in the experimental data and in the MD simulation data, the lateral extent fits remarkably well with the MD simulation results.[152]

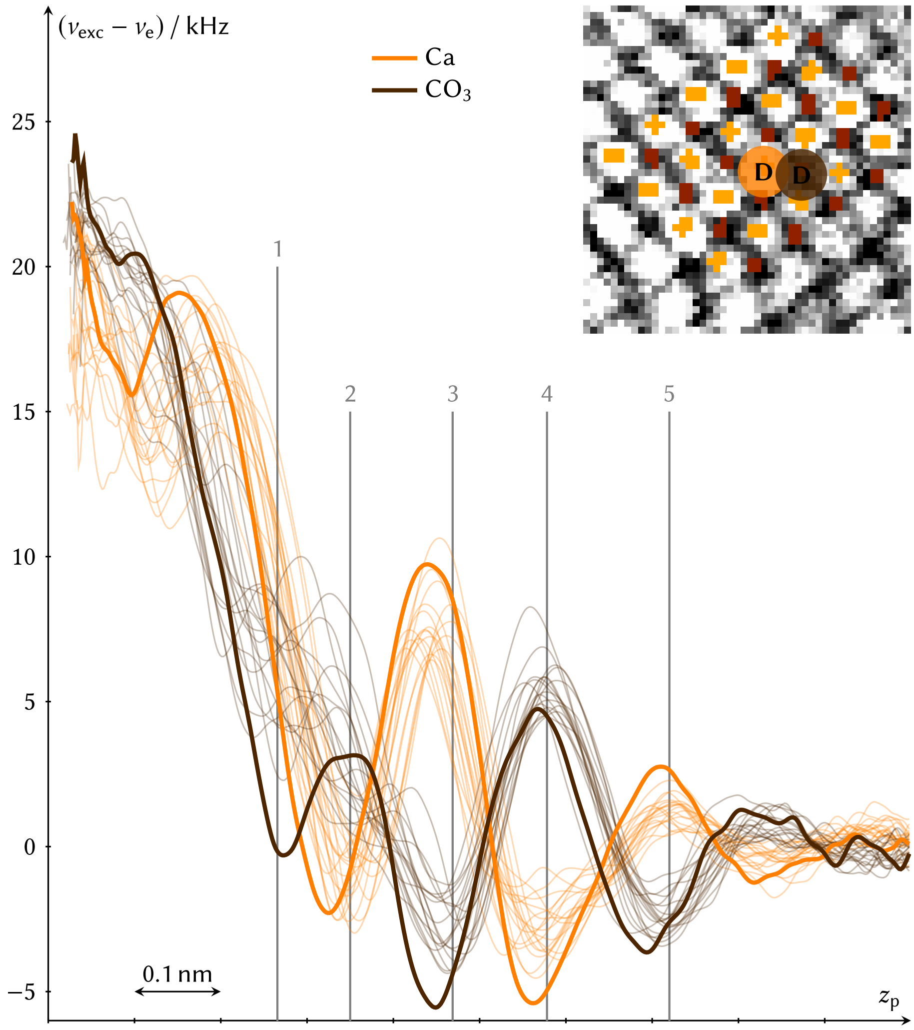

Figure 3.21: Excitation frequency shift profiles extracted above calcium ions (yellow) and carbonate groups (brown) at different sites. The extraction sites are shown in the inset. Profiles extracted at the defect site (marked with “D” in the inset) correspond to the dark curves, all other curves are opaque. The vertical lines (with numbers 1–5) indicate the tip-sample distance, at which the slices a–e presented in figure 3.20 have been extracted.

In figure 3.21, I compare profiles of the excitation frequency (as function of the z-piezo displacement) obtained above defect and non-defect sites. The procedure for extracting the profiles is similar to the procedure described in section 3.3.4: First, the standard deviation of all excitation frequency profiles within the volume is used to identify z-piezo displacements where the tip was scanned within a layer. Next, profiles were extracted at the position of local minima and maxima visible in lateral slices extracted within a layer. As detailed in section 3.3.4, the profiles with the minimum in the first layer (brown curve) corresponds to a carbonate site, the other set of curves (yellow) to Ca sites. The profiles shown in figure 3.21 are drawn using faint lines for the non-defect sites and with darkened lines at the defect site (indicated by the arrow in 3.20 a and b. The extraction sites are marked in the third layer (inset of figure 3.21) by the yellow and brown overlay, the defect sites are additionally marked with “D”. The curves extracted above the defect sites exhibit some minor, yet systematic, differences compared to the non-defect sites: The profile corresponding to the Ca defect site (yellow darkened line) consistently exhibits the largest local maxima and the smallest local minima in the fourth, third, and (with one exception) the second layer. This corresponds to the enhanced contrast visible at the defect site in figure 3.20. Moreover, in the first and second layer, the defect profile extracted above the Ca site is shifted closer to the surface compared to the other Ca profiles. The other defect profile (corresponding to a carbonate site) shows a local minimum in the first layer that is more pronounced compared to the non-defect profiles. The experimental data suggests that point defects indeed causes a minute, yet detectable change in the hydration structure above calcite.

3.4.4 Reproduction data

I present two additional data set obtained above different point defects. Lateral slices of the excitation frequency extracted at different z-piezo displacements are shown in figures 3.22 and 3.23. In the figures, the position of a point defect is marked by the arrow, the calcite unit cell by the black rectangle. In both cases, the lateral extent of the defect is again within the range of a single unit cell. Moreover, the checkerboard-like arrangement of water is only slightly perturbed, similar to the data set shown in figures 3.20 and 3.21.

3.4.5 Conclusion

In this section, I investigated the hydration structure above point defects at the calcite–water interface. High-resolution 3D AFM maps show that the hydration structure near point defects is perturbed – both laterally as well as vertically. The lateral extent of the perturbation in the hydration structure due to the point defects is in the order of a single unit cell. This is in good agreement with previous MD simulations. To the best of my knowledge, this is the first experimental observation of the hydration structure in the vicinity of point defects with high-resolution 3D AFM in liquids.

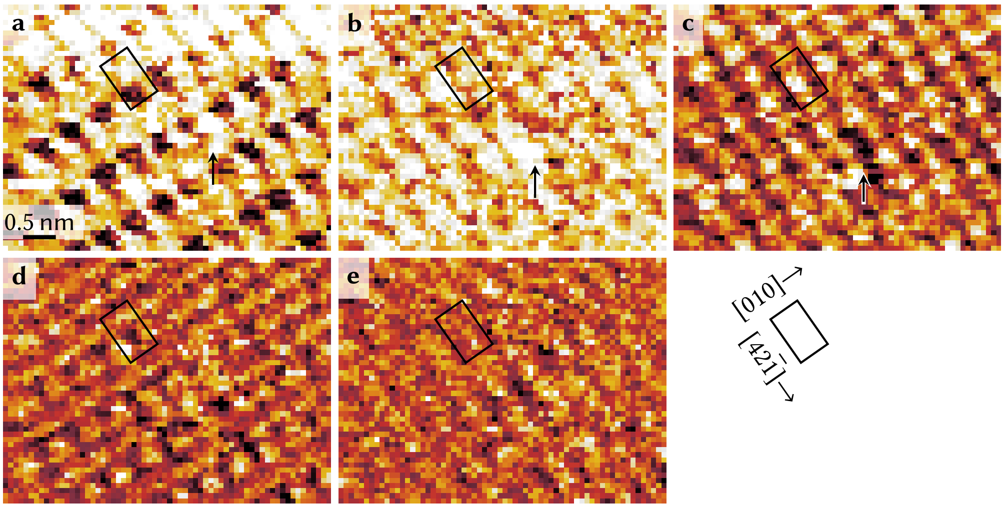

Figure 3.22: Another set of (lateral slices extracted from a 3D excitation frequency shift dataset showing a lateral inhomogeneity that is interpreted as a defect (marked by an arrow). The vertical distance between the consecutive lateral slices (from small z_p in panel a to large z_p in panel e) is in the order of 0.1 nm.

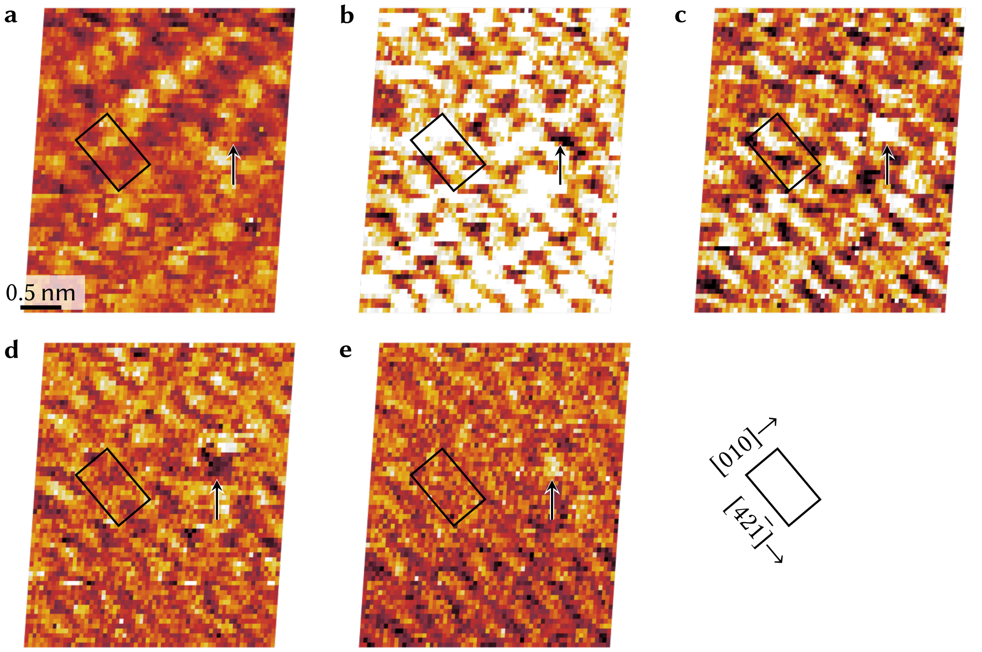

Figure 3.23: A third example of a set of lateral slices from a 3D excitation frequency shift dataset showing a defect. The vertical distance between the consecutive lateral slices (a–e) is in the order of 0.1 nm. The slices have been distorted so that the periodicity matches the calcite unit cell dimensions.

3.5 Influence of ions on the hydration structure of calcite

3.5.1 Introduction

A further step towards a more comprehensive understanding of the calcite–water interface is to study the effect of dissolved ions in the solution on the hydration structure. Additional dissolved ions in the solution (reflecting a change in ionic strength and pH) mimic many natural environments, *e.g.*, sea water. In previous studies, ions in the solution have been found to influence the dissolution and growth behavior of calcite.[158–160] In some of these studies, the influence of ions was in parts explained by their influence on the hydration structure of calcite.

Moreover, ions have a particularly interesting role in the context of imaging calcite with AFM in water. In the past, AFM images have been recorded in solutions that contain ions to "facilitate the imaging".[90] It has been furthermore reported that ions in the solution improve the atomic-scale imaging contrast.[48] According to the authors of reference 48, the addition of ions leads to an effective screening of charges. Consequently, electrostatic force contributions to the tip-sample force are reduced. A clear systematic demonstration of the relationship between added ions and the imaging contrast, however, is still lacking.

Only a few experimental studies focus on the influence of ions on the hydration structure of calcite. Ricci *et al.*[161] have studied the effect of monovalent ions, such as sodium, calcium, rubidium and chloride ions on the calcite–water interface using 2D AFM images. They observed atomic-scale "protrusions" that have been interpreted as single adsorbed ions on the surface. However, no 3D data has been presented by the authors, making it difficult to deduce the impact of the ions on the hydration structure.

The influence of Mg ions and a synthetic polypeptide on the calcite surface have been studied with vertical (xz) slices by Araki *et al.*[50] The authors analyzed the *number of observed hydration layers* and the overall tip-sample force magnitude. From the observed number of hydration layers they have concluded that Mg ions enhance the hydration. However, they have performed the experiments with different tips and different samples. Given the different levels of noise typically observed in different measurement sessions (*e.g.*, due to using different cantilevers and laser alignment), the number of observed layers might also be exposed to large statistical fluctuations. Moreover, the reproduction data presented in section 3.3 reveals that the overall magnitude of the observed forces can also significantly differ when using different tips, despite preparing the sample and solution in similar ways.

Therefore, I here explore four different experimental approaches for assessing the influence of ions on the hydration structure of calcite. I focus on the influence of hydronium and hydroxide ions (by varying the pH), since these ions are always present in aqueous solutions. Moreover, I consider different concentrations of Na and Cl ions, as these are relevant when considering, *e.g.*, sea water.

3.5.2 Experimental method and results

Vertical slices in solutions of different pH

In a first step, I investigate vertical slices of the negative cap-averaged tip-sample force gradient $-\langle k_{\mathrm{ts}}\rangle_{\cap}$ obtained above calcite in solutions of different pH. For this, the setup described in section 3.2 was used, according to the procedure described in section 3.3. The solutions with pH = 4.01 and pH = 9.92 were obtained by adding aqueous hydrochloric acid (HCl) and aqueous sodium hydroxide (NaOH) solutions, respectively. For the solution with pH = 8.20, no HCl and NaOH was added. Instead, the overall concentration of added electrolytes was set to $10^{-4}\,\mathrm{mol\,L^{-1}}$ by dissolving NaCl. Thereby, all solution are expected to exhibit a comparable ionic strength in the order of $10^{-4}\,\mathrm{mol\,L^{-1}}$. For the AFM measurements in the different solutions, different cantilevers (type TAP300 GB-G) and calcite samples have been used. Sample preparation and data acquisition have been performed by S. Klassen.

From a large collection of 2D (xz) slices, I selected a representative slice for each solution, which is shown in the first column of figure 3.24 (a–c). The slices are aligned approximately along the $[48\bar{1}]$ direction (figure 3.7). All data show the checkerboard-like arrangement of water at the calcite–water interface that has been discussed in the previous sections. While there are slight differences in the observed patterns, the overall vertical extent and contrast are very similar. Importantly, no clear systematic trend can be recognized as function of pH.

Vertical slices in buffer solutions

One could argue that the dissolution of calcite (which releases Ca and CO_3 species such as H_2CO_3, HCO_3^- and CO_2) influences the pH of the solution – particularly in the proximity to the surface. As described by Ricci *et al.*, aqueous solutions that contain calcite eventually exhibit a pH of approximately 8 due to the dissolution of calcite. A possible reason for the similarity of the reported data in figure 3.24 a–c could therefore be that the pH is similar in each case – at least in the interfacial volume at the surface.

Therefore, the experiments were repeated: Instead of using aqueous solutions with added HCl or NaOH, *buffer solutions* were used. Buffer solutions contain both acidic molecules and molecules of their conjugate base. Any hydronium ions resulting from, *e.g.*, the dissolution of calcite protonate the conjucated base of the buffer and, thereby, do not significantly alter the hydronium concentration of the solution. Similarly, additional hydroxide ions deprotonate the buffer acid. Consequently, the pH of the solution is expected to be nearly constant, allowing a more systematic study of the effect of the hydronium and hydroxide ion concentration. In the experiments presented here, buffer solutions with pH = 4.00 (Carl Roth, P712.3, containing citric acid, sodium hydroxide and sodium chloride), pH = 6.865 (Carl Roth, 4284.1, containing potassium di-hydrogene phosphate and di-sodium hydrogene phosphate) and with pH = 10.00

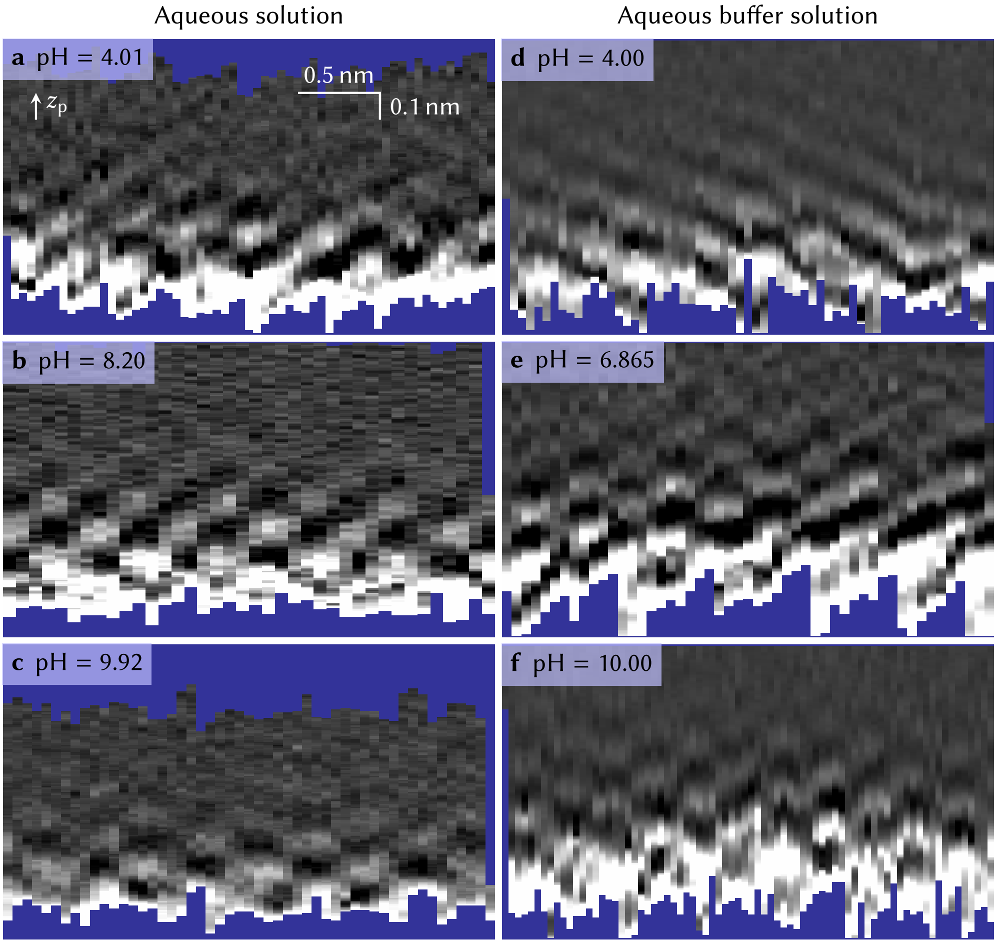

Figure 3.24: Vertical slices of the negative cap-averaged tip-sample force gradient $-\langle k_{\mathrm{ts}} \rangle_{\cap}$ as function of the z-piezo displacement. The slices are aligned approximately along the $[48\bar{1}]$ direction. Data shown in the first column was obtained in aqueous solutions at different pH, data shown on the right was obtained in buffer solutions. The color scale is adjusted in each case to maximize the contrast.

(Carl Roth, P716.2, containing boric acid, sodium hydroxide, potassium chloride) were used. Experimental slices of the negative cap-averaged tip-sample force gradient at the calcite–water interface obtained in buffer solutions are shown in the second column of figure 3.24 (d–f). In all cases the checkerboard-like arrangement of water is observed. Again, no clear systematic trend as function of pH is apparent from the presented data.

3.5.3 Solution exchange experiment: Influence of pH

So far, different cantilevers and samples have been used in different aqueous solutions. A possible reason for not observing any systematic trend when changing the pH could result from using different tips. Moreover, only 2D (xz) slices have been presented.

For a more comprehensive analysis, 3D datasets in different aqueous solutions (with different pH) were recorded on the calcite (10.4) surface. I used a flow-through setup that allows to exchange the measurement solution while using the same sample and cantilever. Thereby, changes to the cantilever, the cantilever tip and the sample are minimized, which facilitates a comparison. The exchanged liquid volume was 0.4 mL, the exchange was performed using a push-pull pump system (KD Scientific). I performed the measurements shown in figures 3.25 and 3.26 in Kanazawa (Japan) with the setup and cantilevers described in section 3.4.2. In contrast to section 3.4.2, optically clear calcite crystals with a significantly lower surface defect density (as observed with AFM) were used for the data shown in this section. As detailed in section 3.4.2, I show the excitation frequency shift $\nu_{\mathrm{exc}} - \nu_{\mathrm{e}}$ for data obtained with this setup. The pH of the solution was adjusted by adding aqueous HCl solution, no buffer was used.

In all cases, the 3D data exhibited the characteristic checkerboard pattern that has been previously observed for calcite (10.4) in pure water.[48–51,53] To systematically asses the influence of dissolved ions on the hydration structure, two aspects of the 3D datasets obtained for different concentrations have been compared (figure 3.25): (1) The averaged excitation frequency shift profiles as a measure for the average negative cap-averaged tip-sample force gradient, (2) the standard deviation of the excitation frequency shift profiles as a measure for the lateral contrast. The first row of figure 3.25 (a, b) shows data obtained within the same tip and sample during a solution exchange experiment. For the data presented in the second row (c, d), only the cantilever was exchanged. The sample and the solutions are the same as the ones used while acquiring the data presented in the first row.

The averaged profiles shown in figure 3.25 a exhibit an increase of the excitation frequency shift for the approaching tip. The overall slope of the profile is rather similar and again no clear systematic trend is visible from the data. In the profiles in figure 3.25 b, an increase in the standard deviation $s_{\nu_{\mathrm{exc}}}$ is observed when approaching the tip towards the sample–corresponding to increased lateral contrast in the proximity to the sample. Shoulders and inflection points in the profiles correspond to hydration layers (section 3.3.4). Again, the profiles are rather similar and do not show a clear dependency on the pH. Similar results are obtained for the same sample and the same set of solutions in a solution experiment carried out with a different cantilever, *i.e.*, a different tip. Again, both the averaged frequency shift profiles (figure 3.25 c) and the corresponding standard deviations (figure 3.25 d) are strikingly similar. Interestingly, both the slope of the averaged profiles (c) and the order of magnitude of the standard deviation (d) does significantly differ from the measurement shown in

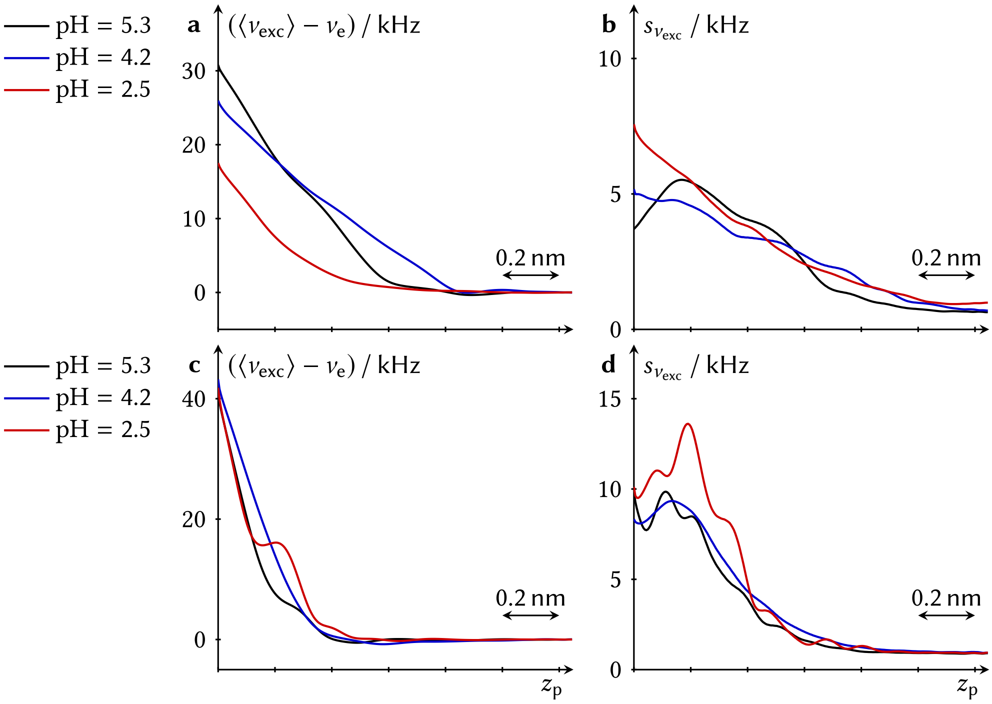

Figure 3.25: Averaged excitation frequency shift profiles (a, c) and the corresponding standard deviation (b, d) for varying pH in aqueous solution at the calcite–water interface. Data shown within each row was recorded with the same cantilever and the same sample in a solution exchange experiment. The order of the solution exchange is reflected in the figure legend, starting with the first solution on top.

figure 3.25 a and b, respectively. This demonstrates that the tip-sample interactions indeed strongly depends on the tip – which fits well to the reproduction data discussed in section 3.3.6.

3.5.4 Solution exchange experiment: Influence of sodium chloride concentration

A similar solution exchange experiment was performed (again with the setup described in section 3.4.2) to assess the influence of the concentration of sodium and chloride ions on the hydration structure of calcite. The solutions were prepared by dissolving solid NaCl in pure water (MilliPore). Using the flow-through system, I exchanged the solutions starting from pure water over concentrations of 0.01 $\mathrm{mol\,L^{-1}}$ to 1 $\mathrm{mol\,L^{-1}}$ and back within one measurement series.[1] Figure 3.26 shows the resulting

---

[1] For similarly large sodium chloride concentrations of 4 $\mathrm{mol\,L^{-1}}$, Martin-Jimenez*et al.*[64] observed the formation of a large interfacial structure extending several nanometer into the liquid at the mica–

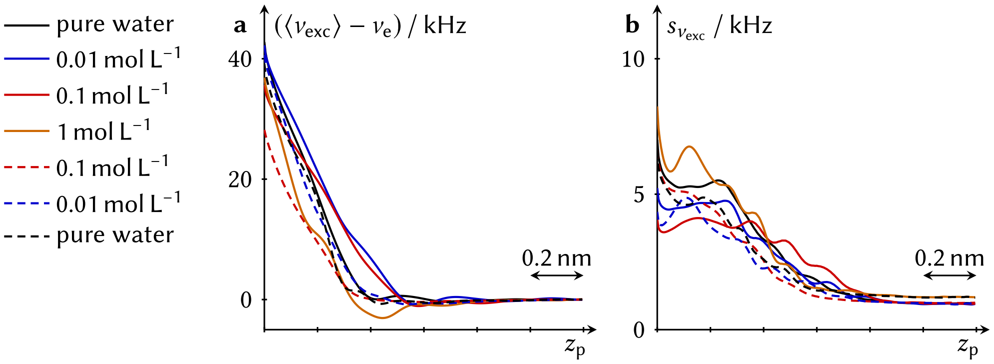

Figure 3.26: Averaged excitation frequency shift profiles (a) and the corresponding standard deviation (b) for varying concentration of sodium chloride in aqueous solution. The data was recorded with the same cantilever and the same sample in a solution exchange experiment. The solution exchange was performed according to the order of the figure legend, starting with the first solution (pure water) on top.

average excitation frequency shift curves (a) and their corresponding standard deviation (b). Again, this measurement does not show clear systematic differences in the hydration structure when varying the concentration of sodium chloride.

3.5.5 Conclusion

In this section, I described several experiments that aimed towards assessing the influence of ions (hydronium, hydroxide, sodium and chloride ions) on the hydration structure of calcite. The checkerboard-like arrangement of water on calcite was observed, regardless of the composition of the solution. This includes a pH range from 4 to 10 and concentrations of sodium chloride of up to 1 mol L^{-1}. The lateral contrast obtained from 3D data acquired at the calcite–water interface did not increase in the presence of sodium and chloride ions. Moreover, none of the data show a clear systematic trend as function of the respective ion concentration. This allows to conclude that possible changes of the hydration structure due to a change of pH and ionic strength are smaller compared to variations of the measured hydration structure due to tip changes or other statistical variations in the course of the experiment. The results also demonstrate the robustness of observing the checkerboard-like water arrangement at the calcite–water interface. This points toward the fact that the depiction of the calcite–water interface based on the data presented in the previous sections (obtained

---

water interface. In some measurements, I also have observed similar long-range structures. However, I found that the observation is unsystematic – even in solutions of pure water, I was able to observe such structures, both at the calcite–water, magnesite–water and calcite–ethanol interfaces. Due to their unsystematic nature, these experiments are not discussed here.

in pure water) remains valid in more complex (*e.g.*, natural) environments of different pH and ionic strength.

3.6 Beyond water: The calcite–ethanol interface

3.6.1 Introduction

In nature, calcite is often found in the presence of organic molecules. The interaction between calcite and these molecules is of far-reaching importance, for example in the field of biomineralization:[9] Specific molecules have been identified to influence the dissolution and growth behavior of calcite. The molecules can cause changes in surface morphologies[95,162] and even the formation of complex mineral compounds.[9,163] It is largely unclear, how these interactions take place.[11]

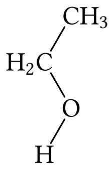

As a step towards understanding the interaction between calcite and organic molecules, I here investigate the interface between calcite (10.4) and ethanol. A single ethanol molecule (shown on the right) exhibits both a hydroxyl group and a hydrocarbon chain, which are common building blocks of molecules. Therefore, ethanol acts as a model molecule for more complex organic compounds.

Theoretically, the calcite–ethanol interface has been investigated previously by using density functional theory (DFT)[164,165] and molecular dynamics (MD) simulations,[166–169] which are summarized in the following: It has been found that ethanol molecules strongly bind towards calcite (10.4) terraces – even stronger than water.[164,166,168,169] Ethanol molecules bind towards calcite with their hydroxyl group: The oxygen of the hydroxyl group binds towards a Ca ion, while the hydrogen of the hydroxyl group binds towards a carbonate group (this is similar to the bonding configuration of an isolated ethanol molecule on calcite obtained with DFT calculations).[165] Consequently, the hydrocarbon chains of the ethanol molecules point upwards, away from the surface. This results in one ethanol molecule per $CaCO_3$ unit at the calcite (10.4) surface. This ordered first layer of ethanol molecules above the calcite surface is followed by a region of low ethanol density, which has been referred to as *gap*.[167,169] Beyond the gap, ethanol again arranges in several horizontal layers. In contrast to the first layer, however, both the lateral order and the orientational order of the ethanol molecules in the upper layers is significantly less pronounced. The vertical distance between the layers is in the order of approximately 0.5 nm.

Isolated aspects of the above mentioned theoretical studies have been confirmed experimentally: With AFM, the calcite (10.4) surface has been *laterally* resolved in ethanol at the atomic scale.[170–172] The observed periodicity matched the surface unit cell dimensions. However, from AFM images it is not straightforward to determine at which vertical distance the tip was scanned above the surface. Therefore, it remains unclear whether the observed lateral structure corresponds to the first ordered layer of ethanol on calcite. The *vertical* structure of ethanol on calcite has been investigated in a combined X-ray reflectivity and MD study.[167] As a result, ethanol was found to form layers above the calcite surface. Due to the lack of lateral resolution of X-ray reflectivity measurements, however, no experimental information on the lateral order within the first layer has been obtained form this measurement.

To provide a more comprehensive experimental study of the calcite–ethanol interface, I here report on high-resolution 3D AFM data obtained at the calcite (10.4) surface in ethanol to asses *both* the lateral and the vertical order at the interface. This approach is similar to the work in references 171 and 172.

3.6.2 Experimental method

All experiments shown in this section were performed with the setup described in section 3.2. S. Klassen assisted with the sample preparation and data acquisition. Apart from the description below, measurements and calibrations were performed according to the same protocol as in section 3.3. After cleaving calcite in air, ethanol (Sigma Aldrich, article number 32205, purity ≥ 99.8 %) was injected in the liquid cell. Since the ethanol was exposed to air during the measurement, it sometimes evaporated, making it necessary to repeatedly inject ethanol during a measurement session. Cantilever of type TAP300 GB-G were used. The acquisition time for each vertical slice (trace and retrace) of a 3D map was 10 s and the frequency of the (approach and retract) z-modulation was 10 Hz, corresponding to 50 approach and 50 retract curves per vertical slice. During the acquisition of the reproduction dataset shown at the end of this section (figure 3.29), a large voltage drift (possibly caused by the evaporation of ethanol) in the low-pass filtered signal from the photo diode prohibits to obtain the static deflection. Therefore, in this figure the data is plotted against the z-piezo displacement z_p.

3.6.3 Experimental results

A vertical slice of the negative cap-averaged tip-sample force gradient ($-\langle k_\mathrm{ts} \rangle_\cap$) obtained in ethanol on calcite (10.4) is shown in figure 3.27 a. The slice measures 3 nm (laterally) by 3.5 nm (vertically). The average over all data shown in the slice is shown as a profile in figure 3.27 b.

As for the calcite–water case discussed in the previous sections, the negative tip-sample force gradient shows local minima and maxima. Close to the surface (at the bottom), laterally alternating local maxima with a periodicity of approximately 0.3 nm can be observed. As the vertical slice is recorded approximately along the $[48\bar{1}]$ direction, this distance roughly fits to the Ca-Ca repeat distance of $\sqrt{a^2 + (b/2)^2} \approx 0.6$ nm, when using the surface unit cell dimensions[112] $a = 0.5$ nm and $b = 0.81$ nm (a schematic drawing of the surface unit cell is shown in figure 3.7 a on page 61).[2] Therefore, it

---

[2] The discrepancy between the observed repeat distance (0.3 nm) and the expected repeat distance (0.6 nm) might be the result of lateral drift. The lateral drift cannot be quantified from the data, since

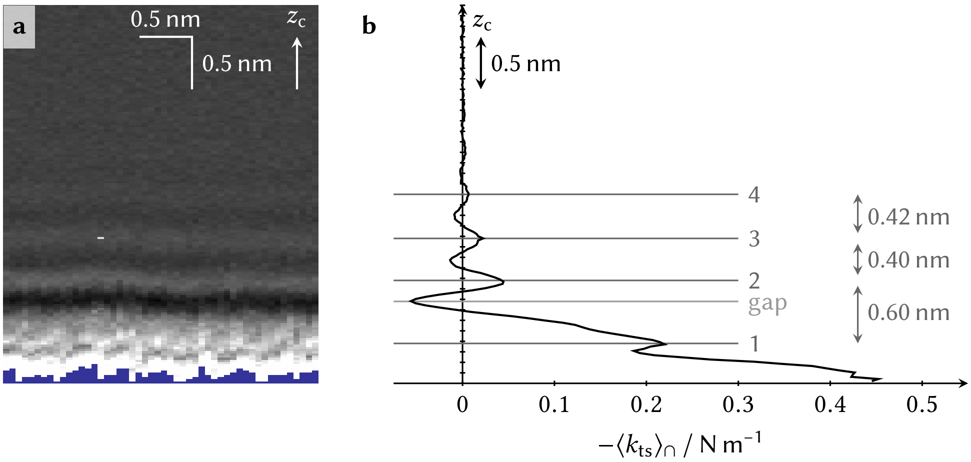

Figure 3.27: Vertical slice of the negative cap-averaged tip-sample force gradient (a) at the calcite–ethanol interface. Panel b shows the average of all profiles shown in panel a. In both cases, $-\langle k_{ts}\rangle_\cap$ is shown as function of the center position of the tip z_c. The black-to-white color scale in a ranges from −0.1 N m^{-1} to 0.3 N m^{-1}.

appears reasonable to assign this lateral structure to the ordered first layer of ethanol molecules. This is in accordance with the MD simulations,[166–169] which have shown that ethanol arranges in a ordered first layer above calcite, where one ethanol molecule binds towards one $CaCO_3$ unit.

The experimental data shows further layers above the first layer (indicated by the markers in figure 3.27 b). In analogy to the discussion in section 3.3.4, the layers are identified as maxima in $-\langle k_{ts}\rangle_\cap$ according to the numbers indicated in figure 3.27 b. In this assignment, the minimum observed between the first and second layer corresponds to the gap. Importantly, no lateral structure is visible in the upper layers, further supporting the previous assignment of the first layer. Observing no order in the upper layers fits well to the MD simulations from previous theoretical studies, which do not indicate significant lateral order in the layers above the first layer.[166–169] Moreover, the layer-to-layer distances indicated in figure 3.27 b are in the order of approximately 0.5 nm, which again agrees well with the MD simulations.

Figure 3.28 shows additionally the cap-averaged tip-sample damping constant $\langle \gamma_{ts}\rangle_\cap$ as function of the center position z_c of the tip. The data corresponds to the same slice as shown in figure 3.27 and is again shown as a vertical slice (a) and as an average profile (b). To facilitate the comparison, the numbered markers from figure 3.27 b are again shown. Similar to what has been observed for the carbonate minerals in water (section 3.3, figure 3.15 on page 71), the tip-sample damping constant does not show

---

only a few vertical slices have been acquired.

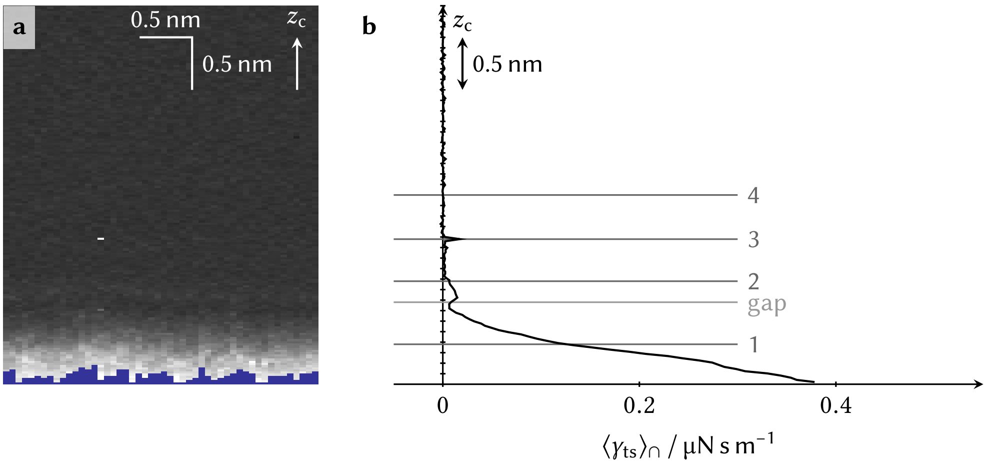

Figure 3.28: Vertical slices (a) and averaged profiles (b) showing $\langle \gamma_{ts} \rangle_\cap$ at the calcite–ethanol interface. The slice correspond to the same dataset as shown in 3.27. The black-to-white color scale ranges from −0.1 N s m^{-1} to 0.4 N s m^{-1}.

a clear layering as pronounced as in $-\langle k_{ts} \rangle_\cap$.

3.6.4 Reproduction data

Experimentally, the observation of lateral order in the first layer of ethanol has been difficult compared to achieving lateral resolution on calcite in water. It appears likely that this is a consequence of ethanol binding more strongly towards calcite (compared to water).[165,166,168,170] To show that the lateral order can be reproducibly observed, another measurement of ethanol in water (performed with a different tip and a different calcite sample) is shown in figures 3.29 a–d. Overall, the reproduction data sets show very similar features:

- Lateral order is obtained in one layer close to the surface. At smaller z_p, no clear lateral order is visible.
- Above the first layer, additional layers can be recognized. These upper layers do not exhibit a lateral structure.
- The layer-to-layer distances are again in the order of approximately 0.5 nm.

Interestingly, the reproduction data shows a faint lateral contrast in $\langle \gamma_{ts} \rangle_\cap$ within the distance range of the first layer (figure 3.29). Following the discussion in figure 3.3.5, it might be speculated that the nanoscopic tip apex might have been larger compared to the tip with which the data presented in figures 3.27 and 3.28 was obtained.

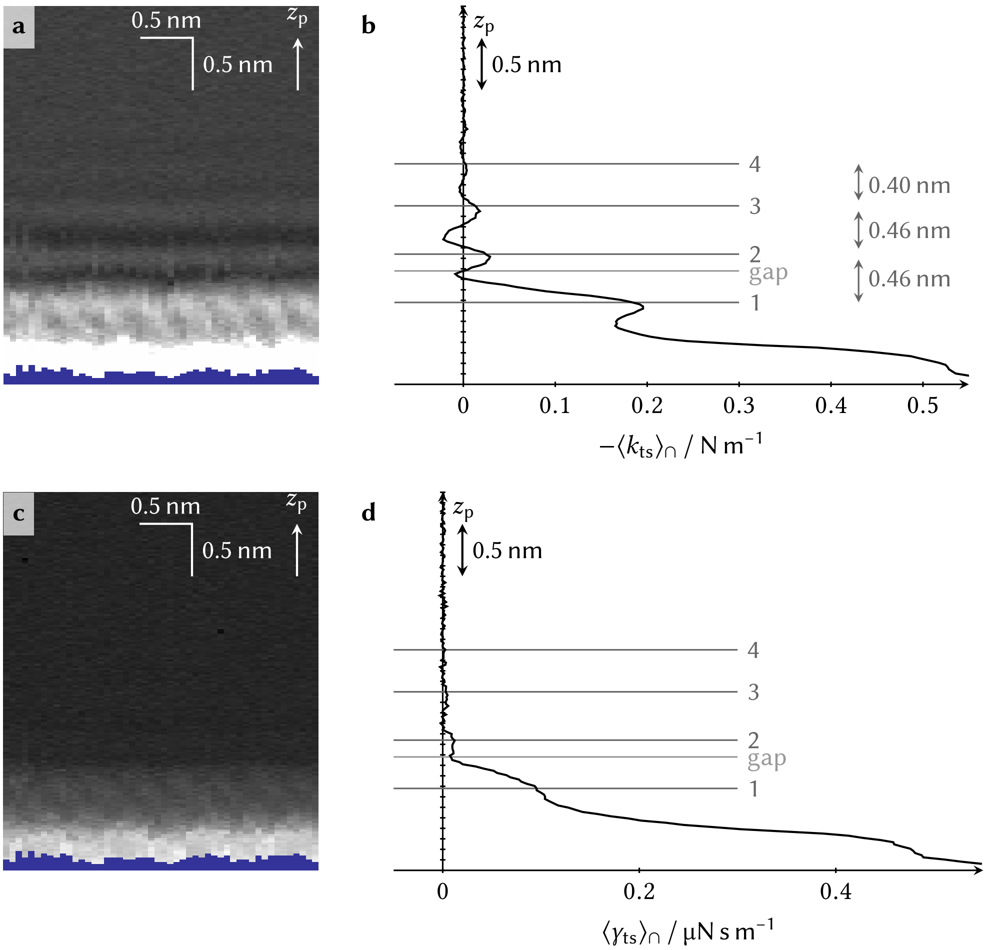

Figure 3.29: Vertical slice of the negative cap-averaged tip-sample force gradient (a) and the cap-averaged tip-sample damping constant (b) above the calcite surface obtained in ethanol. In contrast to figures 3.27 and 3.28, both data are shown as function of the z-piezo displacement z_p. The black-to-white color scale ranges from $-0.1\,\mathrm{N\,m^{-1}}$ to $0.3\,\mathrm{N\,m^{-1}}$ (a) and from $-0.1\,\mathrm{N\,s\,m^{-1}}$ to $0.6\,\mathrm{N\,s\,m^{-1}}$ (c).

3.6.5 Conclusion

In this section, the solvation structure of ethanol above the calcite (10.4) surface was investigated. High-resolution AFM data revealed a layered structure above the calcite surface. In the first layer, a lateral structure is visible in the data. In contrast, the layers above the first layer do not show lateral contrast. Therefore, the experimental data indicate that ethanol molecules form an ordered layer directly above the calcite surface. In the layers above the first layer, the order of the molecules is not as pronounced.

These findings fit remarkably well to previously reported MD simulations. The measurements furthermore highlight the advantage of 3D AFM, as *both* the lateral and the vertical structure at the calcite–ethanol interface can be analyzed to provide a more comprehensive understanding.

4 Quantitative KPFM

4.1 Derivation of the KPFM signal

Section 4.1 was written both by P. Rahe and H. Söngen and has been submitted in similar form as a chapter to the book "Kelvin Probe Force Microscopy – From Single Charge Detection to Device Characterization", edited by S. Sadewasser and T. Glatzel. Most of the section is reproduced verbatim, changes were made to make the section consistent with the other sections in this thesis. As a major change, I shortened and modified section 4.1.2.

We analyze Kelvin probe force microscopy (KPFM) for tip-sample systems that contain static charges by presenting a rigorous derivation for the respective KPFM signal in all common KPFM modes, namely amplitude modulation, frequency modulation, and heterodyne detection in the static, open-loop and closed-loop variant. The electrostatic model employed in the derivation is based on a general electrostatic analysis of an arbitrary tip-sample geometry formed by two metals, and which can include a static charge distribution and dielectric material in-between. The effect of the electrostatic force on the oscillating tip is calculated from this model within the harmonic approximation, and the observables for each of the above KPFM modes are derived from the tip oscillation signal.

Our calculation reveals that the KPFM signal can for all modes be written as a weighted sum over all charges, whereby each charge is multiplied with a position-dependent weight function depending on the tip-sample geometry, the KPFM mode, and the oscillation amplitude. Interestingly, as the weight function does not depend on the charges itself, the contribution of the void tip-sample system and the charge distribution can be well-separated in the KPFM signal. The weight function for charges allows for a detailed understanding of the KPFM contrast formation, and enables to trace the dependence of the KPFM signal on different parameters such as the tip-sample geometry and the oscillation amplitude.

4.1.1 Introduction

There is now a large body of experimental work available showing variations in the Kelvin probe force microscopy (KPFM) signal on a variety of samples, including contrast on adsorbed molecular systems,[173–180] on metallic nanoclusters,[177,181] on charged species[182–185] and on surfaces with atomic-scale resolution.[186–189] Although

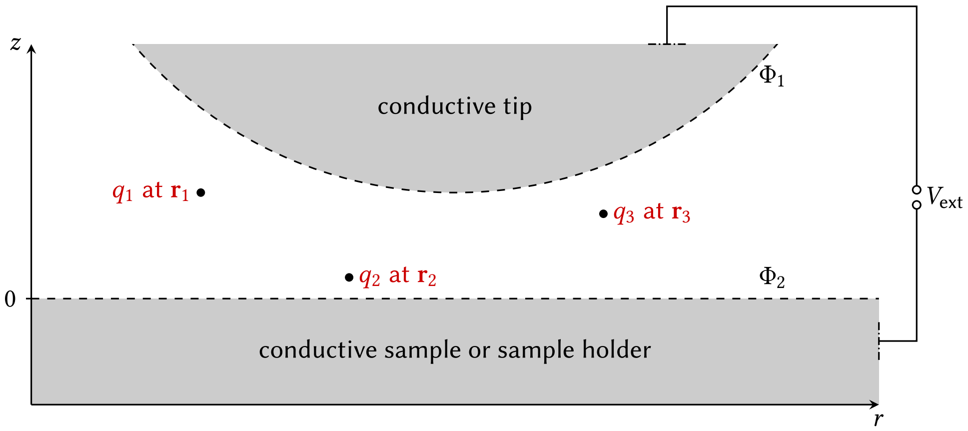

Figure 4.1: Setup of a tip-sample system including a conductive tip and a conductive sample or conductive sample holder between which an external voltage V_ext is applied. Additionally, we have included $N = 3$ exemplary point charges located in-between the two conductors. A dielectric sample and a dielectric medium would be considered by a different local dielectric permittivity in specific parts of the space between the two conductors.

KPFM has developed into an invaluable tool to investigate electric properties at the nanoscale, the general interpretation of the KPFM signal V_KPFM is still controversially discussed. For example, attempts to explain the KPFM signal of molecule-on-insulator systems following the concepts developed for metal surfaces have been made.[173,180,190] Furthermore, a number of explanations have been put forward that relate the KPFM signal V_KPFM to dipole and charge densities,[182,184,185] the electrostatic surface potential,[191] and the normal component of the electric field.[192]

Besides the complexity of the KPFM signal interpretation due to the diverse range of the investigated samples, there are additionally a number of experimental KPFM modes available, namely the amplitude modulation (AM), frequency modulation (FM) and heterodyne mode used in static, open-loop or closed-loop configuration.[193,194] Each technique is optimized for usage in different environments and for different samples, but all techniques result in a voltage signal, the KPFM signal V_KPFM.

In this section, we will investigate the central question how the KPFM signal is related to the physical sample properties, namely the contact potential difference and the charge distribution within the tip-sample system, by a rigorous derivation for the formulas describing the KPFM signal V_KPFM for the different KPFM modes.

The system under consideration is depicted in figure 4.1. It is formed by a two-electrode setup with the upper electrode representing the tip and the lower representing the sample side, which is either the metallic sample, or a metallic sample back contact in case of dielectric material in the gap. Dielectric material is accounted for by assigning a local dielectric permittivity to the respective region between the two metals. Moreover, we include a static charge distribution inside the tip-sample system formed by the two metals to model the presence of atomic or molecular species. This layout represents a common case of atomic or molecular species adsorbed and assembled on surfaces of insulating or conducting materials,[175,195,196] as well as for species on insulating thick films.[183,184] The derivation that is presented herein follows our recent work,[197,198] and also reflects similar evaluations for specific tip-sample systems,[199,200] or for short-range electrostatic forces.[201]

The derivation starts in section 4.1.2 with a general electrostatic description based on a model presented by Kantorovich *et al.*[202] This model allows to calculate the electrostatic force on the probing tip for an arbitrary geometry. After a description of experimental measurement strategies in section 4.1.3, we can analytically calculate in section 4.1.4 the resulting KPFM signal for the different experimental KPFM modes.

The central result of this section is the introduction of the *KPFM weight function for charges*, W_{KPFM}, in section 4.1.5, which allows to write the KPFM signal in a straightforward way as a sum over the weighted charges. Specifically, each charge q_i of a total of N charges is multiplied by the weight function W_{KPFM} evaluated at the position $\mathbf{r}_i$ of the respective charge,

$$V_{\mathrm{KPFM}} = V_{\mathrm{CPD}} + \sum_{i=1}^{N} q_i W_{\mathrm{KPFM}}(\mathbf{r}_i), \tag{4.1}$$

where V_{CPD} is the contact potential difference of the two metals. The weight function W_{KPFM} is an implicit function of the tip-sample geometry, which includes the tip position, as well as of the oscillation amplitude. Furthermore, the weight function depends on the KPFM mode used in the experiment, namely on whether the AM or FM detection is used. The KPFM signal V_{KPFM} can therefore be understood as a convolution of the charge distribution with the weight function.[197,198]

4.1.2 Electrostatic description

The starting point to understand the physical origin of the KPFM signal for all KPFM modes and diverse sample systems is to calculate the tip-sample force arising due to the electrostatic interaction. Here, we first review the *total electrostatic energy* U_{es} for the tip-sample system including external sources, *i.e.*, batteries or power supplies, that fix the electric potentials on the conductors. From this total electrostatic energy we calculate the tip-sample force. The KPFM signal then follows from evaluating specific observables for the different KPFM modes with respect to the externally applied voltage.

The electrostatic calculation fundamental to our KPFM model has initially been performed by Kantorovich *et al.*[202] They have analyzed a system containing an arbitrary number of finite metallic conductors m at fixed potentials $\{\Phi_m\}$, an arbitrary number of point charges $\{q_i\}$ located at positions $\{\mathbf{r}_i\}$ outside of the conductors, and external batteries keeping the potentials $\{\Phi_m\}$ on the metals constant upon moving any metal within the system. Consequently, the total energy consists of the energy stored in the electrostatic field as well as the energy contribution due to the external batteries.

Here, we adapt the original result from Kantorovich *et al.*[202] to the case of a KPFM tip-sample system by reducing their general case to two metals and N point charges (figure 4.1). In the KPFM setup, the upper metal (1) represents the metallic tip and the lower metal (2) represents the sample side, defined by the metallic sample or a metallic sample holder in case of dielectric material in the tip-sample gap. As result for the electrostatic energy of the system, Kantorovich *et al.* obtained the sum of four terms:[202]

$$U_{\mathrm{es}} = U_{\mathrm{C}} + U_{\text{q-C}} + U_{\text{q-q}} + U_{\mathrm{im}}. \tag{4.2}$$

The first term describes the negative potential energy of the *void* (*i.e.*, charge-free) tip-sample system:

$$U_{\mathrm{C}} = -\frac{1}{2} C_{\mathrm{void}} V^2. \tag{4.3}$$

In the above equation, C_{void} is the capacitance of the *void* tip-sample system. Without loss of generality,[202] we can set the potential difference $V = \Phi_1 - \Phi_2$ to $V_{\mathrm{ext}} - V_{\mathrm{CPD}}$ with an externally applied voltage V_{ext} and the contact potential difference V_{CPD} between the two metals. By introducing a *constant* contact potential difference, we assume that each metal surface is homogeneous with respect to their work function. The second term describing the interaction between the point charges and the metal plates (excluding any image charges) is given by

$$U_{\text{q-C}} = \sum_{i=1}^{N} q_i \Phi_{\mathrm{void}}(\mathbf{r}_i) = \sum_{i=1}^{N} q_i \hat{\Phi}_{\mathrm{void}}(\mathbf{r}_i) V. \tag{4.4}$$

Here, Φ_{void} is the electric potential of the *void* tip-sample system. Since in the case described here only two metals (tip and sample side) are present, the electric potential Φ_{void} of the void capacitor directly scales with the potential between the plates, allowing us to introduce the normalized electric potential $\hat{\Phi}_{\mathrm{void}} = \Phi_{\mathrm{void}}/V$. The third terms describes the pairwise Coulomb-interaction between all point charges (the summation excludes terms where $i = j$).

$$U_{\text{q-q}} = \frac{1}{8\pi\varepsilon_0} \sum_{i=1}^{N} \sum_{j=1}^{N} \frac{q_i q_j}{\left|\mathbf{r}_i - \mathbf{r}_j\right|} \tag{4.5}$$

The potential energy contribution due to the image charges is given according to

$$U_{\mathrm{im}} = \frac{1}{2} \sum_{i=1}^{N} \sum_{j=1}^{N} q_i q_j \Phi_{\mathrm{ind}}(\mathbf{r}_i, \mathbf{r}_j). \tag{4.6}$$

Here, $\Phi_{\mathrm{ind}}(\mathbf{r}_i, \mathbf{r}_j)$ describes the potential at $\mathbf{r}_i$ due to the image charges caused by unity charge at position $\mathbf{r}_j$.

As the final result of this section we can now calculate the electrostatic contribution F_{es} to the tip-sample force F_{ts}. The normal component of the electrostatic force results directly from differentiating the total electrostatic energy (equation 4.2) with respect to the tip-sample distance z_{ts},

$$\begin{aligned} F_{\mathrm{es}}(z_{\mathrm{ts}}, V) &= -\frac{\partial U_{\mathrm{es}}}{\partial z_{\mathrm{ts}}} && (4.7) \\ &= \frac{1}{2}\frac{\partial C_{\mathrm{void}}}{\partial z_{\mathrm{ts}}} \cdot V^2 && (4.8) \\ &\quad - \sum_{i=1}^{N} q_i \frac{\partial \hat{\Phi}_{\mathrm{void}}}{\partial z_{\mathrm{ts}}}(\mathbf{r}_i) \cdot V \\ &\quad - \frac{1}{2}\sum_{i=1}^{N}\sum_{j=1}^{N} q_i q_j \frac{\partial \Phi_{\mathrm{ind}}}{\partial z_{\mathrm{ts}}}(\mathbf{r}_i, \mathbf{r}_j). \end{aligned}$$

The formula reduces to three terms as the Coulomb interaction is not dependent on the tip-sample distance z_{ts}. Before discussing this result, we briefly revisit the assumptions made for the derivation of this formula:

- All metals and dielectric materials are described macroscopically, and the dielectric materials modeled by a relative permittivity $\varepsilon_{\mathrm{r}}(\mathbf{r})$ are isotropic and linear.
- All metals have homogeneous surfaces and all charges reside on their surfaces.
- The presence of the tip does neither modify the position of the point charges $\{q_i\}$, nor the position of the dielectric media. Therefore, we do not consider relaxations due to the tip-sample interaction.

Equation 4.8 is in agreement with several findings known from experiments. First, the force scales quadratically with the voltage V, and terms $q_i V$ will change the parabolic shape depending on the charges in the system. Second, for the charge-free system ($N = 0$), where all terms containing q_i evaluate to zero, equation 4.8 reduces to the first term U_{C}. This term is identical to the description of a void tip-sample capacitor as given by equation 4.3, and it is furthermore the common starting point when describing the KPFM signal for conducting substrates.[203]

The force described by equation 4.8 conveniently separates the contribution from the void tip-sample system – which depends on the geometry of the two metals, the dielectric media, and the applied potential, but not on the point charges – from the image interactions of the point charges – where the charges and the geometry of the metals contribute, but which is independent from the external voltage. While a description of the void tip-sample capacitor by the capacitance C_{void} and the electrostatic potential Φ_{void} can be performed analytically,[202,204,205] calculating the image interaction U_{im} analytically can be a rather difficult challenge, in particular for realistic geometries and multiple charges. As one of the important results of this section, we will derive in the following section that the image interaction terms do not contribute to the KPFM signal and, consequently, do not have to be evaluated for a KPFM signal analysis.

4.1.3 KPFM detection

Based on this electrostatic model, we now turn to the calculation of the KPFM signal for the various KPFM modes based on an analysis of the tip motion. In this and the next section, we will quantitatively derive observables that are recorded in the AM-KPFM mode, the FM-KPFM mode, and the heterodyne KPFM modes, each in the static, open-loop, and closed-loop variants.[193,194] Despite the difference of the KPFM mode-specific observables, it is possible to condense all different observables into *one* generalized equation that allows for a quantitative description of KPFM for *all* operation modes. Our derivation does not rely on mode-specific assumptions or approximations – we will only employ the *harmonic approximation*, which is the prevalent approximation used for the quantitative analysis of atomic force microscopy (AFM) data (see section 2.1).

The electrostatic force F_{es} (equation 4.8) contributes to the tip-sample force F_{ts}, which can also include, *e.g.*, chemical, van-der-Waals or magnetic force contributions.[206] Generally, the tip-sample force $F_{\mathrm{ts}}(z_{\mathrm{ts}}, \dot{z}_{\mathrm{ts}}, V)$ depends on the tip-sample distance z_{ts}, the tip velocity $\dot{z}_{\mathrm{ts}}$ as well as the voltage V between the tip and sample side metal. We assume in the following that only the electrostatic contribution F_{es} to the total tip-sample force F_{ts} is dependent on the voltage between the metals.

In the most general case, the voltage V between the tip and the sample side metal is a sum of the contact potential difference V_{CPD} and an externally applied voltage V_{ext}, which in turn can be defined by the sum of a static (DC) bias V_{bias} and a sinusoidal voltage with amplitude V_{es} and electrostatic excitation frequency ν_{es},

$$V = -V_{\mathrm{CPD}} + V_{\mathrm{bias}} + V_{\mathrm{es}} \cos(2\pi \nu_{\mathrm{es}} t). \tag{4.9}$$

For KPFM experiments in which only the static voltage V_{bias} is applied, we can set $V_{\mathrm{es}} = 0$. Similarly, for treating experiments where no static voltage, but only a sinusoidal voltage is applied, we can set $V_{\mathrm{bias}} = 0$.

The electrostatic force F_{es} in equation 4.8 can be rewritten in the form of three terms when using the voltage V according to equation 4.9,[1]

$$\begin{aligned} F_{\mathrm{es}}(z_{\mathrm{ts}},V) = \quad & F_{\mathrm{es,a}}(z_{\mathrm{ts}}) \\ & + F_{\mathrm{es,b}}(z_{\mathrm{ts}})\cos(2\pi\nu_{\mathrm{es}}t) \\ & + F_{\mathrm{es,c}}(z_{\mathrm{ts}})\cos(2\pi(2\nu_{\mathrm{es}})t), \end{aligned} \tag{4.10}$$

where

$$\begin{aligned} F_{\mathrm{es,a}}(z_{\mathrm{ts}}) = & +\frac{1}{2}\frac{\partial C_{\mathrm{void}}}{\partial z_{\mathrm{ts}}}\left((V_{\mathrm{bias}}-V_{\mathrm{CPD}})^2+\frac{1}{2}V_{\mathrm{es}}^2\right) \\ & -(V_{\mathrm{bias}}-V_{\mathrm{CPD}})\sum_{i=1}^{N} q_i\frac{\partial\hat{\Phi}_{\mathrm{void}}}{\partial z_{\mathrm{ts}}}(\mathbf{r}_i) \\ & -\frac{1}{2}\sum_{i=1}^{N}\sum_{j=1}^{N} q_i q_j\frac{\partial\hat{\Phi}_{\mathrm{ind}}}{\partial z_{\mathrm{ts}}}(\mathbf{r}_i,\mathbf{r}_j) \end{aligned} \tag{4.11}$$

$$F_{\mathrm{es,b}}(z_{\mathrm{ts}}) = +V_{\mathrm{es}}\left(\frac{\partial C_{\mathrm{void}}}{\partial z_{\mathrm{ts}}}(V_{\mathrm{bias}}-V_{\mathrm{CPD}})-\sum_{i=1}^{N} q_i\frac{\partial\hat{\Phi}_{\mathrm{void}}(\mathbf{r}_i)}{\partial z_{\mathrm{ts}}}\right) \tag{4.12}$$

$$F_{\mathrm{es,c}}(z_{\mathrm{ts}}) = +\frac{1}{4}\frac{\partial C_{\mathrm{void}}}{\partial z_{\mathrm{ts}}}V_{\mathrm{es}}^2. \tag{4.13}$$

Because F_{es} contributes to the tip-sample force F_{ts}, the latter force can in analogy to equation 4.10 also be written in the form of three terms

$$\begin{aligned} F_{\mathrm{ts}}(z_{\mathrm{ts}},\dot{z}_{\mathrm{ts}},V) = \quad & F_{\mathrm{ts,a}}(z_{\mathrm{ts}},\dot{z}_{\mathrm{ts}}) \\ & + F_{\mathrm{ts,b}}(z_{\mathrm{ts}},\dot{z}_{\mathrm{ts}})\cos(2\pi\nu_{\mathrm{es}}t) \\ & + F_{\mathrm{ts,c}}(z_{\mathrm{ts}},\dot{z}_{\mathrm{ts}})\cos(2\pi(2\nu_{\mathrm{es}})t). \end{aligned} \tag{4.14}$$

Here, $F_{\mathrm{ts,a}}$ contains $F_{\mathrm{es,a}}$ and all other voltage-independent contributions to the interaction force. In contrast, the other two terms include *only* electrostatic forces, we can therefore use the identities $F_{\mathrm{ts,b}} = F_{\mathrm{es,b}}$ and $F_{\mathrm{ts,c}} = F_{\mathrm{es,c}}$.

Next, we discuss the effect of the tip-sample force (including F_{es}) on the motion of the AFM resonator. This description closely follows the approach detailed in section 2.1. This resonator is described as an harmonic oscillator with effective mass m, spring constant k, and damping constant γ. The derivation of the oscillator's behavior starts with the equation of motion considering all involved forces: Besides the tip-sample force F_{ts}, the force acting on the resonator consists of the restoring force $-kq$ and a

---

[1] The three quantities $F_{\mathrm{es,a}}$, $F_{\mathrm{es,b}}$ and $F_{\mathrm{es,c}}$ might firsthand appear to be spectral components of F_{es} – they would represent a static component (at zero frequency), a first harmonic (at frequency ν_{es}) and a second harmonic (at frequency $2\nu_{\mathrm{es}}$). However, it is important to remember that during dynamic AFM and dynamic KPFM measurements, the tip-sample distance z_{ts} is also a function of time. Therefore, considering $F_{\mathrm{es,a}}$, $F_{\mathrm{es,b}}$ and $F_{\mathrm{es,c}}$ to be spectral components of F_{es} is only reasonable under the assumption that z_{ts} is fixed.

damping force $-\gamma\dot{q}$. Moreover, for conventional dynamic AFM imaging, we consider an external excitation force $F_0\cos(2\pi\nu_{\mathrm{exc}}t)$, where F_0 is the excitation force amplitude and ν_{exc} is the excitation frequency. The equation of motion is then given by

$$\begin{aligned} m\ddot{q} = &-kq - \gamma\dot{q} \\ &+ F_0\cos(2\pi\nu_{\mathrm{exc}}t) \\ &+ F_{\mathrm{ts}}(z_{\mathrm{ts}}, \dot{z}_{\mathrm{ts}}, V). \end{aligned} \tag{4.15}$$

An analytical solution of equation 4.15 for an arbitrary tip-sample force is generally not possible since F_{ts} depends on the tip-sample distance z_{ts}. We therefore employ the *harmonic approximation*, in which the deflection of the resonator is approximated as

$$\tilde{q} = q_{\mathrm{s}} + A\cos(2\pi\nu_{\mathrm{exc}}t + \varphi) \tag{4.16}$$

and, consequently, the tip-sample distance z_{ts} is given as

$$\tilde{z}_{\mathrm{ts}} = z_{\mathrm{c}} + A\cos(2\pi\nu_{\mathrm{exc}}t + \varphi). \tag{4.17}$$

In the above equations, q_{s} is the static deflection, A is the oscillation amplitude, and φ is the phase shift between the excitation at frequency ν_{exc} and the deflection. The tip oscillates around z_{c}, the center position of the oscillation.

When *only* discussing dynamic AFM (as is done in section 2.1), this approximation can consistently be used for the deflection and the tip-sample distance by replacing q with $\tilde{q}$ and z_{ts} with $\tilde{z}_{\mathrm{ts}}$ in equation 4.15. However, the approximation implies that the only spectral components of the deflection are the static deflection and the first harmonic at frequency ν_{exc} – there would not be any additional spectral components for a KPFM measurement to detect. Therefore, we only use the harmonic approximation for the *sampling* of the tip-sample and electrostatic force in equation 4.15. This means that we only substitute $F_{\mathrm{ts}}(z_{\mathrm{ts}}, \dot{z}_{\mathrm{ts}}, V)$ with $F_{\mathrm{ts}}(\tilde{z}_{\mathrm{ts}}, \dot{\tilde{z}}_{\mathrm{ts}}, V)$ in equation 4.15, but do not replace the other occurrences of q, thereby allowing arbitrary spectral components to the deflection. The thought underlying this approximation is that the additional spectral components to the deflection, which are not expressed in equation 4.16, do not significantly affect the path along which the tip-sample force is sampled. Combining the harmonic approximation with equations 4.14 and 4.15 yields

$$\begin{aligned} m\ddot{q} = &-kq - \gamma\dot{q} \\ &+ F_0\cos(2\pi\nu_{\mathrm{exc}}t) \\ &+ F_{\mathrm{ts,a}}(\tilde{z}_{\mathrm{ts}}, \dot{\tilde{z}}_{\mathrm{ts}}) \\ &+ F_{\mathrm{es,b}}(\tilde{z}_{\mathrm{ts}})\cos(2\pi\nu_{\mathrm{es}}t) \\ &+ F_{\mathrm{es,c}}(\tilde{z}_{\mathrm{ts}})\cos(2\pi(2\nu_{\mathrm{es}})t)\,. \end{aligned} \tag{4.18}$$

When F_{ts} is periodically sampled due to the oscillation of the tip-sample distance as described in equation 4.17, $F_{\mathrm{ts,a}}$, $F_{\mathrm{es,b}}$ and $F_{\mathrm{es,c}}$ are periodic functions of time with period ν_{exc}^{-1} since they depend on the tip-sample distance. They can be developed in a Fourier series. However, before doing so, we split $F_{\mathrm{ts,a}}$ into an odd and an even part according to $F_{\mathrm{ts,a}} = F_{\mathrm{even,a}} + F_{\mathrm{odd,a}}$. Here, the force $F_{\mathrm{even,a}}$ is even with respect to the tip-velocity ($F_{\mathrm{even,a}}(z_{\mathrm{ts}}, \dot{z}_{\mathrm{ts}}) = F_{\mathrm{even,a}}(z_{\mathrm{ts}}, -\dot{z}_{\mathrm{ts}})$), while $F_{\mathrm{odd,a}}$ is odd with respect to the tip velocity ($F_{\mathrm{odd,a}}(z_{\mathrm{ts}}, \dot{z}_{\mathrm{ts}}) = -F_{\mathrm{odd,a}}(z_{\mathrm{ts}}, -\dot{z}_{\mathrm{ts}})$). The Fourier series of $F_{\mathrm{ts,a}}$ can then be written as

$$\begin{aligned} F_{\mathrm{ts,a}} = F_{\mathrm{even,a}}^{(0)} + \sum_{n=1}^{\infty} F_{\mathrm{even,a}}^{(n)} \cos(2\pi n \nu_{\mathrm{exc}} t + \varphi) \\ + F_{\mathrm{odd,a}}^{(n)} \sin(2\pi n \nu_{\mathrm{exc}} t + \varphi). \end{aligned} \tag{4.19}$$

The model we use for the electrostatic description of the system results in a purely conservative electrostatic force F_{es}, which does not depend on the tip velocity. Therefore, $F_{\mathrm{es,b}}$ and $F_{\mathrm{es,c}}$ are even with respect to the tip-velocity and, consequently, do only carry the even-force terms in their Fourier series:

$$F_{\mathrm{es,b}} = F_{\mathrm{es,b}}^{(0)} + \sum_{n=1}^{\infty} F_{\mathrm{es,b}}^{(n)} \cos(2\pi n \nu_{\mathrm{exc}} t + \varphi) \tag{4.20}$$

$$F_{\mathrm{es,c}} = F_{\mathrm{es,c}}^{(0)} + \sum_{n=1}^{\infty} F_{\mathrm{es,c}}^{(n)} \cos(2\pi n \nu_{\mathrm{exc}} t + \varphi) \tag{4.21}$$

Within the harmonic approximation, this Fourier series is truncated after the linear term with $n = 1$. The resulting spectral components describing $F_{\mathrm{ts,a}}$, $F_{\mathrm{es,b}}$ and $F_{\mathrm{es,c}}$ can furthermore be written as weighted averages over the tip-sample distance range $[-A + z_{\mathrm{c}}, z_{\mathrm{c}} + A]$, namely

$$F_{\mathrm{ts,a}}(\tilde{z}_{\mathrm{ts}}, \dot{\tilde{z}}_{\mathrm{ts}}) \approx \langle F_{\mathrm{even,a}} \rangle_{\cup} + \langle k_{\mathrm{ts,a}} \rangle_{\cap} (z_{\mathrm{ts}} - z_{\mathrm{c}}) - \langle \gamma_{\mathrm{ts,a}} \rangle_{\cap} \dot{z}_{\mathrm{ts}}, \tag{4.22}$$

$$F_{\mathrm{es,b}}(\tilde{z}_{\mathrm{ts}}) \approx \langle F_{\mathrm{es,b}} \rangle_{\cup} + \langle k_{\mathrm{es,b}} \rangle_{\cap} (z_{\mathrm{ts}} - z_{\mathrm{c}}), \tag{4.23}$$

$$F_{\mathrm{es,c}}(\tilde{z}_{\mathrm{ts}}) \approx \langle F_{\mathrm{es,c}} \rangle_{\cup} + \langle k_{\mathrm{es,c}} \rangle_{\cap} (z_{\mathrm{ts}} - z_{\mathrm{c}}). \tag{4.24}$$

The derivation of these expression is analogously to the discussion in section 2.1.8. In the above equations, we introduced the tip-sample force gradient $k_{\mathrm{ts,a}}$ and the electrostatic force gradients $k_{\mathrm{es,b}}$ and $k_{\mathrm{es,c}}$ as

$$k_{\mathrm{ts,a}} = \frac{\partial F_{\mathrm{even,a}}}{\partial z_{\mathrm{ts}}} \tag{4.25}$$

$$k_{\mathrm{es,b}} = \frac{\partial F_{\mathrm{es,b}}}{\partial z_{\mathrm{ts}}} \tag{4.26}$$

$$k_{\mathrm{es,c}} = \frac{\partial F_{\mathrm{es,c}}}{\partial z_{\mathrm{ts}}} \tag{4.27}$$

as well as the tip-sample damping coefficient $\gamma_{\mathrm{ts,a}}$ according to $F_{\mathrm{odd,a}} = -\gamma_{\mathrm{ts,a}} \dot{q}$. The cup ($\cup$) and cap ($\cap$) averages are defined by equations 2.20 and 2.21 on page 16. Both averages can be considered as function of, *e.g.* the oscillation center position z_c and the amplitude A.

Inserting equations 4.22, 4.23 and 4.24 into equation 4.18 results in the differential equation of the harmonic oscillator using the harmonic approximation and the modulated electrostatic forces,

$$\begin{aligned} m\ddot{q} \approx & -(k - \langle k_\mathrm{ts,a}\rangle_\cap)q \\ & -(\gamma + \langle \gamma_\mathrm{ts,a}\rangle_\cap)\dot{q} \\ & + F_0 \cos(2\pi\nu_\mathrm{exc}t) \\ & + \langle F_\mathrm{even,a}\rangle_\cup \\ & + \langle F_\mathrm{es,b}\rangle_\cup \cos(2\pi\nu_\mathrm{es}t) \\ & + \langle F_\mathrm{es,c}\rangle_\cup \cos(2\pi(2\nu_\mathrm{es})t) \\ & + A/2\,\langle k_\mathrm{es,b}\rangle_\cap \cos(2\pi(\nu_\mathrm{exc} + \nu_\mathrm{es})t + \varphi) \\ & + A/2\,\langle k_\mathrm{es,b}\rangle_\cap \cos(2\pi(\nu_\mathrm{exc} - \nu_\mathrm{es})t + \varphi) \\ & + A/2\,\langle k_\mathrm{es,c}\rangle_\cap \cos(2\pi(\nu_\mathrm{exc} + 2\nu_\mathrm{es})t + \varphi) \\ & + A/2\,\langle k_\mathrm{es,c}\rangle_\cap \cos(2\pi(\nu_\mathrm{exc} - 2\nu_\mathrm{es})t + \varphi) \end{aligned} \tag{4.28}$$

The harmonic oscillator is now characterized by its effective mass m, effective spring constant $k' = k - \langle k_\mathrm{ts,a}\rangle_\cap$ and effective damping constant $\gamma' = \gamma + \langle \gamma_\mathrm{ts,a}\rangle_\cap$. For practical reasons, we consider all other contributions as being contributions to the excitation force. In contrast to equation 4.15, the excitation force components here only depend on the center position z_c and the amplitude A, and not on z_ts. This allows us to solve the approximation in equation 4.28 analytically: The resulting spectrum of the deflection can be directly obtained by applying the Fourier transform to both sides of equation 4.28. Since the Fourier transform of the first and second time-derivative is given equations 2.25 and 2.26 (page 21), we obtain the following relation between the spectrum of the deflection and the spectrum of the tip-sample force and the external excitation force (see also section 2.1.6)

$$\begin{aligned} \mathcal{F}[q] = G'_\mathrm{ho}(\nu)\mathcal{F}\Big[& + F_0 \cos(2\pi\nu_\mathrm{exc}t) \\ & + \langle F_\mathrm{even,a}\rangle_\cup \\ & + \langle F_\mathrm{es,b}\rangle_\cup \cos(2\pi\nu_\mathrm{es}t) \\ & + \langle F_\mathrm{es,c}\rangle_\cup \cos(2\pi(2\nu_\mathrm{es})t) \\ & + A/2\,\langle k_\mathrm{es,b}\rangle_\cap \cos(2\pi(\nu_\mathrm{exc} + \nu_\mathrm{es})t + \varphi) \\ & + A/2\,\langle k_\mathrm{es,b}\rangle_\cap \cos(2\pi(\nu_\mathrm{exc} - \nu_\mathrm{es})t + \varphi) \\ & + A/2\,\langle k_\mathrm{es,c}\rangle_\cap \cos(2\pi(\nu_\mathrm{exc} + 2\nu_\mathrm{es})t + \varphi) \\ & + A/2\,\langle k_\mathrm{es,b}\rangle_\cap \cos(2\pi(\nu_\mathrm{exc} - 2\nu_\mathrm{es})t + \varphi)\Big]. \end{aligned} \tag{4.29}$$

We can therefore conclude that the spectral components of the deflection are connected to the spectral components of the excitation force by the transfer function G'_ho

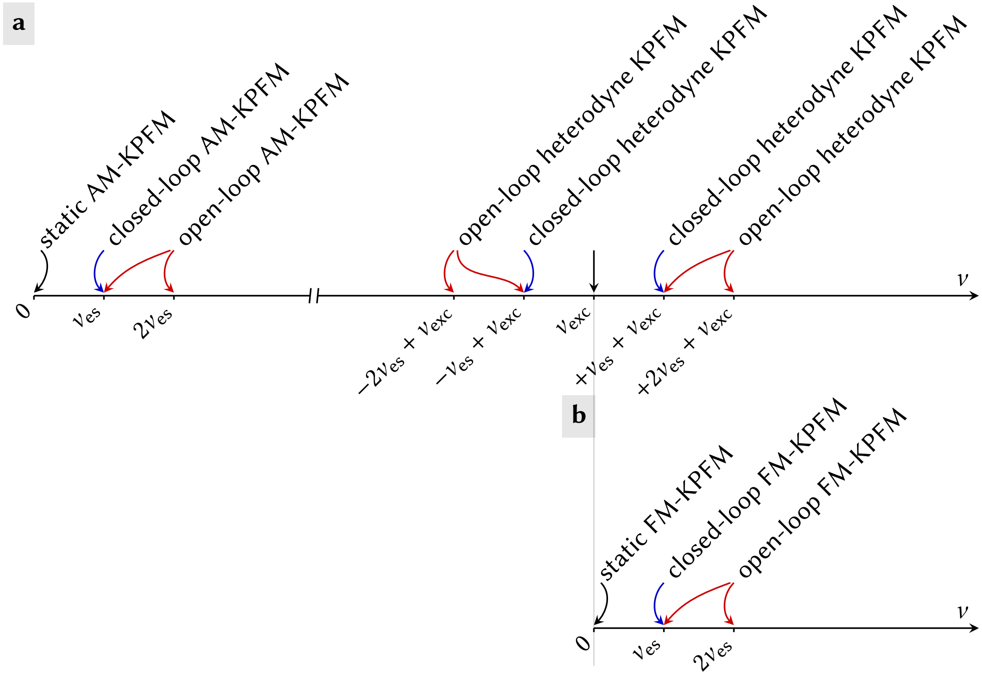

Figure 4.2: Panel a shows the frequencies of all spectral components of the deflection that are described with equation 4.29. Panel b presents the spectral components of the demodulated deflection signal (the demodulation is performed at the frequency ν_{exc}). The spectral components that are measured in the different KPFM modes are indicated by black arrows for the static methods, blue arrows for the closed-loop methods and red arrows for open-loop methods

defined as

$$G'_{\mathrm{ho}}(\nu) = \frac{1}{k' - (2\pi\nu)^2 m + 2\pi\nu \mathrm{i}\gamma'} = \left|G'_{\mathrm{ho}}(\nu)\right| \exp\left(\mathrm{i}\varphi'_{\mathrm{ho}}(\nu)\right). \tag{4.30}$$

The prime indicates that the transfer function depends on k' and γ', as opposed to k and γ. We can identify the spectral components of the cantilever deflection q by inspection of equation 4.29. As schematically plotted with respect to a frequency axis in figure 4.2 a, the spectral components are given by

- a static deflection due to the static force components,
- a first harmonic (due to the external excitation) at the frequency ν_{exc},
- a first and second harmonic mode due to the electrostatic excitation at frequencies ν_{es} and $2\nu_{\mathrm{es}}$, and
- sidebands at $\nu_{\mathrm{exc}} \pm \nu_{\mathrm{es}}$ and $\nu_{\mathrm{exc}} \pm 2\nu_{\mathrm{es}}$.

Table 4.1: Summary of the various KPFM implementations categorized via the applied voltage.

no KPFM	$V_{\text{bias}} = 0,$	$V_{\text{es}} = 0$
static KPFM	$V_{\text{bias}} \neq 0,$	$V_{\text{es}} = 0$
open-loop KPFM	$V_{\text{bias}} = 0,$	$V_{\text{es}} \neq 0$
closed-loop KPFM	$V_{\text{bias}} \neq 0,$	$V_{\text{es}} \neq 0$

All spectral components listed above can be measured experimentally. However, depending on the choice on the KPFM mode, the experimentalist only evaluates certain spectral components of the deflection as we will discuss in the next section 4.1.4.

4.1.4 The KPFM signal

To calculate the KPFM signals obtained in the different KPFM modes, we start the categorization of the modes from the choice of the applied voltage as given by equation 4.9. First, the experimentalist chooses whether a static bias voltage and/or an sinusoidal voltage is applied (table 4.1). We refer to the case of only applying a DC bias voltage as *static* KPFM, while the case of only applying a sinusoidal voltage without DC bias is known as the *open-loop* KPFM mode. If the DC bias voltage is regulated by an additional feedback loop and added to the sinusoidal voltage, this third mode is known as *closed-loop* KPFM.

Next, and depending on the above choice of the applied voltage, the experimentalist chooses which spectral components to detect. The schemes are classified using the terms *amplitude-modulation* (AM), *frequency-modulation* (FM) and *heterodyne* detection.

Excursus: Measuring spectral components

Before starting the quantitative evaluation of the KPFM signal in these different modes, we discuss the procedure of quantitatively measuring spectral components as we will frequently refer to measuring spectral components of the electrostatic force in the following. The experimentally accessible quantity is in all cases the deflection of the resonator. Measuring the spectral components of this deflection provides the basis for measuring spectral components of the electrostatic force.

In the laboratory, a lock-in amplifier usually performs this task (see section 2.2). This device measures the Fourier components of a signal around a fixed frequency within a given bandwidth. Since the spectrum of a signal is a complex number, the lock-in amplifier outputs either the real and imaginary part, or the magnitude (“amplitude”) and the argument ("phase shift") of the input signal relative to the reference signal. To give one example, the inverse Fourier transform of the spectral component of the deflection at frequency ν_{es} is (according to equation 4.29)

$$\underbrace{\left|G'_{\mathrm{ho}}(\nu_{\mathrm{es}})\right| \cdot \left|\langle F_{\mathrm{es,b}}\rangle_{\cup}\right|}_{\text{amplitude } A(\nu_{\mathrm{es}})} \cos\left(2\pi\nu_{\mathrm{es}}t + \underbrace{\varphi'_{\mathrm{ho}}(\nu_{\mathrm{es}}) + \pi\Theta(-\langle F_{\mathrm{es,b}}\rangle_{\cup})}_{\text{phase shift } \varphi(\nu_{\mathrm{es}})}\right).$$

Consequently, the amplitude $A(\nu_{\mathrm{es}})$ is the product of the gain function and the *magnitude* of the first spectral component of the electrostatic tip-sample force. To obtain the *sign* of the spectral component of the electrostatic excitation force, the phase shift $\varphi(\nu_{\mathrm{es}})$ needs to be evaluated additionally. The measured phase shift consists of the phase shift due to the harmonic oscillator $\varphi'_{\mathrm{ho}}(\nu_{\mathrm{exc}})$ and an additional phase shift of π in case $\langle F_{\mathrm{es,b}}\rangle_{\cup} < 0$. For the above equation, the phase shift of π for negative spectral components of the electrostatic force is written using the Heaviside function Θ.

AM-KPFM

Static AM-KPFM

Only a DC bias voltage is applied in static AM-AFM,[207] therefore $V_{\mathrm{es}} = 0$. All spectral components of the electrostatic force except for the static term vanish in this case as is apparent from equation 4.29. Consequently, the only spectral components of the deflection that remain are the static deflection and the oscillating at ν_{exc} (see figure 4.2). The observable in static AM-KPFM is the static deflection as a function of the applied bias voltage, which can directly be accessed experimentally.

The contribution to the static deflection that depends on the bias voltage is according to equation 4.29 proportional to $\langle F_{\mathrm{es,a}}\rangle_{\cup}$. This term $\langle F_{\mathrm{es,a}}\rangle_{\cup}$ depends in turn parabolically on the bias voltage. We find the KPFM signal for static AM-KPFM directly as the bias voltage at the extremum of this term,

$$\begin{aligned} & \frac{\partial \mathcal{F}[q](0)}{\partial V_{\mathrm{bias}}} = 0 \\ \Leftrightarrow \quad & \frac{\partial \langle F_{\mathrm{even,a}}\rangle_{\cup}}{\partial V_{\mathrm{bias}}} = 0 \\ \Leftrightarrow \quad & \frac{\partial \langle F_{\mathrm{es,a}}\rangle_{\cup}}{\partial V_{\mathrm{bias}}} = 0 \quad \text{for} \quad V_{\mathrm{bias}} = V_{\mathrm{AM}} \text{ (and } V_{\mathrm{es}} = 0). \end{aligned} \tag{4.31}$$

We can evaluate this condition using equation 4.11 and arrive at the AM-KPFM signal V_{AM}

$$V_{\mathrm{AM}} = V_{\mathrm{CPD}} + \sum_{i=1}^{N} q_i \frac{\left\langle \frac{\partial \hat{\Phi}_{\mathrm{void}}}{\partial z_{\mathrm{ts}}}(\mathbf{r}_i) \right\rangle_{\cup}}{\left\langle \frac{\partial C_{\mathrm{void}}}{\partial z_{\mathrm{ts}}} \right\rangle_{\cup}} \tag{4.32}$$

where the electrostatic potential Φ_{void} and the capacitance C_{void} of the charge-free tip-sample system are averaged using the cup averaging function $\langle.\rangle_{\cup}$.

Closed-loop AM-KPFM

In closed-loop AM-KPFM, both a static bias voltage and an oscillatory voltage at frequency ν_{es} are applied. The first harmonic resulting from the electrostatic excitation (at ν_{es}) is detected in closed-loop AM-KPFM from the deflection signal q of the oscillating cantilever.[208,209] A feedback loop is used to nullify the amplitude of this spectral component by adjusting the bias voltage V_{bias},

$$\begin{aligned} &\mathcal{F}[q](\nu_{\mathrm{es}}) = 0 \\ \Leftrightarrow \quad &\langle F_{\mathrm{es,b}}\rangle_{\cup} = 0 \quad \text{for} \quad V_{\mathrm{bias}} = V_{\mathrm{AM}}. \end{aligned} \tag{4.33}$$

According to equation 4.12, the KPFM signal is

$$V_{\mathrm{AM}} = V_{\mathrm{CPD}} + \sum_{i=1}^{N} q_i \frac{\left\langle \frac{\partial \hat{\Phi}_{\mathrm{void}}}{\partial z_{\mathrm{ts}}}(\mathbf{r}_i) \right\rangle_{\cup}}{\left\langle \frac{\partial C_{\mathrm{void}}}{\partial z_{\mathrm{ts}}} \right\rangle_{\cup}}. \tag{4.34}$$

Thus, static AM-KPFM and closed-loop AM-KPFM give the same KPFM signal.

Open-loop AM-KPFM

Both, the first and the second harmonic signal at ν_{es} and $2\nu_{\mathrm{es}}$ due to the electrostatic excitation at ν_{es} are measured in open-loop AM-KPFM.[210] In a post-processing step, the components $\langle F_{\mathrm{es,b}}\rangle_{\cup}$ and $\langle F_{\mathrm{es,c}}\rangle_{\cup}$ of the electrostatic force are then evaluated from measuring the spectral components at ν_{es} and $2\nu_{\mathrm{es}}$ of the deflection signal as exemplified in section 4.1.4. The open-loop AM-KPFM signal follows finally from

$$V_{\mathrm{AM}} = \frac{V_{\mathrm{es}}}{4} \frac{\langle F_{\mathrm{es,b}}\rangle_{\cup}}{\langle F_{\mathrm{es,c}}\rangle_{\cup}} = V_{\mathrm{CPD}} + \sum_{i=1}^{N} q_i \frac{\left\langle \frac{\partial \hat{\Phi}_{\mathrm{void}}}{\partial z_{\mathrm{ts}}}(\mathbf{r}_i) \right\rangle_{\cup}}{\left\langle \frac{\partial C_{\mathrm{void}}}{\partial z_{\mathrm{ts}}} \right\rangle_{\cup}}. \tag{4.35}$$

From this analysis we conclude that all AM-KPFM modes give the same measured signal – despite the detection of different experimental observables.

FM-KPFM

In the AM-KPFM modes discussed before, spectral components are detected directly from the deflection signal. In contrast, the deflection signal is demodulated at frequency ν_{exc} using a demodulator in the FM-KPFM modes, and observables are evaluated from this demodulated signal. The demodulator can be thought of effectively shifting all spectral components of the deflection by ν_{exc}, and is commonly implemented using a phase-locked loop in an experimental setup. The demodulation is based on multiplication of the deflection signal q with $\cos(2\pi\nu_{\mathrm{exc}}t)$.

Static FM-KPFM

Similar to static AM-KPFM, only a DC bias voltage is applied in static FM-KPFM,[176,211–213] therefore $V_{\mathrm{es}} = 0$. In static FM-KPFM, the static component of the demodulated deflection signal[2] is recorded as function of the applied bias voltage V_{bias}. The KPFM signal corresponds in this case to the applied bias voltage, at which the demodulated signal is extremal

$$\begin{aligned} & \frac{\partial \mathcal{F}[q\cos(2\pi\nu_{\mathrm{exc}}t)](0)}{\partial V_{\mathrm{bias}}} = 0 \\ \Leftrightarrow \quad & \frac{\partial \mathcal{F}[q](\nu_{\mathrm{es}})}{\partial V_{\mathrm{bias}}} = 0 \\ \Leftrightarrow \quad & \frac{\partial \langle k_{\mathrm{es,a}} \rangle}{\partial V_{\mathrm{bias}}} = 0 \quad \text{for} \quad V_{\mathrm{bias}} = V_{\mathrm{FM}}. \end{aligned} \tag{4.36}$$

When using equation 4.12 and 4.26, this condition yields the static mode FM-KPFM signal

$$V_{\mathrm{FM}} = V_{\mathrm{CPD}} + \sum_{i=1}^{N} q_i \frac{\left\langle \frac{\partial^2 \hat{\Phi}_{\mathrm{void}}}{\partial z_{\mathrm{ts}}^2}(\mathbf{r}_i) \right\rangle_{\cap}}{\left\langle \frac{\partial^2 C_{\mathrm{void}}}{\partial z_{\mathrm{ts}}^2} \right\rangle_{\cap}}. \tag{4.37}$$

In contrast to the AM-KPFM modes, the second derivative of the electrostatic potential Φ_{void} and of the capacitance C_{void} of the charge-free tip-sample system is calculated here.

Closed-loop FM-KPFM

The first harmonic signal resulting from the electrostatic excitation at ν_{es} is detected from the demodulated deflection signal in closed-loop FM-KPFM, and this signal is nullified by adjusting the bias voltage V_{bias}.[193,212] This is experimentally achieved by using a feedback loop regulating V_{bias} to nullify the magnitude of this spectral component. In this case, the KPFM signal equals to the adjusted bias voltage V_{bias} at which the magnitude of the spectral component is zero,

$$\mathcal{F}[q\cos(2\pi\nu_{\mathrm{exc}}t)](\nu_{\mathrm{es}}) = 0$$

$$\Leftrightarrow \mathcal{F}[q](\nu_{\mathrm{exc}} \pm \nu_{\mathrm{es}}) = 0 \tag{4.38}$$

$$\Leftrightarrow \quad \langle k_{\mathrm{es,b}} \rangle_{\cap} = 0 \quad \text{for} \quad V_{\mathrm{bias}} = V_{\mathrm{FM}}. \tag{4.39}$$

---

[2] In a FM-AFM experiment, the demodulated deflection signal is typically available as the excitation frequency or the excitation frequency shift relative to a reference frequency.

According to equation 4.12, the KPFM signal is

$$V_{\mathrm{FM}} = V_{\mathrm{CPD}} + \sum_{i=1}^{N} q_i \frac{\left\langle \frac{\partial^2 \hat{\Phi}_{\mathrm{void}}}{\partial z_{\mathrm{ts}}^2}(\mathbf{r}_i) \right\rangle_{\cap}}{\left\langle \frac{\partial^2 C_{\mathrm{void}}}{\partial z_{\mathrm{ts}}^2} \right\rangle_{\cap}}. \tag{4.40}$$

Open-loop FM-KPFM

The first and the second harmonic at ν_{es} and $2\nu_{\mathrm{es}}$, respectively, are both extracted from the demodulated deflection signal in open-loop FM-KPFM.[214] Similar to the open-loop AM-KPFM mode, the corresponding components of the electrostatic interaction, here the force gradients $\langle k_{\mathrm{es,b}} \rangle_{\cap}$ and $\langle k_{\mathrm{es,c}} \rangle_{\cap}$ (equation 4.29), are calculated from the two spectral components in the demodulated signal using the transfer function of the demodulator (section 4.1.4). The open-loop FM-KPFM signal follows from

$$V_{\mathrm{FM}} = \frac{V_{\mathrm{es}}}{4} \frac{\langle k_{\mathrm{es,b}} \rangle_{\cap}}{\langle k_{\mathrm{es,c}} \rangle_{\cap}} = V_{\mathrm{CPD}} + \sum_{i=1}^{N} q_i \frac{\left\langle \frac{\partial^2 \hat{\Phi}_{\mathrm{void}}}{\partial z_{\mathrm{ts}}^2}(\mathbf{r}_i) \right\rangle_{\cap}}{\left\langle \frac{\partial^2 C_{\mathrm{void}}}{\partial z_{\mathrm{ts}}^2} \right\rangle_{\cap}}. \tag{4.41}$$

Thus, the KPFM signals obtained in static FM-KPFM, open-loop FM-KPFM and closed-loop FM-KPFM are identical, but different to the AM-KPFM signal.

Heterodyne FM-KPFM

The spectral components at the sidebands $\nu_{\mathrm{exc}} \pm \nu_{\mathrm{es}}$ and $\nu_{\mathrm{exc}} \pm 2\nu_{\mathrm{es}}$ are directly measured from the deflection signal in heterodyne KPFM.[215] The heterodyne detection scheme allows the implementation of a closed-loop and an open-loop method: In closed-loop heterodyne KPFM, the spectral components at $\nu_{\mathrm{exc}} \pm \nu_{\mathrm{es}}$ are measured and nullified by adjusting V_{bias} with a feedback loop. This is described by equation 4.38. Therefore, closed-loop heterodyne KPFM gives the same signal as FM-KPFM.

In the open-loop variant of heterodyne KPFM, spectral components of the deflection at $\nu_{\mathrm{exc}} \pm \nu_{\mathrm{es}}$ and $\nu_{\mathrm{exc}} \pm 2\nu_{\mathrm{es}}$ are measured. Similar to the other open-loop methods, the components of the corresponding electrostatic tip-sample interaction are calculated in a post-processing step. The two components that can be obtained in the open-loop heterodyne mode are $\langle k_{\mathrm{es,b}} \rangle_{\cap}$ and $\langle k_{\mathrm{es,c}} \rangle_{\cap}$, and with the definition for V_{FM} in equation 4.41, the signal is identical to the open-loop FM-KPFM mode.

Consequently, heterodyne open-loop KPFM allows to obtain the same KPFM signal as heterodyne closed-loop KPFM, and both signals are identical to the open- and closed-loop FM-KPFM modes.

Table 4.2: Summary of the spectral components of the deflection q or the demodulated deflection $q\cos(2\pi\nu_{\mathrm{exc}}t)$ relevant in the KPFM modes discussed in this section (see also figure 4.2). The entries in the right column show either the condition for which the KPFM signal equal to V_{bias} is calculated, or the experimentally obtained quantity that is directly the KPFM signal.

static AM-KPFM	$\frac{\partial\mathcal{F}[q](0)}{\partial V_{\mathrm{bias}}} = 0$
static FM-KPFM	$\frac{\partial\mathcal{F}[q\cos(2\pi\nu_{\mathrm{exc}}t)](0)}{\partial V_{\mathrm{bias}}} = 0$
open-loop AM-KPFM	$(V_{\mathrm{es}}/4)\cdot\frac{\mathcal{F}[q](\nu_{\mathrm{es}})}{\mathcal{F}[q](2\nu_{\mathrm{es}})}$
open-loop FM-KPFM	$(V_{\mathrm{es}}/4)\cdot\frac{\mathcal{F}[q\cos(2\pi\nu_{\mathrm{exc}}t)](\nu_{\mathrm{es}})}{\mathcal{F}[q\cos(2\pi\nu_{\mathrm{exc}}t)](2\nu_{\mathrm{es}})}$
closed-loop AM-KPFM	$\mathcal{F}[q](\nu_{\mathrm{es}}) = 0$
closed-loop FM-KPFM	$\mathcal{F}[q\cos(2\pi\nu_{\mathrm{exc}}t)](\nu_{\mathrm{es}}) = 0$

Summary of the KPFM modes

The detection schemes that have been discussed in the this section are summarized in table 4.2 by listing the components of the deflection signal which are evaluated in each respective mode. Despite the different detection schemes, all AM-KPFM modes result in the same KPFM signal V_{AM} and all FM-KPFM modes give the same KPFM signal V_{FM}.

4.1.5 The weight function for charges

The KPFM signal for all six KPFM modes discussed before can be written as

$$V_{\mathrm{KPFM}} = V_{\mathrm{CPD}} + \sum_{i=1}^{N} q_i W_{\mathrm{KPFM}}(\mathbf{r}_i). \tag{4.42}$$

This formula allows us to introduce the *KPFM weight function for charges* W_{KPFM}, which weights the contribution of each charge q_i at its position $\mathbf{r}_i$. The resulting KPFM signal is then given as the sum over all weighted charges with an additional offset given by the contact potential difference between the tip and sample side metal.

For the AM-KPFM modes, the weight function for charges is defined by the ratio of the cup-averaged first z_{ts}-derivative of $\hat{\Phi}_{\mathrm{void}}$ and C_{void}

$$W_{\mathrm{AM}}(\mathbf{r}) = \frac{\left\langle \frac{\partial \hat{\Phi}_{\mathrm{void}}}{\partial z_{\mathrm{ts}}}(\mathbf{r}) \right\rangle_{\cup}}{\left\langle \frac{\partial C_{\mathrm{void}}}{\partial z_{\mathrm{ts}}} \right\rangle_{\cup}}. \tag{4.43}$$

For the FM-KPFM modes, the weight function for charges is given by the ratio of the cap-averaged second z_{ts}-derivative of $\hat{\Phi}_{\mathrm{void}}$ and C_{void}

$$W_{\mathrm{FM}}(\mathbf{r}) = \frac{\left\langle \frac{\partial^2 \hat{\Phi}_{\mathrm{void}}}{\partial z_{\mathrm{ts}}^2}(\mathbf{r}) \right\rangle_{\cap}}{\left\langle \frac{\partial^2 C_{\mathrm{void}}}{\partial z_{\mathrm{ts}}^2} \right\rangle_{\cap}}. \tag{4.44}$$

The cup $\langle . \rangle_{\cup}$ and cap $\langle . \rangle_{\cap}$ averages are each performed over the tip-sample distance interval that is probed by the oscillating tip, *i.e.* $z_{\mathrm{ts}} \in [-A + z_{\mathrm{c}}, z_{\mathrm{c}} + A]$. The weight of each charge therefore depends on the tip position range characterized by, *e.g.*, the center position z_{c} of the tip and the oscillation amplitude A.

Moreover, the weight function only depends on two electrostatic quantities of the *void* (*i.e.*, charge free) tip-sample system, namely the normalized electrostatic potential $\hat{\Phi}_{\mathrm{void}}$ and the capacitance C_{void}. While the image charge interaction contributes to the total electrostatic force, it does not appear in the weight function and, therefore, does not contribute to the KPFM signal. The weight function is consequently a property of the charge-free tip sample system. This important conclusion simplifies the interpretation of KPFM data, and especially allows to calculate the KPFM signal for charge distributions in a straightforward manner.

4.1.6 Conclusions and Outlook

This section introduced the KPFM weight function for charges, which is identified to be the central quantity for the calculation and interpretation of KPFM data for physical systems that include charge distributions. Based on an electrostatic model describing a general tip-sample system with tip and sample formed by two metals, a charge distribution, and, optionally, dielectric material in the tip-sample gap, we derived the KPFM signal for all experimentally implemented KPFM modes. In all these KPFM modes, namely static, open-loop, and closed-loop variants for the AM, FM, or heterodyne detection, the KPFM signal is given from a weighted sum over all charges in the tip-sample system.

The weight function for charges depends on the electrostatic properties of the charge-free tip-sample system, such as the sample geometry and composition, the tip geometry, the displacement between tip and sample, and the medium surrounding tip and sample. The weight function for charges, and thus the resulting KPFM signal, depends furthermore on the oscillation amplitude of the tip.

The next section 4.2 will give a detailed account on several properties of this weight function, and will investigate the dependency on different parameters such as the tip-sample geometry or the oscillation amplitude.

4.2 Analysis of the weight function for charges

Section 4.2 by H. Söngen, P. Rahe, R. Bechstein and A. Kühnle has been submitted in similar form as a chapter to the book "Kelvin Probe Force Microscopy – From Single Charge Detection to Device Characterization", edited by S. Sadewasser and T. Glatzel. I have written the code for calculating the KPFM weight function and KPFM signal, analyzed the calculated data, prepared the figures, and wrote most of the chapter with input by all authors. Most of the chapter is reproduced verbatim, changes were made to make this section consistent with the other sections in this thesis. As a major change, I shortened section 4.2.5 (previously the appendix).

The KPFM signal for systems containing local charges can be expressed as a weighted sum over all local charges. The weight function for charges *quantifies the contribution of each charge, depending on its position. In this section, we evaluate the KPFM weight function for charges by analyzing several application-relevant model systems. The intention of this section is to provide insights into the KPFM contrast formation in order to facilitate the KPFM data interpretation. For this, we concentrate on three model systems: (A) a conductive sample in ultra-high vacuum, (B) a dielectric sample in ultra-high vacuum, and (C) a dielectric sample in water. We calculate the weight function for charges for each of these systems using a conductive sphere as a tip model. While the analysis substantiates a number of known experimental observations, it reveals surprising effects in some environments. For example, the sign of the FM-KPFM signal reflects the sign of the charges measured in the systems A and B, but in system C the sign of the KPFM signal is found to be tip-sample distance dependent. Additionally, we deduce the lateral KPFM resolution limits and finally discuss the lateral decay of the weight function to assess how charges contribute to the signal. Our discussion is accompanied by an interactive visualization available at* `www.self-assembly.uni-mainz.de/kpfm`*.*

4.2.1 Introduction

Atomic force microscopy (AFM) has most successfully been joined with the Kelvin probe technique to specifically probe voltage-dependent contributions to the tip-sample interaction force.[203,208] This Kelvin probe force microscopy (KPFM) has extensively been used to investigate a large variety of different tip-sample systems, including conductive,[216] semi-conductive[217] and dielectric[174,179] materials in air,[218] ultra-high vacuum[176,219] and in liquid[106,220] environments.

Recently, the KPFM signal has been derived for a most general system that consists of a conductive tip, a conductive sample or a dielectric sample with a metallic back contact, and N point charges q_i located at positions $\mathbf{r}_\mathrm{i}$.[197,198] This model also has been introduced in section 4.1. Both major KPFM modes, namely the amplitude modulation

(AM) and the frequency modulation (FM) mode[194] have been considered in their most prominent technical implementations, which are the static, closed-loop and open-loop methods. It was found that for all cases, the KPFM signal V_{KPFM} can been written as

$$V_{\text{KPFM}} = V_{\text{CPD}} + \sum_{i=1}^{N} q_i W_{\text{KPFM}}(\mathbf{r}_i) \tag{4.45}$$

where the KPFM signal contains the contact potential difference V_{CPD} between the homogeneous tip and conductive sample (or the conductive sample back contact in case of insulating samples) and, most importantly, a weighted sum over all charges q_i located within the tip-sample system. Each charge in the sum is multiplied by a weight function W_{KPFM} that is evaluated at the position $\mathbf{r}_i$ of each charge. The weight function is fully defined by the properties of the charge-free tip-sample system, the oscillation amplitude of the tip and the KPFM mode.

In this section, we closely inspect equation 4.45 with the motivation to facilitate the interpretation of experimental KPFM data. In particular, we answer the following questions:

- How does the sign of the KPFM signal reflect the sign of the charges beneath the tip?
- How does the oscillation amplitude of the tip influence the KPFM signal?
- What is the lateral resolution for resolving charges with KPFM?
- What is the KPFM signal generated by electric dipoles?
- How large is the contribution of surface charges distributed across the whole sample to the KPFM signal?

For this, we first review the weight function for charges in section 4.2.2. Here, we also introduce the tip-sample systems we consider in this section. In section 4.2.3 we discuss properties of the weight function for charges W_{KPFM}, in particular its sign. Next, in section 4.2.4, we discuss both qualitative and quantitative aspects of the KPFM signal by using the weight function for charges. For the purpose of this discussion, we calculate the KPFM signal V_{KPFM} for simple charge distributions such as single point charges, dipoles and a layer of surface charges.

Most of the calculations we present in the following sections can also be explored with our interactive *KPFM visualization*. The KPFM visualization runs within the browser and is accessible at `www.self-assembly.uni-mainz.de/kpfm`.

4.2.2 The weight function for charges

Depending on using AM oder FM-KPFM, there are different expressions for the weight function for charges.[197,198] The AM-KPFM weight function is given by

$$W_{\mathrm{AM}}(\mathbf{r}) = \frac{\left\langle \frac{\partial \hat{\Phi}_{\mathrm{void}}}{\partial z_{\mathrm{ts}}}(\mathbf{r}) \right\rangle_{\cup}}{\left\langle \frac{\partial C_{\mathrm{void}}}{\partial z_{\mathrm{ts}}} \right\rangle_{\cup}}, \tag{4.46}$$

and the FM-KPFM weight function is written as

$$W_{\mathrm{FM}}(\mathbf{r}) = \frac{\left\langle \frac{\partial^2 \hat{\Phi}_{\mathrm{void}}}{\partial z_{\mathrm{ts}}^2}(\mathbf{r}) \right\rangle_{\cap}}{\left\langle \frac{\partial^2 C_{\mathrm{void}}}{\partial z_{\mathrm{ts}}^2} \right\rangle_{\cap}}. \tag{4.47}$$

Both KPFM weight functions are determined by two electrostatic quantities: the normalized electric potential[3] $\hat{\Phi}_{\mathrm{void}}$ and the capacitance C_{void}, both calculated for the *void*, *i.e.*, the charge-free tip-sample system. There are two distinct differences between the AM and FM-KPFM weight function: First, depending on considering the AM or the FM mode, either the first or second derivative of $\hat{\Phi}_{\mathrm{void}}$ and C_{void} with respect to the tip-sample distance z_{ts} appears in the respective weight function. Second, different averages are calculated for the two KPFM modes. The two derivatives are averaged over the tip-sample distance range $[-A + z_{\mathrm{c}},\ z_{\mathrm{c}} + A]$ covered during the tip oscillation with amplitude A around the center position z_{c}. We introduce the cup average $\langle . \rangle_{\cup}$ and the cap average $\langle . \rangle_{\cap}$ for AM-KPFM and FM-KPFM, respectively, as detailed in the previous section 4.1 and in section 2.1. The averaging functions are both positive and normalized.

The weight function W_{KPFM} for charges is evaluated at the positions $\mathbf{r}_i$ of each charge to calculate the KPFM signal V_{KPFM} (equation 4.45). The weight function depends on properties of the void tip-sample system, including the geometry of both tip and sample, as well as their relative displacement. Moreover, the weight function for charges depends on the electrostatic properties, such as the dielectric permittivity of the medium surrounding the tip. Since the weight function contains quantities that are averaged over the tip-sample distance oscillation range, the weight function additionally depends on the oscillation amplitude of the tip.

The void tip-sample system

The quantitative evaluation of equation 4.45 requires to pick a suitable model for the geometry of the void tip-sample system. Within this section we use a simple, yet

---

[3] The quantity $\hat{\Phi}_{\mathrm{void}}$ is the electric potential normalized with respect to the voltage V between the conductive tip and sample (or sample back contact in case of dielectric samples), *i.e.*, $\hat{\Phi}_{\mathrm{void}} = \Phi_{\mathrm{void}}/V$.

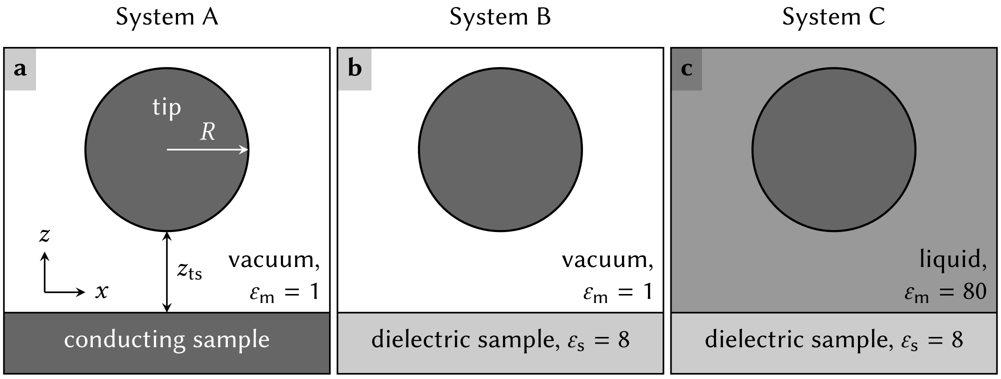

Figure 4.3: Three *void* tip-sample systems we consider for calculating the KPFM weight functions. A conducting sample ($\beta = 1$) is present in system A. While the samples in system B and system C are given by dielectric material with $\varepsilon_s = 8$, the dielectric constant of the medium where the tip is located differs. System B represents the ultra-high vacuum environment where the tip is located in a vacuum ($\varepsilon_m = 1$), while system C corresponds to measurements in the liquid environment using $\varepsilon_m = 80$.

realistic, model consisting of a conductive sphere as a tip. The reader is free to pick a different model appropriate for the respective application. We are confident that the qualitative statements of this section regarding the properties of the weight function are correct irrespective of the choice of the model.

In the model we use here, the tip is placed above either a conductive or a dielectric sample filling the semi-infinite half-space at $z < 0$ below the surface located at $z = 0$. We denote the relative dielectric permittivity of the medium surrounding the tip as ε_m. In case of a dielectric sample, we denote the relative dielectric permittivity of the sample as ε_s. According to the electrostatic model we use, a conductive sample is obtained in the limiting case $\varepsilon_s \longrightarrow \infty$ (corresponding to setting the factor $\beta = (\varepsilon_s - \varepsilon_m)/(\varepsilon_s + \varepsilon_m)$ to 1, see section 4.2.5). Unless otherwise stated, the tip radius is in the following set to $R = 20\,\text{nm}$. The tip-sample distance is denoted as z_{ts} (see figure 4.3 a). Details on the calculation of W_{KPFM} can be found in section 4.2.5.

Similar to our previous analysis of the weight function,[198] we discuss here three different tip-sample systems as drawn in figure 4.3. First, we consider as “system A” a conductive substrate ($\beta = 1$) in ultra-high vacuum ($\varepsilon_m = 1$). Second, we consider a thick dielectric sample in vacuum as “system B”, where we set the permittivity of the sample to $\varepsilon_s = 8$ to exemplary resemble the bulk insulating material calcite.[221] Third, while we consider for “system C” again a dielectric sample with $\varepsilon_s = 8$, we set the permittivity of the medium to a value larger than the permittivity of the sample. Specifically, we choose $\varepsilon_m = 80$ to represent water.[222] In all considered cases, we set $V_{CPD} = 0$, *i.e.*, we only consider the KPFM signal arising from charges in the tip-sample system. We thereby ignore any offset as a result of the contact potential difference

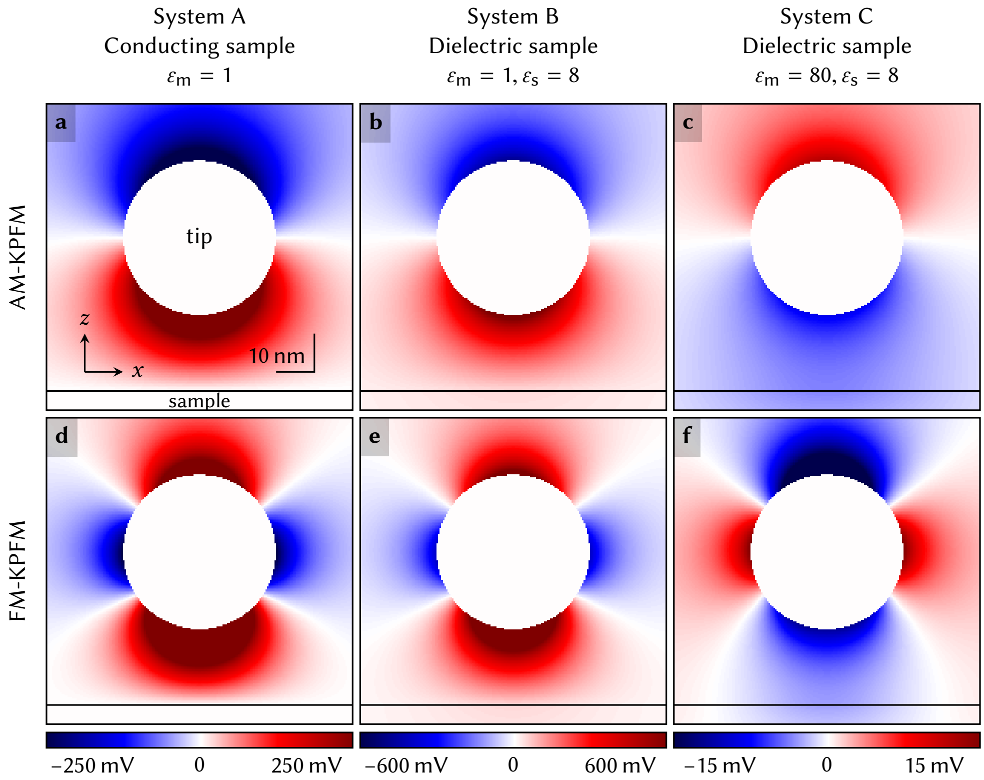

Figure 4.4: Weight function for charges in AM-KPFM (top row) and FM-KPFM (bottom row). The considered tip-sample systems A, B and C are shown in the first, second and third column, respectively. The tip-sample distance is $z_{ts} = 20$ nm, the tip radius is $R = 20$ nm and the amplitude is $A = 0$. The weight function corresponding to other parameters can interactively explored at `www.self-assembly.uni-mainz.de/kpfm`. The coordinate system and scale bar shown in panel a apply to all panels. The sample surface at $z = 0$ is indicated by a horizontal black line.

between the two metallic electrodes. Note that, within the electrostatic model we employ here, V_{CPD} is only a property of the metallic electrodes and does not depend on their geometry, the tip displacement and the oscillation amplitude.

4.2.3 Properties of the weight function for charges

Using the electrostatic model introduced in the last section, we can evaluate the weight function for charges as is shown in figure 4.4.

The value of the weight function in the area below the tip (the tip sphere is indicated by a white circle) is of primary interest as charges are typically located in the tip-sample gap and in close proximity to the sample surface. It is a common assumption, especially in UHV-based experiments, that the sign of the KPFM signal corresponds to the sign of the charges in the tip-sample gap.[176,182,184,185] For systems A and B in both the AM and FM-KPFM mode, we find indeed that the sign of the weight function below the tip is positive, thus the sign of the charges q_i in equation 4.45 is maintained in the KPFM signal V_{KPFM}. In sharp contrast, the sign of the KPFM weight function below the tip is negative in system C for the tip-sample distance evaluated in figure 4.4. The inversion of the sign of the weight function is readily explained by the sign of the derivative of the capacitance that enters the weight function, as detailed in reference 198 and in the following section:

For the conductive sample (system A) the capacitance of the system is at its maximum when the distance between the tip and the conductive sample is at its minimum ($z_{\mathrm{ts}} \longrightarrow 0$), similar to a parallel-plate capacitor. Consequently, the capacitance decreases for increasing tip-sample distance, leading to a negative first derivative of C_{void} with respect to z_{ts}. For dielectric samples, the capacitance of the void tip-sample system is additionally influenced by the permittivity of both, sample and medium. For system B ($\varepsilon_{\mathrm{m}} < \varepsilon_{\mathrm{s}}$) the capacitance is again at its maximum when the tip is placed directly above the sample, since here the tip is surrounded by both, the dielectric sample and the dielectric medium. In the limit of a large tip-sample distance, the tip is only surrounded by the medium, which has a smaller permittivity than the sample. Therefore, for system B, the first derivative of C_{void} with respect to z_{ltp} is again negative. In system C, however, the capacitance decreases for decreasing tip-sample distances, since the sample has a smaller dielectric permittivity compared to the medium. This effect readily explains the observation of an inversed sign when performing KPFM measurements in a medium with a permittivity ε_{m} larger than the permittivity ε_{s} of the sample.[198] We discuss the far-reaching consequences of this sign inversion in the next section.

Despite the change in sign for system C, a different overall magnitude of the weight function for charges as well as a different decay can be recognized in figure 4.4 when comparing different modes and sample systems – both aspects are again discussed in the next section. Finally, to illustrate that the KPFM weight function depends on the displacement between tip and sample, we exemplary plot the AM-KPFM weight function for system A in figure 4.5 for three different tip-sample distances. As the tip approaches the sample, the asymmetry of the weight function (when comparing the area beneath and above the tip) becomes more pronounced.

4.2.4 KPFM signal for relevant charge distributions

In this section, we calculate the KPFM signal V_{KPFM} using equation 4.45 for different charge distributions that resemble, for example, charged adsorbates such as molecules or atoms, deposited on metallic and insulating surfaces. The charges in the tip-sample system are all defined by their magnitudes q_i and positions $\mathbf{r}_{\mathrm{i}}$. For a given displacement

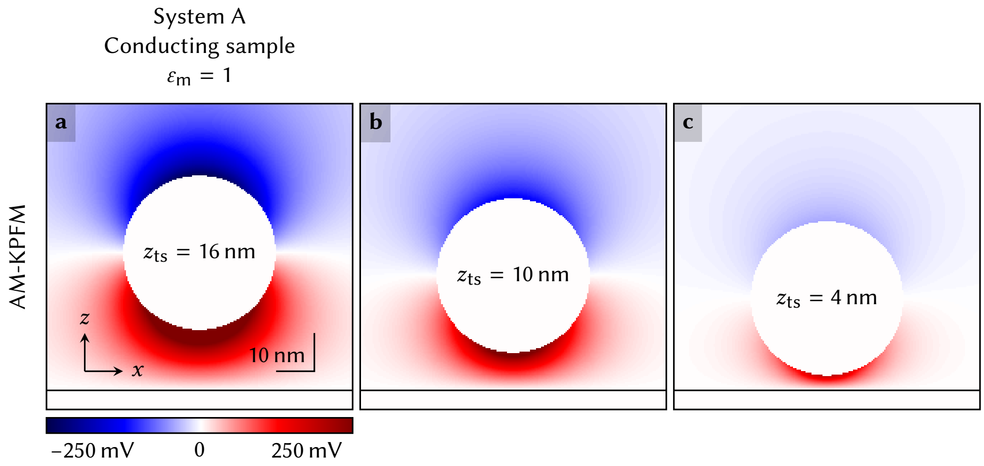

Figure 4.5: The weight function for charges in AM-KPFM for system A is shown for different tip-sample distances z_{ts}. The color bar applies to all panels.

between tip and sample, the weight function is then evaluated at the positions of the charges.

We start with considering a single point charge, for which we discuss the sign of the KPFM signal and the influence of the oscillation amplitude. Next, we investigate the signal for two point charges to quantify the lateral resolution of KPFM and the imaging of differently-oriented dipoles. We continue with considering samples that exhibit a layer of surface charge to reveal the dependency of the KPFM signal on the sample size.

Imaging a single point charge

We consider a single positive point charge of magnitude e, located at a height of $z = 0.2$ nm above the surface and in the center ($x = 0, y = 0$) of our coordinate system. To disentangle effects in the KPFM signal due to the tip-sample geometry from the averaging over the oscillation cycle, we start by setting the oscillation amplitude A to zero. This corresponds to experiments in the static AFM mode. We will close this section by discussing the effect of increasing the oscillation amplitude.

Lateral images

We show images of the calculated KPFM signal as a function of x_{ts} and y_{ts} in figure 4.6, where the tip-sample distance z_{ts} is held constant at 0.5 nm. The upper panel of figure 4.6 shows the AM-KPFM signal, the lower panel shows the FM-KPFM signal.

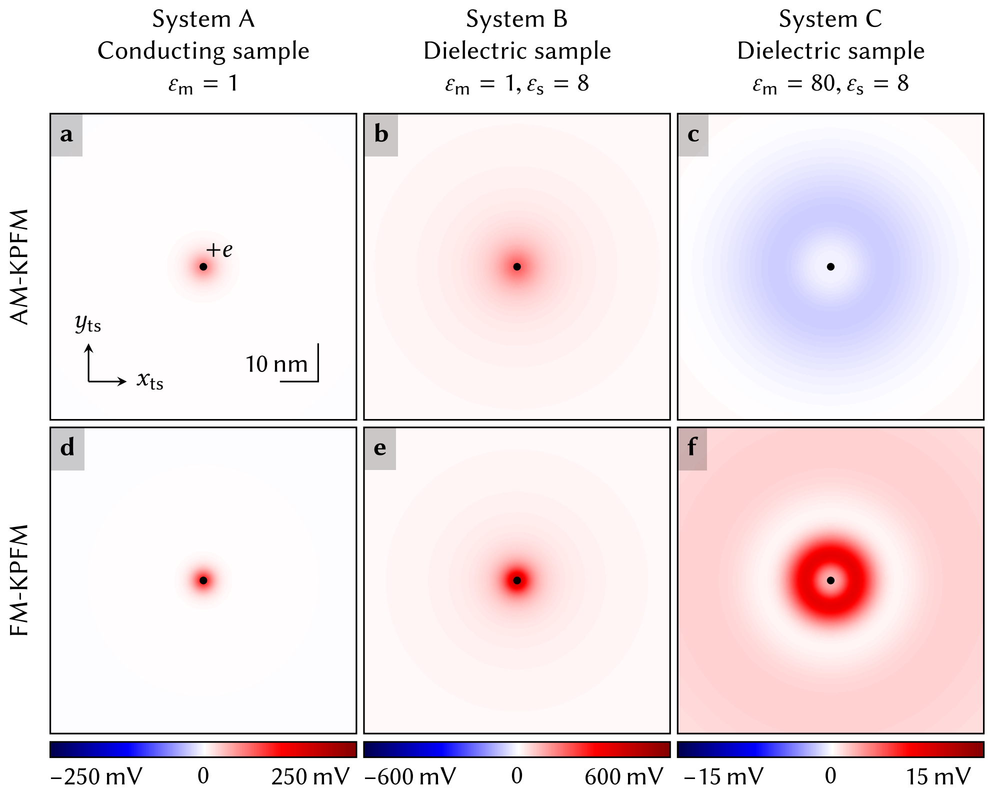

Figure 4.6: Lateral images of the KPFM signal calculated for a point charge $+e$ (black dot) located at $x = 0$, $y = 0$ and $z = 0.2$ nm. The sample surface is located at $z = 0$. The oscillation amplitude A is set to zero and the tip-sample distance is $z_{ts} = 0.5$ nm. The coordinate system and scale bar shown in panel a apply to all panels, the color bars to both images above each bar.

For the conductive sample (system A, panel a and d) and the dielectric sample with $\varepsilon_m < \varepsilon_s$ (system B, panel b and e), the positive charge results in a positive KPFM signal at the position of the charge. Although the magnitude of V_{KPFM} is different for the different sample systems, the sign of the KPFM signal corresponds to the sign of the charge regardless of using AM-KPFM or FM-KPFM. Moreover, the KPFM signal is at its maximum when the tip is positioned directly above the point charge. The charge is imaged with radial symmetry and with a lateral extend in the order of several nanometer.

In sharp contrast, the *positive* point charge yields within the shown image an overall *negative* AM-KPFM signal for the dielectric sample with $\varepsilon_m > \varepsilon_s$ (system C, figure 4.6 c), and is furthermore in both modes (figure 4.6 c and f) imaged as a toroidal ring with a local minimum at the position of the charge. Consequently, the qualitative interpreta-

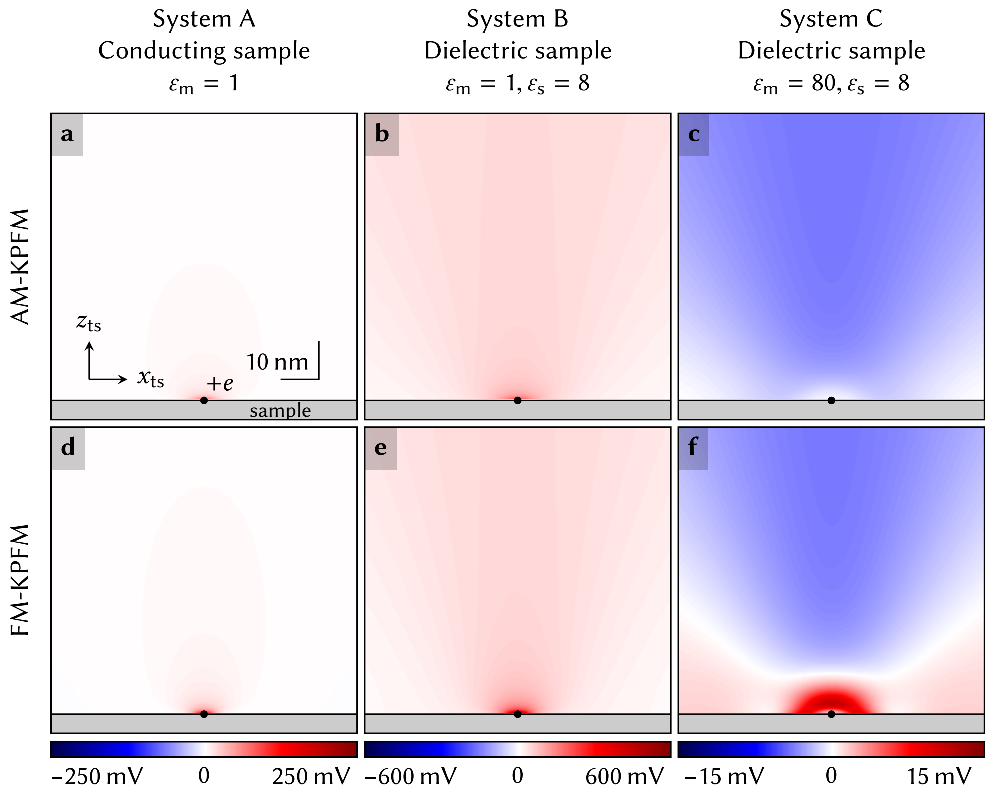

Figure 4.7: Vertical slice of the KPFM signal calculated for a point charge $+e$ (black dot) located at $x = 0$, $y = 0$ and $z = 0.2$ nm. The oscillation amplitude A is set to zero. The coordinate system and scale bar shown in panel a apply to all panels, the color bars to both images above each bar.

tion of AM-KPFM in system C is different compared to systems A and B, especially since the sign of the KPFM signal reverses in the AM-KPFM mode. The physical reason for the sign reversal of the KPFM signal is the sign reversal of the derivatives of the capacitance, as discussed in section 4.2.3.

Vertical slices

Next, we consider the same systems A, B and C, but evaluate the KPFM signal in the form of slices as shown in figure 4.7. Thereby, we investigate the dependence of the KPFM signal on the tip-sample distance.

For systems A and B, we see that the KPFM signal for both the AM and the FM-KPFM mode has the same sign in the entire z_{ts} range of up to $z_{ts} = 75$ nm as shown in figures 4.7 a, b, d and e. In contrast, the AM-KPFM signal obtained in system C (figure 4.7 c) has an inverted sign throughout the investigated tip-sample distance regime, and the sign of the KPFM signal for system C in the FM mode (figure 4.7 f) differs *within* the evaluated tip-sample distance regime. This finding highlights that qualitative statements regarding the sign of the point charge can be a challenge in FM-KPFM experiments for systems of type C (where $\varepsilon_\mathrm{m} > \varepsilon_\mathrm{s}$), and especially require knowledge of the tip-sample distance when using the FM-KPFM mode for systems of type C.

The vertical slices furthermore show that the KPFM signal changes monotonically upon approaching the tip closer to the charge for both system A and B, while the behavior for system C is more complex as the KPFM signal can even change the sign (see figure 4.7 f).

Lateral and vertical profiles

It is common practice to experimentally measure the KPFM signal along specific surface directions in order to obtain the KPFM signal in profiles, *e.g.*, as function of x_ts or z_ts. To facilitate comparison of these experiments with the KPFM signal of a single point charge, we show lateral and vertical profiles of the KPFM signal in this section. Using our model we calculate lateral profiles obtained at three different tip-sample distances ($z_\mathrm{ts} = 0.5$ nm, 2 nm and 10 nm) as shown in figure 4.8.

For systems A and B (black and blue lines), the KPFM signal shows a single peak in the lateral profiles, for the AM- and the FM-KPFM mode. The signal is at maximum when the tip is positioned centered on the charge. Moreover, the width of the peak increases for increasing tip-sample distances. As already discussed for the lateral and vertical slices, a non-monotonic shape of the KPFM signal is observed for system C when approaching the tip to the charge (red solid lines). Additionally, the AM-KPFM signal in system C is negative for all tip-sample distances shown in figure 4.8. In contrast, the FM-KPFM signal for system C changes depending on the tip-sample distance (figure 4.8 e and 4.8 f).

Vertical profiles of the KPFM signal extracted at the lateral position of the point charge are shown in figure 4.9. For system A and B, the KPFM signal increases for decreasing tip-sample distances. The increase in the KPFM signal is particularly steep when the tip is close to the sample, and the signal magnitudes clearly differ for the different KPFM modes. The absolute value of the KPFM signal in system C decreases for the AM mode when increasing the tip-sample distance and, again, a non-monotonic behavior is observed for system C in the FM mode, where the KPFM signal exhibits a maximum in the vertical profile (red dashed line) shown in figure 4.9.

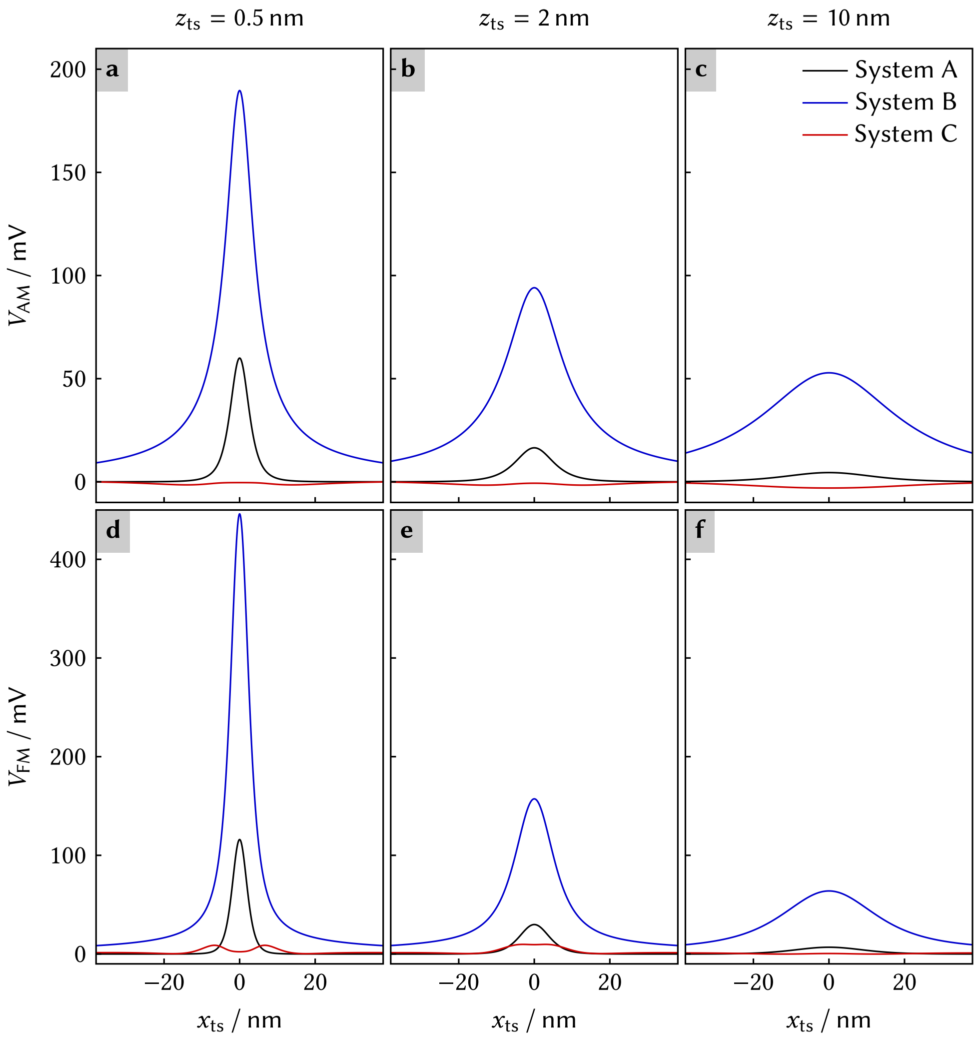

Figure 4.8: Lateral profiles of the KPFM signal calculated for a point charge $+e$ located at $x = 0$, $y = 0$ and $z = 0.2$ nm. The oscillation amplitude A is set to zero. The tip-sample distance z_{ts} at which the tip has been scanned is indicated above the top panel.

Influence of the oscillation amplitude

We have so far chosen the oscillation amplitude A to be zero for all calculations of the KPFM signal, corresponding to the static AFM case. However, in dynamic AFM the oscillation amplitude is not zero. Therefore, we explore the effect of a non-zero oscillation amplitude on the KPFM signal in this section. According to the definition of the weight functions (equations 4.46 and 4.47), both the derivative of the normalized

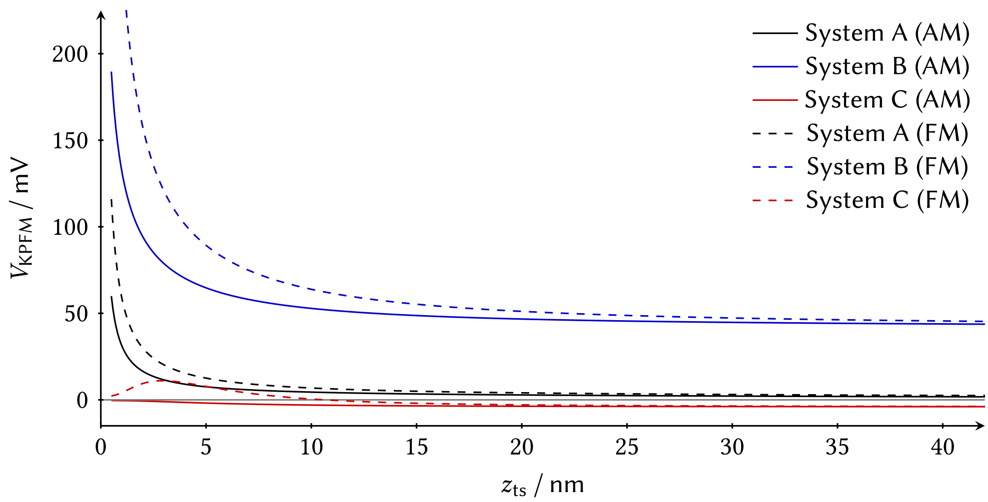

Figure 4.9: Vertical profiles of the KPFM signal calculated for a point charge $+e$ located at $x = 0$, $y = 0$ and $z = 0.2$ nm. The oscillation amplitude A is set to zero. The tip was positioned directly above the charge at $x_{\text{ts}} = 0$ and $y_{\text{ts}} = 0$.

electric potential of the void tip-sample system $\hat{\Phi}_{\text{void}}$ and the corresponding derivative of the capacitance C_{void} are averaged over the tip-sample distance range sampled during one oscillation cycle.

To illustrate the effect of this averaging, we calculate in figure 4.10 the KPFM signal along the same line profile shown in figure 4.8 with amplitudes of 0.1 nm, 1 nm, 10 nm and 100 nm and compare them with the $A = 0$ case. In all cases, we set the lower turning point of the tip oscillation to $z_c - A = 0.5$ nm. Therefore, the tip-sample distance range considered for the averages (equations 2.20 and 2.21) is $z_{\text{ts}} \in [-A + z_c, z_c + A]$.

Figure 4.10 a presents the AM-KPFM signal for a conductive sample (system A). The profile lines indicate that the KPFM signal at the position of the charge decreases for increasing oscillation amplitudes by a factor of about two. A qualitatively similar behavior can be found for FM-KPFM (figure 4.10 f) in system A and for system B (figure 4.10 b and g). For system C in FM-KPFM, even the sign of the KPFM signal can change depending on the oscillation amplitude (figure 4.10 h). While the KPFM signal of a charge-free system does not depend on the oscillation amplitude,[193] it is clearly emphasized from figure 4.10 that a quantitative comparison of KPFM signals between different experiments cannot be made without considering the amplitude when considering systems containing charges.

For an investigation of the peak shape we normalize the profiles with respect to the maximum value of the peak (at $x_{\text{ts}} = 0$). Normalized profiles are only calculated for

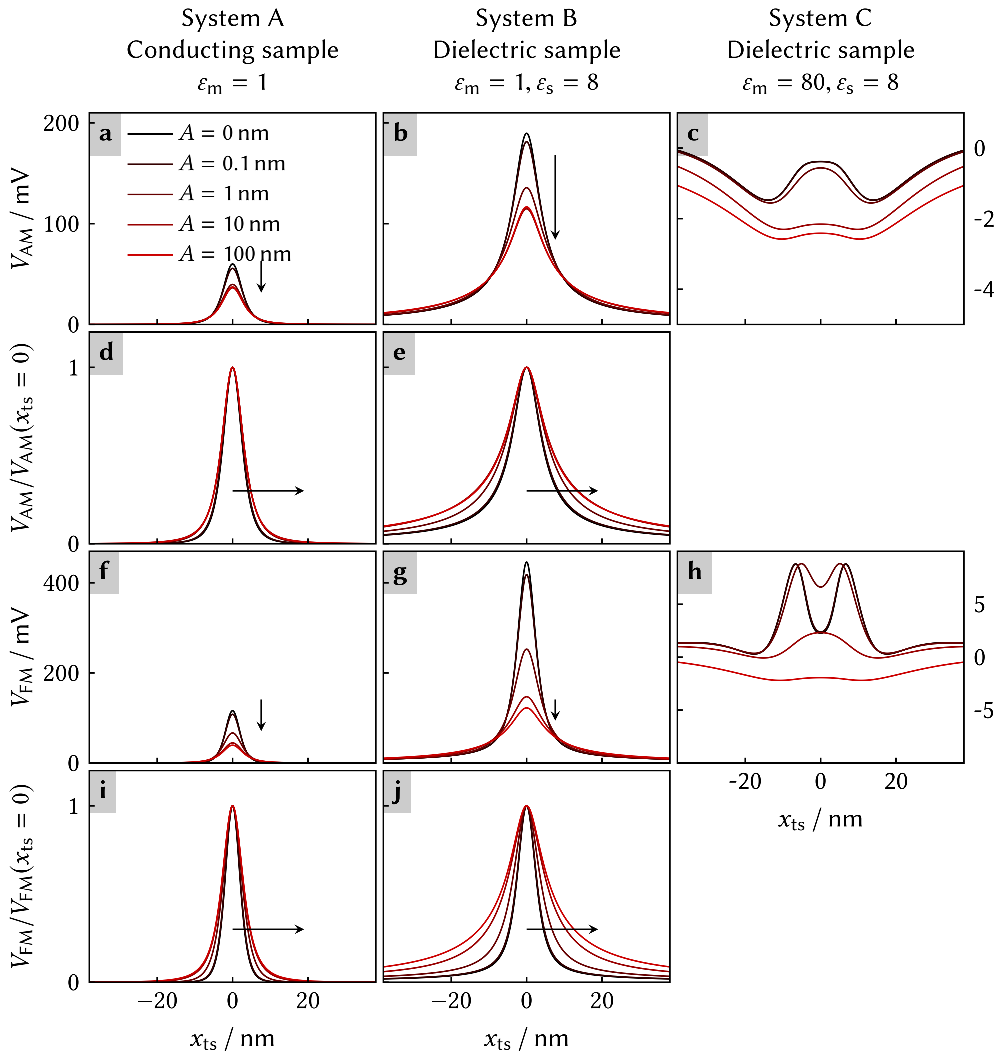

Figure 4.10: Lateral profiles of the KPFM signal calculated for a point charge $+e$ located at $x = 0$, $y = 0$ and $z = 0.2$ nm calculated for several oscillation amplitudes A, namely 0 nm, 1 nm, 10 nm and 100 nm (increasing the amplitude is indicated by the black arrow). The lower turning point of the tip oscillation was held constant at $z_c - A = 0.5$ nm. Panels in the second and fourth row present the KPFM signal normalized to the respective maximum value at $x_{ts} = 0$.

systems A and B, since only here the KPFM signal has a consistent sign and peak-like shape in lateral profiles. The results in figure 4.10 d, e, i and j clearly show an increase in the width of the peaks with increasing the oscillation amplitude. This finding is related to the peak-broadening observed for increasing tip-sample distances (figure 4.8) combined with the fact that the properties at larger tip-sample distances increasingly contribute with increasing the oscillation amplitude. As we will discuss in the next section, the lateral resolution in KPFM experiments is effectively reduced with larger peak widths.

These conclusions can also be drawn for system A in the FM-KPFM mode as well as for system B in both, the AM and the FM-KPFM mode as is apparent from figure 4.10. Thus, for system A and B, increasing the oscillation amplitude causes a decrease in the KPFM signal at the charge position and an increase of the peak width. However, the sign of the KPFM signal does not change as function of the oscillation amplitude. This allows qualitative statements regarding the sign of the charge to be made independent of the oscillation amplitude for system A and B.

Lateral resolution for imaging charges with KPFM

The lateral resolution of KPFM experiments is an important figure to assess when aiming to image charges with KPFM. We define the lateral resolution for imaging charges with KPFM by the minimal lateral distance at which two equally-charged point charges can be distinguished. The lateral resolution is influenced by several parameters, such as the vertical tip position z_{ts} and the oscillation amplitude A. In the previous sections, we have found that the KPFM signal images a single point charge as a single peak (for systems A and B in both, AM- and FM-KPFM modes). We obtained the sharpest peaks for the smallest considered tip-sample distance of $z_{\text{ts}} = 0.5\,\text{nm}$ (figure 4.8) and for the smallest considered oscillation amplitude $A = 0$ (figure 4.10). We will use these two parameters in the following for illustrating the lateral resolution.

Figure 4.11 presents lateral profiles of the KPFM signal for two positive point charges (each $+e$, each located at $z = 0.2\,\text{nm}$ above the surface). The charges are positioned at different lateral distances indicated by the dots. The corresponding KPFM line profiles are shifted vertically for clarity. When the charges are placed 10 nm apart, they appear as two clearly separable peaks in the profiles shown in figure 4.11. When ignoring measurement noise, these charges can be resolved if there is a minimum between the two peaks. However, KPFM experiments are always subject to measurement noise,[223]. Therefore, the resolution will be limited by a minimum detectable signal difference between the minimum between the peaks and the peak maximum. Upon moving the charges towards each other, eventually the two peaks merge to a single peak. For all considered cases (system A and B, AM-KPFM and FM-KPFM), they appear as one peak at the smallest considered charge separation of 2 nm.

So far, we considered the lateral resolution for a fixed tip radius of $R = 20\,\text{nm}$. To investigate the influence of the tip radius on the lateral resolution, we plot the depth of the minimum between the charges (the “dip” voltage indicated as V_{dip} in figure 4.11 a) as a function of the tip radius R for two charges spaced 3 nm apart. Larger V_{dip} values

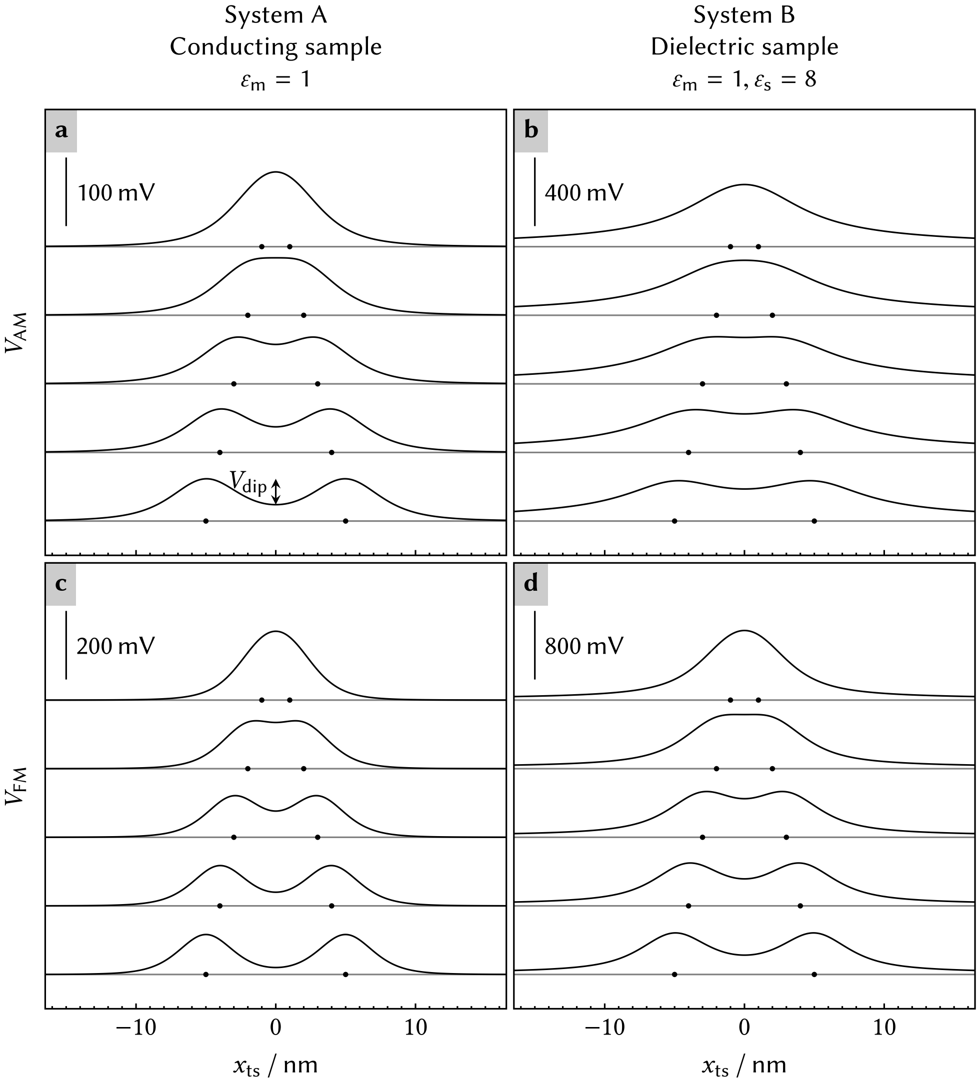

Figure 4.11: Lateral profiles of the KPFM signal for two point charges (+e located at $z = 0.2$ nm as indicated by arrows) and separated by increasing distances ranging from 2 nm to 10 nm. The individual profiles are shifted by the amount stated at the scale bar. In all cases, the oscillation amplitude A was set to zero and the tip-sample distance z_{ts} was held constant at 0.5 nm.

lead to more robust measurements of the two charges as larger noise can be accepted. If there is no minimum between the two charges, the charges cannot be distinguished.

The corresponding curves of V_{dip} vs. R are shown in figure 4.12 for system A and B in both, the AM and FM mode. In case there was no dip, no data is shown. With a

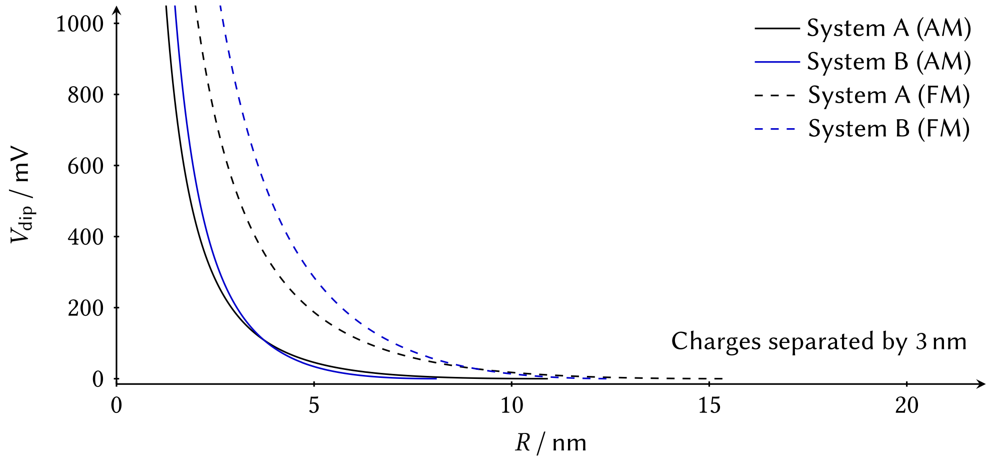

Figure 4.12: Lateral resolution quantified by the depth of the minimum V_{dip} between the two charge peaks as function of the tip radius for two charges separated by an arbitrarily chosen distance of 4 nm. No data denotes the absence of a dip between the signals at the two charge positions.

tip radius of $R > 20$ nm, the two charges cannot be separated, regardless of considering system A or B or by using AM-KPFM or FM-KPFM. Moreover, the dip voltage is consistently larger in the FM-KPFM modes (dashed lines) compared to the AM-KPFM modes (solid line), indicating that the resolution is increased in FM-KPFM measurements when compared to AM-KPFM. This conclusion is in agreement with KPFM experiments on conducting surfaces of different local composition, where an increased lateral resolution was found for the FM-KPFM mode as well.[194]

Imaging dipoles

Molecules that adsorb on surfaces often exhibit a dipole moment. To investigate the KPFM signal produced by such a molecular adsorbate, we calculate the KPFM signal that arises from either a vertical or a horizontal dipole. In each case, the dipole results from placing two charges of opposite sign.

Vertical dipole

First, we consider the KPFM signal for a system containing a *vertical* dipole centered at $x = 0$ and $y = 0$ as shown in figure 4.13. The dipole points upwards, *i.e.*, a negative charge is located at $z = 0.15$ nm and a positive charge at $z = 0.25$ nm, which results in a dipole length of 0.1 nm and a dipole moment of $1e\text{Å} \approx 4.8$ D. The oscillation amplitude of the tip is set to zero.

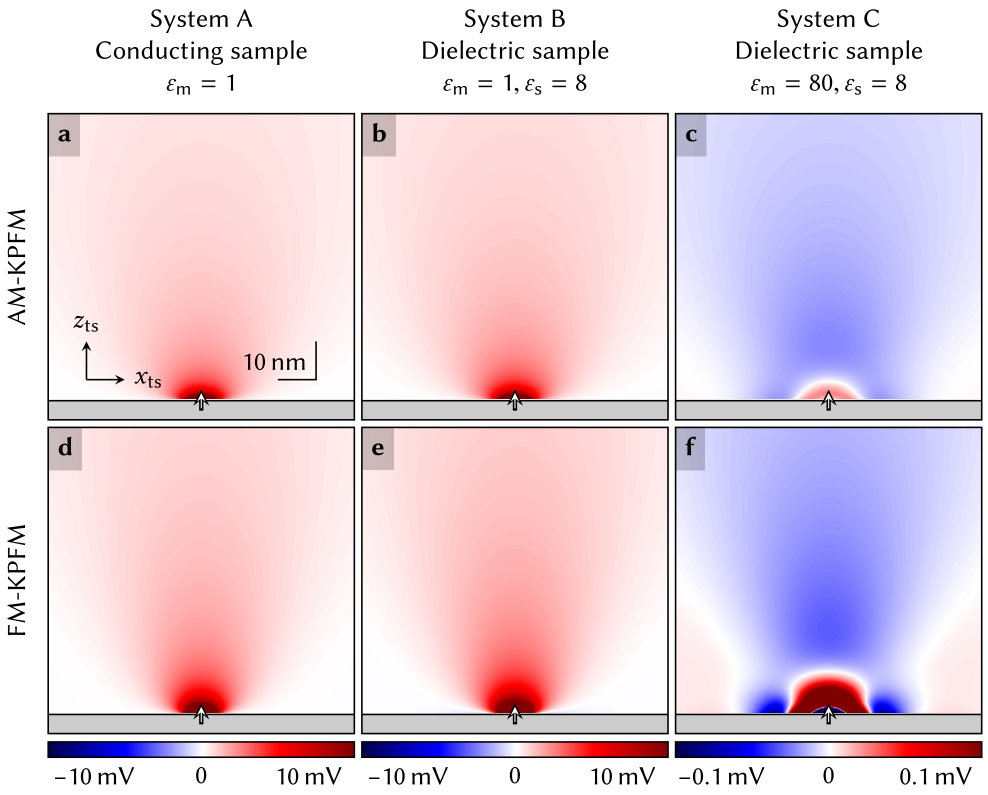

Figure 4.13: Vertical slice of the KPFM signal calculated for a vertical dipole (pointing upwards) located at $x = 0$, $y = 0$ and $z = 0.2$ nm. The oscillation amplitude A is set to zero. The coordinate system, scale bar and position of the dipole shown in panel a apply to all panels, the color bar to both images above each bar.

For systems A and B, the vertical slice reveals a KPFM signal qualitatively similar to the one obtained for a single positive point charge (see figure 4.7). The KPFM signal for the upward-pointing dipole is positive in both, AM- and FM-KPFM mode. This is a result from the weight function for charges having its maximum directly beneath the tip (for system A and B) and then falling off for increasing distances. Therefore, the upper charge of the dipole is closer to the tip and its contribution to the KFPM signal is larger compared to the lower charge. However, the presence of the lower charge of the dipole readily explains the overall smaller magnitude of the KPFM signal when compared to a single point charge (see figure 4.7).

In contrast to systems A and B, the vertical slice of the KPFM signal for the vertical dipole obtained for system C is qualitatively different than the vertical slice of the single point charge (figure 4.7). The KPFM signal in AM-KPFM is positive when the tip is directly above the dipole. In FM-KPFM, the vertical dipole produces negative side lobes. The sign of the KPFM signal in system C depends again on the tip-sample distance as was found for the single point charge in system C before, and the KPFM signal for the dipole is furthermore smaller than the point charge signal in figure 4.7.

Horizontal dipole

A vertical slice of the KPFM signal obtained for a *horizontal* dipole is shown in figure 4.14. The dipole is again centered at $y = 0$ and $z = 0.2\,\text{nm}$ and results from two charges, $-e$ at $x = -0.05\,\text{nm}$ and $+e$ at $x = 0.05\,\text{nm}$. Consequently, the dipole is pointing in the positive x direction. For systems A and B and in both, AM- and FM-KPFM mode (figures 4.14 a, b, d and e), the dipole produces a negative KPFM signal for $x_{\text{ts}} < 0$ and a positive KPFM signal for $x_{\text{ts}} > 0$. Since the weight function has a radial symmetry for the spherical tip used within this section, the KPFM signal is zero at $x_{\text{ts}} = 0$ as both charges cancel each other. Imaging the lateral dipole with a different sign depending on the lateral position provides means to distinguish the lateral dipole clearly from a single point charge. The KPFM signal obtained for system C shows a rather complex behavior including different signs depending on the vertical and lateral tip position, as expected from the insights obtained for the single point charge.

Surface charge distribution

We have so far calculated the KPFM signal for one and two point charges, but neglected that a substrate, which is usually large compared to the tip dimensions, is often covered by *e.g.* charged defects or charged atoms or molecules. Therefore, we now extend the analysis by quantifying the contribution to the KPFM signal due to a large number of point charges, most of which are located at large distances from the tip.

We plot the KPFM weight function W_{KPFM} in figure 4.15 for a fixed tip position $\mathbf{r}_{\text{ts}} = (0, 0, 5\,\text{nm})$ centered above the origin as function of distance $r = \sqrt{x^2 + y^2 + z^2}$ from the origin. The lateral distance interval is evaluated from $r = 0.2\,\text{nm}$ (*i.e.*, close to the tip) up to $r = 1\,\text{mm}$ (representing the edge of the sample far away from the tip). The profile of the weight function is computed for a fixed height $z = 0.2\,\text{nm}$ (with the tip at $z_{\text{ts}} = 5\,\text{nm}$) and we set again the oscillation amplitude A to zero.

For all considered tip-sample systems A, B and C and for both, AM- and FM-KPFM modes, the weight function decays to zero in the limit $r \longrightarrow \infty$. However, there is a striking difference in the fall-off behavior when comparing the conductive sample (system A) with the dielectric samples (systems B and C). The AM-KPFM and FM-KPFM weight functions decay both with r^{-3} for the conductive sample (system A). On dielectric samples, however, the AM-KPFM and FM-KPFM weight functions both decay more slowly with r^{-1}.

To illustrate the consequences of the different lateral decays of the weight function, we consider a sample that is homogeneously covered with surface charges. These surface

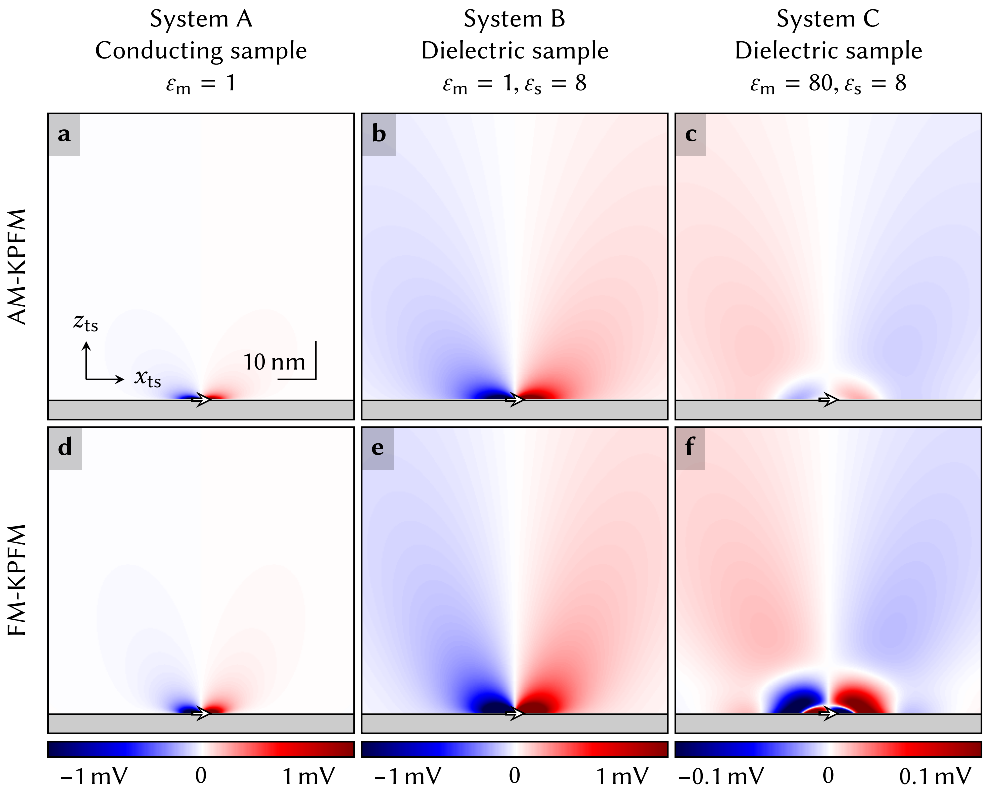

Figure 4.14: Vertical slices of the KPFM signal calculated for a horizontal dipole pointing to the right (centered at $x = 0$, $y = 0$ and $z = 0.2$ nm. The oscillation amplitude A is set to zero. The coordinate system, scale bar and position of the dipole shown in panel a apply to all panels, the color bar to both images above each bar.

charges could, *e.g.*, arise from defects as well as from polar or charged adsorbates. We model the surface charges as a charged circular-shaped island with surface charge density σ and radius r_σ (see figure 4.16). We assume that the charges are located at a height of $z = 0.2$ nm above the sample, *i.e.* at the same distance at which the weight function was analyzed in figure 4.15.

Using this charge distribution, we first model a sample where an island with a radius of $r_\sigma = 100$ nm covers the surface. The corresponding KPFM signal is shown as a function of the surface charge density σ in figure 4.17 for the (a) AM-KPFM and (b) FM-KPFM modes and for systems A (conductive sample and $\varepsilon_m = 1$, dotted black lines) and B (dielectric sample with $\varepsilon_s = 8$ and $\varepsilon_m = 1$, dotted blue lines).

Next, we compare the KPFM signal with the signal that is produced by a charged island that covers a large portion of the sample by setting its radius to $r_\sigma = 1$ mm. On the conductive sample (system A), the KPFM signal remains nearly constant (solid

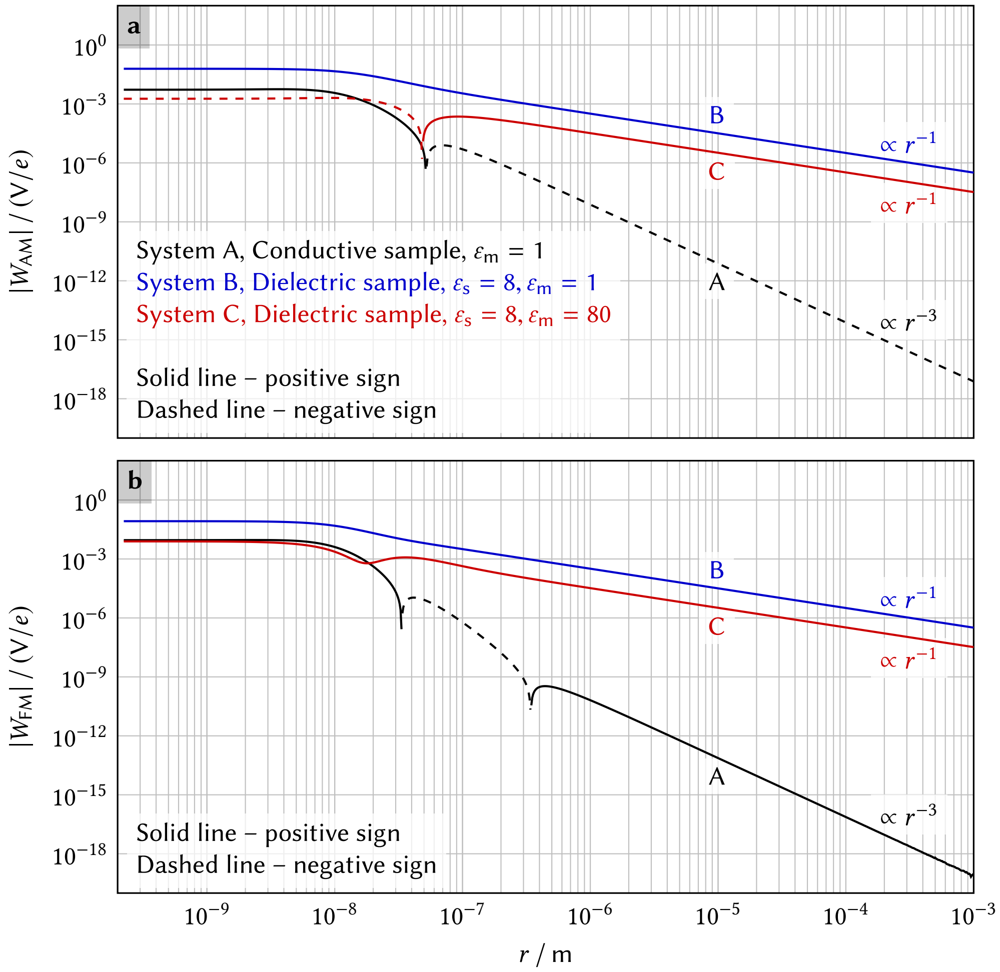

Figure 4.15: Lateral profiles of the AM-KPFM weight function for charges (a) and the FM-KPFM weight function for charges (b) as function of the distance r from the origin in a double-logarithmic plot.

black lines in figure 4.17) when compared to the KPFM signal obtained for the smaller charged island with radius $r_\sigma = 100$ nm. This indicates that the charges that contribute to the KPFM signal are overwhelmingly located beneath the tip.[4] In this case, the KPFM signal converges with respect to the radius of the charged island.

In sharp contrast, the KPFM signal obtained for the dielectric sample (system B) differs *several orders of magnitude* compared to the smaller island with $r_\sigma = 100$ nm. In this

---

[4] The slight decrease in the KPFM signal when increasing r_σ from 100 nm to 1 mm originates from the negative sign of the weight function for system A in the distance range of $r \gtrsim 100$ nm (see black solid and dashed line in figure 4.15 a).

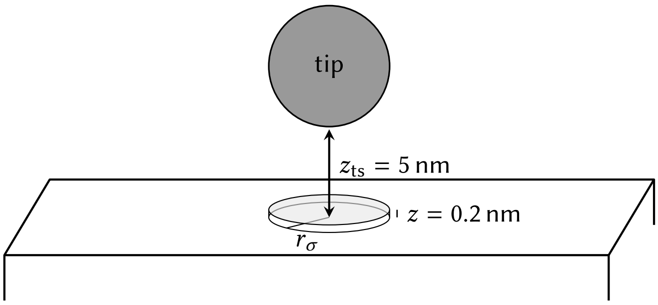

Figure 4.16: Illustration showing the charged island (gray circle) with radius r_σ located at a height of $z = 0.2\,\text{nm}$ above the sample. The tip (with tip radius $R = 20\,\text{nm}$) is placed at a distance of $z_{ts} = 5\,\text{nm}$ above the sample. The illustration is not to scale.

case, even for a surface charge density of $\sigma = 10^{-6}\,e/\text{nm}^2$, the KPFM signal obtained for the dielectric sample is in the order of several volts. Indeed, Kelvin voltages on surfaces of especially freshly cleaved insulating materials have been found to be of the order of several 10 V.[224] As already clear from the decay in figure 4.15, charges from the whole sample contribute critically to the KPFM signal when considering dielectric samples. Here, the KPFM signal does not converge with respect to the radius of the charged island.

Thus, the different lateral decay of the weight function for charges in KPFM that is obtained for a conductive sample compared to a dielectric sample has a significant impact on the interpretation of KPFM data. For conductive samples, the major contribution to the KPFM signal arises from charges that are in the proximity of the tip. On dielectric samples, in contrast, charges located on the *whole* sample can significantly contribute to the KPFM signal. In this case, the KPFM signal consequently depends on the size of the sample.

4.2.5 Electrostatic model

In this final section, we present details on the calculation of $\hat{\Phi}_{\text{void}}$ and C_{void} – the two electrostatic quantities necessary for calculating the KPFM weight function for charges. Since we use the model of a spherical tip, we will here revisit the solution for a metallic sphere against a dielectric or metallic sample following previous works, which are based on infinite image charge series.[205,225] The method of infinite image charge series for both the sphere-conductor and the sphere-dielectric setup is based on two concepts for solving electrostatic boundary problems using image charges: (a) the case of a point charge in front of a dielectric (or metallic) half-space and (b) the case of a point charge in front of a conducting sphere.

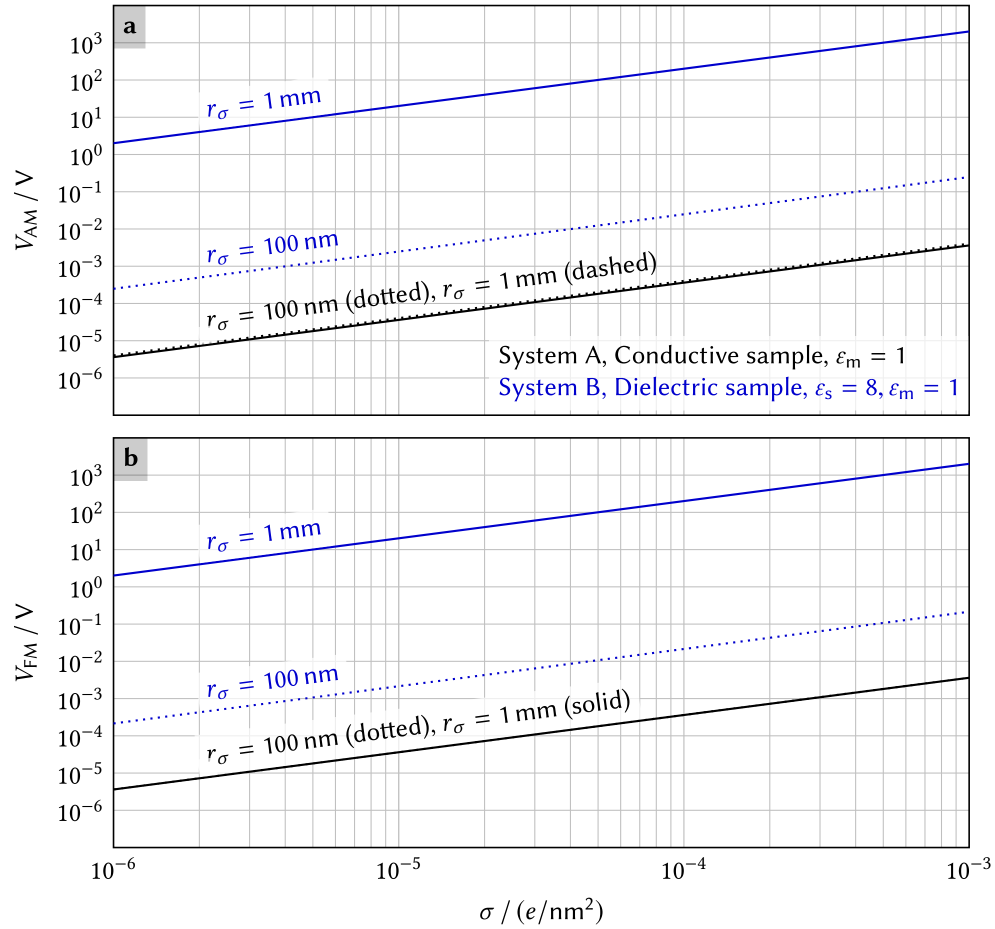

Figure 4.17: Calculated AM-KPFM signal (a) and FM-KPFM signal (b) for a homogeneously charged island with radius r_σ as function of the island's surface charge density σ. The tip is positioned above the center of the charged island at $r_{\mathrm{ts}} = 0$ and $z_{\mathrm{ts}} = 1\,\mathrm{nm}$. The charges within the island are located at $z = 0.2\,\mathrm{nm}$, the oscillation amplitude is set to zero

Point charge in front of conductive or dielectric half-space

For a point charge q in a medium with relative permittivity ε_{m} at a distance b in front of a dielectric or conductive half-space, an image charge with magnitude $\xi' = -\beta q$ placed at $b' = -b$ yields the correct boundary condition at the interface.[226] The factor β is defined by the dielectric permittivities according to

$$\beta = \frac{\varepsilon_{\mathrm{s}} - \varepsilon_{\mathrm{m}}}{\varepsilon_{\mathrm{s}} + \varepsilon_{\mathrm{m}}}, \tag{4.48}$$

where ε_{s} is the permittivity of the lower half-space. For a metal, $\beta = 1$.[205]

The potential for the upper half-space ($z \geq 0$) is then defined by the point charge q and image charge ξ'

$$\Phi(\mathbf{r}) = \frac{1}{4\pi\varepsilon_0\varepsilon_\mathrm{m}} \left(\frac{q}{\sqrt{x^2 + y^2 + (b-z)^2}} + \frac{-\beta q}{\sqrt{x^2 + y^2 + (b+z)^2}} \right). \tag{4.49}$$

To calculate the electrostatic potential for the lower half-space ($z < 0$) it is necessary to place a different image charge ξ'' with magnitude $\xi'' = q - \xi' = q(1+\beta)$ in the upper half space at the same position as the charge q. The potential for $z < 0$ then reads

$$\Phi(\mathbf{r}) = \frac{q(1+\beta)}{4\pi\varepsilon_0\varepsilon_\mathrm{s}\sqrt{x^2 + y^2 + (b-z)^2}}. \tag{4.50}$$

Point charge outside of a conductive sphere

For a point charge q located outside of a conducting sphere at a distance y from the center, an image charge ξ' is placed on the line connecting the point charge q with the center of the sphere. The image charge of magnitude $\xi' = -\frac{a}{y}q$ is placed at distance $d = \frac{a^2}{y}$ from the sphere center to match the boundary condition at the sphere surface.[226] Then, the total electrostatic potential for the conducting sphere of radius R at potential V in a medium with relative permittivity ε_m and a point charge at distance y is given from the sum of potentials for three point charges:

$$\Phi(\mathbf{r}) = \frac{1}{4\pi\varepsilon_0\varepsilon_\mathrm{m}} \left(\frac{q}{|\mathbf{r} - \mathbf{y}|} + \frac{-\frac{R}{y}q}{\left|\frac{a^2}{y^2}\mathbf{y} - \mathbf{r}\right|} + \frac{RV}{|\mathbf{r}|} \right) \tag{4.51}$$

for $|\mathbf{r}| \geq R$. While the first two terms ensure the boundary condition on the sphere surface for a neutral sphere due to the external charge, the last term includes the potential distribution due to the charged surface.

Conductive sphere in front of dielectric or conductive half-space

Using these two concepts, the solution for the conducting sphere in front of the conductive or dielectric half-space can be found using series of image charges.[205,225]

A single point charge $\xi_0 = 4\pi\varepsilon_0\varepsilon_\mathrm{m}RV$ is placed at $z_0 = R + z_\mathrm{ts}$, representing a conducting sphere of radius R at constant potential V in the medium with ε_m and with the center positioned at $R + z_\mathrm{ts}$ from the lower half-space, see also figures. 4.3 and 4.18. The dielectric material ε_s is modeled with an infinite thickness where the metallic back contact resides at $z \longrightarrow -\infty$. In practice, this approximation is usually fulfilled as the sample thickness is much larger compared to the sphere radius R and the tip-sample

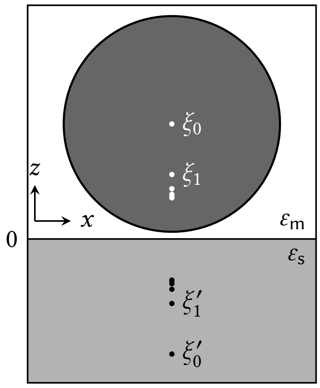

Figure 4.18: Geometry of the sphere-dielectric system including the positions of the image charges.

separation z_ts. Furthermore, and without loss of generality, the potential can be set to ground at this back electrode.

While the boundary condition at the sphere is fulfilled with the point charge ξ_0, the boundary condition at the dielectric boundary is not. The latter can be corrected by placing an image charge

$$\xi_0' = -\beta\xi_0 \qquad \text{at} \quad z_0' = -z_0 \tag{4.52}$$

and $x = 0, y = 0$. The image charges series $\{\xi_i\}$ and $\{\xi_i'\}$ define the electrostatic potential in the upper half-space (above the sample, at $z \geq 0$). The electrostatic potential at $z < 0$ is given from placing an image charge of magnitude

$$\xi_0'' = \xi_0 - \xi_0' = (1+\beta)\xi_0 \qquad \text{at} \quad z_0'' = z_0 \tag{4.53}$$

in the upper half-space. Now the image charge ξ_0' violates the boundary condition on the sphere, which can again be fixed by placing according image charges. The concept of infinite charge series relies on an alternating correction of the two boundary conditions, whereby the infinite series fulfills all boundary conditions.

The infinite series of image charges continues with

$$\xi_1 = \frac{R}{2(R+z_\mathrm{ts})}\beta\xi_0 \quad \text{at} \quad z_1 = R + z_\mathrm{ts} - \frac{R^2}{2(R+z_\mathrm{ts})}, \tag{4.54}$$

fulfilling the boundary condition at the sphere for ξ_0'. The series of image charges ξ_i, ξ_i' and ξ_i'' is then continued to alternatively fulfill the boundary conditions at the sphere and at the dielectric boundary. The magnitudes ξ_i and positions z_i of these image charges placed inside the sphere are given by the following recursive equations

(for $i > 0$)

$$z_i = z_0 - \frac{R^2}{z_0 + z_{i-1}} \quad \text{with} \quad z_0 = R + z_{\text{ts}} \tag{4.55}$$

$$\xi_i = \frac{R}{z_0 + z_{i-1}} \beta \xi_{i-1} \quad \text{with} \quad \xi_0 = 4\pi\varepsilon_0\varepsilon_{\text{m}} RV. \tag{4.56}$$

This charge series is accompanied by two further image charge series, namely ξ_i' and ξ_i'' according to

$$z_i' = -z_i, \tag{4.57}$$

$$\xi_i' = -\beta\xi_i, \tag{4.58}$$

$$z_i'' = z_i, \tag{4.59}$$

$$\xi_i'' = (1 + \beta)\xi_i. \tag{4.60}$$

Using the series of these charges, the potential Φ_{void} for both half-spaces follows directly from the superposition of the point charge potentials, namely

$$\Phi_{\text{void}}(\mathbf{r}) = \frac{1}{4\pi\varepsilon_0\varepsilon_{\text{m}}} \sum_{i=0}^{\infty} \left[\frac{\xi_i}{\sqrt{x^2 + y^2 + (z_i - z)^2}} + \frac{\xi_i'}{\sqrt{x^2 + y^2 + (z_i' - z)^2}} \right] \quad (\text{for } z \geq 0) \tag{4.61}$$

for the upper half-space and

$$\Phi_{\text{void}}(\mathbf{r}) = \frac{1}{4\pi\varepsilon_0\varepsilon_{\text{s}}} \sum_{i=0}^{\infty} \frac{\xi_i''}{\sqrt{x^2 + y^2 + (z_i'' - z)^2}} \quad (\text{for } z < 0) \tag{4.62}$$

for the lower half-space. The capacitance C_{void} of the system is given by the sum over all image charges ξ_i divided by the tip voltage V:

$$C_{\text{void}} = \frac{1}{V} \sum_{i=0}^{\infty} \xi_i. \tag{4.63}$$

As the magnitudes of the image charges converge quickly to zero, it is practical to only consider a finite number of terms. Since the positions of the charges converge quickly, the high-index elements can furthermore be represented by a single charge holding the sum of the remaining infinite charge series.[202,205]

For all calculations shown within this section, we truncated the infinite image charge series after 100 image charges and consider the additional single charge holding the sum of the remaining charges in the series.[202,205] After calculating the normalized electric potential and the capacitance, we numerically determined the derivatives needed for computing the weight functions in equations 4.46 and 4.47 using a central finite difference scheme of second order.

4.2.6 Conclusions and Outlook

In this section, we discussed the KPFM signal arising from charge distributions that represent charged adsorbates such as atoms or molecules on surfaces. As tip-sample system we considered a spherical tip surrounded by either vacuum, air, or liquid above either a conductive or dielectric sample. The KPFM signal of a single point charge, a pair of charges (dipole), a charged island and a layer of charges was calculated by convolution of the respective charge distributions with the weight function for charges.

For a single point charge we discussed lateral and vertical images and profiles of the KPFM signal. Interestingly, on dielectric samples, the KPFM signal arising from a single positive point charge can be positive or negative, depending on the dielectric permittivities of medium and sample. In some cases, the sign even depends on the tip-sample distance. This demonstrates that knowledge of the weight function for charges and the tip-sample distance is crucial, even for a qualitative interpretation of charges beneath the tip. Furthermore, the quantitative value of the obtained KPFM signal depends on the oscillation amplitude of the probe tip.

We provided means to quantify the lateral resolution of KPFM. For the spherical tip model we used here, two charges can only be resolved if their distance is at least in the range of the tip radius.

We considered two charges of equal magnitude but different sign, *i.e.* dipoles. Considering a sample in vacuum and air, a vertical dipole produces a KPFM signal with the same sign as its upper point charge. Only dipoles that are oriented horizontally on the surface can be clearly differentiated from a single point charge, since the sign of the KPFM signal inverts depending on the lateral position of the tip.

We compared the KPFM signal generated by an island of charges for different island sizes. Our analysis revealed that the KPFM signal does not converge with respect to the island size when considering dielectric samples. In case of dielectric samples, charges can significantly contribute to the KPFM signal, even if they are far away (in the range of mm) from the tip. Therefore, the KPFM signal obtained for dielectric samples that are covered with a layer of charges depends on the sample size. In contrast, on conductive samples, the charges that contribute to the KPFM signal are more locally confined within several tens of nanometers, since here the KPFM signal converges.

With this discussion of the KPFM weight function for charges, we aim for a coherent understanding of the KPFM signal generation to enable KPFM data interpretation.

4.3 Open-loop KPFM at mineral–water interfaces

In sections 4.3.1 to 4.3.3 I summarize selected aspects of my work "Probing charges on an insulating surface in liquids" (supervised by A. Kühnle, Johannes Gutenberg-Universität Mainz, reference 227), which I conducted as part of the qualification as a fast-track doctorate candidate.

4.3.1 Introduction

KPFM at solid–liquid interfaces (including mineral–water interfaces) is a recently introduced field of research.[105,106,108,220] The aim of KPFM at solid–liquid interfaces is to specifically probe electrostatic interactions, which arise from, *e.g.*, the presence of ions and, consequently, the accumulation of surface charges.[61,62] Since the method is based on applying a voltage between tip and sample, the presence of a liquid adds two major difficulties, compared to KPFM measurements in air and vacuum:[105] Applying a voltage can cause electrochemical reactions, *i.e.*, an electron transfer from the electrodes where the voltage is applied to molecular species in the liquid. Thereby, the composition of the solid–liquid interface is modified by the measurement. Moreover, if the liquid contains mobile ions, the ions can migrate in the electric field resulting from the applied voltage.[108] Again, this process can modify the composition of the solid–liquid interface.

For the minerals studied within this thesis, electrochemical reactions are not likely to occur, since the (non-conducting) minerals provide sufficient electrical insulation. For limiting the migration of ions in the electric field, it has been proposed[105,214] to only apply an alternating voltage to the tip, and no static bias voltage. Thereby, ions are expected to be only periodically displaced and not statically into a fixed direction.

4.3.2 Implementation

Based on the work by Kobayashi *et al.*,[105] I extended the setup described in section 3.2 to also perform open-loop AM-KPFM experiments at the solid–liquid interface. For this I added electrical contacts to both the cantilever (left part of figure 4.19) and the backside of the mineral samples (right part of figure 4.19 b). The alternating voltage applied between tip and cantilever (with frequency ν_{es} and an amplitude within the order of several volts) was generated by the HF2LI (described in detail in section 3.2.2). In some cases, this voltage was additionally amplified by a high-voltage amplifier (Model 7500, Krohn-Hite, USA) to achieve detectable signals. Both amplitude and phase shift of the first harmonic (at ν_{es}) and at the second harmonic (at $2\nu_{\mathrm{es}}$) were extracted from the deflection signal using two lock-in amplifiers within the HF2LI. The data

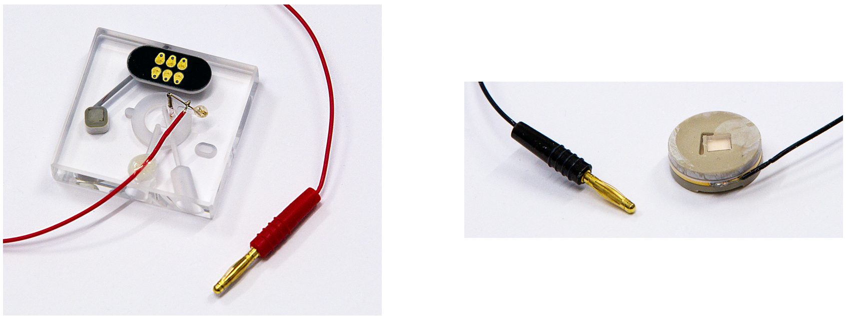

Figure 4.19: Cantilever holder (left) and sample holder (right) with a magnesite sample above a gold-coated metal plate. Both the cantilever and the backside contact to the sample allow to be electrically contacted. Images taken from reference 227.

acquisition was performed using the HF2LI in combination with the synchronization with respect to the scan movement as described in section 3.2.2.

4.3.3 Transfer function measurements

As detailed in section 4.1.4 on page 110, the measurement of spectral components of the tip-sample force requires the knowledge on the transfer function of the resonator. According to section 2.1.6, the transfer function of the resonator is modeled as the transfer function of the harmonic oscillator. In figure 4.20, I summarize results for the cantilever transfer function measurement for two systems: A magnesite sample in air (left) and a magnesite sample in pure water (right). For both cases I present the amplitude (a, b) and phase shift (c, d) at the first harmonic resulting from the electrostatic cantilever excitation used in KPFM. I compare the measured amplitude and phase shift (solid black lines) with the gain function and phase shift function of the harmonic oscillator (solid red lines) that have been fitted to the data. For the measurement in air, the cantilever transfer function fits well to the transfer function of the harmonic oscillator (figure 4.19 a, c). This is not the case for the measurement in liquid water (b, d). Here, in sharp contrast to the measurement in air, additional peaks appear in both the amplitude and phase shift. In reference 227 I demonstrate that the measured transfer function with the additional peaks resembles the transfer function obtained during piezoelectric cantilever excitation. Piezoelectric cantilever excitation produces additional peaks due to the excitation of additional resonances within the setup, in particular the liquid cell (figure 4.19 a).[228] I therefore speculated that the additional peaks also result from the excitation of unwanted additional resonances.[227] Importantly, the peaks render quantitative open-loop KPFM measurements on insulating samples in water challenging, since the measurement is obviously not described by the model in the previous sections.

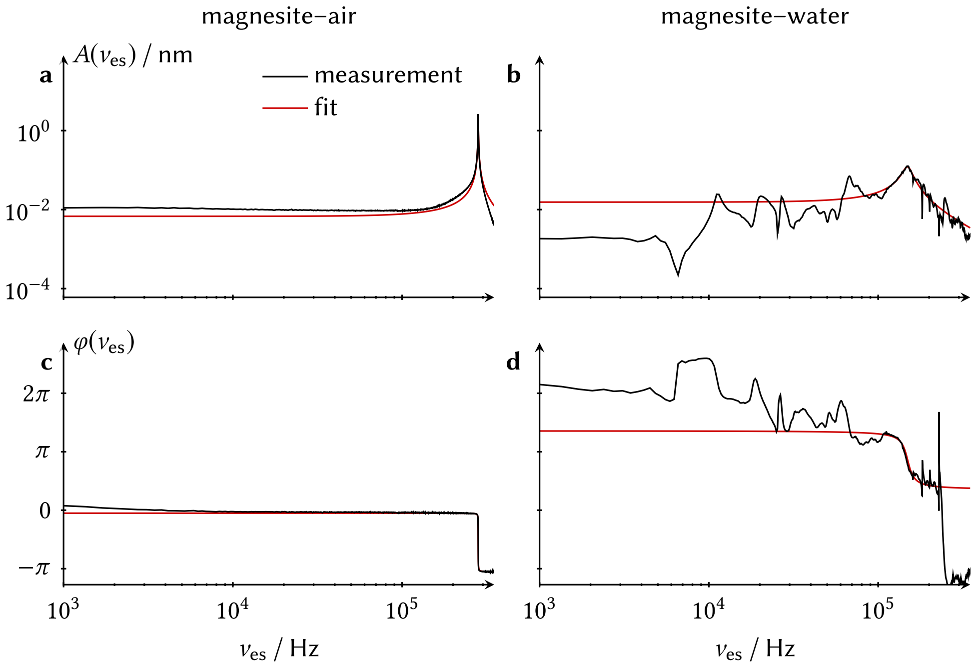

Figure 4.20: Experimental measurement of the transfer function of the cantilever on magnesite in air (first column) and in water (second column) with comparisons of the transfer function expected for a harmonic oscillator. An additional phase shift offset was included in the fit of the phase shift function. Data is taken from reference 227, in which also data acquisition parameters and data processing are detailed.

4.3.4 Demonstration of KPFM data acquisition

To demonstrate that the setup is – in principle – capable of recording KPFM data, I present the amplitude and phase shift at the first and second harmonic (ν_{es} and $2\nu_{es}$) obtained during high-resolution 3D AFM measurements on dolomite (10.4) immersed in pure water. The dolomite sample preparation is described in section 3.3. A cantilever of type PPP-NCHAuD was used.[5] In this measurement, the eigenfrequency of the cantilever was approximately 120 kHz, the electrostatic excitation frequency was set to $\nu_{es} = 150$ kHz and the electrostatic excitation voltage amplitude was approximately 100 V. For reference, figure 4.21 a shows the excitation frequency ν_{exc}, which reveals the checkerboard-like pattern discussed in section 3.3. Amplitude and phase shift of the first and second electrostatic harmonics are shown in b–e. Data in each channel is constant when the tip is away from the sample. Only in the distance range where the checkerboard-like pattern is observed in the excitation frequency data (a),

---

[5] Cantilevers of this type are made of (highly-doped) silicon. Therefore, they are not metallic conductors as assumed in the theoretic model presented before.

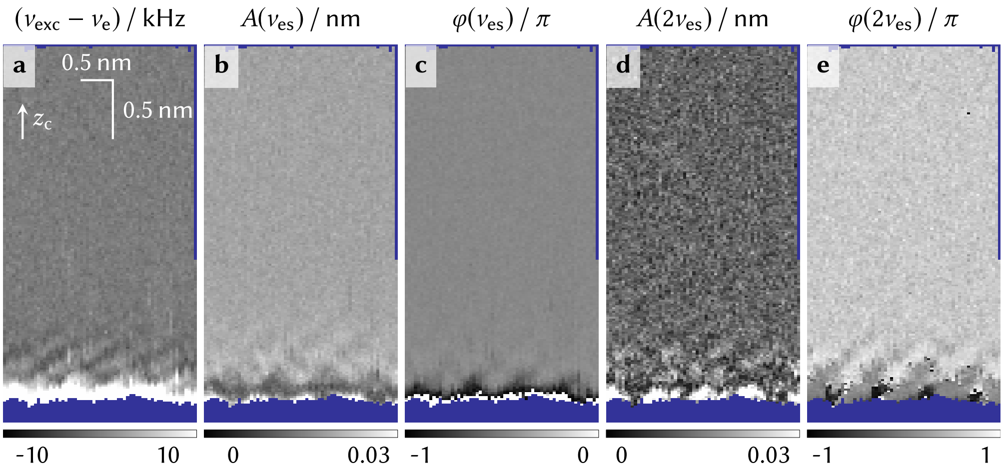

Figure 4.21: Experimental measurement of the excitation frequency (a) and the four additional channels necessary for performing quantitative open-loop KPFM. The data was collected at the dolomite–water interface.

lateral and vertical contrast variations can be recognized in the KPFM data channels (b–e). Due to the additional peaks in the electrostatic excitation spectrum, the transfer function of the system is not described by the transfer function of the harmonic oscillator. It is, consequently, not feasible to further process the data according to the analysis for the open-loop methods presented in section 4.1. From the presented data, it is therefore not possible to determine whether the observed contrast in b–e is the result of a voltage-dependent contribution to the tip-sample force or not. The data thereby demonstrates the necessity of the quantitative consideration of the cantilever transfer function.

4.3.5 Conclusion

I summarized in this chapter experiments on open-loop AM-KPFM at the solid–liquid interface. The electrostatic excitation of the cantilever was achieved by applying a voltage between cantilever and a back contact to dielectric mineral samples. In air, the response of the cantilever was described by the transfer function of the harmonic oscillator. In sharp contrast, the measurement of the cantilever transfer function in liquid water yielded additional peaks in the electrostatic excitation spectra. This experiment demonstrates that KPFM at mineral–water interfaces introduces significant challenges. To encourage further developments in this exciting research field, I demonstrate that open-loop AM-KPFM can easily be combined with 3D AFM measurements by using the highly-flexible data acquisition system described in section 3.2.

5 Summary

This thesis reports on atomic-scale insights into the structure of the interface between carbonate minerals and liquid water. The fundamental and atomistic understanding of mineral–water interfaces is relevant in industrial processes and in diverse fields of research, such as geology and biomineralization.

Three-dimensional dynamic AFM is the ideal tool to investigate mineral–water interfaces in real space. First, I present a unifying theory for the quantitative analysis of AFM data by deriving the *three AFM equations*. In contrast to previous works, this analysis is not specifically geared towards individual AFM modes. Instead, the theory allows for a quantitative analysis in *all* commonly-used AFM modes, such as the AM and FM mode. Moreover, an interactive virtual AFM is described in this thesis. The virtual AFM allows to assess the validity of the harmonic approximation (the only approximation used for deriving the three AFM equations).

In this thesis, the highly-demanding data acquisition for quantitative AFM became possible by the development of a fast and flexible data acquisition system. For a full quantitative dynamic AFM measurement, five data channels need to be recorded in parallel. When additionally combining the measurement with KPFM, even more data channels are necessary. This is beyond the capabilities of most commercially-available AFM controllers. The system presented in this thesis allows to record up to 20 data channels in parallel and works in combination with many available AFM controllers. Moreover, I describe the implementation of 3D AFM mapping using a custom-programmed microcontroller. By combining the data acquisition system with 3D mapping, I obtain 3D AFM datasets of mineral–water interfaces with atomic resolution.

By using both, the quantitative AFM analysis and the 3D AFM setup, I investigate the hydration structure at the aqueous interface of carbonate minerals. In particular, I focus on the most stable (10.4) surface of the minerals calcite, dolomite and magnesite. In all cases, water forms a highly-ordered checkerboard-like arrangement at the interface, which agrees well with the water density obtained from MD simulations. On the dolomite surface, which contains both calcium and magnesium cations, the equally-charged cations exhibit a different hydration structure: Above magnesium ions, water is shifted more closely to the surface compared to calcium ions. This subtle difference in the hydration structure allows for their chemical identification. So far, the identification of chemically-alike atoms (*i.e.*, with same net charge) has only been achieved in the well-controlled ultra-high vacuum environment. Transferring this capability to solid–liquid interfaces significantly advances the 3D AFM technique for investigating a wide range of application-relevant phenomena (such as corrosion, catalysis and friction) at the atomic scale.

In the vicinity of point defects at the calcite–water interface, I reveal minute distortions of the hydration structure. As point defects are often critical for the dissolution and growth of minerals, these experiments can provide valuable input for further experimental and theoretical studies on the detailed dissolution and growth mechanism. Moreover, I determine that the checkerboard-like water structure at the calcite–water interface is consistently obtained in a wide range of pH and ionic strength. Finally, I provide 3D AFM results at the calcite–ethanol interface. Due to its hydrocarbon chain and the hydroxyl group, the ethanol molecules act as a simple model for more complex organic molecules relevant during, *e.g.*, biomineralization processes. The data I present reveals experimental evidence for the presence of an ordered first layer of ethanol molecules at the calcite (10.4) surface. Simultaneously, the data reveal that this first layer is followed by additional layers with significantly less-pronounced lateral order.

In this thesis, a comprehensive theory for KPFM is provided, with a particular focus on open-loop AM-KPFM at mineral–water interfaces. Starting from a previously-introduced electrostatic model, the KPFM signal in all KPFM modes is quantitatively derived. Similar to the quantitative AFM theory, also the KPFM signal can be generalized: Regardless of the operation mode, a weighted sum over local charges in the tip-sample system is obtained. I provide a detailed description of the weight function for charges, which is central for quantitatively understanding KPFM. By considering a simple, yet relevant tip-sample-model, I reveal that positive charges can contribute either positively or negatively to the KPFM signal – depending on the dielectric medium surrounding the tip. This demonstrates that even for determining the sign of a charge distribution, a careful consideration of the weight function for charges is necessary. As an outlook, I discuss critical checks necessary for performing quantitative open-loop AM-KPFM experiments at mineral–water interfaces.

In summary, this work constitutes a comprehensive study on AFM and KPFM – both with respect to a quantitative data analysis and technical implementation. The high-resolution insights into the hydration structure of mineral–water interfaces presented in this thesis allow for chemical identification of individual surface atoms and even the investigation of single point defects.

Bibliography

[1] G. E. Brown and G. Calas. Mineral-Aqueous Solution Interfaces and Their Impact on the Environment. *Geochem. Perspect.*, 1(4):483–742, 2012.

[2] A. Putnis. Why Mineral Interfaces Matter. *Science*, 343(6178):1441–1442, 2014.

[3] J. C. Orr, V. J. Fabry, O. Aumont, L. Bopp, S. C. Doney, R. A. Feely, A. Gnanadesikan, N. Gruber, A. Ishida, F. Joos, R. M. Key, K. Lindsay, E. Maier-Reimer, R. Matear, P. Monfray, A. Mouchet, R. G. Najjar, G.-K. Plattner, K. B. Rodgers, C. L. Sabine, J. L. Sarmiento, R. Schlitzer, R. D. Slater, I. J. Totterdell, M.-F. Weirig, Y. Yamanaka, and A. Yool. Anthropogenic ocean acidification over the twenty-first century and its impact on calcifying organisms. *Nature*, 437(7059):681–686, 2005.

[4] R. A. Berner, A. C. Lasaga, and R. M. Garrels. The carbonate-silicate geochemical cycle and its effect on atmospheric carbon dioxide over the past 100 million years. *Am. J. Sci.*, 283(7):641–683, 1983.

[5] F. Nudelman and N. A. J. M. Sommerdijk. Biomineralization as an Inspiration for Materials Chemistry. *Angew. Chem. Int. Ed.*, 51(27):6582–6596, 2012.

[6] G. E. Brown. How Minerals React with Water. *Science*, 294(5540):67–69, 2001.

[7] C. V. Putnis and E. Ruiz-Agudo. The Mineral-Water Interface: Where Minerals React with the Environment. *Elements*, 9(3):177–182, 2013.

[8] W. A. Deer, R. A. Howie, and J. Zussman. *An introduction to the rock-forming minerals.* 2nd edition, 1992.

[9] F. C. Meldrum. Calcium carbonate in biomineralisation and biomimetic chemistry. *Int. Mater. Rev.*, 48(3):187–224, 2003.

[10] S. Baconnier, S. B. Lang, M. Polomska, B. Hilczer, G. Berkovic, and G. Meshulam. Calcite microcrystals in the pineal gland of the human brain: First physical and chemical studies. *Bioelectromagnetics*, 23(7):488–495, 2002.

[11] S. Weiner. An Overview of Biomineralization Processes and the Problem of the Vital Effect. *Rev. Mineral. Geochem.*, 54(1):1–29, 2003.

[12] G. Binnig, C. F. Quate, and C. Gerber. Atomic Force Microscope. *Phys. Rev. Lett.*, 56(9):930–933, 1986.

[13] T. Fukuma, K. Kobayashi, K. Matsushige, and H. Yamada. True atomic resolution in liquid by frequency-modulation atomic force microscopy. *Appl. Phys. Lett.*, 87(3):034101, 2005.

[14] T. Fukuma, M. Kimura, K. Kobayashi, K. Matsushige, and H. Yamada. Development of low noise cantilever deflection sensor for multienvironment frequency-modulation atomic force microscopy. *Rev. Sci. Instrum.*, 76(5):053704, 2005.

[15] S. Rode, R. Stark, J. Lübbe, L. Tröger, J. Schütte, K. Umeda, K. Kobayashi, H. Yamada, and A. Kühnle. Modification of a Commercial Atomic Force Microscopy for Low-Noise, High-Resolution Frequency-Modulation Imaging in Liquid Environment. *Rev. Sci. Instrum.*, 82(7):073703, 2011.

[16] H. Adam, S. Rode, M. Schreiber, K. Kobayashi, H. Yamada, and A. Kühnle. Photothermal Excitation Setup for a Modified Commercial Atomic Force Microscope. *Rev. Sci. Instrum.*, 85(2):23703, 2014.

[17] T. Fukuma, Y. Ueda, S. Yoshioka, and H. Asakawa. Atomic-Scale Distribution of Water Molecules at the Mica-Water Interface Visualized by Three-Dimensional Scanning Force Microscopy. *Phys. Rev. Lett.*, 104(1):016101, 2010.

[18] H. Söngen, R. Bechstein, and A. Kühnle. Quantitative Atomic Force Microscopy. accepted for publication in Journal of Physics: Condensed Matter, 2017.

[19] Y. Martin, C. C. Williams, and H. K. Wickramasinghe. Atomic force microscope–force mapping and profiling on a sub 100-Å scale. *J. Appl. Phys.*, 61(10):4723–4729, 1987.

[20] R. Nishi, I. Houda, T. Aramata, Y. Sugawara, and S. Morita. Phase Change Detection of Attractive Force Gradient by Using a Quartz Resonator in Noncontact Atomic Force Microscopy. *Appl. Surf. Sci.*, 157(4):332–336, 2000.

[21] T. R. Albrecht, P. Grütter, D. Horne, and D. Rugar. Frequency modulation detection using high-Q cantilevers for enhanced force microscope sensitivity. *J. Appl. Phys.*, 69(2):668–673, 1991.

[22] F. J. Giessibl. Forces and frequency shifts in atomic-resolution dynamic-force microscopy. *Phys. Rev. B*, 56(24):16010–16015, 1997.

[23] F. J. Giessibl. Advances in atomic force microscopy. *Rev. Mod. Phys.*, 75(3):949–983, 2003.

[24] U. Dürig. Relations between interaction force and frequency shift in large-amplitude dynamic force microscopy. *Appl. Phys. Lett.*, 75(3):433–435, 1999.

[25] U. Dürig. Conservative and dissipative interactions in dynamic force microscopy. *Surf. Interface Anal.*, 27(5-6):467–473, 1999.

[26] U. Dürig. Extracting interaction forces and complementary observables in dynamic probe microscopy. *Appl. Phys. Lett.*, 76(9):1203–1205, 2000.

[27] U. Dürig. Interaction Sensing in Dynamic Force Microscopy. *New J. Phys.*, 2(5):5, 2000.

[28] N. Sasaki, M. Tsukada, R. Tamura, K. Abe, and N. Sato. Dynamics of the cantilever in noncontact atomic force microscopy. *Appl. Phys. A*, 66:287–291, 1998.

[29] N. Sasaki and M. Tsukada. The Relation between Resonance Curves and Tip-Surface Interaction Potential in Noncontact Atomic-Force Microscopy. *Jpn. J. Appl. Phys.*, 37(5A):533–535, 1998.

[30] N. Sasaki and M. Tsukada. Theory for the effect of the tip-surface interaction potential on atomic resolution in forced vibration system of noncontact AFM. *Appl. Surf. Sci.*, 140(3-4):339–343, 1999.

[31] N. Sasaki and M. Tsukada. Effect of Microscopic Nonconservative Process on Noncontact Atomic Force Microscopy. *Jpn. J. Appl. Phys.*, 39(12B):1334–1337, 2000.

[32] H. Hölscher. Quantitative measurement of tip-sample interactions in amplitude modulation atomic force microscopy. *Appl. Phys. Lett.*, 89(12):123109, 2006.

[33] H. Hölscher and U. D. Schwarz. Theory of Amplitude Modulation Atomic Force Microscopy with and without Q-Control. *Int. J. Nonlinear Mech.*, 42(4):608–625, 2007.

[34] H. Hölscher. Theory of phase-modulation atomic force microscopy with constant-oscillation amplitude. *J. Appl. Phys.*, 103(8):064317, 2008.

[35] D. Ebeling and H. Hölscher. Analysis of the constant-excitation mode in frequency-modulation atomic force microscopy with active Q-Control applied in ambient conditions and liquids. *J. Appl. Phys.*, 102(11):114310, 2007.

[36] A. F. Payam, D. Martin-Jimenez, and R. García. Force reconstruction from tapping mode force microscopy experiments. *Nanotechnology*, 26(18):185706, 2015.

[37] A. J. Katan, M. H. van Es, and T. H. Oosterkamp. Quantitative force versus distance measurements in amplitude modulation AFM: a novel force inversion technique. *Nanotechnology*, 20(16):165703, 2009.

[38] J. E. Sader, T. Uchihashi, M. J. Higgins, A. Farrell, Y. Nakayama, and S. P. Jarvis. Quantitative force measurements using frequency modulation atomic force microscopy—theoretical foundations. *Nanotechnology*, 16(3):94–101, 2005.

[39] E. I. Green. The Story of *Q*. *Amer. Sci.*, 43:584–594, 1955.

[40] S. Kawai, T. Glatzel, S. Koch, B. Such, A. Baratoff, and E. Meyer. Time-averaged cantilever deflection in dynamic force spectroscopy. *Phys. Rev. B*, 80(8):085422, 2009.

[41] J. P. Cleveland, B. Anczykowski, A. E. Schmid, and V. B. Elings. Energy dissipation in tapping-mode atomic force microscopy. *Appl. Phys. Lett.*, 72(20):2613–2615, 1998.

[42] H. Hölscher, B. Gotsmann, W. Allers, U. D. Schwarz, H. Fuchs, and R. Wiesendanger. Measurement of conservative and dissipative tip-sample interaction forces with a dynamic force microscope using the frequency modulation technique. *Phys. Rev. B*, 64(7):075402, 2001.

[43] K. Suzuki, K. Kobayashi, A. Labuda, K. Matsushige, and H. Yamada. Accurate formula for dissipative interaction in frequency modulation atomic force microscopy. *Appl. Phys. Lett.*, 105(23):233105, 2014.

[44] F. J. Giessibl. A direct method to calculate tip-sample forces from frequency shifts in frequency-modulation atomic force microscopy. *Appl. Phys. Lett.*, 78(1):123–125, 2001.

[45] J. E. Sader and S. P. Jarvis. Accurate formulas for interaction force and energy in frequency modulation force spectroscopy. *Appl. Phys. Lett.*, 84(10):1801–1803, 2004.

[46] J. E. Sader and Y. Sugimoto. Accurate Formula for Conversion of Tunneling Current in Dynamic Atomic Force Spectroscopy. *Appl. Phys. Lett.*, 97(4):043502, 2010.

[47] S. Kawai, F. F. Federici Canova, T. Glatzel, A. S. Foster, and E. Meyer. Atomic-scale dissipation processes in dynamic force spectroscopy. *Phys. Rev. B*, 84(11):115415, 2011.

[48] H. Imada, K. Kimura, and H. Onishi. Water and 2-Propanol Structured on Calcite (104) Probed by Frequency-Modulation Atomic Force Microscopy. *Langmuir*, 29(34):10744–10751, 2013.

[49] C. Marutschke, D. Walters, J. Cleveland, I. Hermes, R. Bechstein, and A. Kühnle. Three-dimensional hydration layer mapping on the (10.4) surface of calcite using amplitude modulation atomic force microscopy. *Nanotechnology*, 25(33):335703, 2014.

[50] Y. Araki, K. Tsukamoto, R. Takagi, T. Miyashita, N. Oyabu, K. Kobayashi, and H. Yamada. Direct Observation of the Influence of Additives on Calcite Hydration by Frequency Modulation Atomic Force Microscopy. *Cryst. Growth Des.*, 14(12):6254–6260, 2014.

[51] T. Fukuma, B. Reischl, N. Kobayashi, P. Spijker, F. F. Canova, K. Miyazawa, and A. S. Foster. Mechanism of atomic force microscopy imaging of three-dimensional hydration structures at a solid-liquid interface. *Phys. Rev. B*, 92(15):155412, 2015.

[52] H. Söngen, C. Marutschke, P. Spijker, E. Holmgren, I. Hermes, R. Bechstein, S. Klassen, J. Tracey, A. S. Foster, and A. Kühnle. Chemical Identification at the Solid–Liquid Interface. *Langmuir*, 33(1):125–129, 2017.

[53] H. Söngen, M. Nalbach, H. Adam, and A. Kühnle. Three-Dimensional Atomic Force Microscopy Mapping at the Solid-Liquid Interface with Fast and Flexible Data Acquisition. *Rev. Sci. Instrum.*, 87(6):063704, 2016.

[54] S. Kuhn, M. Kittelmann, Y. Sugimoto, M. Abe, A. Kühnle, and P. Rahe. Identifying the absolute orientation of a low-symmetry surface in real space. *Phys. Rev. B.*, 90(19):195405, 2014.

[55] J. Polesel-Maris and S. Gauthier. A virtual dynamic atomic force microscope for image calculations. *J. Appl. Phys.*, 97(4):044902, 2005.

[56] Nony. L., A. Baratoff, D. Schär, O. Pfeiffer, A. Wetzel, and E. Meyer. Noncontact atomic force microscopy simulator with phase-locked-loop controlled frequency detection and excitation. *Phys. Rev. B*, 74(23):235439, 2006.

[57] J. Tracey, F. Canova, O. Keisanen, D. Z. Gao, P. Spijker, B. Reischl, and A. S. Foster. Flexible and modular virtual scanning probe microscope. *Comput. Phys. Commun.*, 196:429–438, 2015.

[58] G. Couturier, J. P. Aimé, J. Salardenne, R. Boisgard, A. Gourdon, and S. Gauthier. A mechanical approach to the dissipation process in NC-AFM: experiments, model and simulation. *Appl. Phys. A*, 72(S1):47–50, 2001.

[59] T. Trevethan, L. Kantorovich, J. Polesel-Maris, and S. Gauthier. Is atomic-scale dissipation in NC-AFM real? Investigation using virtual atomic force microscopy. *Nanotechnology*, 18(8):084017, 2007.

[60] J. Tracey, K. Miyazawa, P. Spijker, K. Miyata, B. Reischl, F. F. Canova, A. L. Rohl, T. Fukuma, and A. S. Foster. Understanding 2D atomic resolution imaging of the calcite surface in water by frequency modulation atomic force microscopy. *Nanotechnology*, 27(41):415709, 2016.

[61] H.-J. Butt, K. Graf, and M. Kappl. *Physics and Chemistry of Interfaces.* 2nd edition, 2006.

[62] J. N. Israelachvili. *Intermolecular and Surface Forces.* 3rd edition, 2011.

[63] W. D. Kaplan and Y. Kauffmann. Structural Order in Liquids Induved by Interfaces with Crystals. *Annu. Rev. Mater. Res.*, 36(1):1–48, 2006.

[64] D. Martin-Jimenez, E. Chacon, P. Tarazona, and R. Garcia. Atomically resolved three-dimensional structures of electrolyte aqueous solutions near a solid surface. *Nat. Commun.*, 7:12164, 2016.

[65] K. Suzuki, N. Oyabu, K. Kobayashi, K. Matsushige, and H. Yamada. Atomic-Resolution Imaging of Graphite–Water Interface by Frequency Modulation Atomic Force Microscopy. *Appl. Phys. Express*, 4(12):125102, 2011.

[66] T. Utsunomiya, Y. Yokota, T. Enoki, and K.-i. Fukui. Potential-dependent hydration structures at aqueous solution/graphite interfaces by electrochemical frequency modulation atomic force microscopy. *Chem. Commun.*, 50(98):15537–15540, oct 2014.

[67] T. Utsunomiya, S. Tatsumi, Y. Yokota, and K.-i. Fukui. Potential-dependent structures investigated at the perchloric acid solution/iodine modified Au(111) interface by electrochemical frequency-modulation atomic force microscopy. *Phys. Chem. Chem. Phys.*, 17(19):12616–12622, 2015.

[68] P. Spijker, T. Hiasa, T. Musso, R. Nishioka, H. Onishi, and A. S. Foster. Understanding the Interface of Liquids with an Organic Crystal Surface from Atomistic Simulations and AFM Experiments. *J. Phys. Chem. C*, 118(4):2058–2066, 2014.

[69] H. Onishi. Elastic and Viscous Responses of Interfacial Liquids (Talk in Mainz, March 17, 2017).

[70] J. Huisman, W, J. F. Peters, M. J. Zwanenburg, S. A. de Vries, T. E. Derry, D. Abernathy, and J. F. van der Veen. Layering of a liquid metal in contact with a hard wall. *Nature*, 390(6658):379–381, nov 1997.

[71] P. Geysermans, D. Gorse, and V. Pontikis. Molecular dynamics study of the solid–liquid interface. *J. Chem. Phys.*, 113(15):6382–6389, oct 2000.

[72] S. H. Oh, Y. Kauffmann, C. Scheu, W. D. Kaplan, and M. Rühle. Ordered Liquid Aluminum at the Interface with Sapphire. *Science*, 310(5748):661–663, oct 2005.

[73] L. Cheng, P. Fenter, K. L. Nagy, M. L. Schlegel, and N. C. Sturchio. Molecular-Scale Density Oscillations in Water Adjacent to a Mica Surface. *Phys. Rev. Lett.*, 87(15):156103, sep 2001.

[74] P. Geissbühler, P. Fenter, E. DiMasi, G. Srajer, L. B. Sorensen, and N. C. Sturchio. Three-dimensional structure of the calcite–water interface by surface X-ray scattering. *Surf. Sci.*, 573(2):191–203, 2004.

[75] S. Pintea, W. de Poel, A. E. F. de Jong, V. Vonk, P. van der Asdonk, J. Drnec, O. Balmes, H. Isern, T. Dufrane, R. Felici, and E. Vlieg. Solid–Liquid Interface Structure of Muscovite Mica in CsCl and RbBr Solutions. *Langmuir*, 32(49):12955–12965, dec 2016.

[76] R. G. Horn and J. N. Israelachvili. Direct measurement of structural forces between two surfaces in a nonpolar liquid. *J. Chem. Phys.*, 75(3):1400–1411, 1981.

[77] J. N. Israelachvili and R. M. Pashley. Molecular layering of water at surfaces and origin of repulsive hydration forces. *Nature*, 306(5940):249–250, 1983.

[78] J. Israelachvili and H. Wennerström. Role of hydration and water structure in biological and colloidal interactions. *Nature*, 379(6562):219–225, 1996.

[79] D. Henderson, F. F. Abraham, and J. A. Barker. The Ornstein-Zernike equation for a fluid in contact with a surface. *Mol. Phys.*, 31(4):1291–1295, 1976.

[80] I. K. Snook and D. Henderson. Monte Carlo study of a hard-sphere fluid near a hard wall. *J. Chem. Phys.*, 68(5):2134–2139, 1978.

[81] I. K. Snook and W. van Megen. Structure of dense liquids at solid interfaces. *J. Chem. Phys.*, 70(6):3099–3105, 1979.

[82] P. Kumar, F. W. Starr, S. V. Buldyrev, and H. E. Stanley. Effect of water-wall interaction potential on the properties of nanoconfined water. *Phys. Rev. E*, 75(1):011202, 2007.

[83] L. B. Krott and M. C. Barbosa. Model of waterlike fluid under confinement for hydrophobic and hydrophilic particle-plate interaction potentials. *Phys. Rev. E*, 89(1):012110, 2014.

[84] F. F. Abraham. The interfacial density profile of a Lennard-Jones fluid in contact with a (100) Lennard-Jones wall and its relationship to idealized fluid/wall systems: A Monte Carlo simulation. *J. Chem. Phys.*, 68(8):3713–3716, 1978.

[85] N. Choudhury. Effect of surface hydrophobicity on the dynamics of water at the nanoscale confinement: A molecular dynamics simulation study. *Chem. Phys.*, 421:68–76, 2013.

[86] F. Mozaffari. A molecular dynamics simulation study of the effect of water–graphene interaction on the properties of confined water. *Mol. Simul.*, 42(17):1475–1484, 2016.

[87] J. K. Lee, J. A. Barker, and G. M. Pound. Surface structure and surface tension: Perturbation theory and Monte Carlo calculation. *J. Chem. Phys.*, 60(5):1976–1980, 1974.

[88] F. F. Abraham, D. E. Schreiber, and J. A. Barker. On the structure of a free surface of a Lennard–Jones liquid: A Monte Carlo calculation. *J. Chem. Phys.*, 62(5):1958–1960, 1975.

[89] F. F. Abraham. A theory for the thermodynamics and structure of nonuniform systems, with applications to the liquid–vapor interface and spinodal decomposition. *J. Chem. Phys.*, 63(1):157–164, 1975.

[90] S. Rode, N. Oyabu, K. Kobayashi, H. Yamada, and A. Kühnle. True Atomic-Resolution Imaging of $(10\bar{1}4)$ Calcite in Aqueous Solution by Frequency Modulation Atomic Force Microscopy. *Langmuir*, 25(5):2850–2853, 2009.

[91] Y. Araki, T. Katsuo, O. Noriaki, K. Kobayashi, and H. Yamada. Atomic-Resolution Imaging of Aragonite (001) Surface in Water by Frequency Modulation Atomic Force Microscopy. *Jpn. J. Appl. Phys.*, 51(8S3):08KB09, 2012.

[92] T. Fukuma, A. S. Mostaert, L. C. Serpell, and S. P. Jarvis. Revealing molecular-level surface structure of amyloid fibrils in liquid by means of frequency modulation atomic force microscopy. *Nanotechnology*, 19(38):384010, 2008.

[93] M. Schreiber, M. Eckardt, S. Klassen, H. Adam, M. Nalbach, L. Greifenstein, F. Kling, M. Kittelmann, R. Bechstein, and A. Kühnle. How deprotonation changes molecular self-assembly – an AFM study in liquid environment. *Soft Matter*, 9(29):7145–7149, 2013.

[94] M. Pfreundschuh, D. Alsteens, M. Hilbert, M. O. Steinmetz, and D. J. Müller. Localizing Chemical Groups while Imaging Single Native Proteins by High-Resolution Atomic Force Microscopy. *Nano Lett.*, 14(5):2957–2964, 2014.

[95] R. Momper, M. Nalbach, K. Lichtenstein, R. Bechstein, and A. Kühnle. Stabilization of Polar Step Edges on Calcite (10.4) by the Adsorption of Congo Red. *Langmuir*, 31(26):7283–7287, 2015.

[96] K. Kimura, S. Ido, N. Oyabu, K. Kobayashi, Y. Hirata, T. Imai, and H. Yamada. Visualizing water molecule distribution by atomic force microscopy. *J. Chem. Phys.*, 132(19):194705, 2010.

[97] H. Asakawa, S. Yoshioka, K. Nishimura, and T. Fukuma. Spatial Distribution of Lipid Headgroups and Water Molecules at Membrane/Water Interfaces Visualized by Three-Dimensional Scanning Force Microscopy. *ACS Nano*, 6(10):9013–9020, 2012.

[98] B. J. Albers, T. C. Schwendemann, M. Z. Baykara, N. Pilet, M. Liebmann, E. I. Altman, and U. D. Schwarz. Three-dimensional imaging of short-range chemical forces with picometre resolution. *Nat. Nanotechnol.*, 4(5):307–310, 2009.

[99] C. Moreno, O. Stetsovych, T. K. Shimizu, and O. Custance. Imaging Three-Dimensional Surface Objects with Submolecular Resolution by Atomic Force Microscopy. *Nano Lett.*, 15(4):2257–2262, 2015.

[100] E. T. Herruzo, H. Asakawa, T. Fukuma, and R. García. Three-dimensional quantitative force maps in liquid with 10 piconewton, angstrom and sub-minute resolutions. *Nanoscale*, 5(7):2678–2685, 2013.

[101] K. Umeda, K. Kobayashi, N. Oyabu, K. Matsushige, and H. Yamada. Molecular-scale quantitative charge density measurement of biological molecule by frequency modulation atomic force microscopy in aqueous solutions. *Nanotechnology*, 26(28):285103, 2015.

[102] K. Suzuki, K. Kobayashi, N. Oyabu, K. Matsushige, and H. Yamada. Molecular-scale investigations of structures and surface charge distribution of surfactant aggregates by three-dimensional force mapping. *J. Chem. Phys.*, 140(5):054704, 2014.

[103] K. Kobayashi, N. Oyabu, K. Kimura, S. Ido, K. Suzuki, T. Imai, K. Tagami, M. Tsukada, and H. Yamada. Visualization of hydration layers on muscovite mica in aqueous solution by frequency-modulation atomic force microscopy. *J. Chem. Phys.*, 138(18):184704, 2013.

[104] K. Kobayashi, H. Yamada, H. Itoh, T. Horiuchi, and K. Matsushige. Analog frequency modulation detector for dynamic force microscopy. *Rev. Sci. Instrum.*, 72(12):4383–4387, 2001.

[105] N. Kobayashi, H. Asakawa, and T. Fukuma. Nanoscale potential measurements in liquid by frequency modulation atomic force microscopy. *Rev. Sci. Instrum.*, 81(12):123705, 2010.

[106] A. L. Domanski, E. Sengupta, K. Bley, M. B. Untch, S. A. L. Weber, K. Landfester, C. K. Weiss, H.-J. Butt, and R. Berger. Kelvin Probe Force Microscopy in Nonpolar Liquids. *Langmuir*, 28(39):13892–13899, 2012.

[107] K. Umeda, K. Kobayashi, N. Oyabu, Y. Hirata, K. Matsushige, and H. Yamada. Practical aspects of Kelvin-probe force microscopy at solid/liquid interfaces in various liquid media. *J. Appl. Phys.*, 116(13):134307, 2014.

[108] L. Collins, S. Jesse, J. I Kilpatrick, A. Tselev, O. Varenyk, M. B. Okatan, S. A. L. Weber, A. Kumar, N. Balke, and S. V. Kalinin. Probing charge screening dynamics

and electrochemical processes at the solid–liquid interface with electrochemical force microscopy. *Nat. Comm.*, 5, 2014.

[109] J. Lübbe, M. Temmen, P. Rahe, A. Kühnle, and M. Reichling. Determining cantilever stiffness from thermal noise. *Beilstein J. Nanotech.*, 4:227–233, 2013.

[110] Thomas D. Perry IV., Randall T. Cygan, and Ralph Mitchell. Molecular models of a hydrated calcite mineral surface. *Geochim. Cosmochim. Acta*, 71(24):5876–5887, 2007.

[111] S. Kerisit and S. C. Parker. Free energy of adsorption of water and calcium on the $\{10\bar{1}4\}$ calcite surface. *Chem. Commun.*, (1):52, 2004.

[112] H. Effenberger, K. Mereiter, and J. Zemann. Crystal-structure refinements of magnesite, calcite, rhodochrosite, siderite, smithonite, and dolomite, with discussion of some aspects of the stereochemistry of calcite type carbonates. *Z. Kristallogr.*, 156(3–4):233–243, 1981.

[113] F. J. Giessibl. Atomic Resolution of the Silicon (111)-(7×7) Surface by Atomic Force Microscopy. *Science*, 267(5194):68–71, 1995.

[114] M. A. Lantz. Quantitative Measurement of Short-Range Chemical Bonding Forces. *Science*, 291(5513):2580–2583, 2001.

[115] A. S. Foster, C. Barth, A. L. Shluger, and M. Reichling. Unambiguous Interpretation of Atomically Resolved Force Microscopy Images of an Insulator. *Phys. Rev. Lett.*, 86(11):2373–2376, 2001.

[116] R. Hoffmann, M. A. Lantz, H. J. Hug, P. J. A. van Schendel, P. Kappenberger, S. Martin, A. Baratoff, and H.-J. Güntherodt. Atomic resolution imaging and frequency versus distance measurements on NiO(001) using low-temperature scanning force microscopy. *Phys. Rev. B*, 67(8):085402, 2003.

[117] S. M. Langkat, H. Hölscher, A. Schwarz, and R. Wiesendanger. Determination of site specific interatomic forces between an iron coated tip and the NiO(001) surface by force field spectroscopy. *Surface Science*, 527(1-3):12–20, 2003.

[118] R. Hoffmann, D. Weiner, A. Schirmeisen, and A. S. Foster. Sublattice identification in noncontact atomic force microscopy of the NaCl(001) surface. *Phys. Rev. B*, 80(11):115426, 2009.

[119] P. Rahe, J. Schütte, and A. Kühnle. NC-AFM contrast formation on the calcite $(10\bar{1}4)$ surface. *J. Phys.: Condens. Matter*, 24(8):084006, 2012.

[120] Y. Sugimoto, P. Pou, M. Abe, P. Jelinek, R. Pérez, S. Morita, and Ó. Custance. Chemical identification of individual surface atoms by atomic force microscopy. *Nature*, 446(7131):64–67, 2007.

[121] M. Watkins and A. L. Shluger. Mechanism of Contrast Formation in Atomic Force Microscopy in Water. *Phys. Rev. Lett.*, 105(19):196101, 2010.

[122] O. Björneholm, M. H. Hansen, A. Hodgson, L.-M. Liu, D. T. Limmer, A. Michaelides, P. Pedevilla, J. Rossmeisl, H. Shen, G. Tocci, E. Tyrode, M.-M. Walz, J. Werner, and H. Bluhm. Water at Interfaces. *Chem. Rev.*, 116(13):7698–7726, 2016.

[123] T. Hiasa, K. Kimura, H. Onishi, M. Ohta, K. Watanabe, R. Kokawa, N. Oyabu, K. Kobayashi, and H. Yamada. Aqueous Solution Structure over α-$Al_2O_3(01\bar{1}2)$ Probed by Frequency-Modulation Atomic Force Microscopy. *J. Phys. Chem. C*, 114(49):21423–21426, 2010.

[124] T. Hiasa, K. Kimura, and H. Onishi. Two-dimensional distribution of liquid hydrocarbons facing alkanethiol monolayers visualized by frequency modulation atomic force microscopy. *Colloids Surf. A*, 396:203–207, 2012.

[125] T. Hiasa, K. Kimura, and H. Onishi. Hydration of hydrophilic thiolate monolayers visualized by atomic force microscopy. *Phys. Chem. Chem. Phys.*, 14(23):8419–8424, 2012.

[126] R. Nishioka, T. Hiasa, K. Kimura, and H. Onishi. Specific Hydration on p-Nitroaniline Crystal Studied by Atomic Force Microscopy. *J. Phys. Chem. C*, 117(6):2939–2943, 2013.

[127] S. Plimpton. Fast Parallel Algorithms for Short-Range Molecular Dynamics. *J. Comput. Phys.*, 117(1):1–19, 1995.

[128] William Humphrey, Andrew Dalke, and Klaus Schulten. VMD: Visual molecular dynamics. *J. Mol. Graphics*, 14(1):33–38, 1996.

[129] N. Michaud-Agrawal, E. J. Denning, T. B. Woolf, and O. Beckstein. MDAnalysis: A toolkit for the analysis of molecular dynamics simulations. *J. Comput. Chem.*, 32(10):2319–2327, 2011.

[130] P. Raiteri, J. D. Gale, D. Quigley, and P. M. Rodger. Derivation of an Accurate Force-Field for Simulating the Growth of Calcium Carbonate from Aqueous Solution: A New Model for the Calcite-Water Interface. *J. Phys. Chem. C*, 114(13):5997–6010, 2010.

[131] H. Tomono, H. Nada, F. Zhu, F. Sakamoto, T. Nishimura, and T. Kato. Effects of Magnesium Ions and Water Molecules on the Structure of Amorphous Calcium Carbonate: A Molecular Dynamics Study. *J. Phys. Chem. B*, 117(47):14849–14856, 2013.

[132] P. Raiteri, R. Demichelis, and J. D. Gale. Thermodynamically Consistent Force Field for Molecular Dynamics Simulations of Alkaline-Earth Carbonates and Their Aqueous Speciation. *J. Phys. Chem. C*, 119(43):24447–24458, 2015.

[133] Y. Wu, H. L. Tepper, and G. A. Voth. Flexible simple point-charge water model with improved liquid-state properties. *J. Chem. Phys.*, 124(2):024503, 2006.

[134] S. Kerisit and S. C. Parker. Free Energy of Adsorption of Water and Metal Ions on the $\{10\bar{1}4\}$ Calcite Surface. *J. Am. Chem. Soc.*, 126(32):10152–10161, 2004.

[135] N. H. de Leeuw and S. C. Parker. Surface–water interactions in the dolomite problem. *Phys. Chem. Chem. Phys.*, 3(15):3217–3221, 2001.

[136] M. Watkins and B. Reischl. A simple approximation for forces exerted on an AFM tip in liquid. *J. Chem. Phys.*, 138(15):154703, 2013.

[137] K.-i. Amano, Y. Liang, K. Miyazawa, K. Kobayashi, K. Hashimoto, K. Fukami, N. Nishi, T. Sakka, H. Onishi, and T. Fukuma. Number density distribution of solvent molecules on a substrate: a transform theory for atomic force microscopy. *Phys. Chem. Chem. Phys.*, 18(23):15534–15544, 2016.

[138] K. Miyazawa, N. Kobayashi, M. Watkins, A. L. Shluger, K.-i. Amano, and T. Fukuma. A relationship between three-dimensional surface hydration structures and force distribution measured by atomic force microscopy. *Nanoscale*, 8(13):7334–7342, 2016.

[139] K.-i. Amano, K. Suzuki, T. Fukuma, O. Takahashi, and H. Onishi. The relationship between local liquid density and force applied on a tip of atomic force microscope: A theoretical analysis for simple liquids. *J. Chem. Phys.*, 139(22):224710, 2013.

[140] A. Labuda, K. Kobayashi, K. Suzuki, H. Yamada, and P. Grütter. Monotonic Damping in Nanoscopic Hydration Experiments. *Phys. Rev. Lett.*, 110(6):066102, 2013.

[141] G. B. Kaggwa, J. I. Kilpatrick, J. E. Sader, and S. P. Jarvis. Artifact-free dynamic atomic force microscopy reveals monotonic dissipation for a simple confined liquid. *Appl. Phys. Lett.*, 93(1):011909, 2008.

[142] S. de Beer, W. K. den Otter, D. van den Ende, W. J. Briels, and F. Mugele. Non-monotonic variation of viscous dissipation in confined liquid films: A reconciliation. *Europhys. Lett.*, 97(4):46001, feb 2012.

[143] S. de Beer, W. K. den Otter, D. van den Ende, W. J. Briels, and F. Mugele. Can Confinement-Induced Variations in the Viscous Dissipation be Measured? *Tribol. Lett.*, 48(1):1–9, 2012.

[144] A. Maali, T. Cohen-Bouhacina, G. Couturier, and J.-P. Aimé. Oscillatory Dissipation of a Simple Confined Liquid. *Phys. Rev. Lett.*, 96(8):086105, 2006.

[145] S. J. O'Shea. Comment on "Oscillatory Dissipation of a Simple Confined Liquid". *Phys. Rev. Lett.*, 97(17):179601, 2006.

[146] K. Oura, V. G. Lifshits, A. A. Saranin, A. V. Zotov, and M. Katayama. *Surface science: an introduction.* Springer, 2003.

[147] H. Ibach. *Physics of Surfaces and Interfaces.* Springer, 2006.

[148] A. S. Lea, J. E. Amonette, D. R. Baer, Y. Liang, and N. G. Colton. Microscopic effects of carbonate, manganese, and strontium ions on calcite dissolution. *Geochim. Cosmochim. Acta*, 65(3):369–379, 2001.

[149] A. O. Harstad and S. L. S. Stipp. Calcite dissolution: Effects of trace cations naturally present in Iceland spar calcites. *Geochim. Cosmochim. Acta*, 71(1):56–70, 2007.

[150] M. P. Andersson, K. Dideriksen, H. Sakuma, and S. L. S. Stipp. Modelling how incorporation of divalent cations affects calcite wettability–implications for biomineralisation and oil recovery. *Sci. Rep.*, 6(1):28854, 2016.

[151] J. S. Lardge, D. M. Duffy, M. J. Gillan, and M. Watkins. Ab Initio Simulations of the Interaction between Water and Defects on the Calcite $(10\bar{1}4)$ Surface. *J. Phys. Chem. C*, 114(6):2664–2668, 2010.

[152] B. Reischl, P. Raiteri, J. D. Gale, and A. L. Rohl. Can Point Defects in Surfaces in Solution be Atomically Resolved by Atomic Force Microscopy? *Phys. Rev. Lett.*, 117(22):226101, 2016.

[153] F. Ohnesorge and G. Binnig. True Atomic Resolution by Atomic Force Microscopy Through Repulsive and Attractive Forces. *Science*, 260(5113):1451–1456, 1993.

[154] T. Fukuma and S. P. Jarvis. Development of liquid-environment frequency modulation atomic force microscope with low noise deflection sensor for cantilevers of various dimensions. *Rev. Sci. Instrum.*, 77(4):043701, 2006.

[155] S. M. R. Akrami, H. Nakayachi, T. Watanabe-Nakayama, H. Asakawa, and T. Fukuma. Significant improvements in stability and reproducibility of atomic-scale atomic force microscopy in liquid. *Nanotechnology*, 25(45):455701, 2014.

[156] T. Fukuma. Wideband low-noise optical beam deflection sensor with photothermal excitation for liquid-environment atomic force microscopy. *Rev. Sci. Instrum.*, 80(2):023707, 2009.

[157] T. Fukuma, K. Onishi, N. Kobayashi, A. Matsuki, and H. Asakawa. Atomic-resolution imaging in liquid by frequency modulation atomic force microscopy using small cantilevers with megahertz-order resonance frequencies. *Nanotechnology*, 23(13):135706, 2012.

[158] E. Ruiz-Agudo, M. Kowacz, C. V. Putnis, and A. Putnis. The role of background electrolytes on the kinetics and mechanism of calcite dissolution. *Geochim. Cosmochim. Acta*, 74(4):1256–1267, 2010.

[159] E. Ruiz-Agudo, M. Urosevic, C. V. Putnis, C. Rodríguez-Navarro, C. Cardell, and A. Putnis. Ion-specific effects on the kinetics of mineral dissolution. *Chem. Geol.*, 281(3-4):364–371, 2011.

[160] E. Ruiz-Agudo, C. V. Putnis, L. Wang, and A. Putnis. Specific effects of background electrolytes on the kinetics of step propagation during calcite growth. *Geochim. Cosmochim. Acta*, 75(13):3803–3814, 2011.

[161] M. Ricci, P. Spijker, F. Stellacci, J.-F. Molinari, and K. Voïtchovsky. Direct Visualization of Single Ions in the Stern Layer of Calcite. *Langmuir*, 29(7):2207–2216, 2013.

[162] M. Nalbach, S. Klassen, R. Bechstein, and A. Kühnle. Molecular Self-Assembly Versus Surface Restructuring During Calcite Dissolution. *Langmuir*, 32(39):9975–9981, 2016.

[163] S. Mann, D. D. Archibald, J. M. Didymus, T. Douglas, B. R. Heywood, F. C. Meldrum, and N. J. Reeves. Crystallization at Inorganic-organic Interfaces: Biominerals and Biomimetic Synthesis. *Science*, 261(5126):1286–1292, sep 1993.

[164] M. P. Andersson and S. L. S. Stipp. How acidic is water on calcite? *J. Phys. Chem. C*, 116(35):18779–18787, 2012.

[165] E. Ataman, M. P. Andersson, M. Ceccato, N. Bovet, and S. L. S. Stipp. Functional Group Adsorption on Calcite: I. Oxygen Containing and Nonpolar Organic Molecules. *J. Phys. Chem. C*, 120(30):16586–16596, 2016.

[166] D. J. Cooke, R. J. Gray, K. K. Sand, S. L. S. Stipp, and J. A. Elliott. Interaction of Ethanol and Water with the $(10\bar{1}4)$ Surface of Calcite. *Langmuir*, 26(18):14520–14529, sep 2010.

[167] I. S. Pasarín, M. Yang, N. Bovet, M. Glyvradal, M. M. Nielsen, J. Bohr, R. Feidenhans'l, and S. L. S. Stipp. Molecular Ordering of Ethanol at the Calcite Surface. *Langmuir*, 28(5):2545–2550, feb 2012.

[168] K. K. Sand, M. Yang, E. Makovicky, D. J. Cooke, T. Hassenkam, K. Bechgaard, and S. L. S. Stipp. Binding of Ethanol on Calcite: The Role of the OH Bond and Its Relevance to Biomineralization. *Langmuir*, 26(19):15239–15247, 2010.

[169] N. Bovet, M. Yang, M. S. Javadi, and S. L. S. Stipp. Interaction of alcohols with the calcite surface. *Phys. Chem. Chem. Phys.*, 17(5):3490–3496, 2015.

[170] K. K. Sand, S. L. S. Stipp, T. Hassenkam, M. Yang, D. Cooke, and E. Makovicky. Ethanol adsorption on the $(10\bar{1}4)$ calcite surface: preliminary observations with atomic force microscopy. *Mineral. Mag.*, 72(1):353–357, 2008.

[171] I. Hermes. Solvation layers on carbonate surfaces probed by high-resolution amplitude modulation atomic force microscopy. Diploma thesis, Johannes Gutenberg-Universität Mainz, 2014.

[172] C. Marutschke. Three-Dimensional Imaging of the Solid-Liquid Interface with High-Resolution Atomic Force Microscopy. PhD thesis, Johannes Gutenberg-Universität Mainz, 2015.

[173] S. A. Burke, J. M. LeDue, Y. Miyahara, J. M. Topple, S. Fostner, and P. Grütter. Determination of the local contact potential difference of PTCDA on NaCl: a comparison of techniques. *Nanotechnology*, 20(26):264012, 2009.

[174] M. Kittelmann, P. Rahe, A. Gourdon, and A. Kühnle. Direct Visualization of Molecule Deprotonation on an Insulating Surface. *ACS Nano*, 6(8):7406–7411, 2012.

[175] C. Barth, A. S. Foster, C. R. Henry, and A. L. Shluger. Recent Trends in Surface Characterization and Chemistry with High-Resolution Scanning Force Methods. *Adv. Mater.*, 23(4):477–501, 2011.

[176] L. Gross, F. Mohn, P. Liljeroth, J. Repp, F. J. Giessibl, and G. Meyer. Measuring the Charge State of an Adatom with Noncontact Atomic Force Microscopy. *Science*, 324(5933):1428–1431, 2009.

[177] C. Barth and C. R. Henry. Gold nanoclusters on alkali halide surfaces: Charging and tunneling. *Appl. Phys. Lett.*, 89(25):252119, 2006.

[178] B. Hoff, M. Gingras, R. Peresutti, C. R. Henry, A. S. Foster, and C. Barth. Mechanisms of the Adsorption and Self-Assembly of Molecules with Polarized Functional Groups on Insulating Surfaces. *J. Phys. Chem. C*, 118(26):14569–14578, 2014.

[179] A. Hinaut, A. Pujol, F. Chaumeton, D. Martrou, A. Gourdon, and S. Gauthier. An NC-AFM and KPFM study of the adsorption of a triphenylene derivative on KBr(001). *Beilstein J. Nanotechnol.*, 3:221–229, 2012.

[180] J. L. Neff, P. Milde, C. Pérez León, M. D. Kundrat, L. M. Eng, C. R. Jacob, and R. Hoffmann-Vogel. Epitaxial Growth of Pentacene on Alkali Halide Surfaces Studied by Kelvin Probe Force Microscopy. *ACS Nano*, 8(4):3294–3301, 2014.

[181] C. Barth and C. R. Henry. Kelvin probe force microscopy on MgO(001) surfaces and supported Pd nanoclusters. *J. Phys. Chem. C*, 113(1):247–253, 2009.

[182] B. Hoff, C. R. Henry, and C. Barth. Charging C_{60} Islands with the AFM Tip. *Nanoscale*, 8:411–419, 2015.

[183] W. Steurer, J. Repp, L. Gross, I. Scivetti, M. Persson, and G. Meyer. Manipulation of the Charge State of Single Au Atoms on Insulating Multilayer Films. *Phys. Rev. Lett.*, 114(3):036801, 2015.

[184] W. Steurer, S. Fatayer, L. Gross, and G. Meyer. Probe-based measurement of lateral single-electron transfer between individual molecules. *Nat. Commun.*, 6:8353, 2015.

[185] P. Rahe, R. P. Steele, and C. C. Williams. Consecutive Charging of a Molecule-on-Insulator Ensemble Using Single Electron Tunnelling Methods. *Nano Lett.*, 16:911–916, 2016.

[186] F. Bocquet, L. Nony, C. Loppacher, and T. Glatzel. Analytical approach to the local contact potential difference on (001) ionic surfaces: Implications for Kelvin probe force microscopy. *Phys. Rev. B*, 78(3):035410, 2008.

[187] L. Nony, A. S. Foster, F. Bocquet, and C. Loppacher. Understanding the Atomic-Scale Contrast in Kelvin Probe Force Microscopy. *Phys. Rev. Lett.*, 103(3):036802, 2009.

[188] L. Nony, F. Bocquet, C. Loppacher, and T. Glatzel. On the relevance of the atomic-scale contact potential difference by amplitude-modulation and frequency-modulation Kelvin probe force microscopy. *Nanotechnology*, 20(26):264014, 2009.

[189] G. H. Enevoldsen, T. Glatzel, M. C. Christensen, J. V. Lauritsen, and F. Besenbacher. Atomic Scale Kelvin Probe Force Microscopy Studies of the Surface Potential Variations on the TiO_2(110)Surface. *Phys. Rev. Lett.*, 100(23):236104, 2008.

[190] A. Liscio, V. Palermo, D. Gentilini, F. Nolde, K. Müllen, and P. Samorì. Quantitative Measuremßent of the Local Surface Potential of π-Conjugated Nanostructures: A Kelvin Probe Force Microscopy Study. *Adv. Funct. Mater.*, 16(11):1407–1416, jul 2006.

[191] C. Pérez León, H Drees, S. M. Wippermann, M. Marz, and R. Hoffmann-Vogel. Atomic-Scale Imaging of the Surface Dipole Distribution of Stepped Surfaces. *J. Phys. Chem. Lett.*, 7(3):426–430, feb 2016.

[192] B. Schuler, S.-X. Liu, Y. Geng, S. Decurtins, G. Meyer, and L. Gross. Contrast Formation in Kelvin Probe Force Microscopy of Single π-Conjugated Molecules. *Nano Lett.*, 14(6):3342–3346, 2014.

[193] W. Melitz, J. Shen, A. C. Kummel, and S. Lee. Kelvin probe force microscopy and its application. *Surf. Sci. Rep.*, 66(1):1–27, 2011.

[194] T. Glatzel, S. Sadewasser, and M. C. Lux-Steiner. Amplitude or frequency modulation-detection in Kelvin probe force microscopy. *Appl. Surf. Sci.*, 210(1–2):84–89, 2003.

[195] P. Rahe, M. Kittelmann, J. L. Neff, M. Nimmrich, M. Reichling, P. Maass, and A. Kühnle. Tuning Molecular Self-Assembly on Bulk Insulator Surfaces by Anchoring of the Organic Building Blocks. *Adv. Mater.*, 25(29):3948–3956, 2013.

[196] L. Bartels. Tailoring molecular layers at metal surfaces. *Nat. Chem.*, 2(2):87–95, 2010.

[197] J. L. Neff and P. Rahe. Insights into Kelvin probe force microscopy data of insulator-supported molecules. *Phys. Rev. B*, 91(8):085424, 2015.

[198] H. Söngen, P. Rahe, J. L. Neff, R. Bechstein, J. Ritala, A. S. Foster, and A. Kühnle. The weight function for charges—a rigorous theoretical concept for Kelvin probe force microscopy. *J. Appl. Phys.*, 119(2):025304, 2016.

[199] C. Barth, T. Hynninen, M. Bieletzki, C. R. Henry, A. S. Foster, F. Esch, and U. Heiz. AFM tip characterization by Kelvin probe force microscopy. *New J. Phys.*, 12(9):093024, 2010.

[200] T. Hynninen, A. S. Foster, and C. Barth. Polarized Tips or Surfaces: Consequences in Kelvin Probe Force Microscopy. *e-J. Surf. Sci. Nanotechnol.*, 9:6–14, 2011.

[201] A. Sadeghi, A. Baratoff, S. A. Ghasemi, S. Goedecker, T. Glatzel, S. Kawai, and E. Meyer. Multiscale approach for simulations of Kelvin probe force microscopy with atomic resolution. *Phys. Rev. B*, 86(7):075407, 2012.

[202] L. N. Kantorovich, A. I. Livshits, and M. Stoneham. Electrostatic energy calculation for the interpretation of scanning probe microscopy experiments. *J. Phys.: Condens. Matter*, 12(6):795–814, 2000.

[203] J. M. R. Weaver. High resolution atomic force microscopy potentiometry. *J. Vac. Sci. Technol.*, 9(3):1559, 1991.

[204] S. Hudlet, M. Saint Jean, C. Guthmann, and J. Berger. Evaluation of the capacitive force between an atomic force microscopy tip and a metallic surface. *Eur. Phys. J. B*, 2(1):5–10, 1998.

[205] A. Sadeghi, A. Baratoff, and S. Goedecker. Electrostatic interactions with dielectric samples in scanning probe microscopies. *Phys. Rev. B*, 88(3):035436, 2013.

[206] M. Guggisberg, M. Bammerlin, C. Loppacher, O. Pfeiffer, A. Abdurixit, V. Barwich, R. Bennewitz, A. Baratoff, E. Meyer, and H. J. Güntherodt. Separation of interactions by noncontact force microscopy. *Phys. Rev. B*, 61(16):11151–11155, 2000.

[207] M. Shimizu, H. Watanabe, K. Anazawa, T. Miyahara, and C. Manabe. Studies on electronic structures of semiconductors by atomic force microscopy. *J. Chem. Phys.*, 110(24):12116–12121, 1999.

[208] M. Nonnenmacher, M. P. O'Boyle, and H. K. Wickramasinghe. Kelvin probe force microscopy. *Appl. Phys. Lett.*, 58(25):2921–2923, 1991.

[209] U. Zerweck, C. Loppacher, T. Otto, S. Grafström, and L. M. Eng. Accuracy and resolution limits of Kelvin probe force microscopy. *Phys. Rev. B*, 71(12):125424, 2005.

[210] L. Collins, J. I. Kilpatrick, S. A. L. Weber, A. Tselev, I. V. Vlassiouk, I. N. Ivanov, S. Jesse, S. V. Kalinin, and B. J. Rodriguez. Open loop Kelvin probe force microscopy with single and multi-frequency excitation. *Nanotechnology*, 24(47):475702, 2013.

[211] F. Mohn, L. Gross, N. Moll, and G. Meyer. Imaging the charge distribution within a single molecule. *Nature Nanotech.*, 7(4):227–231, 2012.

[212] S. Kitamura, K. Suzuki, and M. Iwatsuki. High resolution imaging of contact potential difference using a novel ultrahigh vacuum non-contact atomic force microscope technique. *Appl. Surf. Sci.*, 140(3-4):265–270, 1999.

[213] F. Albrecht, J. Repp, M. Fleischmann, M. Scheer, M. Ondráček, and P. Jelínek. Probing Charges on the Atomic Scale by Means of Atomic Force Microscopy. *Phys. Rev. Lett.*, 115(7):076101, 2015.

[214] O. Takeuchi, Y. Ohrai, S. Yoshida, and H. Shigekawa. Kelvin Probe Force Microscopy without Bias-Voltage Feedback. *Jpn. J. Appl. Phys.*, 46(8S):5626–5630, 2007.

[215] Y. Sugawara, L. Kou, Z. Ma, T. Kamijo, Y. Naitoh, and Y. J. Li. High potential sensitivity in heterodyne amplitude-modulation Kelvin probe force microscopy. *Appl. Phys. Lett.*, 100(22):223104, 2012.

[216] U. Zerweck, C. Loppacher, T. Otto, S. Grafström, and L. M. Eng. Kelvin probe force microscopy of C_{60} on metal substrates: towards molecular resolution. *Nanotechnology*, 18(8):084006, 2007.

[217] S. Kawai, T. Glatzel, H.-J. Hug, and E. Meyer. Atomic contact potential variations of Si(111)-7×7 analyzed by Kelvin probe force microscopy. *Nanotechnology*, 21(24):245704, 2010.

[218] V. W. Bergmann, S. A. L. Weber, F. J. Ramos, M. K. Nazeeruddin, M. Grätzel, D. Li, A. L. Domanski, I. Lieberwirth, S. Ahmad, and R. Berger. Real-space observation of unbalanced charge distribution inside a perovskite-sensitized solar cell. *Nat. Commun.*, 5:5001, 2014.

[219] L. Gross, B. Schuler, F. Mohn, N. Moll, N. Pavliček, W. Steurer, I. Scivetti, K. Kotsis, M. Persson, and G. Meyer. Investigating atomic contrast in atomic force microscopy and Kelvin probe force microscopy on ionic systems using functionalized tips. *Phys. Rev. B*, 90(15):155455, 2014.

[220] L. Collins, J. I. Kilpatrick, I. V. Vlassiouk, A. Tselev, S. A. L. Weber, S. Jesse, S. V. Kalinin, and B. J. Rodriguez. Dual harmonic Kelvin probe force microscopy at the graphene–liquid interface. *Appl. Phys. Lett.*, 104(13):133103, 2014.

[221] K. S. Rao and K. V. Rao. Dielectric dispersion and its temperature variation in calcite single crystals. *Z. Physik*, 216(3):300–306, 1968.

[222] C. G. Malmberg and A. A. Maryott. Dielectric Constant of Water from 0 °C to 100 °C. *J. Res. Nat. Bur. Stand.*, 56(1):369131, 1956.

[223] H. Diesinger, D. Deresmes, and T. Mélin. Noise performance of frequency modulation Kelvin force microscopy. *Beilstein J. Nanotechnol.*, 5:1–18, 2014.

[224] C. Barth and C. R. Henry. Kelvin probe force microscopy on surfaces of UHV cleaved ionic crystals. *Nanotechnology*, 17(7):S155, 2006.

[225] W. R. Smythe. *Static And Dynamic Electricity.* Taylor & Francis, 1989.

[226] J. D. Jackson. *Classical Electrodynamics.* De Gruyter, 3rd edition, 2002.

[227] H. Söngen. Probing charges on an insulating surface in liquids. Viermonate Arbeit zur Qualifikation als Fast-track Doktorand, Johannes Gutenberg-Universität Mainz, 2014.

[228] T. E. Schäffer, J. P. Cleveland, F. Ohnesorge, D. A. Walters, and P. K. Hansma. Studies of vibrating atomic force microscope cantilevers in liquid. *J. Appl. Phys.*, 80(7):3622–3627, 1996.

Acknowledgments

[For data privacy reasons, the acknowledgments have been removed from the electronic version of this thesis.]

Publications and presentations

Peer-reviewed journal articles

- *Quantitative Atomic Force Microscopy*
  H. Söngen, R. Bechstein, A. Kühnle
  Journal of Physics: Condensed Matter (2017) *accepted*
- *Generic Nature of Long-Range Repulsion Mechanism on a Bulk Insulator?*
  J. L. Neff, A. Richter, H. Söngen, C. Venturini,
  A. Gourdon, R. Bechstein, A. Kühnle
  Farad. Discuss. (2017) *accepted*
- *Chemical identification at the solid–liquid interface*
  H. Söngen, C. Marutschke, P. Spijker, E. Holmgren,
  S. Klassen, R. Bechstein, J. Tracey, A. S. Foster, A. Kühnle
  Langmuir **33** (2017) 125
- *Three-dimensional atomic force microscopy mapping at the solid–liquid interface with fast and flexible data acquisition*
  H. Söngen, M. Nalbach, H. Adam, A. Kühnle
  Rev. Sci. Instrum. **87** (2016) 063704
- *The weight function for charges in Kelvin probe force microscopy*
  H. Söngen, P. Rahe, J. L. Neff, R. Bechstein, R. Ritala, A. S. Foster, A. Kühnle
  J. Appl. Phys. **119** (2016) 025304
- *Long-Range Order Induced by Intrinsic Repulsion on an Insulating Substrate*
  J. L. Neff*, H. Söngen*, R. Bechstein, P. Maass, A. Kühnle
  J. Phys. Chem. C, **119** (2015) 24927

  * equal contribution

Manuscripts based on sections 2.2, 3.4, 3.5 and 3.6 are in preparation.

Book chapters

- *A comprehensive theory for imaging charges with KPFM*
  P. Rahe, H. Söngen
  Submitted as contribution to the book “Kelvin Probe Force Microscopy – From

Single Charge Detection to Device Characterization", edited by S. Sadewasser and T. Glatzel

- *Interpretation of KPFM data with the weight function for charges*
  H. Söngen, P. Rahe, R. Bechstein, A. Kühnle
  Submitted as contribution to the book "Kelvin Probe Force Microscopy – From Single Charge Detection to Device Characterization", edited by S. Sadewasser and T. Glatzel

Talks

The presenting author is underlined.

- *Investigating the Mineral–Water Interface using in-situ High-Resolution Atomic Force Microscopy Techniques*
  M. Nalbach, H. Söngen, S. Klassen, R. Bechstein, A. Kühnle
  Kolloquium für Kristallographie und technische Mineralogie, Ludwig-Maximilians-Universität München, January 2017, Germany
- *Chemical Identification of Interfacial Cations by their Hydration Structure*
  H. Söngen, C. Marutschke, P. Spijker, E. Holmgren, I. Hermes, R. Bechstein, S. Klassen, J. Tracey, A. S. Foster, A. Kühnle
  Granada-Münster Tagung GMDM4, November 2016, Münster, Germany
- *Influence of monovalent ions on the calcite (10.4) hydration structure*
  H. Söngen
  5th Bio-AFM summer school, August 2016, Kanazawa, Japan.
- *Three-dimensional atomic force microscopy mapping at the solid–liquid interface with fast and flexible data acquisition*
  H. Söngen, R. Bechstein, M. Nalbach, H. Adam, A. Kühnle
  19th International Conference on non contact Atomic Force Microscopy (NC-AFM), July 2016, Nottingham, United Kingdom
- *Molecular self-assembly on an insulating surface: Long-range order induced by an intrinsic repulsion mechanism*
  J. L. Neff, H. Söngen, R. Bechstein, A. Kühnle
  Physics Boat, June 2015, Helsinki, Finland.
- *Probing charges at the solid–liquid interface with KPFM on insulators*
  H. Söngen, P. Rahe, J. L. Neff, R. Bechstein, A. Kühnle
  18th International Conference on non contact Atomic Force Microscopy (NC-AFM), September 2015, Cassis, France

Poster presentations

The presenting author is underlined.

- *Characteristics of the weight function for charges in different Kelvin probe force microscopy modes*
  H. Söngen, P. Rahe, J. L. Neff, R. Bechstein, A. Kühnle
  598. Heraeus Seminar "Frontiers in Scanning Probe Microscopy", November 2016, Bad Honnef, Germany.
- *The solid–liquid interface: Probing charges on insulators with KPFM*
  H. Söngen, P. Rahe, J. L. Neff, R. Bechstein, A. Kühnle
  Physics Boat, June 2015, Helsinki, Finland.
- *Long-range order induced by intrinsic repulsion*
  J. L. Neff, H. Söngen, R. Bechstein, A. Kühnle
  18th International Conference on non contact Atomic Force Microscopy (NC-AFM), September 2015, Cassis, France.
- *The lateral decay and the sign of the sensitivity towards charges in Kelvin Probe Force Microscopy*
  H. Söngen, P. Rahe, J. L. Neff, R. Bechstein, A. Kühnle
  Summer school "Investigating the Solid-Liquid Interface", September 2015, Mainz, Germany.

Software

Interactive KPFM visualization

I have written an interactive visualization of the KPFM weight function for charges (chapter 4, page 99), which is accessible at `www.self-assembly.uni-mainz.de/kpfm`. The visualization also shows the KPFM signal and various electrostatic quantities that play a role in the context of KPFM.

Interactive virtual AFM

The Igor Pro implementation of the interactive virtual AFM (section 2.2, page 31) can be found at `www.self-assembly.uni-mainz.de/software/ivafm`.